Halo bias renormalisation

Dissertation
zur
Erlangung des Doktorgrades (Dr. rer. nat.)
der
Mathematisch-Naturwissenschaftlichen Fakultät
der
Rheinischen Friedrich-Wilhelms-Universität Bonn

von
Kim Fiona Werner
aus
Braunschweig

Bonn, 2019

Angefertigt mit Genehmigung der Mathematisch-Naturwissenschaftlichen Fakultät der Rheinischen Friedrich-Wilhelms-Universität Bonn.

"Da ist der Orion! Herrlicher als der bestirnte Himmel über uns ist nur das Universum der Logik in uns."

—Professor Abronsius, *Tanz der Vampire, 2. Akt*

Abstract

Modern *galaxy redshift surveys* provide a wealth of information about our Universe. It is the goal to observe luminous objects in the whole sky and as far back in time as possible – from a combination of all their data we then want to learn about when the Universe was born and how it evolved. On these cosmological length scales a whole galaxy can be represented as a single point, amongst billions of others. When we measure the two-dimensional position on the sky for many galaxies, and combine it with their distance (given by their cosmological redshift), we obtain a three-dimensional map of the cosmos. In this map we clearly see that galaxies are not randomly distributed in the Universe – instead they build a specific *large-scale structure* and align in form of a *cosmic web*. In our current concordance model of cosmology the spatial distribution of luminous objects depends heavily on an underlying, non-visible cosmic web. It consists of *dark matter* which does not emit electromagnetic radiation and therefore cannot be observed. Its influence on other particles is purely gravitational, and we know that there must be much more dark matter in the Universe than visible matter – otherwise the luminous cosmic web would look completely different from what we observe. Therefore, it is of utmost interest to infer its exact amount and distribution. Theories of gravitational collapse suggest that the formation of dense luminous structures such as galaxies happens in locations where also the dark matter is rather dense. In a two-step process, first the gravitational collapse of dark matter happens, and within the resulting *haloes* form then the galaxies. The distribution of both haloes and galaxies is therefore *biased* with respect to the dark matter density field. This leads to the conclusion that we can infer information about dark matter by observing a large number of galaxies. While the overall idea of halo (or galaxy) bias is intuitive to understand, the exact dynamics are still heavily debated.

In this study, we aim to shed light on some of the issues connected to bias. The relation between haloes and dark matter is often phrased in form of a *bias expansion* up to a certain order that connects various statistical quantities (*bias operators*) and weighs them with numerical factors (*bias parameters*). It remains an open question which of these operators are really needed for an accurate description, and what the exact values of the bias parameters are. To address these questions, in chapter 2, we run a suite of 40 cosmological N-body simulations and then compare existing bias models piece by piece to the numerical data. After validating the theoretically motivated shape of individual terms in the data, we fit various complete bias relations against the halo distribution to measure the bias parameters. For that we employ a novel routine that includes the covariance matrix of all terms. Then, using a statistical model selection criterion, we infer the optimal number of bias operators and parameters. We find that for the large halo masses in our simulations a four-parameter model gives the best results. The bias parameters we measure compare excellently with previous results from the literature.

Furthermore, with even greater emphasis, in both chapters 2 and 3 we address a rather technical, but pressing complication that arises in bias models which, so far, has been only examined from a theoretical perspective. When modeling the individual statistical expressions

within the framework of cosmological perturbation theory, unphysical extra terms arise at different orders in the expansion. These, while solely due to the mathematical formulation of the problem, distort the measurement of the bias parameters. A correct physical interpretation is therefore made impossible. From theoretical efforts results the approach of *bias renormalisation* that aims at eliminating these terms order by order in a consistent way. For the first time, we apply this method to numerical data, therefore providing the crucial test of its validity. We are fully successful in renormalising halo bias in simulations at first order (linear bias) as we demonstrate in chapter 2. At second order (quadratic and tidal bias), the issue is more delicate, as we show in chapter 3, where we highlight restrictions on the range of scales for which the method provides satisfying results.

Overall, our findings motivate an application of our model and the renormalisation technique to numerical and also possibly observational data. However, they also clearly expose the limitations of employing perturbative techniques for describing the formation of the large-scale structure of the Universe.

Contents

Introduction

1.1 The science of cosmology

Since the early ages of mankind humans have been fascinated with the night sky. Whereas in early civilizations astronomical phenomena have been attributed to religious beliefs and were interpreted within the framework of astrology[1], nowadays we employ modern scientific methods to make sense of what we see when are 'looking up'. The naked human eye can recognize several thousands of stars (Hoffleit and Warren, 1987) when located in a dark place, and by now we know that all these bright dots shine because of the same mechanism that is at work in the Sun – and therefore responsible for life on Earth: Mainly hydrogen is fusing to become helium, and integrated over the mass of the Sun an enormous amount of energy is being released during that process. In dark places without any light pollution we can even see our own galaxy, a barred spiral galaxy called the *Milky Way*. It is visible as a hazy band of light, roughly 30° in width, that spans the whole sky, and by now we know that this band is in fact made up of $\sim 10^{11}$ individual stars of various masses and temperatures (Inglis, 2018). They lie bound in a flat disk, with a bulge of stars in the center, and spiral arms towards the outskirts. The Solar System with the Sun in the center and the Earth as the 3rd innermost planet is hosted by the *Orion spiral arm*, at roughly 8 kpc from the center of the Milky Way[2].

When we go beyond observing with the naked eye we will find that there is more than that. Whereas there reside dozens of billions of stars in the Milky Way, similarly there exist dozens of billions of galaxies themselves – we are by no means special! Neither is the existence of the Solar System including planets a unique occurence, nor is the Milky Way a single island in vast empty space. When employing Earth-bound telescopes with meter-size mirrors or even turning to telescopes installed in space we can observe galaxies of various sizes and shapes, and at various distances away from us. They may come on their own, or, more common, may be bound together in the form of galaxy clusters, hosting a few up until several thousands of galaxies (Beckwith et al., 2006). To give an impression on this, in Fig. 1.1 we show the *Hubble Ultra Deep Field*, a small region in the southern sky that was exposed for a long time with the *Hubble Space Telescope* (hereafter HST). It shows about 10^5 galaxies and galaxy clusters of various sizes, colours and shapes, some of them about 13 Gyr old.

---

[1] For example the yearly flooding of the Nile in ancient Egypt was explained with the rising of the star Sirius (Fitzgerald, 1951).

[2] The astronomical unit Parsec, short for *parallax second*, where $1\,\mathrm{pc} \approx 3.26\,\mathrm{ly}$, is the distance from which 1 AU, i.e. the distance between Earth and Sun, appears as $1''$.

Figure 1.1: The *Hubble Ultra Deep Field* (HUDF), a 10^6 s exposure of an $11'$ region in the southern sky (Beckwith et al., 2006). The image was taken with four different filters and contains about 10^5 objects, mostly galaxies, but also some foreground point sources like stars. It shows the large number and variety (e.g. in colour, luminosity, shape) of galaxies that can be found already in only a small patch of the sky.

In between the galaxies (or galaxy clusters) there is almost nothing. However they are not just randomly distributed. Rather it is the case that they cluster together in the form of two-dimensional *sheets* and one-dimensional *filaments*, encapsulating large empty blobs, called *voids*. Where sheets and filaments intersect, and matter collapses due to gravitational forces, *knots* will form. These are tightly-packed regions in space that host many closely-located galaxies. We call the arrangement of galaxies and galaxy clusters in the form of knots, filaments, sheets and voids the *cosmic web* (Bond, Kofman and Pogosyan, 1996) – on these large spatial scales galaxies can be treated as point-like objects. The cosmic web is revealed when we perform observations not only on single objects, but when we conduct astronomical surveys that cover a large part of the sky. A pioneering example for such a survey is the *2dF Galaxy Redshift Survey* (hereafter 2dFGRS) that in the late 1990s and early 2000s observed more than 2.4×10^6 galaxies in a patch of the sky of $\approx 1500\,\mathrm{deg}^2$ and constructed a three-dimensional map of them (Colless et al., 2001). We show their results in Fig. 1.2 where the observer is located at the center, and the cones to each side represent the viewing angle into the Universe. The cosmic web is clearly visible. However, there is a limit for the formation of structure: Beyond $\sim 200\,\mathrm{Mpc}$ so far there has not been found any clustering of matter (Percival, Baugh et al., 2001). It seems that from this threshold on matter is distributed homogeneously. We will turn to the exact description of the spatial distribution of galaxies (and the absence of them) in section 1.3.
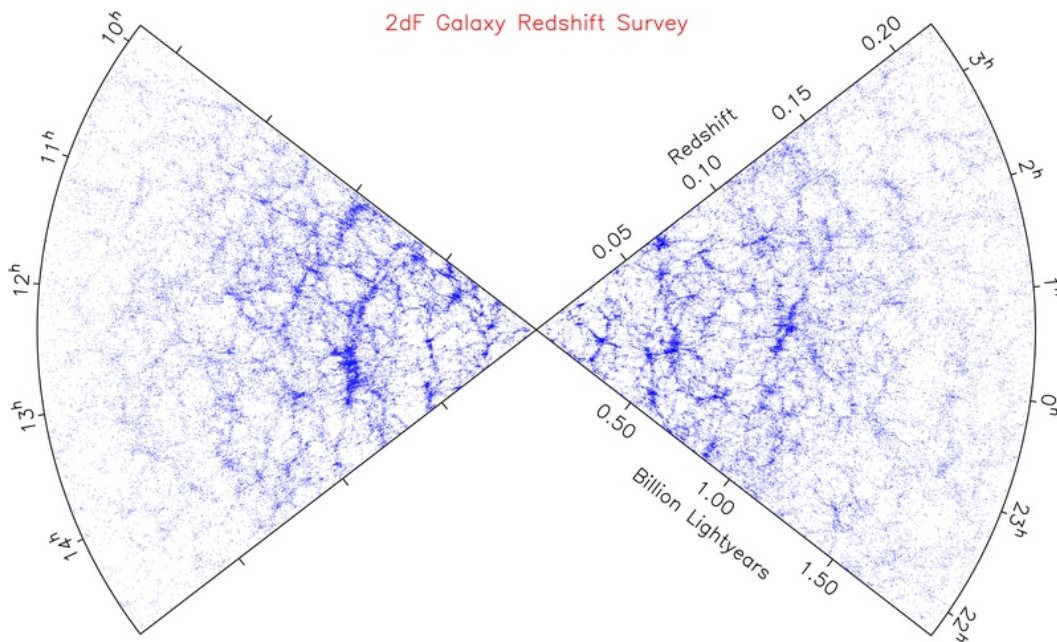
Figure 1.2: The projected two-dimensional spatial distribution of galaxies (represented by the blue dots) as observed with the 2dFGRS (Colless et al., 2001), up until a distance of approximately two billion lightyears. The observer (i.e. the Earth) is in the center, along the sides of the cones we are looking into the Universe. Along the arclength of the cones one of the angular coordinates on the sky changes (the *radial ascension*), the other angular coordinate (the *declination*) was integrated over. The cosmic web is clearly visible especially for small distances from the center. For larger distances it becomes fainter which is due to the observational bias that only the brightest objects can still be observed at these distances.

The enormous space that contains all mentioned above we call the Universe. Per definition, there is only one such object, and it contains all matter that exists. The Universe provides a natural lab where we can study astrophysical objects of various sizes, from planets to the most massive galaxy clusters. The Universe hosts so many of them that we can employ the *scientific method*[3]. For astrophysical objects, we can make claims based on statistical reasoning. However, with only one Universe we need to think a bit differently. The science of exploring and trying to explain the Universe as a whole is the science of cosmology.

Cosmology asks for the most basic questions, grazing even philosophy in some points, and we will name only some of them: How did the Universe come to be? How old and how large is it? Is it static or evolving? What will happen to it in the future? What does it contain? These questions can be easily understood, but the answers are all the more complicated and hard to achieve. We want to understand the Universe as the one thing that it is – this calls for one singular theory that is capable of describing the largest scales of space and time. Ideally it can give insight on the temporal evolution of the Universe, starting from its beginning (commonly dubbed the *Big Bang* – although it did not happen a real Bang; S. Weinberg, 1977) – which was roughly 13.7 Gyr ago, until today. Also it should give information on how its content was produced and which processes govern its distribution and behaviour. Motivated to take on this task, during

---

[3] The scientific method is defined as the intertwinement of deduction and induction to learn about natural phenomena: It means first observing a phenomenon, building a theory from that, making predictions from that theory, and then testing these predictions (and therefore the theory itself) against more observations (more commonly phrased as conducting an experiment).

the last century cosmology evolved into a very active field of research, so that nowadays we have indeed such a *cosmological concordance model* that serves as a theoretical basis to describe the Universe as a whole – on top of this we can then try to explain smaller-scale processes such as astrophysical phenomena. We call this the ΛCDM model (Planck Collaboration, 2018b) which introduces two contributions of yet unknown physical form to the energy or mass budget[4] of the Universe. There are *Dark Energy* (hereafter DE; e.g. Efstathiou, Sutherland and Maddox, 1990, Riess, Filippenko et al., 1998), abbreviated with Λ, and *Cold Dark Matter* (hereafter CDM; e.g. Sofue and Rubin, 2001, Eisenstein et al., 2005). These two substances cannot be observed directly since they do not emit any radiation – but they make up roughly 95% of the energy density! The visible matter that can be directly observed in the form of galaxies, stars etc. and also objects of everyday-life on Earth (like this thesis that you are currently reading) only contributes roughly 5%. Founded on the pillars of *General Relativity* (hereafter GR) – a theory that is able to describe gravity on very larges scales – the ΛCDM model celebrated great success for the last two decades, and matches remarkably well with many observations.

In the following we will elaborate in detail about the cosmological concordance model ΛCDM. We will introduce GR as a tool to describe the evolution of the Universe, which will naturally lead to the result that the behaviour of the Universe as a whole depends much on its content. Building up on this, we will dissect the Universe's matter content into its individual components – in particular we will motivate the introduction of DE and CDM and what 'fingerprints' these two energy density components leave behind in cosmological observables. Further, we will explore the clustering properties of both CDM and the visible matter (hereafter called *baryons*[5]), with explicit focus on the statistical description of the clustering and the connection between CDM and galaxies (*galaxy bias*; Desjacques, Jeong and Schmidt, 2018a). We will introduce the mathematical framework of *cosmological Standard Perturbation Theory* (hereafter SPT; Bernardeau et al., 2002) which serves to understand the formation of the *large-scale structure* of the Universe (hereafter LSS; Peebles, 1980) – and therefore how we can extract cosmological information from galaxy surveys. As a complement to theoretical considerations, we will also elaborate on *cosmological N-body simulations* (e.g. Springel, 2005, Vogelsberger et al., 2014) which have emerged in the last decades as an indispensable tool to understand structure formation down to the very smallest scales, i.e. the inner regions of gravitationally collapsed objects (*haloes*; Navarro, Frenk and S. D. M. White, 1997).

1.2 World models from General Relativity

1.2.1 The Cosmological Principle

If we want to describe the Universe we need to make some *a priori* assumptions from which we can build our whole theory. What we postulate should be reasonable, which means it should be backed up by experiments (or observations in an astrophysical context). Of course one can never completely prove a postulate by definition, but we can find more and more empirical evidence that supports it. In the case of a description of the Universe, we postulate the *Cosmological Principle* (hereafter CP; Linder, 1997). This states that the Universe is homogeneous and

---

[4] From Einstein's theory of *General Relativity* we know that energy and mass can be converted into each other, therefore the two quantities can be used interchangeably.

[5] In a cosmological context the term 'baryons' includes all elementary particles that are not DM, whereas in a particle physics context baryons are only a subgroup of particles, i.e. hadrons with a half-integer spin.

isotropic – it has the same properties in every point and it looks the same in every direction[6]. This assumption is reasonable as can be shown from observations (e.g. Scaramella, Vettolani and Zamorani, 1991, Campanelli et al., 2011, Planck Collaboration, 2018b).

We need to combine the properties of homogeneity and isotropy with GR. In the framework of GR space-time is described as a four-dimensional manifold which is characterized by its metric field $g_{\mu\nu}$. It determines both distances of events (in space and time) and the world-lines of freely falling particles when applying the *geodesic equation*. Distances are computed from the metric tensor as

$$\mathrm{d}s^2 = g_{\mu\nu}\mathrm{d}x^\mu\mathrm{d}x^\nu\,, \tag{1.1}$$

where we apply Einstein's summation convention and sum over indices that appear twice. To compute a metric that incorporates the CP we need to assume that there exists a set of *comoving fundamental observers* who all experience the Universe in the same fashion if they synchronize their clocks, and who all follow the mean motion of matter and radiation. After a lengthy calculation, invoking the afore-mentioned conditions, one arrives at the *Friedmann-Lemaître-Robertson-Walker metric* (hereafter FLRW metric).

1.2.2 The Friedmann-Lemaître-Robertson-Walker metric

Robertson (1935) and Walker (1937) showed that the CP leads to a metric that can be written as

$$\mathrm{d}s^2 = c^2\mathrm{d}t^2 - a^2(t)\left[\mathrm{d}\chi^2 + f_k^2(\chi)\left(\mathrm{d}\theta^2 + \sin^2\theta\,\mathrm{d}\phi^2\right)\right]\,, \tag{1.2}$$

where c is the speed of light[7], χ is the comoving radial coordinate, θ and ϕ are the angular coordinates on a unit sphere, t is the cosmic time and $a(t)$ is the *scale factor*. The scale factor is normalized such that $a(t = 0) = a(t_0) = 1$ and allows the freedom of a spatial expansion or contraction of the metric. Since it only depends on the cosmic time and not on the spatial coordinates, it factorizes, and the expansion will be homogeneous (we will show in section 1.2.3 why only expansion and not contraction describes the real Universe). Using the scale factor we can introduce *comoving coordinates* $\mathbf{x}$ and *physical coordinates* $\mathbf{r}$ that are related via

$$\mathbf{r} = a(t)\,\mathbf{x}\,. \tag{1.3}$$

In the FLRW metric $f_k(\chi)$ is the *comoving angular diameter distance*, i.e. the distance inferred from the diameter under which an observer sees an object of fixed size. It depends on the *curvature parameter k*,

$$f_k(\chi) \equiv \begin{cases} \frac{\sin\left(\sqrt{k}\chi\right)}{\sqrt{k}} & \text{for } k > 0 \\ \chi & \text{for } k = 0 \\ \frac{\sinh\left(\sqrt{-k}\chi\right)}{\sqrt{-k}} & \text{for } k < 0\,. \end{cases} \tag{1.4}$$

Note the difference between the curvature of space at fixed t (which is described by k) and the curvature of space-time (which is described by the *Riemann curvature tensor* in *Einstein's field equations*, hereafter EFEs). Space can be flat (in the case of $k = 0$, where the metric reduces to the Euclidean case), but space-time might and most certainly will still be curved if there is any

---

[6] This is an extension of the *Copernican Principle* that only postulates homogeneity.
[7] $c = 3 \times 10^8\,\mathrm{m\,s}^{-1}$

matter contained in it.

1.2.3 Friedmann-Lemaître models

For now, we are interested in the evolution of the Universe as a whole, as described by the FLRW metric, and not in individual events happening at a certain point in space-time. This means we would like to know a special form of the scale factor $a(t)$ since this contains information about the homogeneous and isotropic scaling. To achieve this, we need to plug in the metric into EFEs, given as

$$G_{\mu\nu} = \frac{8\pi G}{c^4}T_{\mu\nu} - \Lambda g_{\mu\nu}\,, \tag{1.5}$$

where G is the gravitational constant[8], $T_{\mu\nu}$ is the *stress-energy tensor*, dependent on the energy content, Λ is the *cosmological constant* (the same constant we already used to describe DE, we will explore the interpretation later on) and $G_{\mu\nu}$ is the *Einstein tensor*, given as

$$G_{\mu\nu} = R_{\mu\nu} - \frac{1}{2}g_{\mu\nu}R\,. \tag{1.6}$$

Here, $R_{\mu\nu}$ is the *Ricci tensor* and R is the *Ricci scalar*. They can be computed from the Riemann curvature tensor $R^{\sigma}{}_{\mu\nu\rho}$ via contraction,

$$R_{\mu\nu} \equiv R^{\lambda}{}_{\mu\nu\lambda}\,, \tag{1.7}$$

and

$$R \equiv R_{\mu}{}^{\mu} = g_{\mu\nu}R^{\mu\nu}\,. \tag{1.8}$$

The Riemann curvature tensor however consists of a combination of derivatives of the metric up until second order, so that in the end, apart from a few constants, the independent input quantities of EFEs are essentially only the stress-energy tensor and the metric itself. Plugging in the metric, it can be shown that the type of matter contents must be a homogeneous perfect fluid with density $\rho(t)$ and pressure $p(t)$. From this calculation, that we omit here, follow two independent equations, the *Friedmann equations*:

$$\left(\frac{\dot{a}}{a}\right)^2 = \frac{8\pi G}{3}\rho - \frac{kc^2}{a^2} + \frac{\Lambda c^2}{3}\,, \tag{1.9}$$

$$\frac{\ddot{a}}{a} = -\frac{4\pi G}{3}\left(\rho + \frac{3p}{c^2}\right) + \frac{\Lambda c^2}{3}\,, \tag{1.10}$$

where a dot denotes a derivative with respect to the time coordinate. These equations can be interpreted in the sense that the r.h.s., i.e. the different energy densities that were introduced by the stress-energy tensor, govern the l.h.s., i.e. the evolution of the scale factor in time. The individual contributions of the energy density are split into a term for 'normal' matter (known particles with or without mass – where the latter is also called radiation –, described by ρ), a curvature term (described by k) and a term with a constant energy density of yet unknown physical origin (described by Λ; we will soon see why we need this term).

We know that the Universe is expanding. This was shown by Hubble and Humason (1931),

---

[8] $G = 6.67 \times 10^{-11}\,\mathrm{N\,m^2\,kg^{-2}}$

who performed the observations, and Lemaître (1927), who developed the theory. They found that the vast majorities of galaxies in the Universe is moving away from us, and they recede faster the farther they are away. In practice, Hubble and Humason (1931) measured the distance from the pulsation period of cepheids, which is correlated with their intrinsic luminosity. From the comparison of absolute and apparent magnitude one can therefore infer the distance. Velocity measurements via spectroscopy had already been provided earlier by Slipher (1917) where it was found that certain spectral lines were shifted to the side of the spectrum with longer wavelengths. Interpreting this *redshift* as a Doppler shift one can calculate a recession velocity. This relation can be written as the *Hubble-Lemaître law*,

$$v = H_0 D, \tag{1.11}$$

where v is the recession velocity, D is the distance and H_0 is the constant of proportionality, the *Hubble constant*. Its dimension is the inverse of time, and it is often parametrized as $H_0 = h \times 100\,\mathrm{km\,s^{-1}\,Mpc^{-1}}$ where the variable h accounts for the measurement uncertainty that came with the value of H_0 for many decades – even in modern cosmological calculations h is still kept when working in comoving space, e.g. without taking the expansion into account. We show the original Hubble diagram in Fig. 1.3 where the recession velocity is plotted against distance for a set of objects. Apart from some scatter a linear relation is clearly visible. However, Hubble was only able to measure this relation for galaxies that were close by. For farther-away objects, the relation between velocity and distance becomes non-linear, and the redshift cannot be interpreted as a Doppler shift anymore, but rather as a *cosmological redshift*, due to the expansion of the Universe. Related to the Hubble constant we introduce the time-dependent Hubble function that can be computed from the relationship between physical and comoving coordinates as

$$\dot{\mathbf{r}} = \dot{a}(t)\mathbf{x} = \frac{\dot{a}(t)}{a(t)}\mathbf{r} \equiv H(t)\mathbf{r}. \tag{1.12}$$

It is also called the *expansion rate* of the Universe, and one defines $H_0 \equiv H(t = 0)$. From these considerations we can define the beginning of the Universe that was a time t ago as the event when $a(t) = 0$[9]. The evolution of the scale factor and the Hubble function we can then calculate from the Friedmann equations, depending on the matter densitites of the Universe.

1.2.4 The matter content of the Universe

From the two Friedmann equations given in section 1.2.3 we can derive a third equation, the *adiabatic equation*,

$$\mathrm{d}(\rho c^2 r^3) = -p\,\mathrm{d}(r^3), \tag{1.13}$$

which contains information about the time dependence of the matter components. If we assume an equation of state $p = w\rho$ to hold (with w a constant that is specific for each matter component), the adiabatic equation yields the solution

$$\rho(t) = \rho_0 a^{-3(w+1)}, \tag{1.14}$$

which tells us that the matter components scale with a, the exact behaviour depending on w. We normalize the equation such that $\rho_0 = \rho(t = 0)$, i.e. when $a = 1$.

To obtain the exact evolution we need to specify the individual matter components. One of

---

[9] A well-defined beginning of the Universe does not exist in all world models, however.

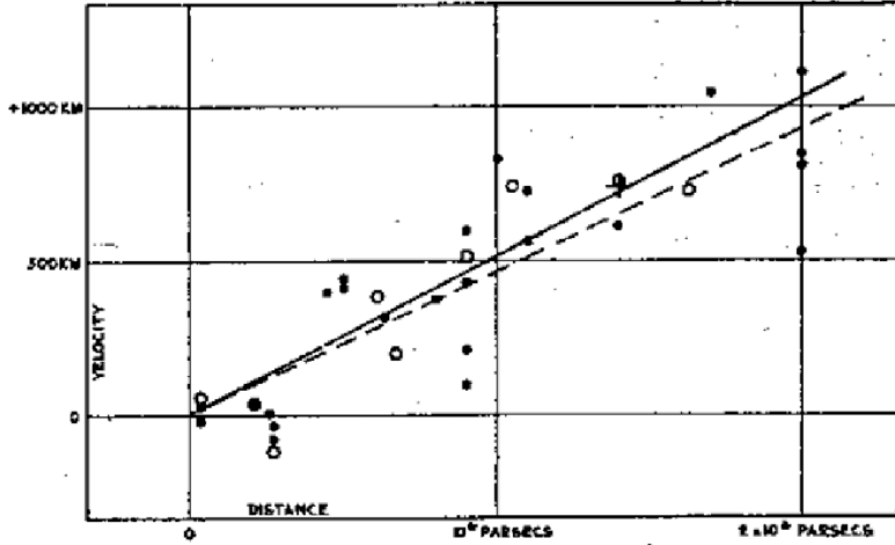**Velocity-Distance Relation among Extra-Galactic Nebulae.**

FIGURE 1

Figure 1.3: The original recession-velocity-versus-distance plot done by Hubble (1929). Plotted are 'extragalactic nebulae' (the term 'galaxy' was not yet common at the time) whose velocity has been inferred from spectroscopy. The distance was calculcated via the period-luminosity relation for variable cepheid stars – the period of the variability is observed, from this the luminosity is inferred, and then from this the distance can be computed via the distance modulus. The solid line is a linear fit to the filled circles that represent the individual nebulae. The dashed line is a fit to the empty circles that represent the nebular grouped together. From the slope of the lines follows the Hubble constant.

them is *dust*, i.e. particles that have mass (such as protons, neutrons, electrons) and that we assume to have zero pressure ($p = 0$ and therefore $w = 0$). This assumption is justified if the particles are non-relativistic, i.e. $p \ll w\rho$. We thus obtain

$$\rho_{\mathrm{m}}(t) = \rho_{\mathrm{m}0}\, a^{-3}(t)\,. \tag{1.15}$$

The next component is *radiation*, i.e. massless relativistic particles. For these it can be shown that the equation of state then needs to be $p = \rho c^2/3$, therefore $w = 1/3$. We find

$$\rho_{\mathrm{r}}(t) = \rho_{\mathrm{r}0}\, a^{-4}(t)\,. \tag{1.16}$$

The third and last component is *vacuum energy*. It is the energy density of empty space and is represented by the cosmological constant Λ. It has the unintuitive equation of state $p = -\rho$, which means that the pressure is negative and $w = -1$. This yields

$$\rho_{\Lambda}(t) = \rho_{\Lambda 0} = \mathrm{const} = \frac{\Lambda c^2}{8\pi G}\,, \tag{1.17}$$

where the last step was obtained from dividing equation (1.9) by $8\pi G/3$ and reading off the expression. To simplify calculations, from now on we interpret the total density ρ as $\rho = \rho_{\mathrm{m}} + \rho_{\mathrm{r}} + \rho_{\Lambda}$.

We also introduce the *critical density* ρ_{cr}. This quantity is the total density in the case of zero curvature (ρ_0 for $k = 0$). We therefore obtain from equation (1.9)

$$\rho_{cr} = \frac{3H_0^2}{8\pi G}.$$
(1.18)

If the total density is larger than the critical, the Universe will be positively curved, if it is smaller, negatively.

1.2.5 The cosmological parameters

We are now in the position to define the *cosmological density parameters*. These dimensionless quantities are defined as the respective matter densities, normalized to the critical density,

$$\Omega_i = \frac{\rho_{i0}}{\rho_{cr}},$$
(1.19)

where we evaluate ρ_i at t_0. We can further define

$$\Omega_0 = \Omega_m + \Omega_r + \Omega_\Lambda.$$
(1.20)

For a flat universe, it will be $\Omega_0 = 1$, for a positively or negatively curved one it will be $\Omega_0 > 1$ or $\Omega_0 < 1$. Using these definitions, we can rewrite equation (1.9) as

$$H^2 = H_0^2 \left[\Omega_r \, a^{-4} + \Omega_m \, a^{-3} + (1 - \Omega_0) \, a^{-2} + \Omega_\Lambda \right].$$
(1.21)

One of the main goals of the observational side of cosmology is to measure these cosmological density parameters plus the Hubble constant to high precision, and a lot of efforts are spent to achieve this. Modern cosmology has various tools at hand that complement each other which allows to cross-check the different methods for systematic errors and break degeneracies between parameters. The basic idea is always the same: Cosmological observables, like the clustering of galaxies that we already mentioned earlier, depend on the cosmological parameters. If the observables can be both modelled and measured properly, the parameters can be inferred. Some more examples of cosmological tools are CMB[10] measurements, weak-lensing[11] surveys, counting of galaxy clusters[12] and Supernovae Ia (hereafter SNeIa) observations[13].

In Table 1.1 we present the results of a few selected cosmological parameters derived from state-of-the-art CMB measurements (Planck Collaboration, 2018b) and SNeIa observations (Riess, Macri et al., 2016, Jones et al., 2018), assuming a flat Universe ($k = 0$ as measured e.g. by Abbott et al., 2019). It becomes clear that while results from different probes are similar,

---

[10] The *Cosmic Microwave Background* is almost-perfect blackbody radiation of $T = 2.73\,\mathrm{K}$, a relic from only $380\,000\,\mathrm{yr}$ after the Big Bang when electrons and nuclei combined for the first time, and the Universe became transparent. See section 1.5.2 for more.

[11] The deflection of light by a gravitational potential, described by GR, is called *Gravitational Lensing*. There are various lensing regimes, in the weak regime, where the potential is small, cosmological information can be inferred using statistical methods.

[12] From counting of singular objects such as galaxy clusters their *mass function*, i.e. the number distribution in mass, can be inferred, which depends on cosmology.

[13] SNeIa are *standard candles* which means that through calibration techniques their luminosity and absolute magnitude can be obtained. The comparison with their apparent magnitude gives their distance. This distance is compared to that inferred from their redshift which is cosmology-dependent. See section 1.2.6 for more.
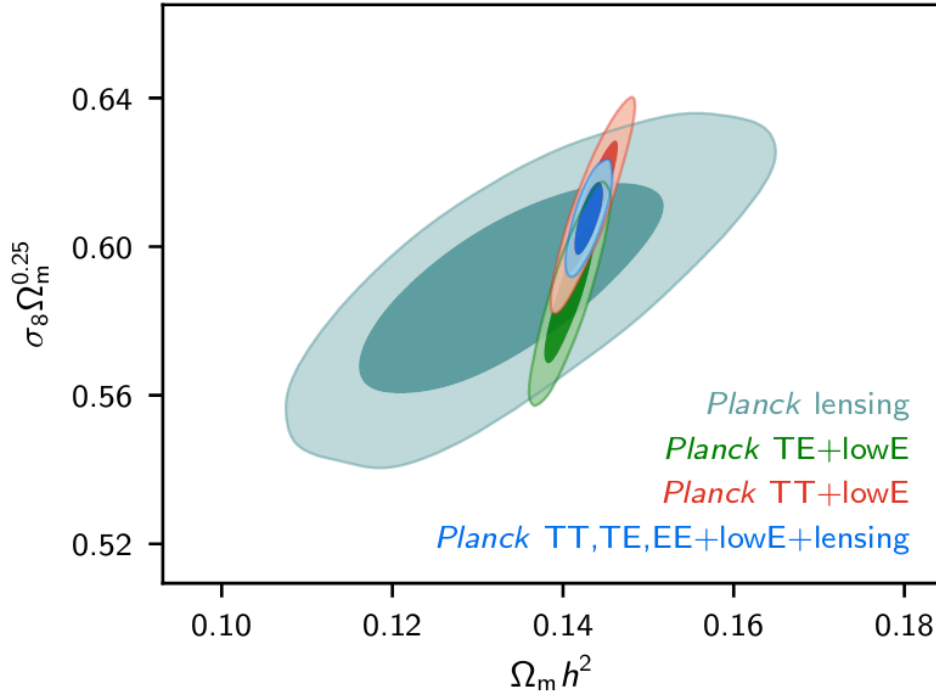
Figure 1.4: The two-dimensional posterior distributions for two degenerate combinations of cosmological parameters, i.e. $\Omega_{\mathrm{m}}h^2$ and $\sigma_8\Omega_{\mathrm{m}}^{0.25}$ for the ΛCDM model (Planck Collaboration, 2018b). The dark-shaded area represents the 68%, the light-shaded area the 95% credibility intervals. The smaller the area covered by the intervals, the better constrained are the parameters. The different colours represent different combinations of data sets taken by the Planck satellite – the more data sets are included, the smaller are the ellipses.

Table 1.1: Four selected cosmological parameters, i.e. the matter density Ω_{m}, the vacuum energy density Ω_Λ, the Hubble constant H_0 and the age of the Universe (Planck Collaboration, 2018b; Riess, Macri et al., 2016; Jones et al., 2018). We compare two different inferences and state both the value and the error range (the age however cannot be inferred from the Riess16+Jones18 analysis).

Parameter	Planck18	Riess16+Jones18
Ω_{m}	0.311 ± 0.006	0.272 ± 0.014
Ω_Λ	0.689 ± 0.006	0.718 ± 0.012
$H_0\,[\mathrm{km\,s^{-1}\,Mpc^{-1}}]$	67.66 ± 0.42	72.52 ± 1.75
Age [Gyr]	13.787 ± 0.020	–

there is still some tension that needs to be alleviated either by introducing new physics or by reducing systematic errors. In Fig. 1.4 we illustrate the interpretation process of cosmological information – plotted against each other are a combination of parameters (h, Ω_{m}, and σ_8 that we will explain in section 1.4.2), and we see that the parameters are slightly degenerate with each other. The darker the respective region in the plot, the more likely is that value for the parameter combination – thus, the smaller the ellipse, the better the constraints.

1.2.6 Dark Matter and Dark Energy – the ΛCDM model

From observational programs it was found that there exist two exotic matter components in the Universe that we call *Dark Matter* and *Dark Energy*. As we already mentioned in section 1.1 this *dark sector* cannot be observed directly, but there is a lot of indirect evidence that calls for its existence.

DM does not emit any electromagnetic radiation, however its gravitational influence emerges on a variety of scales: Rotation curves of galaxies are measured as flat where they should actually drop at large radii if one assumes Keplerian rotation with a potential originating only from visible baryonic matter (Sofue and Rubin, 2001). Similar reasoning can be applied for hot gas in galaxy clusters – from X-ray measurements its temperature can be inferred, which is so high that without the gravitational pull of DM the gas would actually be evaporating from the cluster (Allen, Evrard and Mantz, 2011). Furthermore, the cosmic web would not exist in its observed form without a 'backbone' of DM – clustering processes on large scales would come out much weaker in general (Eisenstein et al., 2005). Theoretical considerations allow for different kinds of DM that are called *cold*, *warm* or *hot*, and correspond to particles that are non-relativistic, relativistic or ultra-relativistic (Primack and Gross, 2001). Comparing quantitative predictions for different DM types against data one finds that DM in our Universe is cold (Bardeen et al., 1986, Jenkins et al., 1998), therefore explaining part of the name of the current concordance model ΛCDM.

The concept of DE was manifested through influential work by Riess, Filippenko et al. (1998) and Perlmutter et al. (1999) which later resulted in a Nobel prize. Using SNeIa as standard candles, they showed that the Universe is currently in a phase of accelerated expansion. This fact has been confirmed in many other works after that (for an overview see Huterer and Shafer, 2018). Such an expansion history is only possible if we infer a contribution to the energy budget whose density stays constant in time, as can be shown from the Friedmann equations. In the ΛCDM framework the physical quantity DE is included via the cosmological constant Λ. Theoretical extensions to this describe DE also as a time-dependent quantity (e.g. Chevallier and Polarski, 2001), but so far no robust observational evidence has been found to support deviance from a constant (Suzuki et al., 2012).

1.2.7 Cosmological distance measurements

For the inference of cosmological information it is crucial to obtain the position of astrophysical sources (i.e. to construct maps) in three dimensions – the two-dimensional position on the sky can be easily measured, more difficult however is to obtain the distance along the line of sight. In curved spaces, there does not exist one 'true' distance – we can define different concepts of distance that need to be applied in the correct context. The issue is complicated even more by the fact that when we look deep into the Universe we are actually looking back in time (along the *past lightcone*) due to the speed of light being finite. One common way to deal with these complications is to introduce the concept of cosmological redshift as a distance indicator.

Astrophysical sources (e.g. galaxies) emit electromagnetic radiation at specific wavelengths. If they are far away, their light will get shifted to longer wavelengths on its way to us due to the expansion of the Universe – it gets redshifted. The farther away a source is, the stronger this effect will be. Therefore, the redshift z that is easily accessible through spectroscopic
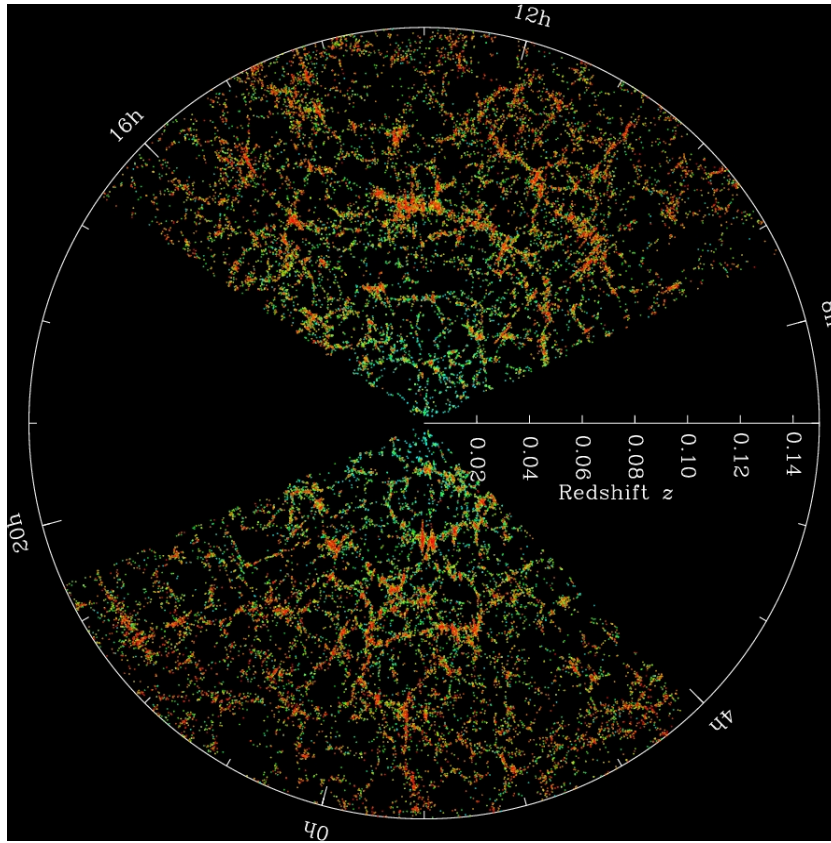
Figure 1.5: Plotted is the same as in Fig. 1.2, but with more recent data taken by the Sloan Digital Sky Survey (Albareti et al., 2017). The map was built from the data of SDSS-III, i.e. stage three of the survey. Stage four is currently in operation, with eBOSS (see text) being one of the surveys most relevant for cosmology.

measurements can be used as a distance indicator. It is defined as

$$z \equiv \frac{\lambda_{\mathrm{obs}} - \lambda_{\mathrm{e}}}{\lambda_{\mathrm{e}}} = \frac{\lambda_{\mathrm{obs}}}{\lambda_{\mathrm{e}}} - 1 \,, \tag{1.22}$$

where λ_{obs} is the observed wavelength on Earth and λ_{e} is the emitted wavelength at the position of the source. This definition is reasonable when we explore how to compute the actual comoving physical separation χ between two objects. From the FLRW metric, we find for radial light rays (i.e. $\mathrm{d}\theta = \mathrm{d}\phi = 0$) that

$$\chi = \int_{t}^{t_0} \frac{\mathrm{d}t'}{a(t')} \,, \tag{1.23}$$

where χ is a quantity independent of time by definition. Therefore, the same holds for the r.h.s. as

$$\frac{\mathrm{d}t}{a(t)} = \frac{\mathrm{d}t_0}{a(t_0)} \,. \tag{1.24}$$

A time interval is the inverse of a frequency so that we find

$$\frac{\mathrm{d}t_0}{\mathrm{d}t} = \frac{\nu}{\nu_0} = \frac{a(t_0)}{a(t)} = \frac{1}{a(t)} = z + 1 \,, \tag{1.25}$$

where in the last step we made use of equation (1.22) since the ratio of two frequencies is the inverse of the ratio of two wavelengths. The redshift therefore emerges as the quantity of choice when we want to give information about the distance of an object or about the *look-back time* towards an object, i.e. the time span that we look into the past when observing said object. Per definition it is $z(t_0) = 0$.

Astronomical surveys that span a large portion of the sky and whose goal is the three-dimensional mapping of the cosmos are therefore called *redshift surveys*, since the information in the third coordinate along the line of sight is given in the form of a redshift. A survey is called the deeper, the higher its maximum obtainable redshift is. Surveys that map the clustering of galaxies and galaxy clusters are of this kind[14]. In section 1.1 we already mentioned the 2dFGRS, a more recent one is the Sloan Digital Sky Survey IV (hereafter SDSS-IV; Albareti et al., 2017), the fourth stage of a survey using a custom-built 2.5 m telescope at the Apache Point Observatory, and of particular interest is their *Extended Baryon Oscillation Spectroscopic Survey* (hereafter eBOSS; Dawson et al., 2016). eBOSS was started in 2014 and aims at precisely mapping more than 2.5×10^5 galaxies in the redshift range of $0.6 < z < 2.2$. It builds upon the legacy of SDSS-III from which we show the projected two-dimensional map in Fig. 1.5. Other planned and upcoming projects are e.g. *Euclid* (Amendola et al., 2018) and the *Large Synoptic Survey Telescope* (Zhan and Tyson, 2018).

1.3 Cosmological structure formation

All the calculations we performed in the previous section only describe a homogeneous and isotropic Universe since we invoked the CP. However, we were also talking about astrophysical objects such as stars and galaxies – obviously homogeneity and isotropy do not hold perfectly. To understand this we need to pay attention that the Universe as a whole and individual objects are modelled on completely different scales. We already mentioned in section 1.1 that structures are only found on scales below $\sim 200\,\mathrm{Mpc}$. This is where the formation of individual objects and the LSS happens. Above this scale, the Universe becomes homogeneous and isotropic, and therefore can be described employing the Friedmann-Lemaître world models. For smaller scales we need another theory whose goal it should be to explain how actually galaxies, galaxy clusters and the cosmic web form. This can be achieved in the framework of *cosmological structure formation*[15].

1.3.1 Dark matter as a fluid

In general, structure formation is a very complicated process – it is in principle an N-body problem with an enormous amount of particles that interact with each other through various forces. When describing cosmological processes we are on such large scales that all other forces besides gravity can be safely neglected – still it is hard and practically impossible to treat structure formation analytically as an N-body problem (this kind of treatment is performed by cosmological N-body simulations that we will describe in section 1.5). The solution is to turn to the framework of hydrodynamics and treat matter as a fluid instead, so that we do not need to follow individual particles, but instead describe smooth fields of density ρ and velocity $\mathbf{u}$.

---

[14] For an overview about cosmology from clustering see Percival (2007).

[15] For an overview and also many detailed derivations see the influential book by Peebles (1980).

We can simplify the problem by only describing the structure formation of DM and forget about baryons for now. This is justified since the dust component of the Universe contains much more DM than baryons[16] (Planck Collaboration, 2018b). Treating DM as a fluid means that this approximation will break down on some smaller scale – this is because DM consists of collisionless particles that only interact gravitationally. Therefore at small scales multi-streams will occur, which means that at one position in space particles will move in different directions so that the velocity field is not well-defined anymore. Another simplification that we already made when introducing dust is the absence of pressure. Also we will only concentrate on the *matter-dominated epoch* of the Universe, i.e. where the matter term in the Friedmann equations dominates. This means we can neglect radiation, $\Omega_r = 0$.

Taking all this into account we can write the fluid equations for the DM density and velocity,

$$\frac{\partial \rho}{\partial t} + \nabla_r(\rho\, \mathbf{u}) = 0 \qquad\qquad \text{Continuity equation,} \qquad (1.26)$$

$$\frac{\partial \mathbf{u}}{\partial t} + (\mathbf{u} \cdot \nabla_r)\mathbf{u} = -\nabla_r \phi \qquad\qquad \text{Euler equation,} \qquad (1.27)$$

$$\nabla_r^2 \phi = 4\pi G\rho - \Lambda \qquad\qquad \text{Poisson equation,} \qquad (1.28)$$

where $\rho = \rho(\mathbf{r}, t)$ and $\mathbf{u} = \mathbf{u}(\mathbf{r}, t)$. We switch from writing the fields in physical coordinates $\mathbf{r}$ to comoving coordinates $\mathbf{x}$, which gives

$$\rho(\mathbf{r}, t) = \hat{\rho}\left(\frac{\mathbf{r}}{a(t)}, t\right) = \hat{\rho}(\mathbf{x}, t), \qquad (1.29)$$

$$\mathbf{u}(\mathbf{r}, t) = \dot{a}\mathbf{x} + \mathbf{v}(\mathbf{x}, t) = \frac{\dot{a}}{a}\mathbf{r} + \mathbf{v}\left(\frac{\mathbf{r}}{a(t)}\right), \qquad (1.30)$$

$$\Phi(\mathbf{x}, t) \equiv \phi(\mathbf{r}, t) + \frac{\ddot{a}a}{2}|\mathbf{x}|^2, \qquad (1.31)$$

where $\mathbf{v}$ can be interpreted as the *peculiar velocity* (i.e. the velocity without the contribution of the expansion of the Universe, the *Hubble flow*) and Φ is defined as the *comoving potential*. We also introduce the *density contrast* $\delta(\mathbf{x}, t)$, defined as

$$\delta = \frac{\hat{\rho} - \bar{\rho}}{\bar{\rho}}. \qquad (1.32)$$

With these expressions we can translate the fluid equations to comoving coordinates in δ and $\mathbf{v}$,

$$\frac{\partial \mathbf{v}}{\partial t} + \frac{\dot{a}}{a}\mathbf{v} + \frac{1}{a}(\mathbf{v} \cdot \nabla_x)\,\mathbf{v} = -\frac{1}{a}\nabla_x \Phi, \qquad (1.33)$$

$$\frac{\partial \delta}{\partial t} + \frac{1}{a}\nabla_x[(1 + \delta)\,\mathbf{v}] = 0, \qquad (1.34)$$

$$\nabla_x^2 \Phi = \frac{3H_0^2\Omega_m}{2a}\delta. \qquad (1.35)$$

Depending on the cosmological parameters H_0 and Ω_m this set of coupled differential equations describes CDM inhomogenities in density and velocity for a certain epoch with scale factor a.

---

[16] In fact the density parameter of matter Ω_m can be split into Ω_c for CDM and Ω_b for baryons, with $\Omega_b/\Omega_c \approx 1/5$.

1.3.2 Linear theory

The set of equations (1.33) – (1.35) cannot be solved analytically. One option is to restrict the analysis to small perturbations in density and small peculiar velocity. In this case the fluid equations can be linearized in these quantities which gives

$$\frac{\partial \delta}{\partial t} + \frac{1}{a}\nabla_x \cdot \mathbf{v} = 0\,, \tag{1.36}$$

$$\frac{\partial \mathbf{v}}{\partial t} + \frac{\dot{a}}{a}\mathbf{v} = -\frac{1}{a}\nabla_x \Phi\,, \tag{1.37}$$

and the Poisson equation which is already linear. After performing some algebra on the set of equations we find the differential equation

$$\frac{\partial^2 \delta(\mathbf{x}, t)}{\partial^2 t} + 2H(t)\frac{\partial \delta(\mathbf{x}, t)}{\partial t} - \frac{3H_0^2 \Omega_{\mathrm{m}}}{2a^3}\delta(\mathbf{x}, t) = 0\,, \tag{1.38}$$

whose solution factorizes in $\mathbf{x}$ and t and therefore we can write the ansatz

$$\delta(\mathbf{x}, t) = D_+(t)\,\delta(\mathbf{x}, 0) + D_-(t)\,\delta(\mathbf{x}, 0)\,. \tag{1.39}$$

From the shape of this expression it becomes clear that in linear theory, the spatial behaviour of the density fluctuations is solely determined by the initial conditions $\delta(\mathbf{x}, 0)$. Their evolution in time is described by the two prefactors $D_+(t)$ and $D_-(t)$. Inserting this ansatz into equation (1.38) we find a differential equation for $D_{\pm}(t)$,

$$\ddot{D}_{\pm} + 2H(t)\dot{D}_{\pm} - \frac{3H_0^2 \Omega_{\mathrm{m}}}{2a^3}D_{\pm} = 0\,. \tag{1.40}$$

The Hubble function $H(t)$ is one solution of this equation, but it is decreasing in time and therefore $\propto D_-(t)$, which means that it is not relevant for structure formation at late times in the Universe. However, following Sturm-Liouville theory, we can use it to construct the second solution,

$$D_+(a) \propto \frac{5\Omega_{\mathrm{m}}H(a)}{2H_0} \int_0^a \frac{\mathrm{d}a'}{\left[\Omega_{\mathrm{r}}a'^{-2} + \Omega_{\mathrm{m}}a'^{-1} + \Omega_{\Lambda}a'^2\right]^{3/2}}\,, \tag{1.41}$$

for a flat universe as is the case for our Universe. We define $D(a)$ (and therefore also $D(t)$) as $D(a) \equiv D_+(a)/D_+(1)$ which is called the *linear growth factor*.

It remains an open problem at this stage how to describe not only the temporal evolution, but to find a theory that gives an explicit expression for the initial conditions $\delta(\mathbf{x}, 0)$. We will come back to this in section 1.4.1.

1.3.3 Non-linear evolution - Standard Perturbation Theory

Until now, we were only describing density fluctuations at the very largest scales. When we perform a spatial Fourier transformation (hereafter FT) on $\delta(\mathbf{x}, t)$, it can be shown that in linear theory each Fourier mode $\mathbf{k}$ evolves independently from the other – the modes do not couple to each other. This changes when we move onto describing more non-linear ('intermediate') scales. The general assumption is that the linear density field still dominates, and non-linear gravitational interaction between particles imposes only small corrections onto it. This means

we can write the spatial behaviour of δ as an ordered expansion,

$$\delta(\mathbf{x}) = \delta_1(\mathbf{x}) + \delta_2(\mathbf{x}) + \cdots + \delta_n(\mathbf{x}) + O(\delta_{n+1}), \qquad (1.42)$$

where δ_n is $O(\delta_1^n)$. This ansatz for the non-linear density field and the following calculations are performed within the framework of cosmological *Standard Perturbation Theory* (hereafter SPT; Bernardeau et al., 2002). The easiest way to proceed and to explicitly calculate the higher-order contributions to δ is to move to Fourier space. We define the FT as

$$y(\mathbf{k}) = \int_{-\infty}^{\infty} y(\mathbf{x}) e^{-i\mathbf{x}\cdot\mathbf{k}} \frac{\mathrm{d}^3 x}{(2\pi)^3}. \qquad (1.43)$$

Applying the FT to the fully non-linear fluid equations (1.33) – (1.35) and performing a bit of algebra, we find a coupled set of differential equations for δ and θ (with $\theta(\mathbf{x}) = \nabla \cdot \mathbf{v}(\mathbf{x})$):

$$\frac{\partial \delta(\mathbf{k}, t)}{\partial t} + \theta(\mathbf{k}, t) = -\int \delta_{\mathrm{D}}[\mathbf{k} - (\mathbf{k}_1 + \mathbf{k}_2)] \, \alpha(\mathbf{k}_1, \mathbf{k}_2) \, \theta(\mathbf{k}_1, t) \, \delta(\mathbf{k}_2, t) \, \mathrm{d}\mathbf{k}_1 \, \mathrm{d}\mathbf{k}_2$$

$$\frac{\partial \theta(\mathbf{k}, t)}{\partial t} + H(t) \, \theta(\mathbf{k}, t) + \frac{3\Omega_{\mathrm{m}} H^2(t)}{2} \, \delta(\mathbf{k}, t) = -\int \delta_{\mathrm{D}}[\mathbf{k} - (\mathbf{k}_1 + \mathbf{k}_2)] \beta(\mathbf{k}_1, \mathbf{k}_2) \, \theta(\mathbf{k}_1, t) \, \theta(\mathbf{k}_2, t) \, \mathrm{d}\mathbf{k}_1 \, \mathrm{d}\mathbf{k}_2,$$

$$(1.44)$$

where δ_{D} represents the Dirac delta function and

$$\alpha(\mathbf{k}_1, \mathbf{k}_2) = \frac{(\mathbf{k}_1 + \mathbf{k}_2) \cdot \mathbf{k}_1}{k_1^2}, \qquad \beta(\mathbf{k}_1, \mathbf{k}_2) = \frac{(\mathbf{k}_1 + \mathbf{k}_2)^2 (\mathbf{k}_1 \cdot \mathbf{k}_2)}{2k_1^2 k_2^2}. \qquad (1.45)$$

In an *Einstein-de Sitter* universe ($\Omega_{\mathrm{m}} = 1$, $\Omega_{\Lambda} = 0$, hereafter EdS universe) these equations can formally be solved by an expansion in Fourier space, in particular for δ

$$\delta(\mathbf{k}, t) = a(t) \, \delta_1(\mathbf{k}) + a^2(t) \, \delta_2(\mathbf{k}) + \cdots + a^n(t) \, \delta_n(\mathbf{k}) + O[a^{n+1}(t) \, \delta_{n+1}(\mathbf{k})], \qquad (1.46)$$

with

$$\delta_n(\mathbf{k}) = \int \delta_{\mathrm{D}}[\mathbf{k} - (\mathbf{q}_1 + \cdots + \mathbf{q}_n)] F_n(\mathbf{q}_1, \ldots, \mathbf{q}_n) \, \delta_1(\mathbf{q}_1) \ldots \delta_n(\mathbf{q}_n) \, \mathrm{d}\mathbf{q}_1 \ldots \mathrm{d}\mathbf{q}_n. \qquad (1.47)$$

We call the linear density field $\delta_1(\mathbf{k})$ the *leading-order term* (hereafter LO term) since it is of the lowest order in the expansion. The terms $\delta_{n\geq 2}(\mathbf{k})$ are higher-order terms, in particular we call $\delta_2(\mathbf{k})$ the *next-to-leading-order term* (hereafter NLO term). $F_n(\mathbf{q}_1, \ldots, \mathbf{q}_n)$ is a function that is constructed from $\alpha(\mathbf{k}_1, \mathbf{k}_2)$ and $\beta(\mathbf{k}_1, \mathbf{k}_2)$ via a recursive relation. We give the explicit expression for $F_2(\mathbf{q}_1, \mathbf{q}_2)$,

$$F_2(\mathbf{q}_1, \mathbf{q}_2) = \frac{5}{7} + \frac{1}{2} \frac{\mathbf{q}_1 \cdot \mathbf{q}_2}{q_1 q_2} \left(\frac{q_1}{q_2} + \frac{q_2}{q_1} \right) + \frac{2}{7} \frac{(\mathbf{q}_1 \cdot \mathbf{q}_2)^2}{q_1^2 q_2^2}, \qquad (1.48)$$

so that we can write the NLO term as

$$\delta_2(\mathbf{k}) = \int \delta_{\mathrm{D}}[\mathbf{k} - (\mathbf{q}_1 + \mathbf{q}_2)] F_2(\mathbf{q}_1, \mathbf{q}_2) \, \delta_1(\mathbf{q}_1) \, \delta(\mathbf{q}_2) \, \mathrm{d}\mathbf{q}_1 \mathrm{d}\mathbf{q}_2. \qquad (1.49)$$

Higher-order terms can be found in Goroff et al. (1986). As mentioned, in principle these expressions only hold true in an EdS universe. However it can be shown that also in our ΛCDM

Universe they still provide a remarkably good approximation (Scoccimarro et al., 1998), so we will use this framework throughout the rest of the study.

We are now in a position to construct the density field at a given time up until an arbitrary order and therefore include non-linear gravitational clustering to our desired precision, if we only know δ_1. The analytical expressions will become immensely complicated though. Also it remains to be seen up until which scale k_{max} this prescription actually holds and accurately describes the real density field – at some point, at the strongly non-linear scales, multi-streaming will kick in and destroy the fluid approximation upon which the whole treatment is built. We cannot derive this threshold from first principles, but we need to make a comparison of our theoretical framework with 'real' data to access it – this problem will be tackled with the help of numerical N-body simulations, that we will explain in section 1.5. For now, we will shift our focus from the large to intermediate scales (and therefore the fluid approximation) towards the strongly non-linear scales, and we will explore a possible theoretical approach in more detail.

1.3.4 Tracers of the LSS – Dark-matter haloes

There are limited possibilities to analytically describe the gravitational N-body interaction at the smallest scales, i.e. in the knots of the cosmic web where collapse in all three dimensions happens. One approach is to consider a spherically-symmetric mass overdensity in an otherwise homogeneous universe, called the *spherical collapse model* (Gunn and Gott, 1972). The basic idea is that for early times shells of matter recede from the center of mass because of the Hubble expansion, i.e. the physical radius of the whole overdensity increases with time. However the recession process is stalled by the gravitational attraction of the shells – the comoving radius shrinks with time. If the initial perturbation is dense enough, at some point the shells will reach a maximum physical size (the *turn-around radius*) and afterwards will collapse. The outcome of this collapse will be a virialized object of finite size in equilibrium (no contraction or expansion anymore), called *dark-matter halo*.

The average density of the halo ρ_{vir} can be computed as $\rho_{vir} = \Delta_{vir} \bar{\rho}_m(t)$ where $\bar{\rho}_m(t)$ is the mean physical matter density of the Universe and the overdensity Δ_{vir} depends on the cosmological parameters and in general on time. For an EdS universe it is $\Delta_{vir} = 18\pi^2 \approx 178$ for all t, for our ΛCDM Universe with the cosmology as given in section 1.2.5 the value varies between the EdS value at very high redshifts and $\Delta_{vir} \approx 333$ at $z = 0$. It can be shown that collapse happens when the initial overdensity field $\delta_1 \gtrsim 1.68$ – this means that already in the linear field we can identify the formation location of haloes.

Of course reality is a much more complicated process than the indealized model we just presented. A density perturbation will never come isolated, but embedded in the complex environment of the cosmic web. The approximation of spherical symmetry has been loosened via the introduction of the *ellipsoidal collapse model* (Bond and Myers, 1996). The formation process and internal structure of haloes is still a very active field and is both studied from an analytical and a numerical point of view (e.g. Borzyszkowski, Ludlow and Porciani, 2014, More, Diemer and Kravtsov, 2015, Borzyszkowski, Porciani et al., 2017). In Fig. 1.6 we show a halo from an N-body simulation (for more detail on simulations see section 1.5) that is being assembled through anisotropic streams of matter from the outsides. The density of the halo is the highest in the center and decreases towards the outskirts.

In this study, we will not explore halo formation in greater detail, but we rather focus on the larger scales – mainly we are interested in haloes approximated as point-like objects that are *tracers* of the LSS. Where we cannot directly observe the DM and the cosmic web that mostly
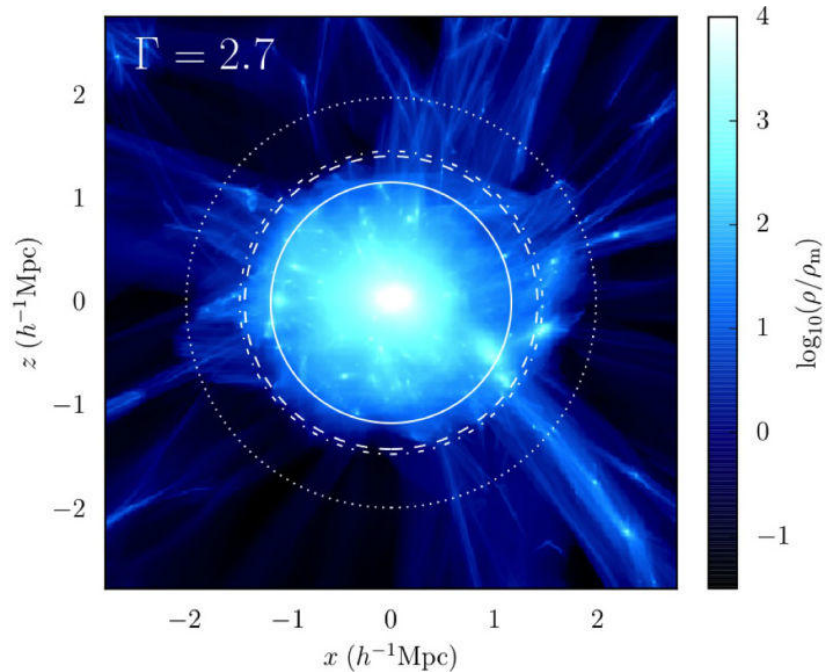
Figure 1.6: A DM halo from a high-resolution cosmological N-body simulation (More, Diemer and Kravtsov, 2015). The halo is approximately spherical in shape and is being fed matter from the outsides via anisotropic filaments. In the center the density is the highest whereas it declines towards the outskirts. The various white lines represent different physical criteria to define the boundaries of the halo.

consists of it (and therefore we do not have immediate access to the cosmological information contained in it), we can observe discrete objects that follow the LSS in a specific way because of their physical formation process. If we make the reasonable assumptions that DM haloes form in dense regions of the LSS (the denser, the higher also the density of the halo and the larger its total mass; Kaiser, 1984, Bardeen et al., 1986) and that in return galaxies form in DM haloes (where baryons can fall into and cool down because of the gravitational potential; H. Mo, van den Bosch and S. D. M. White, 2010), we can use this to infer about cosmology from galaxy surveys. This connection between discrete objects following an underlying continuous distribution is generally known as *tracer bias* or more specifically *halo* and *galaxy bias* (Desjacques, Jeong and Schmidt, 2018a). We will explore a more thorough, quantitative description in the next section.

1.3.5 The concept of halo and galaxy bias

In general moving from the DM distribution to galaxies is a two-step process – we first need a prescription to link the DM density field with the DM haloes, and then another to populate the DM haloes with galaxies (Fry and Gaztanaga, 1993, Cooray and R. Sheth, 2002, Berlind and D. H. Weinberg, 2002). The second step is needed since it is not just the case that each DM halo will host one galaxy with properties that can be directly inferred from the halo properties. Rather depending on the halo size there can reside several galaxies of various masses and luminosities in it. In this study, we will not further explore the problem of connecting galaxies to haloes – rather we want to focus on the first step of the problem, i.e. relating the LSS with the DM haloes.

This can be tackled from two different perspectives essentially. Either one wants to really
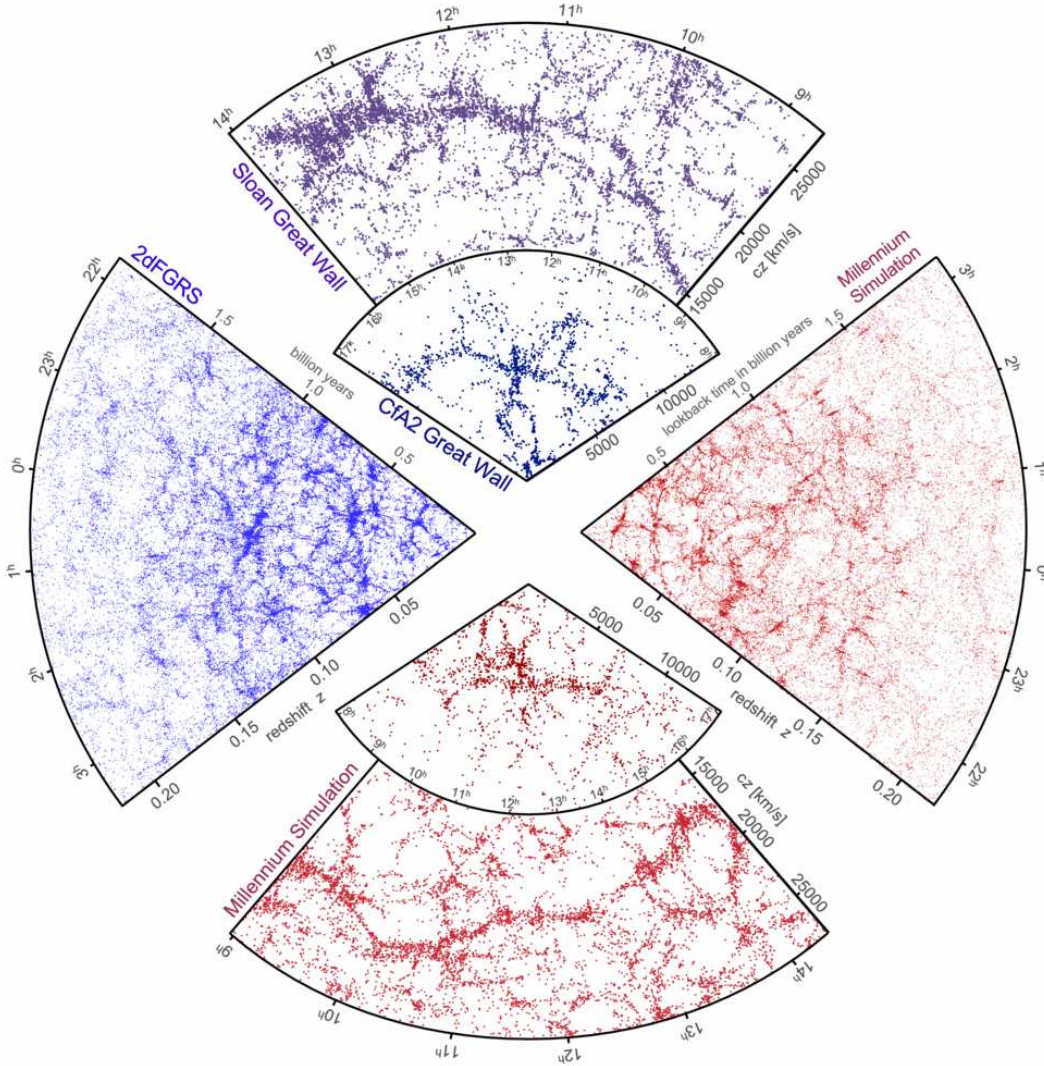
Figure 1.7: Observational spatial distribution of galaxies, compared with the spatial distribution of DM in a numerical simulation (Springel, Frenk and S. D. M. White, 2006). *Left*: observational data from 2dFGRS, *top*: observational data from SDSS and CfA2 (Huchra et al., 1983), *bottom* and *right*: numerical data from the Millennium simulation (Springel, S. D. M. White, Jenkins et al., 2005).

understand the physical processes behind bias which calls for a detailed understanding of the formation processes of haloes (or the distribution of *peaks*, i.e. points in space where the density field lies above a certain threshold). The other option is to treat the problem in a more phenomenological fashion, motivated from physical reasoning on a basic level, but with the main goal in mind of finding a working recipe to apply to observations. We will focus on the second option in this study in general (we give a brief introduction to more physical approaches in section 1.4.6 though). Such a phenomenolgial model that connects haloes (or tracers in general) to the underlying matter distribution is called a *Eulerian biasing scheme* (McDonald and Roy, 2009, Baldauf, Seljak, Senatore et al., 2011, R. K. Sheth, Chan and Scoccimarro, 2013, Desjacques, 2013).

The basic assumption is that the overdensity field of the haloes $\delta_{\mathrm{h}}(\mathbf{x})$ – obtained by smoothing

the discrete halo distribution at an arbitrary scale – is related to the matter density field $\delta(\mathbf{x})$ in some general form $\delta_\mathrm{h}(\mathbf{x}) = F_\mathbf{x}[\delta]$, where $F_\mathbf{x}$ is a functional. In Fig. 1.7 we illustrate the motivation for this assumption: Shown is the observed spatial distribution of galaxies from three different surveys, as well as the spatial distribution of DM in a numerical *dark-matter only* simulation, post-processed in a way to mimic the technical characteristics of the three surveys. The visual statistical similarity between the galaxies (data) and the DM (theory/numerics) is remarkable. A biasing scheme is called *local* if it can be written in the form of an expansion,

$$\delta_\mathrm{h}(\mathbf{x}, t) = \sum_O b_O(t)\, O(\mathbf{x}, t)\,, \tag{1.50}$$

where O denotes an *operator* and b_O the respective *bias parameter*. The bias parameters are numbers that do not depend on spatial coordinates, but may and certainly will depend on time and on halo properties like mass (or e.g. galaxy properties like colour or luminosity). Effectively they can be understood as the result of a marginalization process over the complicated long-time, small-scale processes of halo formation, i.e. biasing can be interpreted as an *Effective Field Theory* (hereafter EFT; Senatore, 2015). The parameters can be positive or negative, and the larger the absolute value of a bias parameter is, the more importance does the respective operator have for describing the halo field. We will give a more thorough, quantitative introduction to the concept of bias as an EFT in chapter 2. Historically, at first the operators O would just be taken as powers of the density field, i.e. $\delta_\mathrm{h} = b_1\delta + b_2\delta^2 + b_3\delta^3 + \ldots$ (Fry and Gaztanaga, 1993), but it has been shown that these do not fully represent the halo field, rather one should also take e.g. various combinations of derivatives of the density field or even the peculiar velocity field into account (Mirbabayi, Schmidt and Zaldarriaga, 2015). We will soon see about this in more detail.

Usually the exact value of the bias parameters is not the most important issue. In observations such as galaxy clustering surveys there will be assumed a bias model, and then the bias parameters are treated as free parameters of that model that will be marginalized over in the process of data analysis (Cole, Percival et al., 2005, Percival, Nichol et al., 2007, Blake et al., 2010, Granett et al., 2012, Beutler et al., 2017, Salazar-Albornoz et al., 2017). The crucial problem is to first find that bias model that correctly describes the actual conditions. This is not straightforward, since the approach from equation (1.50) is designed such that one first has a lot of freedom that needs to be reduced by reasonable arguments. From a mathematical point of view, it is not difficult to write down a complete set of operators (also called a *basis*) up until a certain order in the expansion, but then it remains to be seen which of these operators are actually needed in a real physical context. Also the need for certain operators will certainly depend on the minimum scale that one tries to model. Another question is how one performs the link to cosmology, or to put it differently, how can the operators themselves be modelled such that they depend on cosmological parameters? We will treat this issue in the framework of SPT in this study, i.e. our goal will be to write each operator in such a fashion that the initial density field will be the main input. The question about which operators will be actually needed (i.e. the explicit form of the bias model) can be addressed first from theoretical considerations (Angulo et al., 2015, Mirbabayi, Schmidt and Zaldarriaga, 2015, Desjacques, Jeong and Schmidt, 2018c), but then surely needs to be tested against numerical data.

We will now explore the shape of the operators in more depth in an order-by-order approach. At first order, this will be a simple *linear bias* model (Kaiser, 1984), i.e. $\delta_\mathrm{h} = b_1\delta$. This relation only holds true on the very largest scales (Gaztanaga and Frieman, 1994). At second order two

operators can be introduced, δ^2 and s^2 with respective bias parameters b_2 and b_{s^2} (McDonald and Roy, 2009), where $s^2(\mathbf{x}) = s_{ij}(\mathbf{x})s_{ij}(\mathbf{x})$ with

$$s_{ij}(\mathbf{x}) = \partial_i\partial_j\Phi(\mathbf{x}) - \frac{1}{3}\delta_{ij}^{(\mathrm{K})}\delta(\mathbf{x}), \tag{1.51}$$

and $\delta_{ij}^{(\mathrm{K})}$ the Kronecker symbol. The quantity s_{ij} is called the *tidal tensor* and accounts for shearing effects in the matter field. Furthermore, we introduce the first higher-derivative bias operator, $\nabla^2\delta$ (Desjacques, Crocce et al., 2010), with the respective bias parameter $b_{\nabla^2\delta}$.

The expansion has been also written down at third order (Desjacques, Jeong and Schmidt, 2018a), but it is still unclear which of the operators is actually needed in reality. We will explore the explicit third-order model in more detail and perform the test against numerical simulations in chapter 2.

1.4 Statistics in cosmology

Until this point we were talking a lot about the density field (and the peculiar velocity field that comes with it in linear theory). We investigated how it evolves in time, and gave the equations that describe gravitational clustering. In the following section we shall now derive the explicit spatial dependency, i.e. $\delta(\mathbf{x})$. We want to make clear that it is not possible to develop a theory that describes exactly our Universe with all its peculiarities – like that the Andromeda galaxy resides at $\approx 780\,\mathrm{kpc}$ away from us (Karachentsev et al., 2004), or that the Local Group, the galaxy cluster that the Milky Way is part of, consists of about 70 galaxies[17] (McConnachie, 2012). Such a task would be much too complex, plus we would need to know the exact initial conditions in six-dimensional phase-space which we do not have access to. Rather we can only describe a Universe with the same *statistical* properties, thus we also model the initial density fluctuations in the Universe (upon which structure formation solely depends in the framework of SPT) in a statistical fashion. Also we will derive statistical quantities that will allow to test our theoretical approach against observations.

1.4.1 Initial conditions as Gaussian random fields

We model the initial density field as a *random field* with zero mean, and the real, observable Universe will be one *realization* of this random field. A zero-mean random field describing the overdensity field $\delta(\mathbf{x})$ associates each point $\mathbf{x} \in \mathbb{R}^3$ with a stochastic variable of the sample space $\mathcal{S} = [-1, \infty)$ and is fully characterised by its cumulative distributions $\mathrm{Prob}\{\delta(\mathbf{x}_1) \leq \delta_1, \dots, \delta(\mathbf{x}_n) \leq \delta_n\}$. From the CP we assume homogeneity and isotropy which means the random field is invariant under transformations such as $\mathbf{x} \to \mathcal{R}(\mathbf{x} + \mathbf{y})$, where $\mathcal{R}$ is a rotation matrix and $\mathbf{y}$ is a translational vector. Sampling the distributions gives a certain realization of the random field. By applying the three-dimensional FT to $\delta(\mathbf{x})$ we obtain its Fourier-space equivalent $\delta(\mathbf{k})$. With this quantity we can define a *Gaussian random field* that has two main properties: Its Fourier components are mutually statistical independent, and its probability density is described by a Gaussian. From these properties follow interesting statistical consecquences, as we will see in the following section.

---

[17] The Milky Way and the Andromeda Galaxy (also called M31) are the two largest galaxies and of similar mass. The other galaxies are *substructure*, i.e. satellite dwarf galaxies that move in the gravitational potential of the two main galaxies. Well-known satellites are the Large and Small Magellanic Clouds.
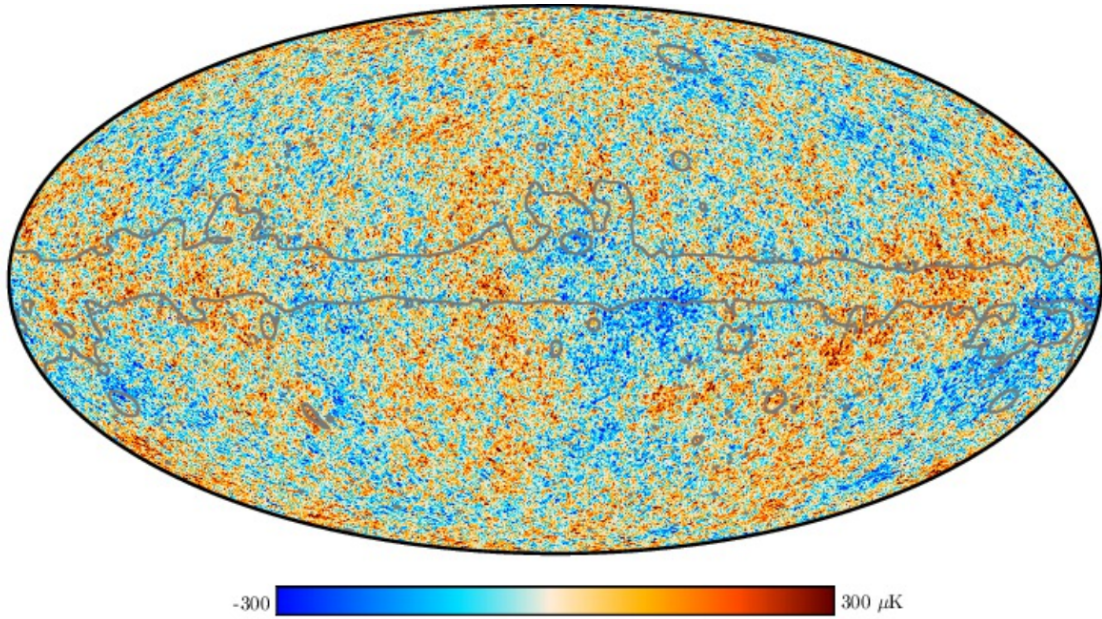
Figure 1.8: The two-dimensional projection of the CMB anisotropy signal measured across the whole sky by the Planck Collaboration (2018a). The spatial resolution is of the order of arcminutes. Red spots indicate regions with increased temperature of the radiation relative to the mean value, blue spots indicate colder regions. The signal is of the order of μK. The grey lines indicate the location of the Milky Way.

Applying the concept of Gaussian random fields to the Universe is justified by observations, since the CMB, which basically tells us the initial conditions of structure formation, is indeed a Gaussian random field within the current constraints (Planck Collaboration, 2019). Imprinted in it are tiny temperature fluctuations of relative size of 10^{-5}. These probably originate from quantum fluctuations that were blown up to macroscopic fluctuations during a period of very rapid expansion right after the Big Bang, called *Inflation*[18], where the Universe expanded $\sim 60e$-folds in a time span of $\sim 10^{-34}$ s. Inflation introduced under- and overdensities into the spatial distribution of matter that would serve as seeds for structure formation. The differences in the gravitational potential were only very small at that time and at the formation time of the CMB, but their impact was large enough. At the location of overdensities the CMB photons had to climb out of a potential well, hence they were losing energy and became redshifted – these are the colder spots in the CMB anisotropy map. At the location of underdensities the process works vice versa. Therefore the CMB temperature map provides an excellent snap shot of the initial conditions of the Universe and one realization of a Gaussian random field. In Fig. 1.8 we show the most recent map of the CMB (Planck Collaboration, 2018a). Red colour denotes hotter spots, blue colder ones. From the colour bar one can see that the maximum amplitude of the inhomogeneities is only $\sim 10^2 \, \mu$K.

Non-linear gravitational evolution (i.e. the formation of the LSS and DM haloes) will introduce non-Gaussianity into the random field – this can also be understood from the shape of the SPT equations: At higher order, i.e. for the calculation of $\delta_{n \geq 2}$, integrals need to be computed that

---

[18] The original idea was introduced by Guth (1981) to solve the *flatness* and *horizon* problem, that state that the flatness of the Universe today would require a very precise fine tuning at early times, and that the whole CMB is nearly isotropic although not all points could have been in causal contact earlier (Tsujikawa, 2003).

couple the Fourier modes at different **k** to each other, where for a Gaussian random field the modes evolve independently.

1.4.2 2-point statistics

Since we are dealing with structure formation from a statistical point of view, it makes sense to introduce also statistical quantities that allow us to give precise information about the statistical properties of the random field. We already qualitatively explained the concept of a Gaussian random field, and how structure formation alters this, and now we want to develop the mathematical tools for a more quantitative approach.

We define the *two-point correlation function* (hereafter 2PCF),

$$\xi(r, t) = \langle \delta(\mathbf{x}, t) \, \delta(\mathbf{x} + \mathbf{r}, t) \rangle, \tag{1.52}$$

where $\langle \dots \rangle$ denotes the average over the ensemble of realizations of the random field. In practice, the ensemble average can be replaced with a volume average. The 2PCF gives information about the degree of correlation between two different points separated by **r**. In the limit $r \to 0$ it coincides with the variance of the field

$$\lim_{r \to 0} \xi(r, t) = \langle \delta^2(\mathbf{x}, t) \rangle \equiv \sigma^2(t). \tag{1.53}$$

The correlation function cannot depend on the two points **x** and **x**+**r** individually, but only on the absolute value of the separation vector r since we assume $\delta(\mathbf{x}, t)$ to be statistically homogeneous and isotropic. We can also calculate the correlator of the Fourier transform $\delta(\mathbf{k})$,

$$\langle \delta(\mathbf{k}) \, \delta(\mathbf{k}') \rangle = \int e^{-i\mathbf{x} \cdot \mathbf{k}} \frac{\mathrm{d}^3 x}{(2\pi)^3} \int e^{i\mathbf{x}' \cdot \mathbf{k}'} \frac{\mathrm{d}^3 x'}{(2\pi)^3} \langle \delta(\mathbf{x}) \, \delta(\mathbf{x}') \rangle \tag{1.54}$$

$$= \int e^{-i\mathbf{x} \cdot \mathbf{k}} \frac{\mathrm{d}^3 x}{(2\pi)^3} \int e^{i(\mathbf{x}+\mathbf{r}) \cdot \mathbf{k}'} \frac{\mathrm{d}^3 r}{(2\pi)^3} \xi(r) \tag{1.55}$$

$$= (2\pi)^3 \delta_{\mathrm{D}}(\mathbf{k} - \mathbf{k}') \int e^{i\mathbf{r} \cdot \mathbf{k}} \xi(r) \frac{\mathrm{d}^3 r}{(2\pi)^3} \tag{1.56}$$

$$\equiv (2\pi)^3 \delta_{\mathrm{D}}(\mathbf{k} - \mathbf{k}') P(k), \tag{1.57}$$

where we substituted $\mathbf{x}' = \mathbf{x} + \mathbf{r}$ and in the end defined the *power spectrum $P(k)$*, i.e. the Fourier transform of the 2PCF,

$$P(k) = \int e^{-i\mathbf{r} \cdot \mathbf{k}} \xi(r) \frac{\mathrm{d}^3 r}{(2\pi)^3}. \tag{1.58}$$

The power spectrum only depends on the absolute value k of the Fourier modes, i.e. it gives information about how strongly clustered the field is depending on scale (analogously to the 2PCF which only depends on r). For a Gaussian random field, all statistical information is contained in the power spectrum, higher-order statistics (see section 1.4.3) will give no improvement. To infer cosmological information from the power spectrum the usual way is to model it based on some physical prescription including cosmological parameters, and then to compare against the power spectrum measured from observations. Of course one can also employ the 2PCF which contains exactly the same information, but often numerical calculations are less complicated and less expensive if performed in Fourier space. In the rest of the study we will solely focus on

power spectra, and not incorporate correlation functions anymore, for exactly these reasons.

The power spectrum can be computed for all sorts of fields, like e.g. the matter or halo overdensity field. It is also possible to build cross spectra that contain information about how strongly two different fields are correlated depending on scale. The formation of the LSS and of individual DM haloes becomes visible when comparing power spectra at different redshifts: The lower the redshift (i.e. the later in the history of the Universe) the more power will accumulate on the smaller scales (Peebles, 1980). There exists an *initial power spectrum* with a specific shape and amplitude that captures all the statistical properties of the initial conditions of the Universe (Harrison, 1970, Zeldovich, 1972). Late-time power spectra will depart from the initial power spectrum in particular on the small and intermediate scales. From now on, we indicate the initial, linear power spectrum by writing $P_{11}(k)$ (in contrast to the non-linear power spectrum).

Its form can be derived from a few cosmological considerations in the framework of inflation. It is of the power-law form

$$P_{11}(k,a) = Ak^{n_\mathrm{s}}T^2(k)D^2(a)\,,\tag{1.59}$$

where $D(a)$ is the linear growth factor, A is a free normalization constant that has to be fixed by observations, n_s is the *spectral index* to be explained below, and $T(k)$ is the *transfer function*. The transfer function describes how structures grow differently depending on scale in linear theory (not to confuse with structure growth depending on scale due to clustering, this is described within non-linear theory). It can be shown that the growth depends on when fluctuations at some scale k enter the horizon[19], with the difference being whether this happens in the radiation- or matter-dominated era (i.e. when either of the terms dominates in the Friedmann equation). For small perturbations that enter in the radiation-dominated era growth is prohibited until the Universe becomes matter-dominated. Furthermore, in the transfer function the effect of *free-streaming* is included. Depending on the type of DM, i.e. whether it is cold, warm or hot, the particles have smaller or higher velocity – faster particles will cluster less than slower ones, they will free-stream, therefore for hot and warm DM small-scale power is decreased in comparison to CDM. This is encoded in the transfer function. Whereas a thorough analytical derivation of $T(k)$ is quite a complex problem, there exist fitting formulae that depend only on the cosmological model and the cosmological parameters (e.g. Bardeen et al., 1986).

The shape of $P_{11}(k)$ is mainly influenced by n_s. It can be predicted from inflation and has been confirmed by observations (Planck Collaboration, 2018b) that this must be slightly smaller than one. We can define the *dimensionless power spectrum*

$$\Delta^2(k) = 4\pi k^3 P_{11}(k)\,,\tag{1.60}$$

for which, in a CDM scenario, we find that it increases with k for a broad range of scales (only for the very smallest scales it follows $\Delta^2(k) \propto k^{n_\mathrm{s}-1}$ and therefore becomes asymptotically small). This means that the largest fluctuations are on small scales and thus will become non-linear first. A scenario where gravitational collapse happens first on small scales and then on larger scales is called a *bottom-up scenario* (the inverse situation would be called a *top-down scenario*). In practice, in a bottom-up Universe such as the one we live in, small structures such as DM haloes (and within them the galaxies) form first. These small haloes fall onto each other and form larger clusters. The fact that we find this situation in observations and simulations confirms that DM is indeed cold (Jenkins et al., 1998). In the case of warm or hot DM large structures

---

[19] The *horizon* is the maximum distance that a photon can travel in a given time interval, i.e. the maximum distance two points can be spatially separated to still be in casual contact within that time interval

would be the first to collapse.

The shape of the power spectrum can be motivated from theory, however the strength of the fluctuations, i.e. the normalization constant A, must be measured. Historically, a special parameterization was introduced which was motivated by observations – it was found that in the context of counting galaxies, the variance of their number N in a sphere of $8\,h^{-1}$ Mpc was very close to one, i.e.

$$\frac{\langle (N - \langle N \rangle)^2 \rangle}{\langle N \rangle^2} \approx 1 \,. \tag{1.61}$$

The most recent data show that the value is in fact smaller than one (see below), but the original idea of parametrizing the amount of structure by counting collapsed objects within a certain radius was kept. One employs the dispersion $\sigma^2(R)$ of the density field $\delta_R(\mathbf{x})$ when smoothed at a certain radius R,

$$\sigma^2(R) \equiv \langle \delta_R^2(\mathbf{x}) \rangle = \int |W(kR)|^2 P(k) \frac{\mathrm{d}^3 k}{(2\pi)^3} = \frac{1}{2\pi^2} \int_0^\infty |W(kR)|^2 k^2 P(k) \,\mathrm{d}k \tag{1.62}$$

where $W(kR)$ is the Fourier representation of a filter function that smooths the density field, and where in the last step we have exploited the spherical symmetry of $W(kR)$ and integrated over the angular part. Setting $R = 8\,h^{-1}$ Mpc gives the cosmological parameter σ_8 that is constrainted to $\sigma_8 = 0.811 \pm 0.006$ by current surveys (e.g. Planck Collaboration, 2018b). This parameter is now commonly used to express the normalization of the power spectrum.

In the framework of SPT we found that non-linear gravitational evolution can be derived from the initial conditions, so now we will extend this treatment to power spectra. From equation (1.42) we build the correlator in Fourier space, and after some algebra obtain $P_{\delta\delta}(k)$ which will be the non-linear power spectrum,

$$\begin{aligned} P_{\delta\delta}(k) &\simeq P_{\delta\delta}^{(\mathrm{LO})}(k) + P_{\delta\delta}^{(\mathrm{NLO})}(k) \\ &= \langle \delta_1(\mathbf{k}) \, \delta_1(\mathbf{k}') \rangle + \langle \delta_2(\mathbf{k}) \, \delta_2(\mathbf{k}') \rangle + 2 \langle \delta_1(\mathbf{k}) \, \delta_3(\mathbf{k}') \rangle \\ &= P_{11}(k) + P_{\delta\delta}^{(22)}(k) + P_{\delta\delta}^{(13)}(k) \,, \end{aligned} \tag{1.63}$$

where we omit writing $(2\pi)^3 \delta_{\mathrm{D}}(\mathbf{k} - \mathbf{k}')$ explicitly. We identify the LO term with $P_{11}(k)$ which is of order two in the expansion. The NLO term consists of two different contributions that are both of order four. For a Gaussian random field it follows from Wick's theorem that all correlators of odd orders vanish, therefore we do not find a contribution of order three as NLO term. The NLO terms can be calculated explicitly,

$$P_{\delta\delta}^{(22)}(k) = 2 \int_{\mathbf{p}} F_2^2(\mathbf{p}, \mathbf{k} - \mathbf{p}) \, P_{11}(p) \, P_{11}(|\mathbf{k} - \mathbf{p}|) \,, \tag{1.64}$$

$$P_{\delta\delta}^{(13)}(k) = 6 P_{11}(k) \int_{\mathbf{p}} F_3(\mathbf{p}, -\mathbf{p}, \mathbf{k}) \, P_{11}(p) \,, \tag{1.65}$$

which is mainly one three-dimensional integral over the linear power spectrum, modulated with a kernel, and where we introduced the compact notation

$$\int_{\mathbf{p}} \cdots \equiv \int \cdots \frac{\mathrm{d}^3 p}{(2\pi)^3} \,. \tag{1.66}$$
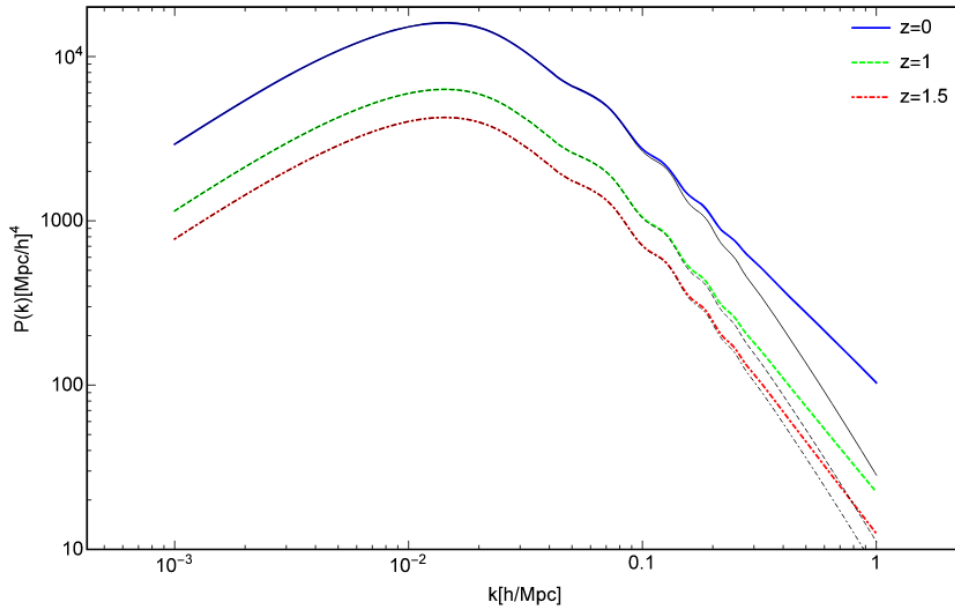
Figure 1.9: The linear power spectrum at three different redshifts (grey lines), compared with the non-linear 1-loop power spectrum at the same redshifts (coloured lines) in the framework of SPT (Lee, Park and Biern, 2014)). The overall amplitude of the spectra grows for smaller redshifts, as described by linear theory. Also, the non-linear power spectra show increased signal for smaller scales and redshifts due to non-linear gravitational clustering.

Because of the integral operation such expressions are also called *loop terms*. The LO term that requires no integration is called *tree term*. Of course one does not have to stop the expansion of the power spectrum at fourth order and compute only the *1-loop terms*. In principle the expansion can be extended to *n*-th loop. The analytical expressions become very complicated though, and such efforts are only reasonable when observational instruments are able to provide the respective precision at the small scales. It is very desirable though to make the effort with the smaller scales, both in theory and observations – most cosmology-constraining power lies in fact there. *Cosmic Variance*, i.e. the fact that our Universe is only one realization of a random field, puts large theoretical errors on the larger scales since only few of the Fourier modes can be fit into the Universe. These errors present a fixed lower limit, they cannot be decreased by increased intrument precision or better modeling (Blot et al., 2016).

At some point writing the power spectrum as an expansion will break down. This scale k_{max} can be explored when comparing the theoretical expressions against N-body data. Accurate modeling of non-linear clustering on even smaller scales calls for other methods, such as the halofit model (Smith et al., 2003). In Fig. 1.9 we show the linear power spectrum in comparison with the SPT 1-loop power spectrum for three different redshifts by Lee, Park and Biern (2014). One can see that the overall amplitude increases, and that especially on small scales power accumulates due to non-linear effects.

1.4.3 3-point statistics

For a Gaussian random field all statistical information is contained within the power spectrum. To detect non-Gaussianity the *bispectrum* $B(k_1, k_2, k_3)$ needs to be employed which is given as

$$\langle \delta(\mathbf{k}_1)\, \delta(\mathbf{k}_2)\, \delta(\mathbf{k}_3) \rangle = (2\pi)^3 \delta_{\mathrm{D}}(\mathbf{k}_1 + \mathbf{k}_2 + \mathbf{k}_3) B(k_1, k_2, k_3)\,, \tag{1.67}$$

i.e. it is the three-point equivalent to the power spectrum (in real space this would be the three-point correlation function). The bispectrum only gives a value for a closed triangle, also it is translationally and rotationally invariant. For a Gaussian random field it is zero since it is a correlator of odd order. In SPT, the full matter bispectrum can be written as an expansion in linear power spectra (as in general a higher-order statistic can be written as an expansion in lower-order statistics),

$$
\begin{aligned}
B^{(\mathrm{LO})}_{\delta\delta\delta}(k_1, k_2, k_3) = 2 \big[&F_2(\mathbf{k}_1, \mathbf{k}_2)\, P_{11}(k_1)\, P_{11}(k_2) + F_2(\mathbf{k}_2, \mathbf{k}_3)\, P_{11}(k_2)\, P_{11}(k_3) \\
&+ F_2(\mathbf{k}_3, \mathbf{k}_1)\, P_{11}(k_3)\, P_{11}(k_1) \big]\,,
\end{aligned}
\tag{1.68}
$$

where we only wrote the tree-level expression which can be derived when plugging in the expansion of δ into the correlator and keeping only LO terms. Of course also for the bispectrum loop terms can be derived that we omit stating explicitly (we refer to e.g. Scoccimarro et al., 1998 for that).

The bispectrum can be used as an independent complement to the power spectrum when exploring the clustering of galaxies and inferring cosmological parameters from that (e.g. Pollack, Smith and Porciani, 2012, Yankelevich and Porciani, 2019), and we will give its possible applications a closer look in chapter 3.

1.4.4 Measuring bias from statistics

In section 1.3.5 we introduced the concept of bias, and in particular the approach of a Eulerian bias scheme. Now we want to explore the possibility of actually measuring the bias parameters from statistics. No matter whether one is really interested in the exact values of the bias parameters and would like to give a physical interpretation to them, or whether one merely sees the bias parameters as nuisance parameters in an observational context that will be marginalized over anyway – to make progress we need a technique to obtain explicit values.

The path that we will take here is measuring the parameters from *n*-point cross spectra (for an overview see Desjacques, Jeong and Schmidt, 2018a). The general technique then is the following: One decides on a basis of operators up until a certain order. This expansion is then cross-correlated with another field, e.g. the matter density field or the halo density field. The bias parameters can then be measured if the resulting cross spectra are available from data or theoretical models. When writing the bias expansion in terms of cross spectra one needs to decide up until which order terms should be included. Similar to equation (1.63), there will be an LO term, and then several 1-loop NLO terms that are all of the same order. One has to make sure that, depending on which bias operators one includes, all possible NLO terms are taken care of. It is inconsistent to take into account only some of them.

In this study our focus is on testing the bias expansion against numerical data, therefore we choose to measure the bias parameters from a cross correlation in Fourier space with $\delta(\mathbf{k})$. The

LO term for this can be calculated easily,

$$\langle \delta_{\mathrm{h}}(\mathbf{k})\,\delta(\mathbf{k}')\rangle^{(\mathrm{LO})} = b_1 \langle \delta_1(\mathbf{k})\,\delta_1(\mathbf{k}')\rangle\,, \tag{1.69}$$

or in terms of spectra

$$P^{(\mathrm{LO})}_{\delta_{\mathrm{h}}\delta}(k) = b_1 P_{11}(k)\,. \tag{1.70}$$

We see that at LO only appears the linear bias parameter b_1 that comes with the linear power spectrum $P_{11}(k)$. The l.h.s. of equation (1.70) consists of the data that is measured from simulations, the r.h.s. consists of the physical model. Of course in a context of actual observations we need to build the cross correlation with $\delta_{\mathrm{h}}(\mathbf{k})$ which gives the halo power spectrum $P_{\delta_{\mathrm{h}}\delta_{\mathrm{h}}}(k)$ on the l.h.s. – this is the only quantity that is actually accessible from real measurements (more precisely only the galaxy power spectrum is accessible, but galaxy bias can be treated with the same methodology as halo bias). When testing the model against numerical data, in principle we have all the cross spectra at hand. A measurement of the parameters is then performed via fitting the data against the model, employing e.g. a *Markov Chain Monte–Carlo* routine (Hastings, 1970) that samples the posterior distribution of the parameters in form of a chain of random numbers.

The LO bias expansion will only be valid on very large scales and break down on the intermediate scales (we will show this explicitly in chapter 2). To model these accurately we need the NLO terms that will consist of operators up until third order. We omit writing them here explicitly since this will be done in detail in chapter 2. The bias parameters can also be measured from cross correlations at bispectrum level, or also from correlation functions at various levels in real space, however we will not focus on this in this study.

1.4.5 Bias renormalisation

Despite not writing the full third-order expansion we want to point out a pecularity when dealing with higher-order operators, and therefore loop terms. Calculating these loops means that technically one has to integrate the linear power spectrum over an infinite range of scales, thus in particular also the very small scales for that SPT is not valid any more per definition. Effectively the large scales, for that we want to obtain the signal, receive power from scales for that the theory fails. To avoid this problem, also called *UV-sensitivity*, one manually introduces an arbitrary cutoff scale Λ, at which the integral of the loop terms is truncated. This eliminates the small scales from the loop, however replaces one problem with another: Now the result of the integration and therefore the whole bias expansion and the bias parameters depend on Λ, which was chosen by hand and has no intrinsic physical meaning.

The procedure to circumvent this, i.e. to make the cross spectra and bias parameters independent of Λ, is called the *renormalisation* of bias parameters (McDonald, 2006, McDonald and Roy, 2009, Assassi et al., 2014), and we want to illustrate it with the example of the second-order operator $\delta^2(\mathbf{x})$ – of course the technique can also be applied to other operators, and we will perform a thorough treatment with more detailed calculations in chapter 2 and 3. Here we will mainly focus on giving a motivation. Writing $\delta^2(\mathbf{x})$ as an expansion gives

$$\begin{aligned}
\delta^2(\mathbf{x}) &= [\delta_1(\mathbf{x}) + \delta_2(\mathbf{x}) + \delta_3(\mathbf{x}) + \ldots][\delta_1(\mathbf{x}) + \delta_2(\mathbf{x}) + \delta_3(\mathbf{x}) + \ldots] \\
&= \delta_1^2(\mathbf{x}) + 2\delta_1(\mathbf{x})\delta_2(\mathbf{x}) + \delta_2^2(\mathbf{x}) + 2\delta_1(\mathbf{x})\delta_3(\mathbf{x}) + \ldots
\end{aligned} \tag{1.71}$$

Cross-correlating the Fourier transform $\delta^2(\mathbf{k})$ of this operator[20] with the density field (and paying attention that correlators of odd order vanish) contributes two terms to the NLO terms of $P_{\delta_h\delta}(k)$, i.e.

$$P_{\delta^2\delta}^{(\text{LO})}(k) = \langle(\delta_1^2(\mathbf{k})\,\delta_2(\mathbf{k}'))\rangle + 2\langle(\delta_1\delta_2)(\mathbf{k})\,\delta_1(\mathbf{k}')\rangle$$
$$= P_{\delta^2\delta}^{(22)}(k) + P_{\delta^2\delta}^{(31)}(k)\,, \tag{1.72}$$

since the LO terms of $P_{\delta_h\delta}(k)$ are of order two, and the NLO terms are of order four, as is the case for equation (1.72). Note that the r.h.s. of equation (1.72) are LO terms of $P_{\delta^2\delta}(k)$, but NLO terms of $P_{\delta_h\delta}(k)$! We can write them explicitly,

$$P_{\delta^2\delta}^{(22)}(k) = 2\int_{\mathbf{p}} F_2(\mathbf{p}, \mathbf{k}-\mathbf{p})\,P_{11}(p)\,P_{11}(|\mathbf{k}-\mathbf{p}|)\,, \tag{1.73}$$

$$P_{\delta^2\delta}^{(31)}(k) = 4P_{11}(k)\int_{\mathbf{p}} F_2(-\mathbf{p}, \mathbf{k})\,P_{11}(p)\,, \tag{1.74}$$

and after some algebra we find that equation (1.74) can be written in the form

$$P_{\delta^2\delta}^{(31)}(k) = \frac{68}{21}\sigma_1^2(\Lambda)P_{11}(k)\,, \tag{1.75}$$

where $\sigma_1^2(\Lambda)$ is given via equation (1.62) (where $\Lambda = 2\pi/R$), using $P_{11}(k)$ in the integral. It becomes clear that $P_{\delta^2\delta}^{(31)}(k)$ is a cutoff dependent quantity since it contains the variance of the density field which is influenced mainly by the cutoff scale Λ – the larger the value of that, the larger will also be $\sigma_1^2(\Lambda)$. In particular, $P_{\delta^2\delta}^{(31)}(k)$ tends to a constant value different from zero for $k \to 0$ which leads to an undesired mixing of power from linear bias and higher-order biases. However, $P_{\delta^2\delta}^{(22)}(k)$ does not contain any cutoff sensitivity at $k \to 0$ as can be shown when performing an explicit numerical calculation of the integral. The fact that the cutoff-dependent part of $P_{\delta^2\delta}^{(\text{LO})}(k)$ can be clearly separated from the actual signal that we are interested in allows to simply subtract it. This means that in the bias expansion we only keep $P_{\delta^2\delta}^{(22)}(k)$, and eliminate the large-scale limit of $P_{\delta^2\delta}^{(31)}(k)$.

This approach cannot only be performed on the level of spectra, but already on the level of fields. We introduce the renormalised operator $[\delta^2]_1(\mathbf{x})$ which is given as

$$[\delta^2]_1(\mathbf{x}) = \delta^2(\mathbf{x}) - \frac{68}{21}\sigma_1^2(\Lambda)\delta(\mathbf{x})\,, \tag{1.76}$$

which is the original cutoff-dependent operator minus a term that, when cross-correlated with $\delta(\mathbf{x})$, gives exactly the UV-sensitive piece, and therefore eliminiates it. We are writing $[\dots]_1$ in equation (1.76) to indicate that this is only the renormalisation of the operator at first order. This comes because we only wrote the LO terms in equation (1.72). Of course there are also NLO terms to this expression that are of order six, eight and so forth. The renormalisation procedure can be extended to second, third etc. order to take care of these terms. We will have a closer look at this in chapter 3.

Writing the renormalisation at the level of spectra allows for a new interpretation: We are

---

[20] This notation means that we first build the square and then perform the FT.

introducing an additional operator, i.e. $\delta(\mathbf{x})$, into the bias expansion. However this operator already appears at LO in the bias expansion (see equation 1.42). We can therefore rearrange the bias expansion and absorb the correction term in equation (1.76) in b_1. In general we can rewrite equation (1.50) in terms of *renormalised operators* $[O]$ and *renormalised bias parameters* b_O^R

$$\delta_{\mathrm{h}} = \sum_{[O]} b_O^{\mathrm{R}} [O].$$ (1.77)

For our example, taking into account the shape of the correction term in equation (1.76), this gives in particular for the renormalised bias parameter b_1^{R}

$$b_1^{\mathrm{R}} = b_1 + \frac{68}{21}\sigma_1^2(\Lambda)b_2.$$ (1.78)

In principle with this technique all operators and bias parameters can be renormalised to an arbitrary order, and only fields that come naturally with the bias expansion anyway are needed to achieve this. It remains to be tested against numerical data however how well this method actually performs, and we will do so in chapter 2 and 3.

1.4.6 Physical models and interpretation of bias

The phenomenological approach to tracer bias, presented in form of the Eulerian bias scheme, is immensely useful for practical applications, e.g. the implementation into the data analysis pipelines of large galaxy surveys. In this section we want to place it into a broader context and compare with other techniques that in part also enable the prediction of actual values for the bias parameters. We will test the results of our own work quantitatively against the literature in chapter 2, here we will introduce the concepts qualitatively in a brief fashion.

The framework of the *peak-background split* (Bardeen et al., 1986; hereafter PBS) offers a possible physical interpretation of the bias parameters. The original idea is that haloes form in the density field where some threshold $\nu\sigma$ is exceeded where ν is a number. This concept can either be applied to extended regions, described via a Heaviside step function, or to point-like peaks. In the limit of $\nu \gg 1$ the result for peaks tends to that for extended regions, and the relation between the correlation function for peaks $\xi_{\mathrm{peaks}}(r)$ and that of the density field $\xi(r)$ is given as

$$\xi_{\mathrm{peaks}}(r) \simeq \frac{\nu^2}{\sigma^2}\xi(r).$$ (1.79)

The original result for overdense regions was derived by Kaiser (1984). A heuristic explanation for peak biasing can be achieved by splitting the density field into a low-amplitude, low-frequency background signal δ_{bg} and a noisy high-amplitude foreground signal δ_{fg}. Peaks form where the foreground signal is subject to constructive interference, and they show a clustering excess when the threshold $\nu\sigma$ is crossed. This process is modulated by the background signal that, on the small scales of tracer formation, acts as a constant shift in the background density. From combining this with a *halo mass function* (i.e. the number density of haloes of a given mass at a given redshift) a biasing relation $b(\nu)$ can be derived. For the Press-Schechter mass function (Press and Schechter, 1974), that builds upon the spherical collapse model where the threshold

for gravitational collapse is $\nu\sigma = \delta_c = 1.68$ (see section 1.3.4), this relation is

$$b(\nu) = 1 + \frac{\nu^2 - 1}{\delta_c}, \tag{1.80}$$

which was derived by Cole and Kaiser (1989). For $\sigma \to 0$ this tends to the Kaiser formula. Equation (1.80) can be improved via the introduction of a moving barrier, $\delta_c(\nu)$, that comes with the ellipsoidal collapse model (R. K. Sheth, H. J. Mo and Tormen, 2001)[21]. To generalize it even more and make it adaptable to more halo formation models and mass functions, Tinker et al. (2010) introduced a flexible fitting function for $b(\nu)$ that depends on δ_c and six parameters. These parameters are either constants or can also depend on halo properties. We will compare the bias parameter results from our simulations with these predictions.

However so far only the linear bias parameter, dubbed b_1 before, was derived. Within the PBS framework also higher-order bias parameters can be predicted. In general, for the case of bias parameters b_n that come with powers of the density field δ^n it is

$$b_n = \frac{\bar{\rho}_m}{\bar{n}_h} \frac{\partial^n \bar{n}_h}{\partial \tilde{\rho}_m^n}\bigg|_{\bar{\rho}_m}, \tag{1.81}$$

with $\bar{n}_h$ the mean number density of haloes, $\bar{\rho}_m$ a fiducial mean matter density and $\tilde{\rho}_m$ a matter density that was shifted by an amount Δ with respect to the fiducial value by the large-scale background amplitude of the PBS. Therefore if we can only predict the number density of haloes as a function of the underlying mean matter density, we can predict the bias parameters by varying that mean matter density and calculating the derivative. In practice this technique can be implemented via the *separate-universe approach* where $\tilde{\rho}_m$ is interpreted as the cosmological matter density of a different universe which means that the complete background cosmology will be different. This can be realized e.g. by running numerical simulations with various cosmologies. From this can then be derived fitting formulas for higher-order bias parameters depending on b_1 as in Lazeyras, Wagner et al. (2016). We will compare our measurement of b_2 to their work[22]. The PBS is consistent with the general perturbative approach to bias since it can be shown that the PBS bias parameters coincide exactly with the renormalised bias parameters that we introduced in section 1.4.5 (Desjacques, Jeong and Schmidt, 2018a).

A relation for b_1 and the tidal bias term s^2 can be derived from the framework of Lagrangian bias (Baldauf, Seljak, Desjacques et al., 2012) where halo formation sites are identified in the initial density field (motivated from peaks that give rise to protohaloes). The bias model is again written as an expansion, where the gravitational evolution of the individual terms can be calculated perturbatively. It turns out that in the expression for the second-order matter density field a term with $2/7s^2$ appears, so that when inserting the matter density into the bias expansion the s^2 term comes with a prefactor that is interpreted as the respective bias parameter b_{s^2}, explicitly

$$b_{s^2} = \frac{2}{7}(1 - b_1). \tag{1.82}$$

---

[21] The framework that deals with halo formation models with respect to barrier crossing is also called the *excursion-set formalism* where halo formation corresponds to a Brownian random walk that upcrosses a barrier for collapse one or multiple times (Bond, Cole et al., 1991).

[22] The PBS and separate-universe approach can also be extended to bias parameters that come with tidal terms or derivatives of the density field, but in this study we will not look into this in detail.

We will test our results against this relation.

A prediction for $b_{\nabla^2\delta}(\nu)$ can be inferred from peak statistics, similar to $b_1(\nu)$, when writing ξ_{peaks} to higher order (Desjacques, 2008, Baldauf, Desjacques and Seljak, 2015). For this bias parameter that is associated with derivatives of the density field not only the peak height is important, but also the mean peak curvature $\bar{u} = G_1/G_0$ (with G_i the i-th moment of the peak curvature u) and the spectral width $\gamma = \sigma_1^2/(\sigma_0\sigma_2)$ (with σ_i the i-th moment of the power spectrum) that reflects the range over which $\Delta^2(k)$ (with $\Delta(k)$ the dimensionless power spectrum as defined in section 1.4.2) is large. The mean peak curvature can be expressed in terms of γ and ν. We will list the explicit expressions and compare our results in chapter 2.

1.5 Numerical simulations

In the last decades cosmological simulations have emerged as a unique testbed to follow structure formation in the Universe down to the very smallest scales (Jenkins et al., 1998, for a recent overview see Kuhlen, Vogelsberger and Angulo, 2012). We can explore the formation of the cosmic web over length scales of several hundred $h^{-1}\,\text{Mpc}$ down to individual DM haloes and the galaxies within them on sub-kpc scales. It is not possible though to access this broad range of scales with one single simulation – instead it has to be decided which problem should be addressed, and the set up of the simulation has to be chosen accordingly. In this study we are not interested in the resolution of the inner structure of individual DM haloes or galaxies, but we rather care for cosmic scales and the statistics that we can measure from that. We will therefore focus on *DM-only simulations* and avoid the treatment of baryons.

1.5.1 Cosmological N-body codes

The basic idea is to study the behaviour of a large number of DM particles which means tracing their position and velocity in time under the influence of the gravitational force in a cubic box of some size that represents a large part of the observable Universe. Of course not actual DM elementary particles can be simulated since their number would need to be huge to achieve results of cosmological relevance. Instead one uses representative particles of masses around $10^7 \ldots 10^{11}\,\text{M}_\odot$. In practice a DM halo in a simulation will then consist of several dozen until millions of representative DM particles.

To set up the simulation we have to fix a few external parameters – the number of DM particles N, the comoving side length L (and therefore the volume $V = L^3$) of the simulation cube, and the cosmological parameters. Common numbers are $N = 1024^3 \approx 1.07 \times 10^9$ and $L = 1\,h^{-1}\,\text{Gpc}$. The matter content of the Universe is about $\Omega_\text{m} \approx 0.3$ and the critical density is $\rho_\text{cr} \approx 27.8 \times 10^{10}\,h^{-2}\,\text{M}_\odot\,\text{Mpc}^{-3}$. From this follows a particle mass of $m_\text{p} \approx 7.8 \times 10^{10}\,h^{-1}\,\text{M}_\odot$, i.e. that of a small galaxy. More particles give a better resolution, but are of course more computationally expensive. Note that in principle such large scales would call for a full GR treatment, but it can be shown that in practice relativistic effects are negligible (Chisari and Zaldarriaga, 2011). It is therefore enough to perform the calculations of the gravitational forces in the Newtonian framework. In order to implement the CP and to allow for using Fourier transformations, we impose *periodic boundary conditions*. This means that particles close to the edge of the simulation box feel the forces from the opposite side, and they will immediately enter from that side when leaving the box.

The explicit expression for the force that is felt by the i-th particle, exerted by the j-th particle,

is

$$\mathbf{F}_i = G \sum_{j \neq i} \frac{m_{\mathrm{p}}(\mathbf{r}_j - \mathbf{r}_i)}{|\mathbf{r}_j - \mathbf{r}_i|^3} \,. \tag{1.83}$$

It would be the most direct way to compute this sum for all the N particles at a certain time step and then accelerate them according to the force they feel. In the next time step this routine would be repeated with updated positions and velocities and so forth. However, for large N this method is not feasible since it scales like N^2 and is therefore very computationally expensive. Modern N-body codes, such as the GADGET-2 code (Springel, 2005) that we are using for our simulation suite introduced in chapter 2, instead employ a hybrid scheme of two more sophisticated methods, called the *TreePM* method. Within this technique the force calculation is split up into large and small scales.

On large scales a *Particle-Mesh* method (hereafter PM method) is employed. The mass of the point-like DM particles is spread on a grid via an interpolation technique[23]. From this, the potential can be computed employing the Poisson equation. The force is easily calculated from this via performing an FT (using a numerical library, such as the *Fastest Fourier Transform of the West*, FFTW, Frigo and Johnson, 2005) and multiplying with $i\mathbf{k}$. Positions and velocities will then be updated by applying this force to the particles, using the same grid interpolation. The method is very fast and of low memory use, but it is lacking accuracy on particle separations of a few grid cells. At these scales the slower, but more accurate *Tree algorithm* is used. This method splits the particle distribution into cubes of successively smaller size (the first one of the hierarchy is called *tree node* and the descending ones are called *leaves*) with increasing particle density. The force onto the particles within these cubes is then calculated via a multipole expansion. The method is very memory-intensive and it is thus reasonable to restrict its application to the smallest scales.

Another effect that has to be taken into account for close particle separations is the two-body relaxation process where a momentum transfer from one DM particle to another takes place. This is not a physical process, but an artifact introduced by treating DM as macroscopic particles in the numerical context. It can be avoided with the use of a *softening parameter* ϵ that modifies the gravitational force below a certain *softening length*,

$$\mathbf{F}(\mathbf{r}) = -\frac{Gm_{\mathrm{p}}^2 \mathbf{r}}{(r^2 + \epsilon^2)^{3/2}} \,, \tag{1.84}$$

where $\mathbf{r} = \mathbf{r}_j - \mathbf{r}_i$ is the separation vector between two particles. The softening length is chosen to be of the order of the mean separation of two particles and for a galaxy-sized halo in GADGET-2 it can be optimally calculated as (Power, Johari and Vij, 2003)

$$\epsilon \approx \frac{4r_{200}}{\sqrt{N_{200}}} \,, \tag{1.85}$$

where N_{200} is the number of particles within a DM halo of radius r_{200} (the radius we will define in section 1.5.3). The modification of the gravitational force eliminates the occurence of strong two-body processes, however it comes with the drawback that scales below the softening length cannot be resolved and are strongly affected by numerical artifacts.

---

[23] One of them is e.g. the *Cloud-In-Cell* (hereafter CIC) method, where the mass of one particle is distributed over its eight neighbouring grid points, weighted with the distance to the grid point (Efstathiou, Davis et al., 1985).

1.5.2 Initial conditions

A cosmological simulation requires an initial density and velocity field, i.e. the *initial conditions* (hereafter IC), that can then be evolved in time. We need to choose the initial redshift z_{IC} in the matter-dominated epoch which should be high enough that the random field is still Gaussian, but also not too high since the accuracy decreases for small δ, plus computational time would be wasted. A common number is $z_{IC} \sim 50$. The amplitude of the Fourier modes $\delta(\mathbf{k})$ of the initial density field are then constructed as

$$P_{11}[\delta(\mathbf{k})] = \frac{1}{\pi\sigma^2(k)} \exp\left[-\frac{\delta^2(\mathbf{k})}{\sigma^2(k)}\right], \tag{1.86}$$

where $P_{11}(k)$ is the theoretical linear power spectrum that can be computed numerically from Boltzmann solvers such as the *Code for Anisotropies in the Microwave Background* (CAMB; Lewis and Challinor, 2011) at the respective z_{IC} for a certain input cosmology. This way for the IC we obtain a Gaussian random field with the correct power spectrum. Now we need to obtain a particle distribution that gives exactly this density field. This can be done via first placing the N particles on a regular grid and shifting them slightly in position such that they have the correct Fourier modes $\delta(\mathbf{k})$, using the *Zel'dovich approximation* (hereafter ZA; Zel'dovich, 1970). The replaced position $\mathbf{x}(\mathbf{q}, t)$ for a particle at initial position $\mathbf{q}$ is given as

$$\mathbf{x}(\mathbf{q}, t) = \mathbf{q} + D(t)\mathbf{\Psi}_1(\mathbf{q}), \tag{1.87}$$

where $\mathbf{\Psi}_1(\mathbf{q})$ is called the displacement field, and it is given via its Fourier modes

$$\mathbf{\Psi}_1(\mathbf{k}) = -i\mathbf{k}\frac{\delta(\mathbf{k})}{k^2}. \tag{1.88}$$

The respective velocity field $\mathbf{v}(t)$ is given as

$$\mathbf{v}(t) = a(t)\frac{\mathrm{d}D(t)}{\mathrm{d}t}\mathbf{\Psi}_1(\mathbf{q}, t). \tag{1.89}$$

The ZA is the first-order term of a more general expansion of the displacement field in the framework of *Lagrangian perturbation theory* (hereafter LPT). In LPT one traces the trajectory of each fluid element via its displacement from $\mathbf{q}$ due the full displacement field $\mathbf{\Psi}$, given as

$$\mathbf{\Psi}(\mathbf{q}, t) = \mathbf{\Psi}_1(\mathbf{q}, t) + \mathbf{\Psi}_2(\mathbf{q}, t) + \mathbf{\Psi}_3(\mathbf{q}, t) + \dots. \tag{1.90}$$

Employing only the ZA introduces spurious effects in the low-redshift power spectrum at percent level which can be avoided when using higher-order LPT for IC generation, such as 2LPT (Crocce and Scoccimarro, 2006; M. White, 2014).

1.5.3 Halo-finding algorithms

After running the simulation from the initial to a final redshift, snapshots of the whole box can be analyzed (where beforehand must be specified at what z the code should produce an output). One has at hand the particle positions and velocities, and from this e.g. correlation functions and power spectra can be built after distributing the particles on a grid, using again e.g. the CIC method. We can also identify the haloes that formed as tightly-bound virialized

DM conglomerates through gravitational collapse and decoupling from the expansion of the Universe. Therefore a halo is more than just a very overdense region and has to be defined and identified in the simulation accordingly. There are various options on how to find a halo in a simulation. Here we will present the two most common ones.

One possibility is to define a halo as an extended region above a certain density threshold $\Delta\bar{\rho}$, i.e. a *spherical overdensity* (hereafter SO) that is Δ-times more dense than the mean density of the Universe $\bar{\rho}$. We start from identifying local overdensities, i.e. peaks, in the density field and then draw gradually expanding spheres around that until the desired SO is reached. The value of Δ is a personal choice, common values are $\Delta = 200, 300$ or 500. This method makes the great simplification that a halo always has spherical shape. Also it only accesses information on the position of the particles, and neglects velocity information – thus we cannot know whether the 'halo' we just identified is actually in virial equilibrium. A popular algorithm that employs the SO criterion is the AMIGA HALO FINDER (AHF; Knollmann and Knebe, 2009).

The second type of halo finders does not treat haloes as objects of fixed shape and density, but rather defines them by collecting and linking particles together that are separated by less than a certain *linking length*. This method is called *Friends-of-Friends* (Davis et al., 1985), and the linking length is commonly chosen 0.2 times the mean particle separation which is motivated from theoretical predictions within the spherical collapse model (Efstathiou, Frenk et al., 1988). Every particle can only belong to one halo, therefore the halo identification is unique. Again the method relies purely on particle position information and neglects velocity information. A popular algorithm of this kind is SUBFIND (Springel, S. D. M. White, Tormen et al., 2001).

In recent years more and more sophisticated halo finders have been developed (for a comparative overview see Knebe et al., 2011). One of these is the ROCKSTAR algorithm (Behroozi, Wechsler and Wu, 2013a) which operates in phase-space and therefore incorporates the full particle information. It starts from an FOF identification with a large linking length of 0.28 and from this builds a hierarchy with gradually decreasing linking length. The *phase-space distance metric* of each FOF subgroup is renormalised by the respective dispersion in position and velocity to allow for an adaptive selection of overdensities at each level. When this process is finished, the FOF groups are converted into haloes, starting at the deepest level, minimizing the metric between the halo and a single particle. Halo centers can then be obtained from averaging the particle positions. We will employ ROCKSTAR in chapters 2 and 3 to study the issue of halo bias with respect to the underlying DM field from a numerical point of view.

1.6 Open questions addressed in this study

In this introduction so far we laid out the state of the art in theory and methodology in the era of precision cosmology, the science that aims to understand the Universe as a whole. We presented the theoretical backbone that leads to our current concordance model of cosmology, the ΛCDM model, which describes the history and contents of the Universe employing only six parameters, among them the density of the illusive components *Dark Matter* (DM) and *Dark Energy* (DE). We emphasized how scientific progress in cosmology is founded on the three pillars of theory, observations and numerical simulations and how strong intertwinement of these different branches is crucial.

In the rest of this study we will focus in particular on the issue of accurate theoretical modeling of galaxy and halo bias – i.e. the relationship between the spatial clustering of said tracers and the underlying DM field – and we will test our model against a suite of 40 cosmological N-body

simulations. Only an accurate bias model across a broad range of scales will allow access to the cosmological information hidden in the statistical properties of the DM distribution. We can group our research into three aspects:

1. Which ingredients, i.e. density fields and powers or derivatives of these, are needed in a *Eulerian bias scheme* to accurately predict the clustering of haloes as tracers down to the non-linear regime? How important are the individual terms at different orders in the expansion and what is the value of the respective *bias parameters*, depending on maximum scale and on halo mass? Where does the optimal trade-off between flexibility and complexity of the model lie?

2. In order for the bias expansion to be valid an arbitrary cutoff scale Λ needs to be applied to the density fields (and therefore also to the statistics such as power spectra) – how can we manipulate the model in a way that the higher-order terms become insensitive to this cutoff scale? Will this *renormalisation* approach that is well-motivated from theory also survive the test to N-body data?

3. Within the framework of *Standard Perturbation Theory* (SPT) the renormalisation of spectra and bias parameters needs to be performed order by order – how can we translate this approach to real data from simulations (or observations in the end)? Is it possible to conduct the renormalisation at n-th order via the precise measurement of n-point statistics from the data? How important are in particular second-order terms, and up until which scale is the order-by-order renormalisation approach valid?

We will first introduce the theoretical bias expansion and the framework of renormalisation in chapter 2. With this we will also describe our set up of cosmological N-body simulations and how they are designed for measuring a set of bias parameters across a broad range of scales and to test the renormalisation procedure at first order (linear bias). We will for the first time measure all the spectra involved directly from the simulation and will therefore provide an explicit test of higher-order operators and spectra in SPT against data. To measure the bias parameters we employ a fitting procedure including correlated errors in the model.

In chapter 3 we extend our analysis to second order in the renormalisation procedure. Whereas before we only had to measure power spectra from the simulation, now we turn to the bispectrum with the goal of renormalising quadratic and tidal bias. This allows to compare the influence of higher-order terms in comparison to the first-order renormalisation results depending on Λ. Additionally, we apply the first-order renormalisation procedure to the halo power spectrum.

Renormalisation of linear halo bias in N-body simulations[1]

2.1 Introduction

The idea that galaxies could be biased tracers of the underlying matter distribution dates back to the 1980s and is intimately linked with the development of the cold-dark-matter (CDM) cosmological model (e.g. Kaiser, 1984; Davis et al., 1985; Rees, 1985; Dekel and Rees, 1987; S. D. M. White et al., 1987). For many years, the leading galaxy-biasing model assumed a local and deterministic relation between the smoothed galaxy density contrast δ_g and the matter density contrast δ evaluated at the same position $\mathbf{x}$, i.e. $\delta_g(\mathbf{x}) = f[\delta(\mathbf{x})]$ where f denotes a generic 'bias function' (Fry and Gaztanaga, 1993). The freedom in the function f was often described in terms of the 'bias parameters' i.e. the Taylor coefficients b_i appearing in the 'bias expansion' $\delta_g = b_0 + b_1\,\delta + b_2\,\delta^2 + \dots$. These parameters depend on the coarse-graining scale used to define δ and δ_g. The reasons for smoothing are multiple: (i) galaxies are discrete objects and we want to define a continuous density field; (ii) our model aims at describing the largest scales only; (iii) the bias expansion should be well-behaved so that it can be truncated at finite order; (iv) the dynamical model we use to evolve cosmological perturbations breaks down on small scales.

This bias model is applicable to any tracers of the large-scale structure (LSS) of the Universe (e.g. galaxy clusters, dark-matter (DM) haloes, galaxies detected with different selection criteria) by picking the appropriate function f or, equivalently, the corresponding set of bias parameters. In particular, if one considers DM haloes, the local ansatz for the bias relation is supported by spherically-symmetric models of gravitational collapse which also provide predictions for the bias parameters as a function of halo mass (e.g. H. J. Mo and S. D. M. White, 1996; H. J. Mo, Jing and S. D. M. White, 1997; Porciani et al., 1998).

It was later realised that anisotropic gravitational collapse generates non-local and stochastic terms in the bias relation (Catelan, Lucchin et al., 1998) and that this originates leading-order (LO) corrections to the galaxy bispectrum (Catelan, Porciani and Kamionkowski, 2000). The implications of this result were fully appreciated only a decade later when local bias was shown to be insufficient to describe the clustering of DM haloes (Manera and Gaztañaga, 2011; Matsubara, 2011; Roth and Porciani, 2011; Pollack, Smith and Porciani, 2012; Pollack, Smith and Porciani, 2014) and evidence for bias corrections that are quadratic in the tidal tensor was found in

---

[1] This chapter has been submitted to MNRAS. A pre-print version has been published in Werner and Porciani (2019).

N-body simulations (Baldauf, Seljak, Desjacques et al., 2012; Chan, Scoccimarro and R. K. Sheth, 2012). At the same time, it was realized that the bias expansion should also contain a series of derivative terms starting with $R^2 \nabla^2 \delta$ because haloes and galaxies collect material from an extended region of space of characteristic size R (e.g. Desjacques, 2008; McDonald and Roy, 2009; Desjacques, Crocce et al., 2010; Schmidt, Jeong and Desjacques, 2013; Fujita et al., 2016). The current consensus is that the bias relation should be compatible with all possible symmetries of gravitational instability (McDonald and Roy, 2009; Kehagias et al., 2014; Senatore, 2015; Eggemeier, Scoccimarro and Smith, 2019) and thus depend on several other fields than δ (see section 2.2.2).

Different techniques have been developed to measure the corresponding bias coefficients for DM haloes in numerical simulations. One possibility is to fit model predictions to the N-body data for various clustering statistics – e.g. power spectra or two-point correlation functions – (Saito et al., 2014; Bel, Hoffmann and Gaztañaga, 2015; Hoffmann, Bel and Gaztañaga, 2015; Hoffmann, Bel and Gaztañaga, 2017; Modi, Castorina and Seljak, 2017; Hoffmann, Gaztañaga et al., 2018) or even at the field level (Roth and Porciani, 2011; Schmittfull et al., 2018). Alternatively, one can measure the response of the halo population to long-wavelength perturbations in the matter density (Li, Hu and Takada, 2016; Baldauf, Seljak, Senatore et al., 2016; Lazeyras, Wagner et al., 2016; Lazeyras and Schmidt, 2019). Lastly, bias parameters can be obtained by cross-correlating the corresponding fields that appear in the bias expansion with the halo density distribution (Abidi and Baldauf, 2018; Lazeyras and Schmidt, 2018).

Another important line of research has examined how measurable clustering statistics of tracers depend on the bias relation and on the statistical properties of the underlying matter-density field. This is, in fact, key to interpret results from galaxy redshift surveys. For a local bias relation and in the presence of a Gaussian matter-density field, the ratio $b_{\mathrm{eff}}^2(k)$ between the (shot-noise subtracted) tracer- and matter power spectra tends to the constant b_1^2 when $k \to 0$ (Szalay, 1988; Coles, 1993; Fry and Gaztanaga, 1993; Gaztanaga and Baugh, 1998). However, for a non-Gaussian matter density distribution, the constant does not coincide with the linear bias parameter and also depends on the cumulants of the matter density as well as higher-order bias parameters (Scherrer and D. H. Weinberg, 1998). In particular, if the statistics of the matter distribution are derived using standard perturbation theory, the LO correction to b_1^2 scales with the variance of the linear density field that grows large when the coarse-graining scale becomes small (Heavens, Matarrese and Verde, 1998, see also our section 2.2.3 for further details). This sensitivity of the theoretical predictions on the smoothing scale that defines the bias function complicates the use of bias models to interpret observational data.

Inspired by applications of the renormalisation group to the perturbative solution of ordinary differential equations, McDonald (2006) proposed a different interpretation of the theoretical predictions. The key concept is that the parameters b_i appearing in the bias expansion do not actually correspond to the physical constants that can be measured in a survey. They are, instead, bare quantities that do not take into account the contribution of perturbative (loop) corrections to the leading terms. One can then rewrite the result of the perturbative calculations for the power spectrum of the tracers in terms of measurable 'renormalised[2]' quantities that do not depend on the smoothing scale. McDonald and Roy (2009) extended this approach to a bias relation that also depends on the tidal field. More recently, by using the diagrammatic representation of perturbation theory (PT), Assassi et al. (2014) derived a set of conditions

---

[2] The whole procedure parallels Wilsonian renormalisation in field theories. The coarse-graining scale of the density fields here replaces the cutoff that regularises the loop integrals in the quantum field theories.

that the bias expansion must satisfy to be perturbatively renormalised order by order (see also Senatore, 2015). From these studies it emerges that only bias expansions that include terms proportional to the tidal field and to derivative of the matter density (e.g. $\nabla^2\delta$) can be renormalised.

Bias renormalisation is analogous to methods used in statistical field theory and quantum field theory. In general, these techniques provide a convenient way to build 'effective theories' that describe physics at a given range of length (and/or time, mass, etc.) scales and with a given accuracy by using a finite set of parameters. This bypasses the need for the 'full theory' that includes physics on all scales but might be intractable or, even, unknown. Likewise, the goal of bias renormalisation is to build an effective model for the clustering statistics of tracers. Much of the jargon used in the literature on bias renormalisation is imported from other branches of physics. Less theoretically inclined researchers shy away from the unfamiliar notation and concepts. One of the motivations of this paper is to provide a pedagogical review of the subject and some concrete examples to see it 'in action'. A second one is that there are a number of questions that are still unanswered. Are all the possible operators allowed by symmetries necessary in the bias expansion? Up to what distances does the renormalised bias expansion (truncated to some order) give an accurate description of the observed clustering statistics of tracers like galaxies?

Although the renormalisation of the bias expansion has always been discussed within the context of cosmological PT, only some of its aspects are fully perturbative. If one writes down a bias expansion in terms of Taylor coefficients, renormalisation is necessary also when one deals with the exact dynamics (extracted e.g. from simulations as in our case) in order to account for the non-linear terms (e.g. δ^2) that generate smoothing-dependent spectra. In general, renormalisation fixes a 'language' problem in the way we describe biasing, and PT provides an approximate solution on how to implement the remedy in practice. Here we present a first step towards implementing renormalisation within a large suite of N-body simulations where the dynamics is non-perturbative. This will shed new light on the limitations of the perturbative approach.

Usually, tests of the renormalised bias models are conducted by fitting the full perturbative expression for some clustering statistics to N-body simulations (e.g. Saito et al., 2014). We instead apply the renormalisation procedure step by step to the numerical data, examining all the contributions due to the relevant fields separately. For simplicity, we focus on the cross power spectral density $P_{\delta_{\rm h}\delta}(k)$ of the matter and halo density fields[3] defined as $\langle \delta_{\rm h}(\mathbf{k})\,\delta(\mathbf{k}')\rangle = (2\pi)^3\,P_{\delta_{\rm h}\delta}(k)\,\delta_{\rm D}(\mathbf{k}+\mathbf{k}')$, where the brackets $\langle\dots\rangle$ denote the average over an ensemble of realizations and $\delta_{\rm D}(\mathbf{k})$ is the Dirac delta distribution in three dimensions.

The detailed goals of this work are to (i) apply the Wilsonian renormalisation-group (RG) method to halo bias in a large suite of N-body simulations and study the behaviour of the fields appearing in the bias expansion as a function of the coarse-graining scale; (ii) measure the bias parameters of the DM haloes extracted from simulations by fitting the halo-matter cross-power spectrum $P_{\delta_{\rm h}\delta}(k)$; (iii) follow their evolution (running) induced by the RG coarse-graining scale; (iv) test that they can be renormalised by re-arranging the terms in the bias expansion; (v) use Bayesian model-selection techniques to determine which bias parameters are necessary to accurately describe $P_{\delta_{\rm h}\delta}(k)$ up to $k = 0.2\ h\,\mathrm{Mpc}^{-1}$. In this paper, we introduce the main concepts of our study and focus on the renormalisation of the linear bias coefficient, b_1. We plan to

---

[3] With a little abuse of notation, we denote by $f(\mathbf{k})$ the Fourier transform of the function $f(\mathbf{x})$ where $\mathbf{x}$ indicates the comoving position.

discuss the renormalisation of the bias parameters at second order in our future work.

The structure of this paper is as follows: The theoretical motivations and methods of bias renormalisation are reviewed in section 2.2 where we also present an original discussion on the impact of filter functions. The numerical techniques and N-body simulations we use are described in section 2.3. Our results on renormalisation are presented in section 2.4 and the measurements of the bias parameter in section 2.5. Finally, our conclusions are laid down in section 2.6.

2.2 Tracer bias in cosmological perturbation theory

2.2.1 Standard perturbation theory in a nutshell

Standard perturbation theory (SPT, for a review, see Bernardeau et al., 2002) describes matter as a pressureless and inviscid fluid to model the growth of density and velocity perturbations in a Friedmann-Robertson-Walker background with expansion factor a. The system formed by the continuity, Euler and Poisson equations is solved perturbatively. At any given time, the fastest growing solution for the density contrast, $\delta(\mathbf{x})$, is expanded as

$$\delta(\mathbf{x}) = \delta_1(\mathbf{x}) + \delta_2(\mathbf{x}) + \delta_3(\mathbf{x}) + \dots \tag{2.1}$$

where δ_1 denotes the growing-mode solution to the linearized set of equations and $\delta_n = O(\delta_1^n)$. The time evolution of δ_1 is governed by the linear growth factor $D(a)$, such that $\delta_1 \propto D$. Similarly, the fastest growing mode for the divergence of the peculiar velocity $\nabla \cdot \mathbf{v} = -aHf\theta$ – where $H = \dot{a}/a$ is the Hubble parameter (the dot indicates differentiation with respect to cosmic time) and $f = \mathrm{d}\ln D/\mathrm{d}\ln a$ – is written as

$$\theta(\mathbf{x}) = \theta_1(\mathbf{x}) + \theta_2(\mathbf{x}) + \theta_3(\mathbf{x}) + \dots \,, \tag{2.2}$$

with $\theta_1 = \delta_1$. In Fourier space,

$$\delta_n(\mathbf{k}) \quad = \quad \int F_n(\mathbf{k}_1, \dots, \mathbf{k}_n)\, \delta_1(\mathbf{k}_1) \dots \delta_1(\mathbf{k}_n)\, \delta_D(\mathbf{k}_1 + \cdots + \mathbf{k}_n - \mathbf{k}) \frac{\mathrm{d}^3 k_1}{(2\pi)^3} \dots \frac{\mathrm{d}^3 k_n}{(2\pi)^3} \tag{2.3}$$

and

$$\theta_n(\mathbf{k}) \quad = \quad \int G_n(\mathbf{k}_1, \dots, \mathbf{k}_n)\, \delta_1(\mathbf{k}_1) \dots \delta_1(\mathbf{k}_n)\, \delta_D(\mathbf{k}_1 + \cdots + \mathbf{k}_n - \mathbf{k}) \frac{\mathrm{d}^3 k_1}{(2\pi)^3} \dots \frac{\mathrm{d}^3 k_n}{(2\pi)^3} \,, \tag{2.4}$$

where the kernels F_n and G_n are homogeneous functions of degree zero that describe the couplings between Fourier modes generated by the dynamical non-linearities. These functions obey recursion relations that can be solved order by order starting from $F_1 = G_1 = 1$ (e.g. Goroff et al., 1986). For instance, the second-order kernels (symmetrized over permutations of their arguments) are

$$F_2(\mathbf{k}_1, \mathbf{k}_2) = \frac{5}{7} + \frac{1}{2} \frac{\mathbf{k}_1 \cdot \mathbf{k}_2}{k_1 k_2} \left(\frac{k_1}{k_2} + \frac{k_2}{k_1} \right) + \frac{2}{7} \left(\frac{\mathbf{k}_1 \cdot \mathbf{k}_2}{k_1 k_2} \right)^2 \,, \tag{2.5}$$

$$G_2(\mathbf{k}_1, \mathbf{k}_2) = \frac{3}{7} + \frac{1}{2} \frac{\mathbf{k}_1 \cdot \mathbf{k}_2}{k_1 k_2} \left(\frac{k_1}{k_2} + \frac{k_2}{k_1} \right) + \frac{4}{7} \left(\frac{\mathbf{k}_1 \cdot \mathbf{k}_2}{k_1 k_2} \right)^2 \,, \tag{2.6}$$

Although these expressions are exact only in an Einstein-de Sitter universe, they provide an excellent approximation also in the ΛCDM scenario (Bernardeau, 1994; Lee, Park and Biern, 2014).

Assuming Gaussian initial conditions allows us to compute perturbative expansions for statistical quantities averaged over an ensemble of realisations of δ_1. For instance, let us consider the power spectrum of matter density perturbations, $P_{\delta\delta}(k)$, defined as $\langle\delta(\mathbf{k})\,\delta(\mathbf{k}')\rangle = (2\pi)^3\,P_{\delta\delta}(k)\,\delta_{\mathrm{D}}(\mathbf{k}+\mathbf{k}')$. Within SPT and up to fourth order in δ_1, we can write the 'correlator' $\langle\delta\delta\rangle \simeq \langle\delta_1\delta_1\rangle + \langle\delta_2\delta_2\rangle + \langle\delta_3\delta_1\rangle$ (the obvious dependence on the wavevectors is understood here to simplify notation). Therefore, $P_{\delta\delta}(k)$ can be approximated as

$$P_{\delta\delta}(k) \simeq P_{\delta\delta}^{(11)}(k) + P_{\delta\delta}^{(22)}(k) + P_{\delta\delta}^{(31)}(k)\,, \tag{2.7}$$

where the LO term $P_{\delta\delta}^{(11)}(k)$ coincides with the linear power spectrum $P_{11}(k)$ while the next-to-leading-order (NLO) corrections are

$$P_{\delta\delta}^{(22)}(k) = 2\int F_2^2(\mathbf{q},\mathbf{k}-\mathbf{q})\,P_{11}(|\mathbf{k}-\mathbf{q}|)\,P_{11}(q)\,\frac{\mathrm{d}^3q}{(2\pi)^3}\,, \tag{2.8}$$

$$P_{\delta\delta}^{(31)}(k) = 3\,P_{11}(k)\int F_3(\mathbf{q},-\mathbf{q},\mathbf{k})\,P_{11}(q)\,\frac{\mathrm{d}^3q}{(2\pi)^3}\,. \tag{2.9}$$

A powerful diagrammatic technique has been introduced to conveniently perform the SPT expansion of ensemble-averaged statistics (e.g. Bernardeau et al., 2002). This is analogous to the method introduced by Feynman in quantum electrodynamics. In most cases, LO contributions are associated with tree diagrams (in the sense of graph theory) and are thus called 'tree-level terms'. Evaluating these quantities does not require any integration (see e.g. $P_{11}(k)$ above). On the other hand, terms associated with diagrams containing n-loops give rise to 'n-loop corrections' that require n integrations (see e.g. the 1-loop term $P_{\delta\delta}^{(22)}(k)+P_{\delta\delta}^{(13)}(k)$). Note that, if the tree-level term vanishes, the LO is given by the 1-loop terms (see e.g. section 2.2.3).

SPT mainly suffers from two limitations. First, being a perturbative technique, it is expected to break down when and where $|\delta(\mathbf{x})| \simeq 1$. Second, the gravitational collapse of an initially cold distribution of collisionless DM develops multi-stream regions where the velocity field is not single-valued. However, the pressureless-fluid approximation adopted by SPT does not account for this phenomenon which alters the dynamics of the system. N-body simulations show that, within the ΛCDM scenario, SPT provides rather accurate predictions for 2- and 3-point statistics at redshifts $z > 1$ and $k \lesssim 0.2\ h\ \mathrm{Mpc}^{-1}$ while it becomes increasingly imprecise at lower redshifts (for the same wavenumbers) as the variance of the density perturbations approaches unity (e.g. Carlson, M. White and Padmanabhan, 2009; Nishimichi et al., 2009; Blas, Garny and Konstandin, 2014).

2.2.2 Biasing as an effective field theory

We are interested in describing how discrete objects (for example DM haloes or galaxies) trace the smooth matter density field throughout the Universe. Since haloes assemble from the gravitational collapse of matter on small scales and galaxies form within them, it is reasonable to assume that some deterministic relationship exists between the density of matter and that of the discrete tracers on large scales. Numerical simulations and simple toy models that associate haloes to peaks in the initial density field provide supporting evidence in favour of this

argument. However, the physics of halo and galaxy formation is complex, highly non-linear and non-perturbative. Although we can simulate it with the help of a computer, we are not able to make analytical predictions. Given these circumstances, for practical applications like the interpretation of galaxy redshift surveys, it makes sense to opt for a simplified description that holds true only on large scales.

Analogous problems in other fields of physics led to the development of effective field theories (EFTs). We highlight here how the basic concepts of an EFT can be used to model large-scale biasing. We first introduce the effective overdensity field of the tracers[4], $\delta_h(\mathbf{x}, t)$, which describes their large-scale clustering, but is blind to their precise distribution on small scales. In order to relate this quantity to the underlying mass-overdensity field, δ, it is necessary to identify all possible dependencies that are compatible with the symmetries of the problem. Assuming that the tracers are non-relativistic implies that gravitational physics is fully described in terms of the (rescaled) peculiar gravitational potential ϕ, defined so that $\nabla^2 \phi = \delta$. Taking into account the equivalence principle and that δ_h is a scalar under rotations, it follows that δ_h can only depend on scalar combinations of second spatial derivatives of the peculiar gravitational potential $\partial_i \partial_j \phi$, and first spatial derivatives of the peculiar velocity field $\partial_j v^i$ (McDonald and Roy, 2009; Kehagias et al., 2014; Senatore, 2015).

The second key step in the construction of an EFT for biasing is to consider that the physics regulating the clustering of tracers is non-local in space and time. The material that forms a tracer was dispersed within an extended patch of characteristic size R at early times and needed a characteristic time T to assemble together. In general, $R \lesssim 10 \; h^{-1} \, \mathrm{Mpc}$ (the Lagrangian size of galaxy clusters) which is small compared with the scales we want to describe using our EFT. On the other hand, T is never short compared to the Hubble time. It follows that the effective theory of biasing should be approximately local in space but non-local in time (Senatore, 2015). In mathematical terms, this means that δ_h should depend on the cosmological perturbations evaluated along the past worldlines of the fluid elements that end up forming the tracers at a given location (or, better, within a given patch).

Since we are only interested in the large spatial scales, the third step is to expand the generic (and unknown) functional δ_h in powers of the cosmological fluctuations and their spatial derivatives (to account for the mild spatial non-locality). Note that the tensor $\partial_i \partial_j \phi$ is a dimensionless quantity and its spatial derivatives need to be multiplied by a length scale of order R in the expansion. It follows that all derivative corrections will be suppressed on scales much larger than R. This is more easily seen in Fourier space. For instance, let us consider the first derivative correction to terms that are proportional to δ, i.e. $\sim R^2 \nabla^2 \delta$ (as we need a scalar under rotations). In Fourier space this term is proportional to $(kR)^2$ and thus heavily suppressed for scales $k \ll R^{-1}$. On the other hand, this also implies that the derivative expansion breaks down on scales of order R.

Finally, the non-locality in time is accounted for by making some further hypotheses, namely by assuming that cosmological perturbations evolve as in SPT. In this case, the expansion of δ_h is re-organised to avoid duplication of terms (for instance the velocity divergence coincides with the overdensity at linear order) and its coefficients are re-defined as integrals over time of the original ones (Mirbabayi, Schmidt and Zaldarriaga, 2015; Angulo et al., 2015; Desjacques, Jeong and Schmidt, 2018b; Desjacques, Jeong and Schmidt, 2018c).

---

[4] The subscript 'h' refers to DM haloes, but the framework is applicable to any tracer.

Up to third order in the cosmological perturbations, one thus obtains

$$\delta_{\rm h} = b_0 + b_1\delta + b_{\nabla^2\delta}\nabla^2\delta + b_2\delta^2 + b_{s^2}s^2 + b_3\delta^3 + b_{\delta s^2}\delta s^2 + b_{s^3}s^3 + b_{\Gamma_3}\Gamma_3 \,, \tag{2.10}$$

where we have (i) decomposed the tensor $\partial_i\partial_j\phi$ into its trace δ and the traceless part,

$$s_{ij} = \partial_i\partial_j\phi - \frac{1}{3}\delta^{\rm K}_{ij}\delta = \left(\partial_i\partial_j\nabla^{-2} - \frac{1}{3}\delta^{\rm K}_{ij}\right)\delta = \gamma_{ij}\delta \,, \tag{2.11}$$

(with ∇^{-2} the inverse of the Laplacian operator and $\delta^{\rm K}_{ij}$ the Kronecker symbol); (ii) introduced the scalars $s^2 = s_{ij}s_{ji}$, $s^3 = s_{ij}s_{jk}s_{ki}$; (iii) used the (rescaled) velocity potential ϕ_v such that $\nabla^2\phi_v = \theta$ to define the tensor $p_{ij} = \partial_i\partial_j\phi_v - \frac{1}{3}\delta^{\rm K}_{ij}\theta$ and the operator[5] $\Gamma_3 = s^2 - p^2 - (2/3)(\delta^2 - \theta^2)$ with $p^2 = p_{ij}p_{ji}$; (iv) included only the leading higher-derivative term $\propto \nabla^2\delta$, for simplicity.

In compact form, the bias expansion can be written as

$$\delta_{\rm h} = \sum_O b_O\, O \,, \tag{2.12}$$

where the sum runs over a fixed basis of operators, O, that are compatible with the symmetries and the evolution of cosmological perturbations while the bias parameters, b_O, depend on the characteristics of the population of tracers (e.g. the halo mass, the galaxy luminosity or the intensity of a particular emission line).

The expressions above are meant to relate the spatial distribution of tracers on large scales with the underlying long-wavelength cosmological perturbations in a deterministic way. However, the short-wavelength fluctuations (to which our effective theory is blind by construction) also play a role in determining the precise location of the tracers. In order to account for this phenomenon in the theory, we introduce a certain degree of randomness in the bias expansion by assuming that the bias coefficients have also a zero-mean stochastic component ϵ_O, i.e.

$$\delta_{\rm h} = \sum_O (b_O + \epsilon_O)\, O \,. \tag{2.13}$$

Furthermore, it is customary to treat each stochastic term as a perturbation $O(\delta)$. For example, to second order, we can write:

$$\delta_{\rm h} = b_0 + \epsilon_0 + b_1\delta + b_{\nabla^2\delta}\nabla^2\delta + \epsilon_1\delta + \epsilon_{\nabla^2\delta}\nabla^2\delta + b_2\delta^2 + b_{s^2}s^2 \,. \tag{2.14}$$

Under the assumption that the stochastic terms do not correlate with the long-wavelength cosmological perturbations, their statistical properties are fully determined by their auto- and cross-correlation functions (or auto- and cross-spectra in Fourier space). In the literature, it is often assumed that the cross-spectrum between ϵ_O and $\epsilon_{O'}$ can be written as a series expansion in k^2,

$$\Upsilon_{OO'}(k) = \Upsilon_{0,OO'} + \Upsilon_{2,OO'}k^2 + \Upsilon_{4,OO'}k^4 + \dots \,. \tag{2.15}$$

Once again, this reflects the fact that $\delta_{\rm h}$ should be determined by the value assumed by the stochastic fields within an extended region of space and not only at one point. However, when

---

[5] The bias expansion is sometimes written using the so-called second- and third-order 'Galileon' operators, $\mathcal{G}_2(\phi)$ and $\mathcal{G}_3(\phi)$ The relation between this set of operators and ours is $\mathcal{G}_2(\phi) = s^2 - (2/3)\delta^2$ and $\mathcal{G}_3(\phi) = -\delta^3/9 - s^3 + \delta s^2/2$. Note that $\Gamma_3 = \mathcal{G}_2(\phi) - \mathcal{G}_2(\phi_v)$.

taken term by term, this expansion makes little sense in configuration space. While $\Upsilon_{0,OO'}$ gives rise to a standard shot-noise term with a 2-point correlation that is proportional to the Dirac delta distribution at zero lag, $\delta_{\mathrm{D}}(r)$, the remaining terms generate contributions proportional to $\nabla^{2n}\delta_{\mathrm{D}}(r)$. These 'contact terms' (as they are generally dubbed in field theory) appear because we are considering an asymptotic expansion in Fourier space that breaks down on small scales. A more sophisticated treatment of the short-wavelength modes should then be used to discuss the statistics of tracers in configuration space.

A note is in order regarding equations (2.10), (2.12), and (2.13). Implicit in the definition of all fields is a low-pass smoothing procedure that isolates the long-wavelength modes to which the theory applies. In particular, it is necessary to specify how the smoothing is done for the non-linear terms like δ^2 and s^2. In fact, the long-wavelength modes of δ^2 depend on the short-wavelength modes of δ implying that δ^2 cannot be reliably computed with a perturbative approach and that it can grow large even at low k. Since we want to consider only the contribution of the large-scale modes of the density perturbations, the only meaningful interpretation of the r.h.s. in equations (2.10), (2.12), and (2.13) is to smooth the matter overdensity field first and then use the low-pass filtered δ to evaluate the non-linear operators (Heavens, Matarrese and Verde, 1998). Filtering out the short-wavelength modes with $k > \Lambda$ is thus necessary for several reasons: (i) as we have already mentioned, to only consider the scales that are described by the theory; (ii) to ensure that $|\delta(\mathbf{x})| \ll 1$ and a series expansion of the bias relation in the cosmological perturbations makes sense; and (iii) to be able to apply SPT.

The ultimate goal of the effective theory of biasing is to model the observed n-point correlation functions (and their corresponding multi-spectra in Fourier space) for tracers on large scales. In this work, we focus on two-point statistics in Fourier space. The model predictions are obtained by correlating the Fourier transform of equation (2.13) either with itself or with the Fourier transform of the overdensity field. This provides a systematic expansion of the spectra organized according to the importance of its terms based on a power-counting argument. The underlying assumption is that there exist two well-defined scales: a non-linearity scale R_{nl} (at which physics becomes non-perturbative and the expansion in powers of the cosmological fluctuations breaks down) and a non-locality scale L (at which the expansion in powers of the higher-derivative terms breaks down). The different contributions to the spectra scale as powers of kL and kR_{nl}. Truncating the expansion at a given order thus provides results with reliable error estimates without referencing any quantity outside of the theory. The bias parameters and the coefficients that define the statistical properties of the stochastic fields are free parameters that need to be tuned in order to match observations. However, since the non-linear operators of the theory are heavily dependent on the smoothing scale, the best-fitting coefficients will inherit a dependence on Λ. As we have already mentioned in the introduction, an analogy can be established between this description of galaxy biasing and the Wilsonian renormalisation in quantum field theory. In brief, the bias series can be re-organized so that to eliminate the so-called 'UV-sensitive' terms that depend on Λ order by order in the perturbative expansion. This is equivalent to expressing the bias relation in terms of a set of 'renormalised' operators $[O]$ built from the original operator basis O

$$\delta_{\mathrm{h}} = \sum_{[O]} (b_{[O]} + \epsilon_{[O]})\,[O]\,. \tag{2.16}$$

2.2.3 Bias renormalisation

The bias renormalisation forms the main subject of our investigation and, for this reason, we explore the related concepts in more detail.

UV-sensitivity of composite operators

The bias expansion given in equation (2.13) contains operators obtained by multiplying two fields evaluated at the same spatial location, like δ^2 and s^2. These 'local operators' or 'composite operators' (as they are generally called in field theories) are very sensitive to the short-wavelength modes of δ that are not accurately modelled by SPT. This can be easily understood, for example, by inspecting the Fourier transform of δ^2:

$$\delta^2(\mathbf{k}) = \int \delta(\mathbf{q})\,\delta(\mathbf{k} - \mathbf{q})\,\frac{\mathrm{d}^3 q}{(2\pi)^3}\;. \tag{2.17}$$

Even for small values of k, δ^2 receives contributions from all scales. For instance, its expectation value,

$$\langle \delta^2(\mathbf{x}) \rangle = \frac{1}{2\pi^2} \int_0^\infty q^2\, P_{\delta\delta}(q)\,\mathrm{d}q \equiv \sigma^2\;, \tag{2.18}$$

can get very large (or even diverge) if the density perturbations have substantial power at small scales. Similarly, the cross spectrum of δ^2 with the matter-density fluctuations, defined as $\langle \delta^2(\mathbf{k})\,\delta(\mathbf{k}') \rangle = (2\pi)^3\,P_{\delta^2\delta}(k)\,\delta_\mathrm{D}(\mathbf{k} + \mathbf{k}')$, coincides with an integral over all scales of the matter bispectrum

$$P_{\delta^2\delta}(k) = \int B_{\delta\delta\delta}(\mathbf{q}, \mathbf{k} - \mathbf{q}, -\mathbf{k})\,\frac{\mathrm{d}^3 q}{(2\pi)^3}\;, \tag{2.19}$$

where $\langle \delta(\mathbf{p})\,\delta(\mathbf{q})\,\delta(\mathbf{k}) \rangle = (2\pi)^3\,B_{\delta\delta\delta}(p, q, k)\,\delta_\mathrm{D}(\mathbf{p} + \mathbf{q} + \mathbf{k})$. All this implies that, if a low-pass filter $W(k, \Lambda)$ is applied to δ, then $\delta^2(\mathbf{k})$ inherits a strong dependence on Λ. In brief, we say that the composite operators δ^2 and s^2 are UV-sensitive.

Composite operators in SPT

To LO in SPT, we can write the matter power spectrum $P_{\delta\delta}^{(\mathrm{LO})}(k) = P_{11}(k)$ and the bispectrum $B_{\delta\delta\delta}^{(\mathrm{LO})}(k_1, k_2, k_3) = B_{\delta\delta\delta}^{(112)}(k_1, k_2, k_3) + B_{\delta\delta\delta}^{(121)}(k_1, k_2, k_3) + B_{\delta\delta\delta}^{(211)}(k_1, k_2, k_3)$. By substituting these approximations in equations (2.18) and (2.19) one obtains

$$\sigma_{(\mathrm{LO})}^2 = \lim_{\Lambda \to \infty} \frac{1}{2\pi^2} \int_0^\Lambda q^2\, P_{11}(q)\,\mathrm{d}q \equiv \lim_{\Lambda \to \infty} \sigma_1^2(\Lambda)\;, \tag{2.20}$$

and

$$\begin{aligned}
P_{\delta^2\delta}^{(\mathrm{LO})}(k) &= \int \left[B_{\delta\delta\delta}^{(112)}(\mathbf{q}, \mathbf{k} - \mathbf{q}, -\mathbf{k}) + \text{cyclical} \right] \frac{\mathrm{d}^3 q}{(2\pi)^3} \\
&= P_{\delta^2\delta}^{(22)}(k) + P_{\delta^2\delta}^{(31)}(k)\;,
\end{aligned} \tag{2.21}$$

with

$$P_{\delta^2\delta}^{(22)}(k) = 2 \int F_2(\mathbf{q}, \mathbf{k} - \mathbf{q}) P_{11}(q) \, P_{11}(|\mathbf{k} - \mathbf{q}|) \frac{\mathrm{d}^3 q}{(2\pi)^3} \,, \tag{2.22}$$

and

$$P_{\delta^2\delta}^{(31)}(k) = 4 P_{11}(k) \int F_2(-\mathbf{q}, \mathbf{k}) P_{11}(q) \frac{\mathrm{d}^3 q}{(2\pi)^3} \,. \tag{2.23}$$

The behaviour of these cross-spectra at large scales ($k \to 0$) is usually determined by using spherical coordinates (with polar axis $\mathbf{k}$) and limiting the integration in q with an upper cutoff Λ. It turns out that

$$P_{\delta^2\delta}^{(31)}(k) = \frac{68}{21} \sigma_1^2(\Lambda) \, P_{11}(k), \tag{2.24}$$

which shows that the normalisation of $P_{\delta^2\delta}^{(31)}(k)$ depends on Λ (Heavens, Matarrese and Verde, 1998). This is an example of a UV-sensitive term. On the other hand, the $k \to 0$ limit of $P_{\delta^2\delta}^{(22)}(k)$ does not show any cutoff dependence.

Renormalisation and counterterms

Fur illustrative purposes only, let us now consider a simplified bias expansion such that

$$\delta_{\mathrm{h}}(\mathbf{x}) = b_0 + b_1 \delta(\mathbf{x}) + b_2 \delta^2(\mathbf{x}) \tag{2.25}$$

and evaluate the expectation value of δ_{h} at NLO in SPT.

It is straightforward to obtain that $\langle \delta_{\mathrm{h}}(\mathbf{x}) \rangle = b_0 + b_2 \sigma_1^2(\Lambda)$. Since $\langle \delta_{\mathrm{h}} \rangle$ is an observable which is identically equal to zero, if we want to identify our truncated perturbative result with the actual measurement, it is necessary to set $b_0 + b_2 \sigma_1^2(\Lambda) = b_0^{\mathrm{R}} = 0$. This leads to the modified bias expansion $\delta_{\mathrm{h}}(\mathbf{x}) = b_0^{\mathrm{R}} + b_1 \delta(\mathbf{x}) + b_2 [\delta^2(\mathbf{x}) - \sigma_1^2(\Lambda)] = b_1 \delta(\mathbf{x}) + b_2 [\delta^2(\mathbf{x}) - \sigma_1^2(\Lambda)]$.

Starting from this expression, we now derive the cross spectrum between the tracer density field and the matter density to 1-loop in SPT. The tree-level result is $b_1 P_{11}(k)$, while the 1-loop corrections give $b_2 [P_{\delta^2\delta}^{(22)}(k) + P_{\delta^2\delta}^{(31)}(k)]$. Equation (2.24) shows that the loop corrections contain a term which coincides with the tree-level result rescaled by a cutoff-dependent coefficient. Remarkably, the combination $[b_1 + b_2 (68/21) \sigma_1^2(\Lambda)] P_{11}(k)$ gives the dominant contribution when $k \to 0$. Inspired by Wilsonian renormalisation of field theories where the UV divergences are cancelled by a redefinition of the parameters of the theory, McDonald (2006) proposes to replace $b_1 + b_2 (68/21) \sigma_1^2(\Lambda)$ with the new ('renormalised' or 'observable') linear bias coefficient b_1^{R}. The resulting expression for the cross spectrum at one loop will thus be

$$P_{\delta_{\mathrm{h}}\delta}(k) = b_1^{\mathrm{R}} P_{11}(k) + b_2 \, P_{\delta^2\delta}^{(22)}(k) \,. \tag{2.26}$$

Here, b_1^{R} should be considered as a free parameter of the model that can be adjusted to fit observational data. On the other hand, the 'bare' linear bias coefficient b_1 should be merely considered as a mathematical tool to perform calculations and should not be assigned any physical meaning. This technique can be iterated to renormalise higher-order bias parameters (McDonald, 2006; McDonald and Roy, 2009). The net effect of this procedure is that no UV-sensitive terms appear in the theoretical expressions for the ensemble averaged statistics of the tracers.

A different way to understand renormalisation is through the introduction of counterterms in

the bias expansion. For instance, let us re-consider the example above. In order to eliminate the UV-sensitive term that appears in the NLO expression for $\langle\delta_{\mathrm{h}}(\mathbf{x})\rangle$, we could add the constant counterterm Δb_0 to the r.h.s. of equation (2.25) and get $\langle\delta_{\mathrm{h}}(\mathbf{x})\rangle = b_0 + \Delta b_0 + b_2\sigma_1^2(\Lambda)$. By requiring that the expectation value of the theory coincides with the observed value (i.e. zero), we thus get $\Delta b_0 = -b_0 - b_2\sigma_1^2(\Lambda)$. The new bias expansion (including the counterterm) can thus be re-organised as follows:

$$\delta_{\mathrm{h}}(\mathbf{x}) = b_1\delta(\mathbf{x}) + b_2\left[\delta^2(\mathbf{x})\right]_0 \, , \tag{2.27}$$

where $\left[\delta^2(\mathbf{x})\right]_0 \equiv \delta^2(\mathbf{x}) - \sigma_1^2(\Lambda)$ denotes a new operator compatible with the renormalisation of b_0.

Next, we could add the counterterm $\Delta b_1\delta(\mathbf{x})$ to the bias expansion in order to cancel out the UV-sensitive term in the NLO expression for the two-point statistic $P_{\delta_{\mathrm{h}}\delta}(k)$. In fact, the new term generates the correction $\Delta P_{\delta_{\mathrm{h}}\delta}(k) = \Delta b_1 P_{11}(k)$ and by imposing that $b_1 + \Delta b_1 + b_2\,(68/21)\,\sigma_1^2(\Lambda) = b_1^{\mathrm{R}}$, we finally obtain

$$\delta_{\mathrm{h}}(\mathbf{x}) = b_1^{\mathrm{R}}\delta(\mathbf{x}) + b_2\left[\delta^2(\mathbf{x})\right]_1 \, , \tag{2.28}$$

where $\left[\delta^2(\mathbf{x})\right]_1 \equiv \delta^2(\mathbf{x}) - \sigma_1^2(\Lambda)\left[1 + (68/21)\,\delta(\mathbf{x})\right]$ represents the quadratic operator which is consistent with the renormalisation of both b_0 and b_1.

The examples above illustrate how the linear bias coefficient b_1 and the field δ^2 can be consistently renormalised starting from the simplified model given in equation (2.25). Considering a more general bias expansion that includes additional composite operators requires further calculations. For instance, we might want to add a non-local bias term proportional to s^2. In this case, all the perturbative calculations we made to compute spectra and cross-spectra for δ^2 can be easily generalised to s^2. By introducing the Fourier-space operator

$$S_2(\mathbf{k}_1, \mathbf{k}_2) = \gamma_{ij}(\mathbf{k}_1)\,\gamma_{ji}(\mathbf{k}_2) = \left(\frac{\mathbf{k}_1 \cdot \mathbf{k}_2}{k_1 k_2}\right)^2 - \frac{1}{3} \, , \tag{2.29}$$

one finds that $\langle s^2(\mathbf{x})\rangle = (4/3)\,\sigma^2$ and

$$P_{s^2\delta}^{(31)}(k) = 4P_{11}(k)\int F_2(-\mathbf{q}, \mathbf{k})\,S_2(\mathbf{q}, \mathbf{k} - \mathbf{q})\,P_{11}(q)\frac{\mathrm{d}^3q}{(2\pi)^3} \, , \tag{2.30}$$

which is UV-sensitive as (McDonald and Roy, 2009)

$$\lim_{k\to 0}\frac{P_{s^2\delta}^{(31)}(k)}{P_{11}(k)} = \frac{136}{63}\sigma_1^2(\Lambda)\,. \tag{2.31}$$

Thus, s^2 needs to be renormalised. Analogous considerations apply to other composite operators.

A systematic procedure for renormalising the bias expansion order by order in PT has been presented by Assassi et al. (2014). The renormalisation conditions for the generic operator O appearing in the bias expansion are

$$\langle[O](\mathbf{q})\,\delta_1(\mathbf{q}_1)\ldots\delta_1(\mathbf{q}_m)\rangle = \langle O(\mathbf{q})\,\delta_1(\mathbf{q}_1)\ldots\delta_1(\mathbf{q}_m)\rangle^{(\mathrm{LO})} \, , \tag{2.32}$$

where $\mathbf{q}_i \to 0\ \forall i$. In a diagrammatic representation, this means that the counterterms should be chosen so that to cancel the loop corrections obtained from diagrams in which different Fourier modes of δ that contribute to the operator O are contracted among themselves as in equations

(2.23) and (2.30).

2.2.4 Cross-spectrum between matter and tracers

In this paper, we use a large suite of N-body simulations to test how accurately the third-order bias expansion given in equation (2.10) describes the spatial distribution of biased tracers (namely, dark-matter haloes with different masses). In order to focus on the deterministic terms, we only consider the cross-spectrum between the matter-density field and the tracers, $P_{\delta_h\delta}(k)$. As a reference, we provide here the perturbative result for this quantity (to NLO) expressed in terms of the renormalised linear bias parameter b_1^R (McDonald and Roy, 2009; Assassi et al., 2014; Saito et al., 2014; Senatore, 2015; Desjacques, Jeong and Schmidt, 2018b):

$$P_{\delta_h\delta}(k) = \left(b_1^R + b_{\nabla^2\delta}k^2\right)[P_{\delta\delta}^{(LO)}(k) + P_{\delta\delta}^{(NLO)}(k)] + b_2\, P_{[\delta^2]_1\delta}(k)$$
$$+ b_{s^2}\, P_{[s^2]_1\delta}(k) + b_{\Gamma_3}P_{\Gamma_3\delta}(k) + \Upsilon_{2,\epsilon_1,\epsilon_m}\, k^2\, . \qquad (2.33)$$

In the expression above, we have introduced the LO cross spectra of the renormalised operators,

$$P_{[\delta^2]_1\delta}(k) = \lim_{\Lambda\to\infty} P_{\delta^2\delta}^{(22)}(k)\, , \qquad (2.34)$$

$$P_{[s^2]_1\delta}(k) = \lim_{\Lambda\to\infty}\left[P_{s^2\delta}^{(22)}(k) + B_{s^2\delta}(k)\right]\, , \qquad (2.35)$$

where[6]

$$P_{s^2\delta}^{(22)}(k) = 2\int F_2(\mathbf{q}, \mathbf{k}-\mathbf{q})\, S_2(\mathbf{q}, \mathbf{k}-\mathbf{q})\, P_{11}(q)\, P_{11}(|\mathbf{k}-\mathbf{q}|)\, \frac{\mathrm{d}^3 q}{(2\pi)^3}\, , \qquad (2.36)$$

$$B_{s^2\delta}(k) = P_{s^2\delta}^{(31)}(k) - \frac{136}{63}\sigma_1^2(\Lambda)\, P_{11}(k)\, . \qquad (2.37)$$

On the contrary, the Γ_3 operator does not require renormalisation (e.g. Assassi et al., 2014) and we have

$$P_{\Gamma_3\delta}(k) = B_{\Gamma_3\delta}(k) = \lim_{\Lambda\to\infty} P_{\Gamma_3\delta}^{(31)}(k)\, , \qquad (2.38)$$

with[7]

$$P_{\Gamma_3\delta}^{(31)}(k) = 4P_{11}(k)\int [F_2(-\mathbf{q}, \mathbf{k}) - G_2(-\mathbf{q}, \mathbf{k})]\left[\left(\frac{\mathbf{q}\cdot(\mathbf{k}-\mathbf{q})}{q\,|\mathbf{k}-\mathbf{q}|}\right)^2 - 1\right]P_{11}(q)\, \frac{\mathrm{d}^3 q}{(2\pi)^3}\, . \qquad (2.39)$$

A few notes are in order here. First, all terms proportional to $P_{11}(k)$ have been used to define the renormalised linear bias parameter as a function of the bare bias coefficients:

$$b_1^R = b_1 + \left(\frac{68}{21}b_2 + \frac{136}{63}b_{s^2} + 3b_3 + \frac{2}{3}b_{\delta s^2}\right)\sigma_1^2(\Lambda)\, . \qquad (2.40)$$

---

[6] Equation (2.24) implies that $B_{\delta^2\delta}(k) = 0$ as $P_{\delta^2\delta}^{(31)}(k) \propto P_{11}(k)$.

[7] The perturbative contributions to Γ_3 vanish at second order.

This makes sure that $P_{\delta_h\delta}(k) \to b_1^R P_{\delta\delta}(k)$ in the limit $k \to 0$. Secondly, although the perturbative calculations give $b_1^R P_{\delta\delta}^{(LO)}(k) + b_1 P_{\delta\delta}^{(NLO)}(k)$, this expression has been replaced with $b_1^R [P_{\delta\delta}^{(LO)}(k) + P_{\delta\delta}^{(NLO)}(k)]$ in equation (2.33), the difference being proportional to $\sigma_1^2 P_{\delta\delta}^{(NLO)}(k)$ and thus higher-order in the perturbations. As we will show later, this substitution is a source of error on mildly non-linear scales. Thirdly, the third-order local bias coefficient b_3 is renormalised into b_1^R and does not appear in equation (2.33). Fourthly, it turns out that the functions $B_{s^2\delta}(k)$ and $B_{\Gamma_3\delta}(k)$ are proportional to each other and therefore a single bias parameter (a linear combination of b_{s^2} and b_{Γ_3}) could be used to scale their total contribution (McDonald and Roy, 2009). Finally, no direct contributions from the stochastic bias coefficients ϵ_O appear in the r.h.s. of equation (2.33). This is because these zero-mean stochastic fields are assumed to be independent of δ. If, however, matter-density perturbations are described in terms of an effective deterministic field $\delta_{\rm eff}$ plus stochastic contributions ϵ_m (from the small-scale modes that are not included in the theory), then the correlation between the stochastic terms ϵ_1 and ϵ_m should contribute to $P_{\delta_h\delta}^{(NLO)}(k)$. The corresponding cross spectrum is represented by the term $\Upsilon_{2,\epsilon_1,\epsilon_m} k^2 = (\partial \Upsilon_{\epsilon\epsilon_m}/\partial k^2)_{k=0} k^2$ in equation (2.33). Theoretical considerations suggest that this term should be highly suppressed with respect to the other NLO corrections (Senatore, 2015; Angulo et al., 2015).

2.2.5 Impact of filter functions

Equations (2.24) and (2.31) are obtained from equations (2.23) and (2.30) by performing the integration over $\mathbf{q}$ in spherical polar coordinates. The integration range extends over the full solid angle around $\mathbf{k}$ but is limited to the region $q < \Lambda$ for the radial component. We show here that this calculation does not exactly give what one would obtain by smoothing the density field with a sharp cutoff in k space as, for instance, we will do later when analyzing N-body data.

As mentioned in section 2.2.2, the bias expansion applies to fields that have been low-pass filtered. Let us consider the smoothed field $W(k)\delta(\mathbf{k})$ with $W(k)$ a low-pass, spherically symmetric, window function. In this case, equation (2.23) should be replaced with

$$P_{\delta^2\delta}^{(31)}(k) = 4P_{11}(k)W(k) \int F_2(-\mathbf{q},\mathbf{k})P_{11}(q)W(q)\,W(|\mathbf{k}-\mathbf{q}|)\frac{\mathrm{d}^3q}{(2\pi)^3}\;. \tag{2.41}$$

For simplicity, in this work, we use a spherical top-hat filter in k space,

$$W(k) = \begin{cases} 1 & \text{if } k < \Lambda\,, \\ 0 & \text{otherwise}\,. \end{cases} \tag{2.42}$$

The factor $W(|\mathbf{k}-\mathbf{q}|)$ in the integrand of equation (2.41) thus limits the integration range to the region where

$$\Lambda^2 > |\mathbf{k}-\mathbf{q}|^2 = k^2 + q^2 - 2qk\mu\,, \tag{2.43}$$

with $\mu = (\mathbf{k}\cdot\mathbf{q})/(kq)$ the cosine of the angle between $\mathbf{k}$ and $\mathbf{q}$. This turns out to be a constraint on μ at fixed q,

$$\mu > \frac{k^2 + q^2 - \Lambda^2}{2qk} = \mu_{\rm min}\,, \tag{2.44}$$

and implies that, for $q > \Lambda - k$, the integration range in μ will have a lower bound $\mu_{\rm min} > -1$.

The complete result for $0 < k < \Lambda$ is

$$P_{\delta^2\delta}^{(31)}(k) = P_{11}(k)W(k)\left[\frac{68}{21}\sigma_1^2(\Lambda - k) + 2\int_{\Lambda-k}^{\Lambda}\int_{\mu_{\min}}^{1}F_2(-\mathbf{q},\mathbf{k})\,\mathrm{d}\mu\,P_{11}(q)\frac{q^2\mathrm{d}q}{2\pi^2}\right], \tag{2.45}$$

where the integral over μ reduces to

$$\int_{\mu_{\min}}^{1}F_2(-\mathbf{q},\mathbf{k})\,\mathrm{d}\mu = \frac{17}{21} - \frac{51}{112}\left(\frac{k}{q} + \frac{q}{k}\right) + \frac{5}{28}\frac{\Lambda^2}{kq} + \frac{17}{336}\left(\frac{k^3}{q^3} + \frac{q^3}{k^3}\right)$$
$$+ \frac{3}{112}\left(\frac{\Lambda^4}{k^3 q} + \frac{\Lambda^4}{kq^3}\right) - \frac{5}{56}\left(\frac{\Lambda^2 k}{q^3} + \frac{\Lambda^2 q}{k^3}\right) + \frac{1}{84}\frac{\Lambda^6}{k^3 q^3}. \tag{2.46}$$

It follows that

$$P_{\delta^2\delta}^{(31)}(k) = P_{11}(k)W(k)\left\{\frac{68}{21}\sigma_1^2(\Lambda - k) + \frac{34}{21}\left[\sigma_1^2(\Lambda) - \sigma_1^2(\Lambda - k)\right]\right.$$
$$+ \left(\frac{17}{168}k^3 - \frac{5}{28}\Lambda^2 k + \frac{3}{56}\frac{\Lambda^4}{k} + \frac{1}{42}\frac{\Lambda^6}{k^3}\right)\mathcal{H}_{-1}(k) + \left(-\frac{51}{56}k + \frac{5}{14}\frac{\Lambda^2}{k} + \frac{3}{56}\frac{\Lambda^4}{k^3}\right)\mathcal{H}_1(k)$$
$$\left.+ \left(-\frac{51}{56}\frac{1}{k} - \frac{5}{28}\frac{\Lambda^2}{k^3}\right)\mathcal{H}_3(k) + \frac{17}{168}\frac{1}{k^3}\mathcal{H}_5(k)\right\}. \tag{2.47}$$

where

$$\mathcal{H}_n(k) = \int_{\Lambda-k}^{\Lambda}q^n P_{11}(q)\frac{\mathrm{d}q}{2\pi^2} \tag{2.48}$$

and $\sigma_1^2(\Lambda) - \sigma_1^2(\Lambda - k) = \mathcal{H}_2(k)$. By Taylor expanding the $\mathcal{H}_n(k)$ functions to fourth order, we obtain the linear expansion of the expression in the curly parentheses in equation (2.47),

$$\frac{P_{\delta^2\delta}^{(31)}(k)}{P_{11}(k)W(k)} = \frac{68}{21}\sigma_1^2(\Lambda) - \frac{1}{3}\frac{\Lambda^3 P_{11}(\Lambda)}{2\pi^2} + \left[-\frac{17}{28}\frac{\Lambda^2 P_{11}(\Lambda)}{2\pi^2} + \frac{1}{8}\frac{\Lambda^3 P_{11}'(\Lambda)}{2\pi^2}\right]k + O(k^2). \tag{2.49}$$

This result has some implications for the renormalisation of the bias expansion. First, the resulting expression for $P_{\delta^2\delta}^{(31)}(k)$ is not proportional to $P_{11}(k)$ at finite wavenumbers. Moreover, the limit for $k \to 0$ of equation (2.49) is not $(68/21)\,\sigma_1^2(\Lambda)$ (contrary to what claimed by Desjacques, Jeong and Schmidt, 2018b, after their equation 2.122) and a different cutoff-dependent coefficient should be used to renormalise b_1. Note, however, that, for a ΛCDM cosmology, the $k \to 0$ limit reduces to (2.24) for $\Lambda \to +\infty$. We will return to these issues and present a comparison with N-body simulations in section 2.4.3. Analogous calculations can also be performed for s^2 and other composite operators.

2.3 Numerical methods

In this section, we introduce our suite of N-body simulations and describe the numerical techniques we use to build the continuous density fields, as well as the auto and cross power spectra that enter the bias expansion.
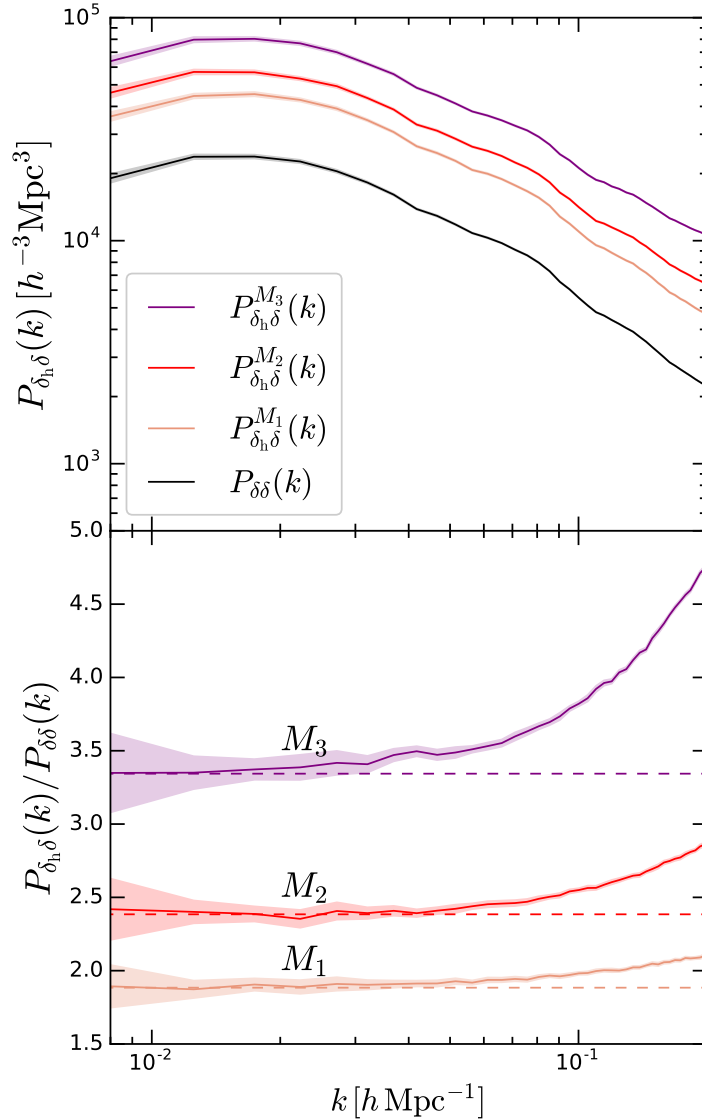
2.3.1 N-body simulations

Figure 2.1: Top: Average matter power spectrum $P_{\delta\delta}(k)$ and halo-matter cross spectra $P_{\delta_h\delta}(k)$ (for the mass bins M_1, M_2, M_3 defined in Section 2.3.1) measured from our 40 simulations. Shaded regions represent the standard error of the mean. Bottom: Corresponding effective bias functions $P_{\delta_h\delta}(k)/P_{\delta\delta}(k)$. The dashed lines indicate a constant fit to the five leftmost data points.

We use the SPH code GADGET-2 (Springel, 2005) to run 40 DM-only simulations. Their main characteristics are summarised in Table 2.1. We set up the initial conditions (IC) at $z_{IC} = 50$ with the MUSIC code (Hahn and Abel, 2011) employing the Planck 2015 (Planck Collaboration, 2016) cosmology, i.e. $h = 0.677$, $\sigma_8 = 0.816$, $n_s = 0.967$, $\Omega_m = 0.3089$, $\Omega_b = 0.0486$ and $\Omega_\Lambda = 0.6911$.

To identify gravitationally bound structures, we use the ROCKSTAR halo finder (Behroozi, Wechsler and Wu, 2013b). This algorithm uses the phase-space distribution of the simulation particles to detect spherical haloes with a virial mass defined as in Bryan and Norman (1998). We split the halo population into three mass bins based on the number of halo particles. In
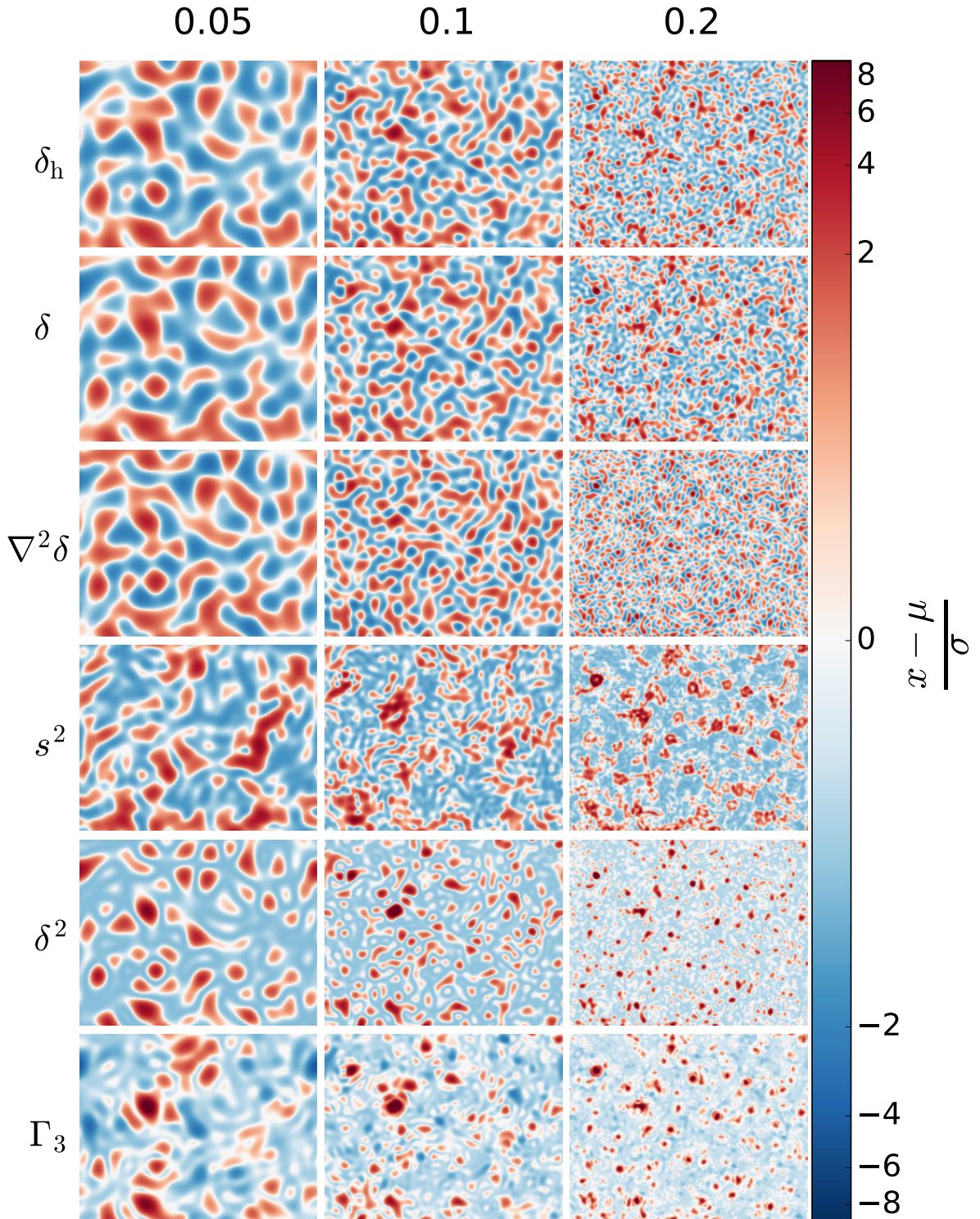
Figure 2.2: The fields that are included in the bias expansion. We show a 2D slice extracted from one N-body simulation. The grid of images shows different fields along the vertical direction (as indicated by the labels) and different values of the cutoff scale Λ (in $h\,\mathrm{Mpc}^{-1}$) in the horizontal direction. All the fields have been standardised to zero mean and unit variance. Note that the images only cover 80 per cent of the box in the vertical direction.

Table 2.1: The set of parameters that characterise our suite of N_{sim} simulations: L_{box} denotes the box length, N_{part} the number of particles, M_{part} the particle mass, L_{soft} the softening length, and z_{IC} the initial redshift.

N_{sim}	L_{box}	N_{part}	M_{part}	L_{soft}	z_{IC}	Cosmology
40	$1200\,h^{-1}\,\text{Mpc}$	512^3	$1.1037 \times 10^{12} h^{-1}\,\text{M}_{\odot}$	$0.078\,h^{-1}\,\text{Mpc}$	50	Planck 2015

Table 2.2: The variance of the matter density field as a function of the cutoff scale Λ at $z = 0$. We contrast the results obtained from linear SPT (σ_1^2) with those measured in the simulations (σ_{sim}^2).

$\Lambda\,[h\,\text{Mpc}^{-1}]$	σ_1^2	σ_{sim}^2
0.05	0.0377	0.0343
0.10	0.1672	0.1513
0.20	0.5430	0.5223

the lowest-mass bin, M_1, haloes contain between 40 and 79 particles, corresponding to a mean mass of $\overline{M}_1 = 6.15 \times 10^{13} h^{-1} M_{\odot}$. The second bin includes haloes with 80 to 159 particles $(\overline{M}_2 = 1.21 \times 10^{14} h^{-1} M_{\odot})$, while more massive structures with ≥ 160 particles fall into the highest-mass bin $(\overline{M}_3 = 3.17 \times 10^{14} h^{-1} M_{\odot})$.

2.3.2 Measuring smoothed fields and spectra

We employ a 'cloud-in-cell' (CIC) interpolation method to build the gridded overdensity fields δ and δ_{h} starting from the positions of the N-body particles and of the haloes, respectively. The fields are sampled on a regular Cartesian mesh with 256^3 cells that fully covers the simulation box. After correcting for the mass-assignment scheme, we use the fast-Fourier-transform (FFT) algorithm to obtain $\delta(\mathbf{k})$ and $\delta_{\text{h}}(\mathbf{k})$. In the top panel of Fig. 2.1, we show the matter power spectrum $P_{\delta\delta}(k)$ and the halo-matter cross spectra $P_{\delta_{\text{h}}\delta}(k)$ averaged over our set of simulations for each halo mass bin. The shaded regions indicate the standard error of the mean. In the bottom panel, we show the ratio $P_{\delta_{\text{h}}\delta}(k)/P_{\delta\delta}(k)$ which can be interpreted as an effective scale-dependent bias. This function grows with k, and this effect becomes more prominent for more massive haloes. In order to emphasize this trend, we fit a constant to the five leftmost data points and plot the result with a dashed line. The discrepancy between the solid and dashed line provides a strong motivation for considering non-linear bias models.

Low-pass smoothing is applied in Fourier space by multiplying the FFT of the fields by the window function $W(k)$ given in equation (2.42). We use three different values for the cutoff scale Λ ensuring that the variance of the δ field is smaller than unity (see Table 2.2). We also apply spectral methods to compute the Fourier transforms of s_{ij} and $\nabla^2 \delta$ starting from $\delta(\mathbf{k})$. In order to compute Γ_3, we first build three momentum grids (one for each Cartesian component of the momentum vector) by applying the CIC interpolation to the particle velocities. To get the velocity grids from these we divide the momentum components by the density. We apply the FFT to these grids so that we can first compute $\theta(\mathbf{k}) = i\mathbf{k} \cdot \mathbf{v}(\mathbf{k})/(aHf)$ and then $p_{ij}(\mathbf{k})$. Finally, we transform all the smoothed fields back to real space and compute the quadratic fields $\delta^2(\mathbf{x})$, $s^2(\mathbf{x})$, $p^2(\mathbf{x})$ and $\Gamma_3(\mathbf{x})$.

A sample slice extracted from one of the simulation boxes at $z = 0$ for all fields is shown in Fig. 2.2. From top to bottom we plot the different fields, from left to right we change the cutoff scale Λ. We standardised the fields such that dark tones indicate large deviations from than the

mean. As expected, larger values of Λ give rise to more detailed structure in all panels. The most striking feature is that δ_h and δ always look very similar. This is not surprising since $\delta_\mathrm{h} \propto \delta$ at LO in the bias expansion. For larger Λ, the similarity is less evident, reflecting the increased importance of higher-order and derivative terms. The Laplacian of δ looks qualitatively similar to δ for small Λ, whereas, for large Λ, short-wavelength Fourier modes are enhanced with respect to the density field. The field δ^2 presents concentrated high positive peaks on top of a rather uniform background, somewhat reminiscent of shot noise (see also Heavens, Matarrese and Verde, 1998). Around those peaks the signal of s^2 becomes strong in almost spherical shells which are particularly evident for large Λ. Finally, for $\Lambda = 0.2\,h\,\mathrm{Mpc}^{-1}$, Γ_3 presents high peaks at the same locations as δ^2 and s^2 while this correspondence is less striking for smaller Λ. Not visible in the figure is that the relative amplitudes of the different fields change dramatically with the cutoff scale. Whereas, for $\Lambda = 0.05\,h\,\mathrm{Mpc}^{-1}$, they are clearly ordered as expected from SPT, for $\Lambda = 0.2\,h\,\mathrm{Mpc}^{-1}$, δ, δ^2, s^2 and Γ_3 are all of order unity.

We employ standard methods to compute the auto and cross power spectra between the fields using 10, 20 and 40 linearly-spaced bins in k for $\Lambda = 0.05, 0.1$, and $0.2\,h\,\mathrm{Mpc}^{-1}$, respectively.

2.4 Renormalisation in simulations

In this section, we measure the UV-sensitivity of the composite operators and implement the renormalisation framework directly in our simulations.

In the top panels of Fig. 2.3, we show the average over the 40 simulations of the cross spectra between different composite operators and δ for three values of Λ. We plot $P_{\delta^2\delta}(k)$ on the left-hand side and $P_{s^2\delta}(k)$ on the right-hand side. As expected, our results are UV-sensitive as the amplitude of the spectra changes dramatically with Λ. Qualitatively, this is consistent with the perturbative calculations presented in Section 2.2.3.

We want to build a procedure that removes the UV-sensitive part from the cross spectra. In the perturbative calculations, this term is $[\lim_{q\to 0} P^{(31)}_{O\delta}(q)/P_{11}(q)]\,P_{11}(k)$. For instance, if $O = \delta^2$, then $P^{(31)}_{O\delta}(q)$ is obtained from the correlator $2\langle(\delta_2\delta_1)\delta_1\rangle$ (parentheses here denote the fields contributing to δ^2). This is the LO term of $\langle\delta^2\delta_1\rangle$. In the simulations, we cannot isolate δ_2 from all the other non-linear terms. However, if the perturbative ansatz holds true on the largest scales, we can safely assume that $\langle\delta^2\delta_1\rangle$ is dominated by the LO part when $k \to 0$. Therefore, it makes sense to measure $P_{\delta^2\delta_1}(k)$ from the simulations and compute the 'renormalised cross spectrum'

$$
\begin{aligned}
P_{[\delta^2]_1\delta}(k) &= P_{\delta^2\delta}(k) - \frac{P_{\delta^2\delta_1}(k_\mathrm{min})}{P_{11}(k_\mathrm{min})}P_{11}(k) \\
&= P_{\delta^2\delta}(k) - \alpha_{\delta^2}(\Lambda)\,P_{11}(k)\,,
\end{aligned}
\tag{2.50}
$$

where k_min denotes the bin containing the lowest wavenumbers that can be accessed in our simulation boxes and $P_{11}(k)$ is computed directly by re-scaling the IC of the simulations. Similarly, for s^2, we have

$$
\begin{aligned}
P_{[s^2]_1\delta}(k) &= P_{s^2\delta}(k) - \frac{P_{s^2\delta_1}(k_\mathrm{min})}{P_{11}(k_\mathrm{min})}P_{11}(k) \\
&= P_{s^2\delta}(k) - \alpha_{s^2}(\Lambda)\,P_{11}(k)\,.
\end{aligned}
\tag{2.51}
$$

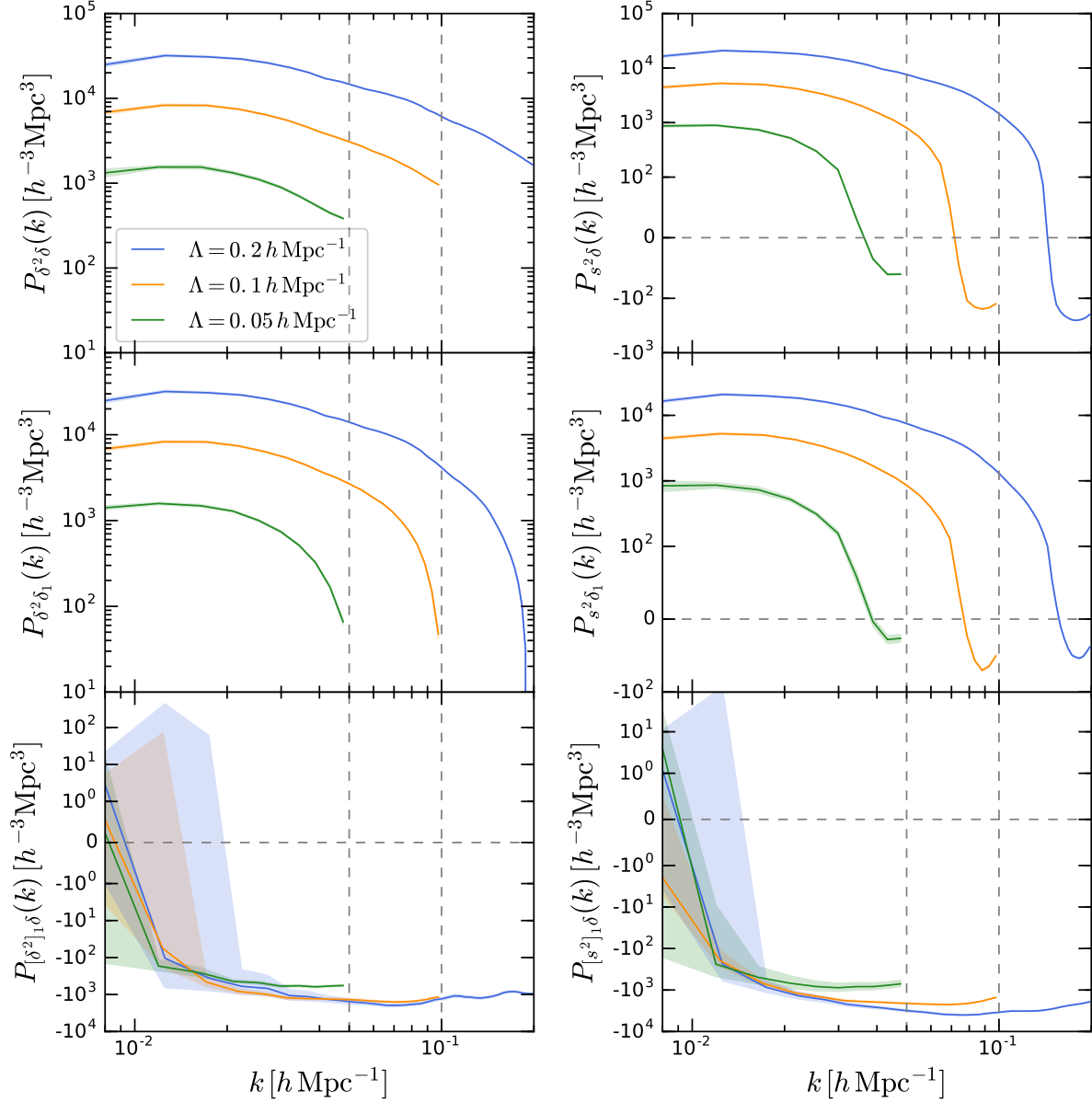Figure 2.3: Average cross spectra $P_{\delta^2\delta}(k)$ and $P_{s^2\delta}(k)$, measured from our 40 simulations for different values of Λ. Shaded regions represent the standard error of the mean. Top: The 'full' spectra, obtained from cross-correlating the quadratic operators δ^2 and s^2 with δ. Middle: The UV-sensitive part of the spectra, obtained by correlating δ^2 and s^2 with δ_1. Bottom: The renormalised spectra, obtained by subtracting the UV-sensitive terms from the full spectra. A symmetric logarithmic scale on the y axis is used for quantities that assume both positive and negative values. The vertical dashed lines indicate the locations of the different cutoff scales.
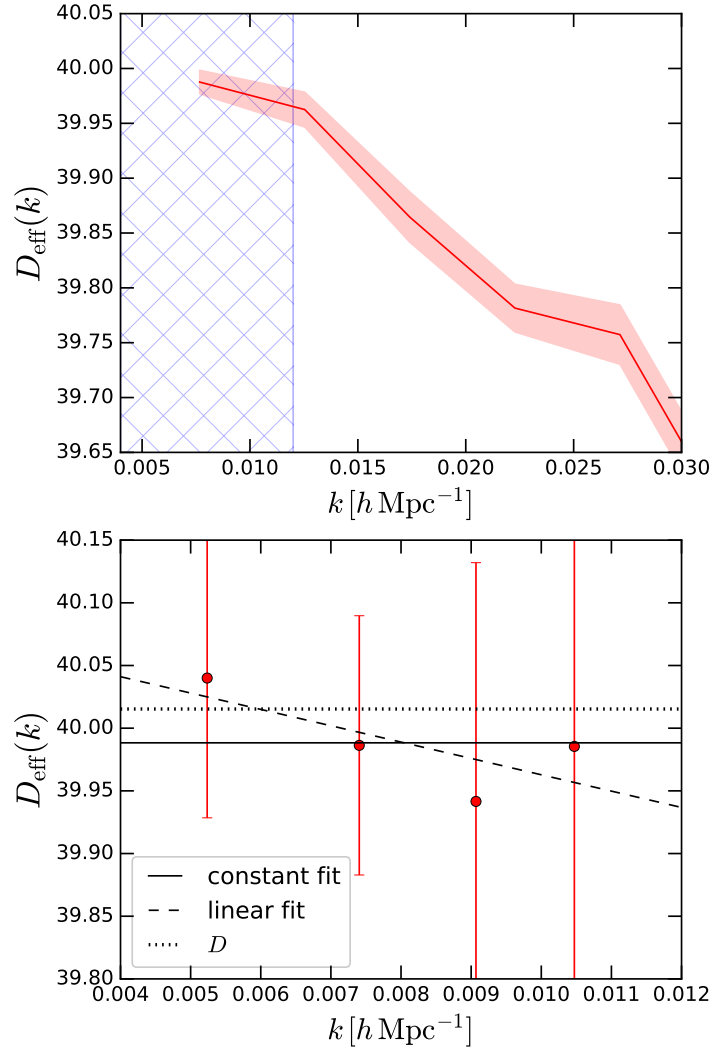
Figure 2.4: The top panel shows the k-dependent growth factor $D_{\mathrm{eff}}(k)$, measured in our simulations by using equation (2.52). The solid line and the shaded region indicate the average over the 40 realisations and its error, respectively. The hatched region is magnified in the bottom panel where we fit a constant (solid) and a linear function of k (dashed) to $D_{\mathrm{eff}}(k)$ measured at the first four multiples of the fundamental frequency $2\pi/L_{\mathrm{box}}$ (data points with error bars). The dotted line represents the linear growth factor for the adopted cosmology, $D = 40.015$.

2.4.1 Measuring the linear growth factor

In order to implement the renormalisation procedure sketched above, we need the linear density field δ_1 evaluated at $z = 0$ in the N-body simulations. This is obtained by multiplying the IC by the linear growth factor D. Although D can be computed from the cosmological parameters by performing a numerical integration ($D = 40.015$ at $z = 0$), the result does not necessarily match the actual growth of perturbations in the simulations which only provide an approximate solution. Previous studies have shown that different N-body codes might differ by up to 0.3 per cent in the large-scale normalization of the matter power spectrum at $z = 0$ which corresponds to a 5 per cent error on D (see e.g. Fig. 1 in Schneider et al., 2016). Since the success of the

Table 2.3: The factors $\alpha_{\delta^2}(\Lambda)$ and $\alpha_{s^2}(\Lambda)$ defined in equations (2.50) and (2.51). The values indicate the average over the simulations and the uncertainty is the standard error of the mean.

$\Lambda\,[h\,\mathrm{Mpc}^{-1}]$	$\alpha_{\delta^2}(\Lambda)$	$\alpha_{s^2}(\Lambda)$
0.05	0.072 ± 0.001	0.046 ± 0.001
0.10	0.349 ± 0.006	0.228 ± 0.004
0.20	1.261 ± 0.017	0.834 ± 0.013

renormalisation procedure relies on the subtraction of two signals with comparable amplitudes to get a much smaller one, we need to make sure that we know the precise value of the growth factor realized in the simulations. Therefore, we proceed as follows. First, we measure an 'effective' scale-dependent growth function directly from our simulations as

$$D_{\mathrm{eff}}(k) = \left\langle \frac{\delta(\mathbf{k}, z = 0)}{\delta_1(\mathbf{k}, z_{\mathrm{IC}})} \right\rangle_{k\,\mathrm{bin}} \tag{2.52}$$

where the average is taken over the same bins of k as the spectra and we have explicitly written the redshift at which the fields are evaluated. The result for $k < 0.03\,h\,\mathrm{Mpc}^{-1}$ is shown in the top panel of Fig. 2.4 where the shaded region indicates the error of the mean over the simulations. Note that, as expected from theoretical considerations, D_{eff} decreases with k on these scales. We are interested in the limit of this function for $k \to 0$. For this reason, we only consider the leftmost bin and analyze the signal at the level of single Fourier modes (see the bottom panel of Fig. 2.4). In order to extract the limit, we fit a constant ($D_{\mathrm{eff}} = 39.98 \pm 0.07$, dotted) and a linear function of k ($D_{\mathrm{eff}}(k) = 40.09 \pm 0.31 - (13 \pm 39)\,(k/1\,h\,\mathrm{Mpc}^{-1})$, dashed) to the measurements. The slope of the linear fit is consistent with zero within the errors. Furthermore, the two fits give consistent limits for $k \to 0$ which are also compatible with the expected value for D. For our calculations, we therefore use $D = 39.98$.

2.4.2 Renormalising the spectra

We are now ready to compute $P_{\delta^2 \delta_1}(k)$ and $P_{s^2 \delta_1}(k)$ as well as the renormalised spectra $P_{[\delta^2]_1 \delta}(k)$ and $P_{[s^2]_1 \delta}(k)$. A note is in order here. The IC of our simulations are Gaussian and all the three-point correlators of δ_1 should, in principle, vanish. In practice, however, we measure very noisy non-zero values for $P_{\delta_1^2 \delta_1}(k)$ and $P_{s_1^2 \delta_1}(k)$. In the perturbative framework, these spectra coincide with the tree-level terms of $P_{\delta^2 \delta}(k)$ and $P_{s^2 \delta}(k)$. Therefore, in order to improve the quality of our results, we subtract the noisy terms from all the non-linear cross spectra appearing on the r.h.s. of equations (2.50) and (2.51). Our final results for $P_{\delta^2 \delta_1}(k)$ and $P_{s^2 \delta_1}(k)$ are shown in the middle panels of Fig. 2.3. As expected, they show a similar behaviour as a function of both Λ and k with respect to $P_{\delta^2 \delta}(k)$ and $P_{s^2 \delta}(k)$. However, when k approaches Λ their signal is suppressed. The corresponding values of $\alpha_{\delta^2}(\Lambda)$ and $\alpha_{s^2}(\Lambda)$ are presented in Table 2.3.

We finally compute the renormalised spectra $P_{[\delta^2]_1 \delta}(k)$ and $P_{[s^2]_1 \delta}(k)$ from equations (2.50) and (2.51). We first obtain them for each simulation individually and then perform an average. The results are shown in the bottom panels of Fig. 2.3. At large scales, spectra obtained with different values of Λ are now compatible within the errorbars while they differ when $k \simeq \Lambda$. This means that the renormalisation procedure was successful.

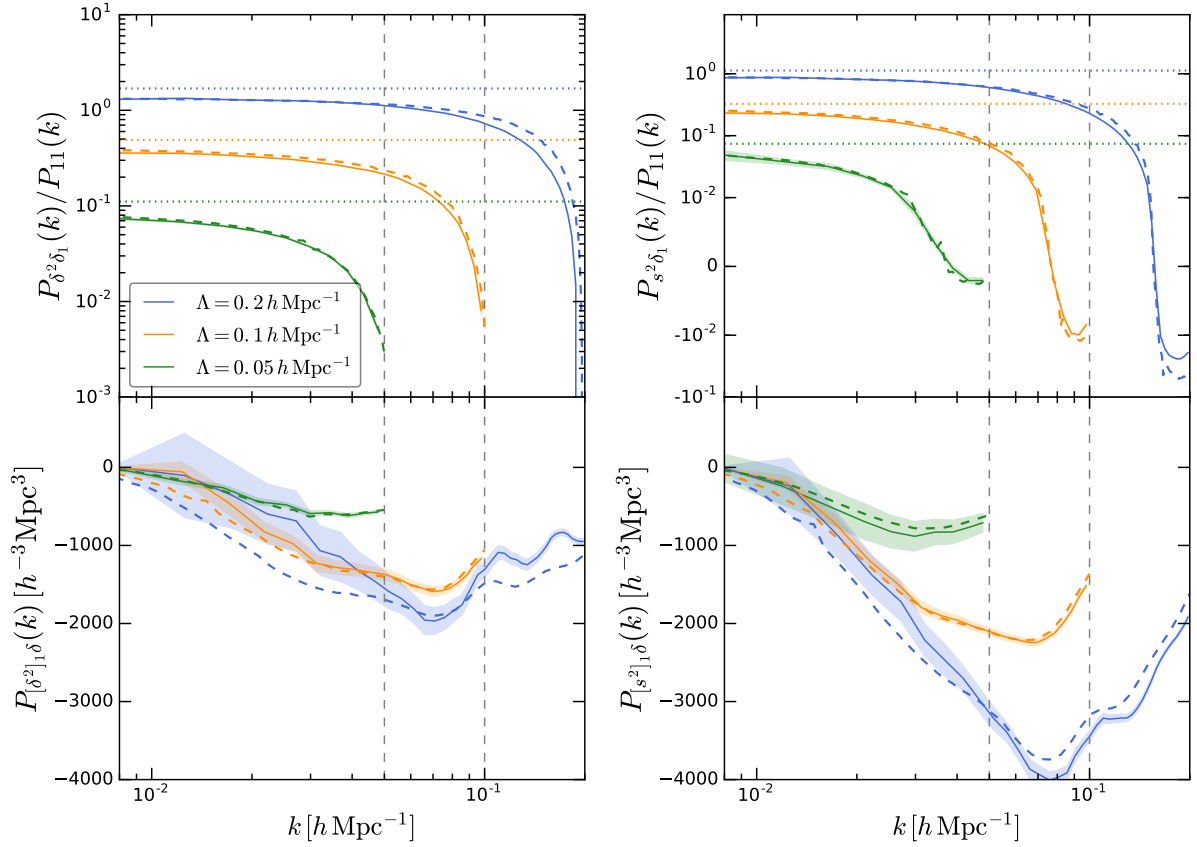### 2.4.3 Comparing spectra from simulations and SPT

Figure 2.5: The top panels show the UV-sensitive spectra $P_{\delta^2\delta_1}(k)$ (left) and $P_{s^2\delta_1}(k)$ (right) divided by the linear matter power spectrum. Plotted are the average spectra measured from the simulations for different values of Λ (solid). Shaded regions represent the standard error of the mean. For comparison, the dashed curves represent $P^{(31)}_{\delta^2\delta}(k)/P_{11}(k)$ and $P^{(31)}_{s^2\delta}(k)/P_{11}(k)$ computed from SPT accounting for the filter functions – see equation (2.41) and the analogue for s^2. Likewise, the horizontal dotted lines indicate the values $68/21\,\sigma^2$ and $136/63\,\sigma^2$ – see equations (2.24) and (2.31). Differently, the vertical dashed lines mark the locations of the different cutoff scales. The bottom panels show the renormalised spectra $P_{[\delta^2]_1\delta}(k)$ (left) and $P_{[s^2]_1\delta}(k)$ (right) measured from the simulations (solid). Shaded regions represent the standard error of the mean. Also plotted are the perturbative results evaluated by taking the filter functions into account (dashed).

In the top-left panel of Fig. 2.5, we show a comparison between $P^{(31)}_{\delta^2\delta}(k)$, calculated with SPT (equation (2.24), dashed-dotted), with SPT including filter functions (equation (2.41), dashed), and $P_{\delta^2\delta_1}(k)$ that we measure from the simulations (solid). We repeat the analysis in the top right panel for $P^{(31)}_{s^2\delta}(k)$ and $P_{s^2\delta_1}(k)$. Equations (2.24) and (2.31) show that in SPT the UV-sensitive terms can be written as a Λ-dependent prefactor times $P_{11}(k)$. Therefore, in order to conveniently compare the numerical results to the SPT predictions, we always plot the ratios of the cross spectra with $P_{11}(k)$. The measurements from the simulations (solid) decrease with k and are in excellent agreement with the SPT results when filter functions are taken into account (dashed). Note that when $k \to 0$, the curves do not assume the values $68/21\,\sigma^2$ and $136/63\,\sigma^2$

(dotted), but stay below them (as described by e.g. the first line of equation (2.49) for δ^2). The logarithmic difference between the solid and dotted curves decreases for larger values of Λ. This result confirms the discussion presented in Section 2.2.5.

In the bottom panels of Fig. 2.5 we compare the renormalised spectra measured from the simulations (shown already in the bottom panels of Fig. 2.3 in logarithmic scale) with the theoretical predictions including filter functions. We find good agreement at all k for small values of Λ. For $\Lambda = 0.2\,h\,\mathrm{Mpc}^{-1}$, however, the theoretical results differ more markedly from the simulation measurements. This suggests either that higher-order terms should be accounted for in order to match the N-body results, or that the perturbative expansion starts breaking down at these scales and redshifts.

2.5 Measuring bias parameters

We now measure the bias parameters by fitting $P_{\delta_h\delta}(k)$ with different bias models, renormalised and not. First, we describe our Bayesian fitting routine that takes into account the correlations between the different spectra extracted from our simulations. Subsequently, we discuss how many bias parameters are needed to optimally describe our data by using Bayesian model-comparison techniques. Finally, we present the best-fitting parameters.

2.5.1 Fitting method

In this section, we introduce the Bayesian method we use to fit the bias parameters. Readers who are more interested in the results than in the statistical techniques can directly move to section 2.5.3.

Our goal is to fit a model for $P_{\delta_h\delta}(k)$ to our simulation suite, that can schematically be written as $P_{\delta_h\delta}(k) = \sum_O b_O\, P_{O\delta}(k)$. Contrary to previous work in the field, we do not rely on perturbation theory, but we measure the spectra $P_{O\delta}(k)$ together with $P_{\delta_h\delta}(k)$ from the simulation boxes. This means that both the dependent and the independent variables in our fit are affected by statistical errors. Since these measurement errors are correlated (as they originate from the same underlying density field), we need to account for their covariance matrix C. In practice, we treat each realisation as a repeated measure of all the spectra and we infer the best-fitting parameters by writing a global likelihood function for the bias parameters.

To simplify the notation, we write all the cross spectra for a given k bin as a multi-dimensional vector $\boldsymbol{y}$ and their noisy estimates as $\hat{\boldsymbol{y}} = \boldsymbol{y} + \boldsymbol{\eta}$, where $\boldsymbol{\eta}$ denotes the measurement error. We assume that the estimator of all y_i is unbiased and that the errors are drawn from a multi-variate Gaussian distribution with covariance matrix C as stated above. It follows that the probability of measuring $\hat{\boldsymbol{y}}$ is

$$\mathcal{P}(\hat{\boldsymbol{y}}) = \frac{1}{4\pi^2\sqrt{\det\mathsf{C}}} \exp\left[-\frac{1}{2}(\hat{\boldsymbol{y}} - \boldsymbol{y})^{\mathrm{T}}\mathsf{C}^{-1}(\hat{\boldsymbol{y}} - \boldsymbol{y})\right]. \tag{2.53}$$

We now order the components of the vectors so that $P_{\delta_h\delta}(k)$ appears first. We can thus write $y_1 = \beta_2 y_2 + \beta_3 y_3 + \cdots + \beta_n y_n$ (where the coefficient β_i represent the $n-1$ bias parameters that characterize a model). The likelihood function for the model parameters $(\boldsymbol{\beta}, \boldsymbol{y})$ given the data is then

$$\mathcal{L}(\boldsymbol{\beta}, \boldsymbol{y}) \propto \mathcal{P}(\hat{\boldsymbol{y}}|\boldsymbol{\beta}, \boldsymbol{y}) = \frac{1}{4\pi^2\sqrt{\det\mathsf{C}}} \exp\left[-\frac{A}{2}\right], \tag{2.54}$$

with[8]

$$A = C_{11}^{-1}(\hat{y}_1 - \beta_i y_i)^2 + 2\,C_{1j}^{-1}(\hat{y}_1 - \beta_i y_i)(\hat{y}_j - y_j) + C_{ij}^{-1}(\hat{y}_i - y_i)(\hat{y}_j - y_j)\,. \tag{2.55}$$

We then marginalize over the unknown true spectra $\boldsymbol{y}$, i.e.

$$\mathcal{L}(\boldsymbol{\beta}) \propto \int_{-\infty}^{\infty} \mathcal{L}(\boldsymbol{\beta}, \boldsymbol{y})\,\mathrm{d}^n y\,. \tag{2.56}$$

This is easily achieved after rewriting the integrand in the form of a n-dimensional Gaussian distribution. We first rewrite A as

$$A = \hat{y}_\mu C_{\mu\nu}^{-1} \hat{y}_\nu + y_i Q_{ij} y_j - 2\omega_i y_i\,, \tag{2.57}$$

where

$$Q_{ij} = C_{ij}^{-1} + C_{11}^{-1}\beta_i\beta_j + \beta_i C_{1j}^{-1} + \beta_j C_{1i}^{-1}\,, \tag{2.58}$$

and

$$\omega_i = C_{i\mu}^{-1}\hat{y}_\mu + \beta_i C_{1\mu}^{-1}\hat{y}_\mu\,. \tag{2.59}$$

We then express the second term on the r.h.s. of equation (2.57) as a function of a generic vector $\boldsymbol{d}$ such that

$$y_i Q_{ij} y_j = (y_i - d_i)Q_{ij}(y_j - d_j) + d_i Q_{ij} y_j + y_i Q_{ij} d_j - d_i Q_{ij} d_j\,, \tag{2.60}$$

and impose that $d_i Q_{ij} y_j + y_i Q_{ij} d_j = 2\omega_i x_i$. This gives $d_i(Q_{ij} + Q_{ji})y_j = 2d_i Q_{ij} y_j = 2\omega_i y_i$, implying that $d_i Q_{ij} = \omega_j$. We finally obtain

$$d_i = \omega_j Q_{ji}^{-1}\,, \tag{2.61}$$

which, inserted into equation (2.57), gives

$$A = \hat{y}_\mu C_{\mu\nu}^{-1}\hat{y}_\nu + (y_i - d_i)Q_{ij}(y_j - d_j) - d_i Q_{ij} d_j\,. \tag{2.62}$$

We now perform the integration in equation (2.56) and arrive at the final expression for one k bin:

$$\mathcal{L}(\boldsymbol{\beta}) \propto [2\pi \det(\mathsf{C}\mathsf{Q})]^{-1/2}\,\exp\left[-\frac{1}{2}\left(\hat{y}_\mu C_{\mu\nu}^{-1}\hat{y}_\nu - d_i Q_{ij} d_j\right)\right]\,. \tag{2.63}$$

To combine all k bins, we consider the total likelihood $\mathscr{L}$ defined as

$$\mathscr{L}(\boldsymbol{\beta}) = \prod_{j=1}^{N} \mathcal{L}_j(\boldsymbol{\beta})\,, \tag{2.64}$$

where N denotes the number of k bins. In practice, we replace the unknown covariance matrix C with an unbiased estimate derived from the 40 simulations. We sample the posterior distribution of the bias parameters by using our own Markov Chain Monte-Carlo (MCMC) code and assuming flat priors.

Table 2.4: The difference ΔWAIC between a model and the preferred one (highlighted with a dash) obtained by fitting $P_{\delta_h\delta}$ for mass bin M_3. Columns two to five indicate which operators are included in each model. Columns six to eight (as well as nine to eleven) refer to different values of Λ expressed in units of $h\,\mathrm{Mpc}^{-1}$.

Model	δ	δ^2	s^2	$\nabla^2\delta$	ΔWAIC (NR & RNL)			ΔWAIC (RL)		
					$\Lambda = 0.05$	0.1	0.2	0.05	0.1	0.2
$\mathcal{M}_1$	x				62.56	1672.15	69339.13	34.99	1683.11	69847.85
$\mathcal{M}_{2a}$	x	x			83.16	492.70	4302.72	4.53	689.03	5188.85
$\mathcal{M}_{2b}$	x		x		40.13	449.46	9308.73	32.54	820.53	7367.62
$\mathcal{M}_{2c}$	x			x	23.79	81.89	846.68	1.03	–	576.55
$\mathcal{M}_{3a}$	x	x	x		12.94	436.73	1797.75	7.24	450.06	4406.97
$\mathcal{M}_{3b}$	x	x		x	10.42	40.97	828.06	–	1.63	575.36
$\mathcal{M}_{3c}$	x		x	x	25.14	82.82	328.83	2.33	1.91	161.92
$\mathcal{M}_4$	x	x	x	x	–	–	–	1.59	3.86	–

Table 2.5: As in Table 2.4, but considering models that include more operators (see columns two and three) with respect to $\mathcal{M}_4$. Results are displayed for $\Lambda = 0.2\,h\,\mathrm{Mpc}^{-1}$, only.

Model	Γ_3	k^2	ΔWAIC (NR & RNL)	ΔWAIC (RL)
$\mathcal{M}_{5a}$	x		1.72	1.02
$\mathcal{M}_{5b}$		x	2.35	1.88
$\mathcal{M}_6$	x	x	1.66	1.41

2.5.2 How many bias parameters are needed?

A generic bias expansion includes all the possible operators allowed by symmetries. Here, we perform a Bayesian model comparison to investigate how many bias parameters are actually needed to fit $P_{\delta_h\delta}(k)$ extracted from our simulations for $k < 0.2\ h\,\mathrm{Mpc}^{-1}$. We focus on the M_3 sample that shows the most prominent scale-dependent bias in Fig. 2.1. We start with fitting the simple linear-bias model $P_{\delta_h\delta}(k) = b_1 P_{\delta\delta}(k)$. Then, we add several combinations of the terms $b_2 P_{\delta^2\delta}(k)$, $b_{s^2} P_{s^2\delta}(k)$ and $b_{\nabla^2\delta} P_{\nabla^2\delta\delta}(k)$ as summarized in Table 2.4. Finally, motivated by the perturbative results presented in section 2.2.4, we also consider the terms $b_{\Gamma_3} P_{\Gamma_3\delta}(k)$ and $b_{k^2} k^2$, as well as a combination of the two (see Table 2.5).

We quantify the relative performance of each model by using the Widely Applicable Information Criterion (Watanabe, 2010), also known as the Watanabe-Akaike Information Criterion (WAIC). This method evaluates the 'predictive accuracy' of a model, i.e. how useful the model will be in predicting new or future measurements. For finite and noisy data, this concept differs from the 'goodness of fit' which quantifies how well a model describes the data that have been used to optimize the model parameters. The WAIC is a Bayesian method that generalizes the Akaike Information Criterion (AIC, Akaike, 1973) by averaging over the posterior distribution of the model parameters. It can be shown that it is asymptotically equivalent to Bayesian cross validation (Watanabe, 2010). Moreover, the WAIC can be seen as an improvement upon the Deviance Information Criterion (DIC, Spiegelhalter et al., 2002) as it is invariant under

---

[8] From now on Greek indices run from 1 to n and Roman indices run from 2 to n. Moreover, C_{ij}^{-1} denotes the ij-element of the inverse of C.

re-parametrization of the model and also works for singular models (where the Fisher information matrix is not invertible). To apply the WAIC, one first estimates the log pointwise predictive density of the model (lppd, Gelman, Hwang and Vehtari, 2014)

$$\text{lppd} = \sum_i \ln \langle P(\mathbf{w}_i|\boldsymbol{\theta}) \rangle_{\text{post}} \tag{2.65}$$

where the sum runs over the data points $\mathbf{w}_i$, and $P(\mathbf{w}_i|\boldsymbol{\theta})$ denotes the probability to measure $\mathbf{w}_i$ under the statistical model and for a given set of model parameters $\boldsymbol{\theta}$. The expectation $\langle \ldots \rangle_{\text{post}}$ is estimated using draws for the model parameters from the posterior distribution given by the MCMC chains. The better the model fits the data, the larger the lppd is. In order to avoid overfitting, the lppd should be penalized for the effective number of model parameters, p_{WAIC}. Two different estimators can be used to measure this quantity from the MCMC chains, namely

$$p_{\text{WAIC},1} = 2 \sum_i \left[\log \langle P(\mathbf{w}_i|\boldsymbol{\theta}) \rangle_{\text{post}} - \langle \log P(\mathbf{w}_i|\boldsymbol{\theta}) \rangle_{\text{post}} \right], \tag{2.66}$$

and

$$p_{\text{WAIC},2} = \sum_i \langle [\log P(\mathbf{w}_i|\boldsymbol{\theta}) - \langle \log P(\mathbf{w}_i|\boldsymbol{\theta}) \rangle_{\text{post}}]^2 \rangle_{\text{post}}. \tag{2.67}$$

Essentially, each model parameter counts as one if all the information about it comes from the likelihood function, as zero if all the information comes from the prior, or as an intermediate number whenever both the data and the prior are informative. For our fits, we do not notice any practical difference between using equation (2.66) or equation (2.67). Following Gelman, Hwang and Vehtari (2014), we finally define the WAIC by using a deviance scale (i.e. by multiplying the lppd by a factor of 2 so that the final result is more easily comparable with the AIC and the DIC):

$$\text{WAIC} = -2(\text{lppd} - p_{\text{WAIC},i}) \tag{2.68}$$

The lower the WAIC is, the better the model performs. It is generally understood that a difference ΔWAIC of 5 (10) provides 'suggestive' ('substantial') evidence in favour of the preferred model.

2.5.3 Bare bias expansion

When we do not apply any renormalisation (hereafter NR, short for 'no renormalisation'), the lowest WAIC is obtained for model $\mathcal{M}_4$,

$$P_{\delta_h \delta}(k) = b_1 P_{\delta\delta}(k) + b_{\nabla^2 \delta} P_{\nabla^2 \delta\delta}(k) + b_2 P_{\delta^2 \delta}(k) + b_{s^2} P_{s^2 \delta}(k), \tag{2.69}$$

for all values of Λ. In Table 2.4, we report the difference ΔWAIC between each model we have considered and the preferred one. Our results clearly rule out models with less than four bias parameters. On the other hand, considering additional terms proportional to Γ_3 and k^2 and their combination gives a WAIC which is slightly worse than for $\mathcal{M}_4$, as we present in Table 2.5 for $\Lambda = 0.2 \, h \, \text{Mpc}^{-1}$ (since higher-order corrections should be most important for this cutoff). This shows that there is no need to include b_{Γ_3} and b_{k^2} in the bias expansion as, for $k < 0.2 \, h \, \text{Mpc}^{-1}$, our measurement of $P_{\delta_h \delta}(k)$ within $\sim 70 \, h^{-3} \, \text{Gpc}^3$ cannot constrain them. We thus conclude that, to describe the $z = 0$ cross spectral density of massive DM haloes and matter on these scales, we need to account for the linear bias b_1, the non-linear bias b_2, the tidal bias b_{s^2} and the first higher-derivative bias $b_{\nabla^2 \delta}$.

In the top panel of Fig. 2.6, we plot the best-fitting model $\mathcal{M}_4$ (solid curve) and the corresponding residuals are shown in the narrow panel below (fourth from the top). The fit never deviates from the measurements in a statistically significant way and sub-percent accuracy is achieved for most values of k. In order to visually illustrate the need for and the concept of renormalisation, in the top panel, we also plot the individual contributions of the different terms appearing on the r.h.s. of equation (2.69). Note that $P_{\delta\delta}(k)$, $P_{\delta^2\delta}(k)$ and $P_{s^2\delta}(k)$ are proportional to each other when $k \to 0$. Moreover, the terms that scale with b_2 and b_{s^2} are never negligible compared with $b_1 P_{\delta\delta}(k)$, even at the largest scales we can probe.

2.5.4 Renormalised bias expansion

For every model expressed in terms of the bare bias parameters, we can renormalise the cross-spectra of the composite operators with δ as in the examples provided by equations (2.50) and (2.51). The subtracted terms proportional to $P_{11}(k)$ will then contribute to the renormalised linear bias parameter. Let us consider, for example, equation (2.69) and re-write it in terms of the renormalised cross spectra

$$P_{\delta_h\delta}(k) = b_1 P_{\delta\delta}(k) + \left(\alpha_{\delta^2} b_2 + \alpha_{s^2} b_{s^2}\right) P_{11}(k) + b_{\nabla^2\delta} P_{\nabla^2\delta\delta}(k) + b_2 P_{[\delta^2]_1\delta}(k) + b_{s^2} P_{[s^2]_1\delta}(k) \,, \quad (2.70)$$

with α_{δ^2} and α_{s^2} the numerical coefficients appearing in equations (2.50) and (2.51). The result of this decomposition for the best-fitting model $\mathcal{M}_4$ is illustrated in the second panel from the top of Fig. 2.6 (labelled IE, short for 'intermediate expansion'). The renormalised cross spectra of the composite operators are now subdominant (and have a different shape) for $k \to 0$ with respect to the linear bias terms. Their relative contributions to $P_{\delta_h\delta}(k)$ grow with k (although their sum nearly vanishes in this particular case).

In perturbative calculations, the spectrum $P_{11}(k)$ appearing in equation (2.70) is promoted to $P_{\delta\delta}(k)$ to write

$$P_{\delta_h\delta}(k) = b_1^{\mathrm{R}} P_{\delta\delta}(k) + b_{\nabla^2\delta} P_{\nabla^2\delta\delta}(k) + b_2 P_{[\delta^2]_1\delta}(k) + b_{s^2} P_{[s^2]_1\delta}(k) \,, \quad (2.71)$$

which is the analog of equation (2.33) with

$$b_1^{\mathrm{R}} = b_1 + \alpha_{\delta^2} b_2 + \alpha_{s^2} b_{s^2} \,. \quad (2.72)$$

In the simulations, however, this expression does not coincide any longer with equation (2.71) as $P_{11}(k) \neq P_{\delta\delta}(k)$ for $k > 0$ (see Fig. 2.7). The only option to renormalise the linear bias coefficient without altering equation (2.69) is to generalize equation (2.50) to the non-linear regime by using

$$P_{[\delta^2]_1\delta}^{(\mathrm{NL})}(k) = P_{\delta^2\delta}(k) - \alpha_{\delta^2}(\Lambda) P_{\delta\delta}(k) \,, \quad (2.73)$$

together with analogous relations for the other composite operators. We can thus re-write equation (2.69) as

$$P_{\delta_h\delta}(k) = b_1^{\mathrm{R}} P_{\delta\delta}(k) + b_{\nabla^2\delta} P_{\nabla^2\delta\delta}(k) + b_2 P_{[\delta^2]_1\delta}^{(\mathrm{NL})}(k) + b_{s^2} P_{[s^2]_1\delta}^{(\mathrm{NL})}(k) \,, \quad (2.74)$$

which we refer to as the RNL, short for 'non-linear renormalisation'. In the third panel from the top of Fig. 2.6, we show the best-fitting model $\mathcal{M}_4$ and its different components. Obviously,
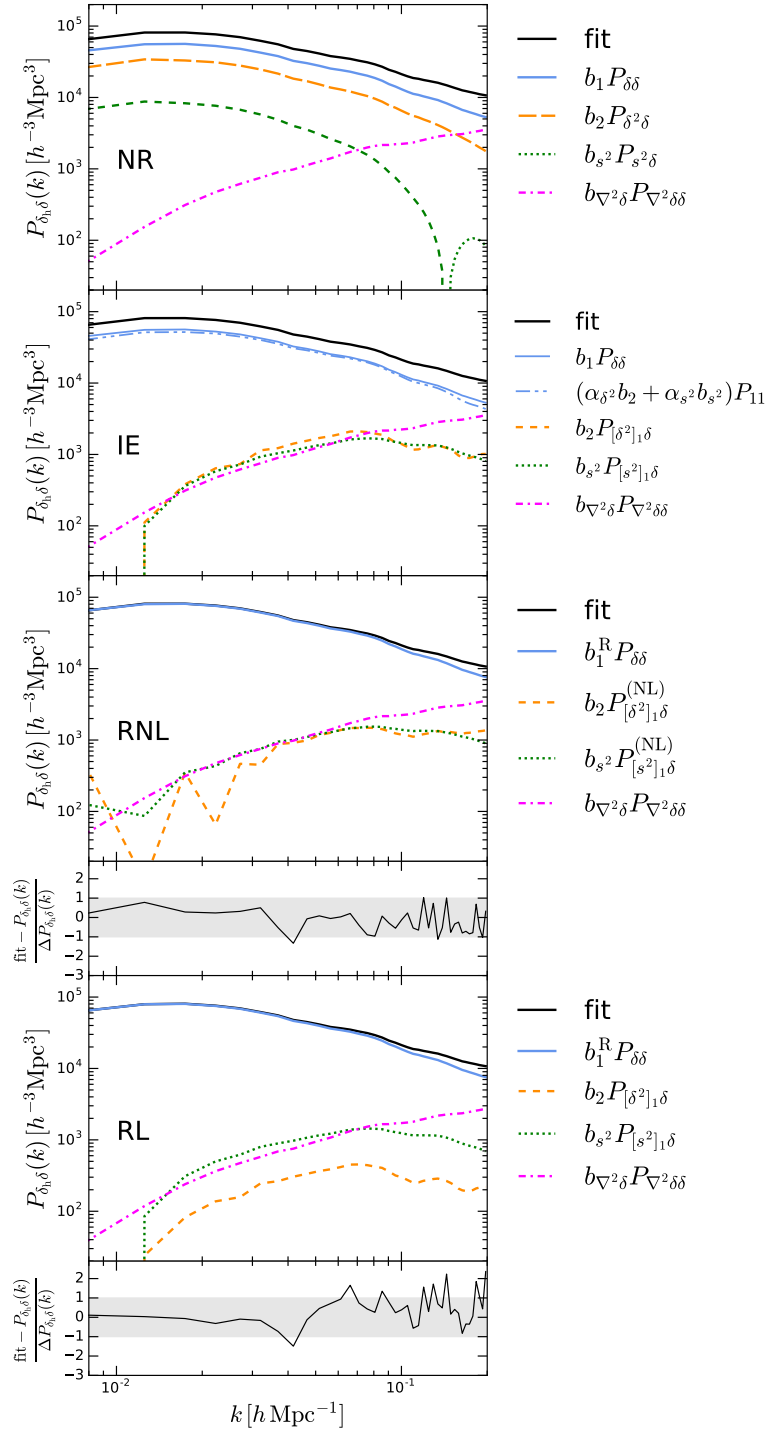
Figure 2.6: The best fit of the bias model $\mathcal{M}_4$ to $P_{\delta_h\delta}(k)$ (solid) and its different components (as indicated in the legend, with short-dashed lines representing negative values) for the halo mass bin M_3 and $\Lambda = 0.2\,h\,\mathrm{Mpc}^{-1}$. To improve readability we neglect the uncertainty in the bias parameters (only using their posterior mean). In the top three panels, we show the results obtained for the NR, IE and RNL cases which give rise to the same fit. The fit residuals normalised to the statistical error of the data $\Delta P_{\delta_h\delta}(k)$ are displayed in the fourth panel. Results for the RL case are displayed in the bottom two panels.
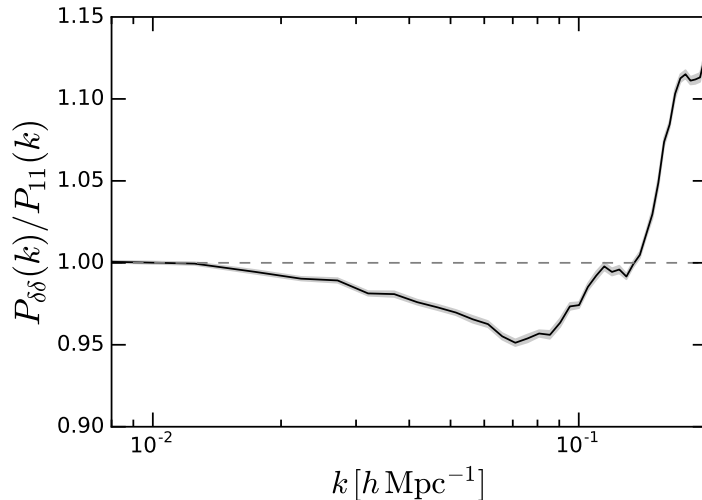
Figure 2.7: Non-linear corrections to the matter power spectrum at $z = 0$. The line shows the average ratio taken over the simulations. Shaded regions indicate the standard error of the mean.

fitting the RNL expression to the numerical data is completely equivalent to fitting the NR one and gives the same constraints on the non-linear and higher-derivative bias parameters. Therefore, the conclusions regarding the optimal number of bias parameters that we have drawn for the bare bias expansion still apply to the RNL case.

On the other hand, in hands-on situations, it is common practice to fit 1-loop perturbative models to survey or simulation data (e.g. Saito et al., 2014). In our study, taking model $\mathcal{M}_4$ as an example, this corresponds to using equation (2.71) together with (2.50) and (2.51). In this case (hereafter dubbed RL, short for 'linear renormalisation'), the best-fitting parameters and the goodness of fit do not coincide with those obtained for NR and RNL models. We thus repeat our model-selection test focusing on RL models. We find that the preferred operator sets vary with the cutoff scale (see the rightmost three columns in Table 2.4). For $\Lambda = 0.05$ and 0.1 $h\,\mathrm{Mpc}^{-1}$, all models that contain a term in $\nabla^2\delta$ are favoured. For $\Lambda = 0.2\,h\,\mathrm{Mpc}^{-1}$, instead, $\mathcal{M}_4$ is singled out by the WAIC (the bottom two panels of Fig. 2.6 display the individual components of $\mathcal{M}_4$ and the fit residuals). Further adding the Γ_3 and/or k^2 operators leads to slightly larger WAIC indicating mild overfitting. These results suggest that, as expected in an effective theory, more bias parameters are needed if smaller scales are considered. In particular, while δ and $\nabla^2\delta$ form the minimal set of operators required for $\Lambda < 0.1\,h\,\mathrm{Mpc}^{-1}$, adding $[\delta^2]_1$ and $[s^2]_1$ is necessary to describe the data with $\Lambda = 0.2\,h\,\mathrm{Mpc}^{-1}$.

2.5.5 Bias parameters

The best-fitting values of the bias parameters obtained for the NR and the RNL cases are displayed in Table 2.6 for all mass bins and cutoff scales. We show both the bare linear bias parameter (b_1) and the renormalised one (b_1^{R}). Similarly, in Table 2.7, we report the best-fitting parameters for the RL fits. Notice that, while b_1 is Λ-dependent, b_1^{R} assumes consistent values for all cutoffs in both the RNL and RL cases. We can thus conclude that the non-perturbative renormalisation procedures we have implemented in the simulations were completely successful. Nevertheless, it is worth pointing out that the best-fitting values of b_2, b_{s^2} and $b_{\nabla^2\delta}$ in Tables 2.6

Table 2.6: The bias parameters obtained by fitting equations (2.69) and (2.74) to $P_{\delta_h \delta}(k)$ from our 40 simulations.

Mass bin	Λ $[h\,\mathrm{Mpc}^{-1}]$	b_1 (NR)	b_1^{R} (RNL)	b_2	b_{s^2}	$b_{\nabla^2 \delta}$ $[h^2\,\mathrm{Mpc}^{-2}]$
	0.05	1.91 ± 0.02	1.89 ± 0.01	-0.09 ± 0.26	-0.14 ± 0.46	5.53 ± 7.34
M_1	0.1	1.91 ± 0.02	1.89 ± 0.01	-0.003 ± 0.10	-0.08 ± 0.08	7.12 ± 1.26
	0.2	2.04 ± 0.04	1.895 ± 0.003	-0.05 ± 0.03	-0.09 ± 0.01	2.45 ± 0.36
	0.05	2.38 ± 0.02	2.39 ± 0.02	0.14 ± 0.39	0.06 ± 0.67	17.87 ± 10.28
M_2	0.1	2.30 ± 0.04	2.38 ± 0.01	0.38 ± 0.15	-0.25 ± 0.12	18.34 ± 1.82
	0.2	2.35 ± 0.05	2.378 ± 0.004	0.12 ± 0.05	-0.15 ± 0.01	10.71 ± 0.55
	0.05	3.26 ± 0.03	3.35 ± 0.02	2.92 ± 0.55	-2.79 ± 0.95	57.75 ± 15.00
M_3	0.1	2.94 ± 0.05	3.36 ± 0.01	1.87 ± 0.20	-1.00 ± 0.15	54.50 ± 2.39
	0.2	2.35 ± 0.07	3.35 ± 0.01	1.07 ± 0.06	-0.42 ± 0.01	40.33 ± 0.67

Table 2.7: As in Table 2.6 but using equation (2.71).

Mass bin	Λ $[h\,\mathrm{Mpc}^{-1}]$	b_1^{R}	b_2	b_{s^2}	$b_{\nabla^2 \delta}$ $[h^2\,\mathrm{Mpc}^{-2}]$
	0.05	1.90 ± 0.01	-0.10 ± 0.27	0.01 ± 0.05	7.81 ± 6.09
M_1	0.1	1.90 ± 0.01	-0.10 ± 0.08	0.02 ± 0.08	7.34 ± 0.96
	0.2	1.898 ± 0.002	0.05 ± 0.01	-0.10 ± 0.01	3.84 ± 0.13
	0.05	2.38 ± 0.01	-0.14 ± 0.40	-0.05 ± 0.07	12.03 ± 8.58
M_2	0.1	2.38 ± 0.01	0.18 ± 0.12	-0.14 ± 0.13	17.33 ± 1.39
	0.2	2.379 ± 0.004	0.12 ± 0.01	-0.15 ± 0.01	10.56 ± 0.17
	0.05	3.35 ± 0.02	-0.87 ± 0.62	-0.07 ± 0.11	42.85 ± 13.53
M_3	0.1	3.36 ± 0.01	-0.05 ± 0.17	-0.07 ± 0.17	41.46 ± 1.96
	0.2	3.35 ± 0.01	0.23 ± 0.02	-0.36 ± 0.02	30.97 ± 0.23

and 2.7 differ for all mass bins when $\Lambda \geq 0.1\,h\,\mathrm{Mpc}^{-1}$. These results demonstrate the limitations of applying perturbative renormalisation at finite values of k. As already discussed in section 2.5.4, in order to retain the measurements of b_2, b_{s^2} and $b_{\nabla^2 \delta}$ from the NR fit in the renormalised case, equation (2.73) (and its analogue for the other operators) must be used instead of (2.50).

2.5.6 Comparison with previous work

We compare the halo bias parameters we obtained from our simulations with previous results in the literature. In Fig. 2.8, we contrast our results for b_1 and b_1^{R} (symbols) with the fit by Tinker et al., 2010 – their equation (6) – evaluated for a mean halo overdensity of $\Delta = 333$ (solid line). The fit quantifies the relative amplitude of the halo and matter power spectra on large scales as measured from a set of N-body simulations with slightly different cosmological parameters. To ease the comparison, we express the mass dependence in terms of the 'peak height' $\nu = \delta_c / \sigma_M$. Here, σ_M denotes the linear rms density fluctuation smoothed over the Lagrangian patch of each halo using a spherical top-hat filter and $\delta_c = 1.686$ is the critical linear overdensity in the spherical collapse model (for an Einstein-de Sitter universe). The horizontal location of the symbols is obtained by computing ν for every halo and averaging over each mass bin. In the NR
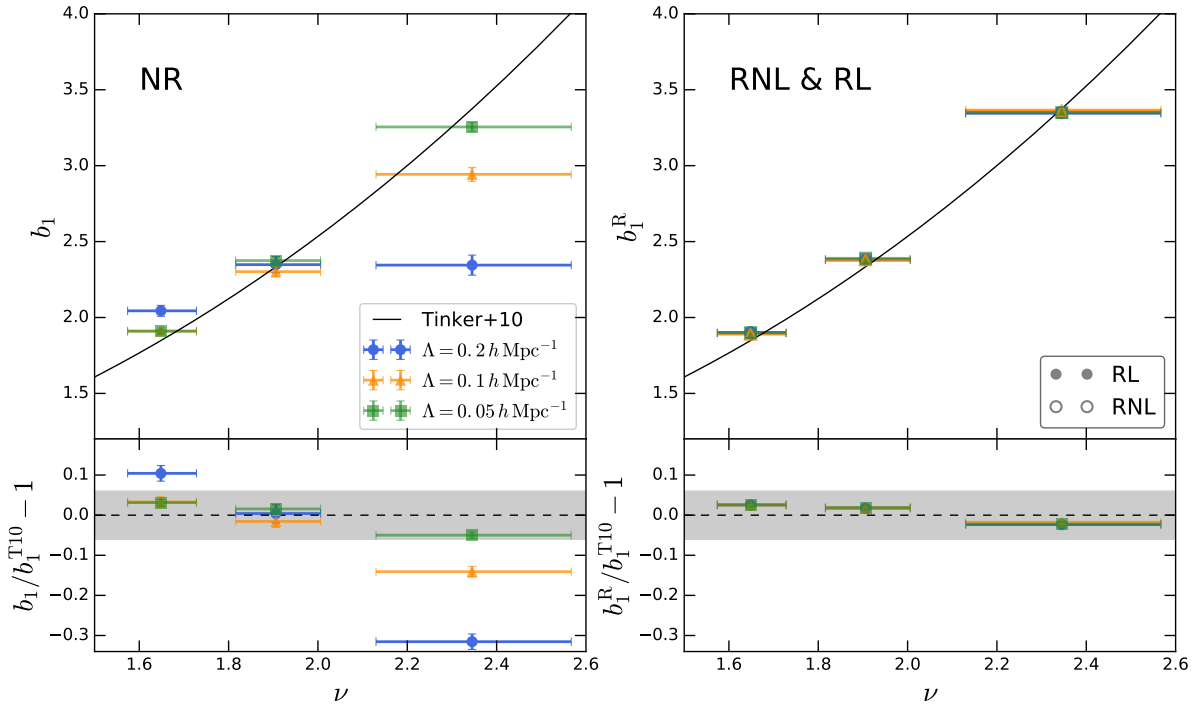
Figure 2.8: The best-fitting linear bias parameter as a function of the peak height, ν, for different cutoff scales, Λ. The left-hand side panel refers to the NR case in which b_1 runs with Λ. On the contrary, the right-hand side panel shows the results obtained by fitting b_1^{R}. Although solid and open symbols characterize the RNL and RL cases, respectively, all symbols referring to the same mass bin overlap and cannot be distinguished. As a reference, we also show the fitting function by Tinker et al. (2010) (solid) and its relative deviation from our results (bottom panels). The shaded area represents the intrinsic scatter about the mean relation found by Tinker et al. (2010).

case (left), our best-fitting values run with Λ and differ from the fit by Tinker et al. (2010) by up to 30 per cent. After renormalisation (right), the Λ-independent data points obtained in the RNL and RL cases are in excellent agreement with each other and also match the results by Tinker et al. (2010) to better than 2 per cent which is a factor of three smaller than the intrinsic scatter about the mean relation between linear bias and halo mass found in Tinker et al. (2010). This shows that by renormalising the spectra we automatically obtain a consistent and robust value of b_1^{R} for all the mass bins.

In Fig. 2.9, we compare our measurements of b_2 and b_{s^2} with other results in the literature. For the quadratic bias (top panels), we consider three different fitting functions for the relation $b_2(b_1)$ extracted from N-body simulations. The first was obtained by applying the peak-background split to measurement of the halo mass function (Hoffmann, Bel and Gaztañaga, 2015). The second was determined with the 'separate-universe' technique in which one studies the response to infinite-wavelength perturbations (Lazeyras, Wagner et al., 2016). The third, instead, was derived from measurements of the halo reduced three-point correlation function (Hoffmann, Bel and Gaztañaga, 2017). Note that these methods measure the renormalised b_2 while we only renormalise b_1. Therefore, we do not expect that our Λ-dependent best-fitting values for b_2 should perfectly coincide with the other results in the literature. Nevertheless, in the NR case (left panel) and for large-scale cutoffs (i.e $\Lambda = 0.05$ and $0.1\,h\,\mathrm{Mpc}^{-1}$), our measurements
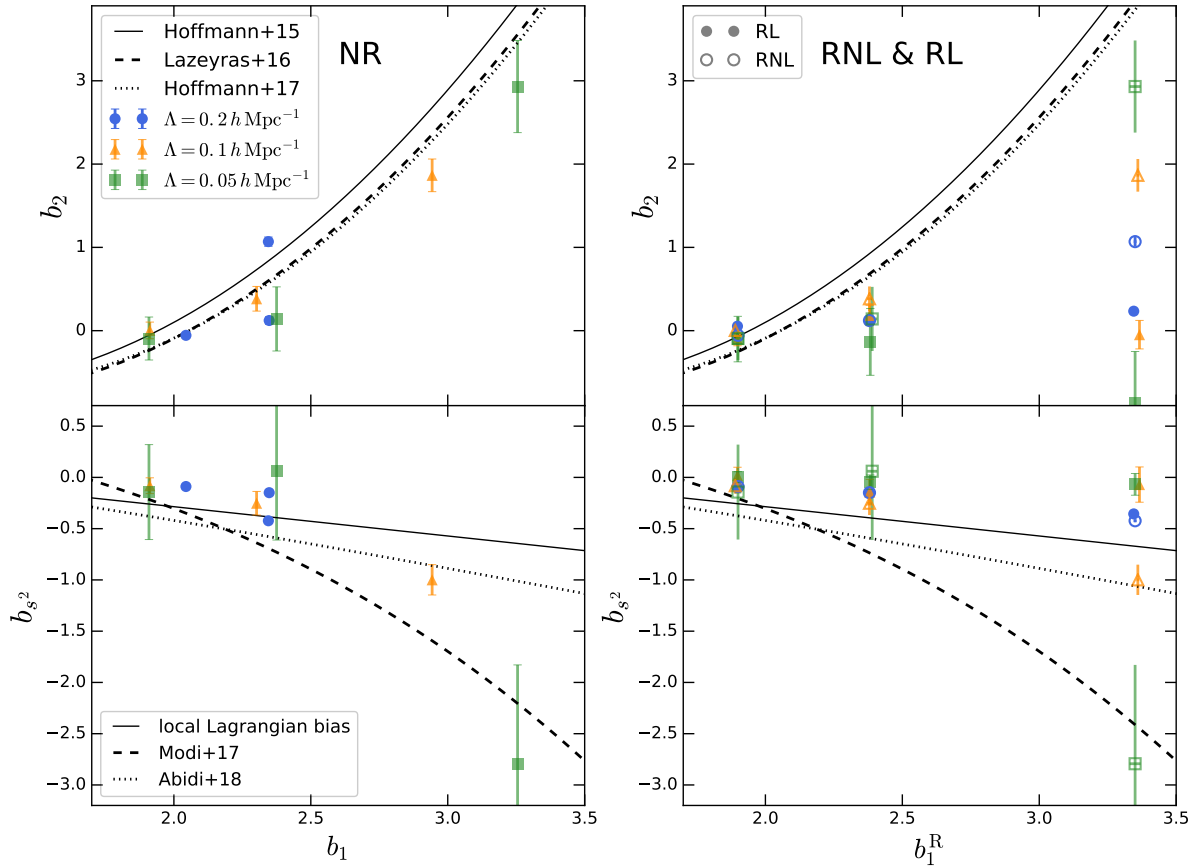
Figure 2.9: Symbols with errorbars indicate the best-fitting non-linear bias parameters b_2 (top) and b_{s^2} (bottom) as a function of b_1 for different cutoff scales. The panels on the left-hand side show the bare bias parameters (NR) while the results on the right-hand side are obtained after renormalising b_1 (here, empty and filled symbols correspond the RNL and RL cases, respectively). As a reference, we overplot several theoretical models and fitting functions for the renormalised parameters (see the main text for details).

approximately run along the fitting functions for the relation $b_2(b_1)$. After renormalising b_1 (right panel), however, our b_2 measurements for the two highest mass bins tend to lie below the previously published results. Moreover, as already mentioned, we obtain different b_2 values in the RNL and RL cases. The RNL results with small Λ are in much better agreement with the fitting functions in the literature. This suggests that it should be possible to further improve the agreement by extending the RNL technique to renormalise b_2. We will explore this possibility in our future work. For the tidal bias (bottom panels), we also compare our best-fitting values to three different literature results. We consider the theoretical prediction for a local Lagrangian biasing scheme (Catelan, Porciani and Kamionkowski, 2000), $b_{s^2}(b_1) = -(2/7)(b_1 - 1)$ (Baldauf, Seljak, Desjacques et al., 2012; Chan, Scoccimarro and R. K. Sheth, 2012) together with two fitting functions that account for a non-vanishing Lagrangian tidal-tensor bias in N-body simulations (Modi, Castorina and Seljak, 2017; Abidi and Baldauf, 2018, their equations 22 and 5.1 plus 2.32, respectively). In agreement with these fitting functions, our measurements provide evidence for large negative tidal biases at high halo masses. After renormalising b_1, this conclusion holds only in the RNL case while b_{s^2} always assumes values close to zero in the RL
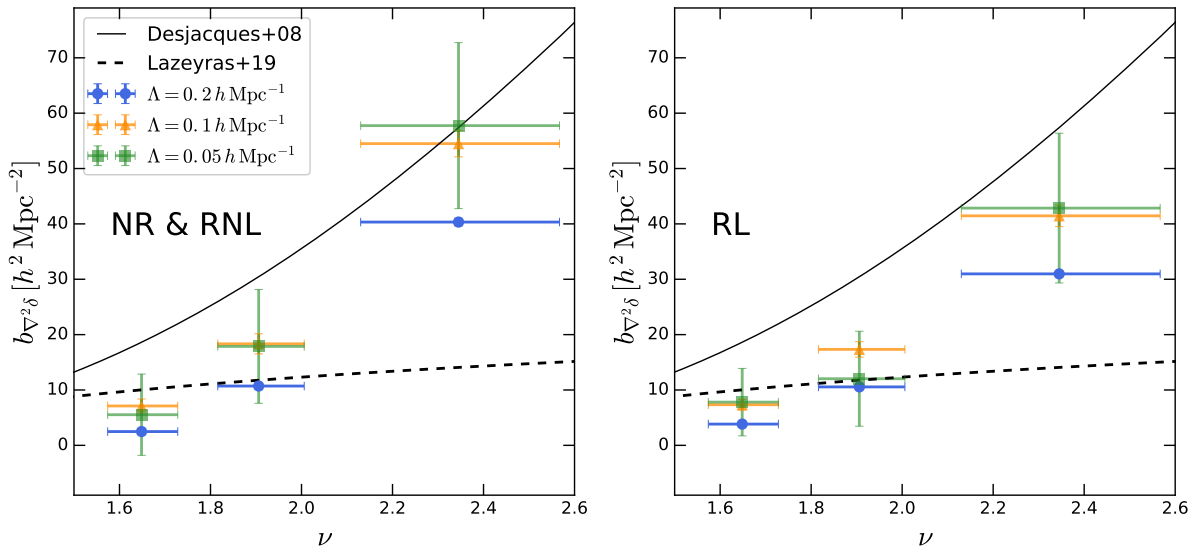
Figure 2.10: The best-fitting first higher-derivative bias parameter, $b_{\nabla^2\delta}$, as a function of the peak height, ν, for different cutoff scales. As a reference, we show the the fit to numerical simulations by Lazeyras and Schmidt (2019, dashed) and the predictions from peak statistics presented in Desjacques (2008, solid).

case.

In Fig. 2.10, we plot our results for $b_{\nabla^2\delta}$ as a function of ν. The NR and RNL fits are shown together in the left-hand side panel since $b_{\nabla^2\delta}$ assumes the same value in these cases. On the contrary, the RL results are plotted in the right-hand side panel. As a benchmark, we also show the fitting function obtained with the 'amplified-mode' simulation technique by Lazeyras and Schmidt (2019, their equation 5.4 but note that we adopt the opposite sign convention for $b_{\nabla^2\delta}$) as well as the predictions for density peaks (Desjacques, 2008) computed using the filter function given in Chan, R. K. Sheth and Scoccimarro (2017). In agreement with Elia, Ludlow and Porciani (2012), our measurements for the haloes scale with ν in a similar way as the theoretical peak model but assume lower values in the ν-range we can probe. Compared with the fit by Lazeyras and Schmidt (2019), we find comparable results in bins M_1 and M_2 and substantially higher values for M_3. Overall our NR and RNL measurements display a steeper ν-dependence than expected based on their results.

2.6 Summary

We have investigated a number of issues related to the clustering of biased tracers of the LSS. In particular, we have focused on the renormalisation of the linear bias parameter. After reviewing the literature on the subject, we have applied a bias expansion to N-body simulations and studied the UV-sensitivity of the composite operators that contribute to the halo-matter cross spectrum $P_{\delta_h\delta}(k)$. We have then successfully mastered the challenge to renormalize these terms without resorting to perturbation theory. Finally, we have identified how many bias parameters are needed to accurately describe halo clustering for $k < 0.2\,h\,\mathrm{Mpc}^{-1}$ without overfitting. Our main results can be summarized as follows.

1. We have run a suite of 40 N-body simulations and measured $P_{\delta_h\delta}(k)$ for three different

halo-mass bins selected at $z = 0$. Consistently with previous work, we have found that the ratio $P_{\delta_h\delta}(k)/P_{\delta\delta}(k)$ grows with k and that this effect becomes more prominent for more massive haloes (Fig. 2.1). The scale dependence of the ratio provides a compelling motivation for considering non-linear bias models.

2. We have measured all fields that enter a non-linear bias expansion to third order in the density fluctuations using different values of the coarse-graining scale ($\Lambda = 0.05, 0.1$ and $0.2\,h\,\mathrm{Mpc}^{-1}$, Fig. 2.2). By cross-correlating these fields with the mass overdensity, we have computed all partial contributions to $P_{\delta_h\delta}(k)$. Focusing on the composite operators appearing in the bias expansion (e.g. δ^2 and s^2), we have shown that the amplitude of their cross spectra with δ strongly depends on Λ (top panels of Fig. 2.3). We have demonstrated that this 'UV-sensitivity' is fully captured by the cross correlation between the composite operators and the linear density field (middle panels of Fig. 2.3). Thus, we have successfully obtained the renormalised spectra by subtracting this UV-sensitive term from the original spectra (bottom panels of Fig. 2.3).

3. We have compared $P_{\delta^2\delta_1}(k)$ and $P_{s^2\delta_1}(k)$ extracted from the simulations to perturbative predictions at LO. An excellent agreement over a broad range of scales can be achieved by properly accounting for the window functions that define the coarse-graining procedure in the perturbative integrals (top panels of Fig. 2.5). The values $68/21\,\sigma_1^2$ and $136/63\,\sigma_1^2$, that are usually quoted for the limit $k \to 0$, overpredict our measurements, as they are obtained neglecting the influence of the window function. The relative difference, however, decreases with increasing Λ.

4. For $\Lambda = 0.05$ and $0.1\ h\,\mathrm{Mpc}^{-1}$, we have shown that the 'renormalised spectra' $P_{[\delta^2]_1\delta}(k)$ and $P_{[s^2]_1\delta}(k)$ measured in the simulations are in very good agreement with the perturbative calculations obtained by taking the window functions into account (bottom panels of Fig. 2.5). For $\Lambda = 0.2\ h\,\mathrm{Mpc}^{-1}$, however, the 1-loop results show non-negligible deviations from the numerical data.

5. We have fit bias models with a different number of parameters to $P_{\delta_h\delta}(k)$ by using a Bayesian method that accounts for correlations between all spectra entering the model. With a model-selection criterion (WAIC), we have determined the optimal number of bias parameters that are needed as a function of Λ for both the renormalised and non-renormalised spectra. The preferred set of bias operators includes $\delta, \nabla^2\delta, \delta^2$ and s^2 in most cases (model $\mathcal{M}_4$ in Table 2.4).

6. In Fig. 2.6, we have illustrated the renormalisation procedure of the linear bias parameter for the optimal model. We have identified two different modi operandi. The first (RL) parallels perturbative renormalisation while the second (RNL) generalizes the renormalisation procedure to the fully non-linear regime.

7. We have presented the fits we obtained for the optimal bias model (see Tables 2.6 and 2.7, as well as Figs. 2.8 – 2.10) and compared them to previous results in the literature. While the best-fitting values for the bare linear bias b_1 run with Λ, those for the renormalised linear bias b_1^R stay constant as a function of the cutoff scale (for both RL and RNL). This confirms that our numerical renormalisation was successful.

8. Finally, we have shown that only RNL leaves the non-linear and higher-derivative bias parameters unchanged with respect to the bare bias expansion (NR). This casts some doubts on the accuracy and robustness of using NLO perturbative expressions to fit low-redshift observational and N-body data at $k \gtrsim 0.1\ h\,\mathrm{Mpc}^{-1}$.

Renormalisation of quadratic and tidal halo bias in N-body simulations[1]

3.1 Introduction

The spatial distribution of gravitationally collapsed tracers of the large-scale structure (LSS) of the Universe (e.g. dark-matter (DM) haloes, galaxies), $\delta_h(\mathbf{x})$, can be described in form of a 'bias relation' with respect to the underlying DM field. In the framework of an effective field theory (EFT), this model can be written as an expansion, truncated at some order, which contains all possible symmetries of gravitational instability, weighted by a numerical factor, the 'bias parameter'. The quantities in the expansion (called 'operators' O) are powers of the DM overdensity field $\delta(\mathbf{x})$, as well as derivative (e.g. $\nabla^2\delta(\mathbf{x})$) and non-local (e.g. the square of the tidal tensor, $s^2(\mathbf{x})$) terms. In a recent paper (Werner and Porciani, 2019, hereafter W19) we provided a pedagogical review on the topic of bias (in particular the issue of 'renormalisation' that we will briefly explain below), and we refer the reader interested in a detailed presentation to this work and the many references contained therein. This paper presents a follow-up analysis to our previous work and is therefore largely built upon it.

It is generally of interest – depending on certain tracer quantities and on scale – which operators are actually needed in the bias expansion and what values the corresponding bias parameters should have. On the one hand, an accurate bias model is crucial for cosmological inference from large-scale galaxy redshift surveys. The bias parameters are then treated as free parameters that are fitted to the measurements from the survey. On the other hand, for testing physical bias relations, it is interesting to compare the predicted bias parameter values with those measured from numerical data. In order to address these two issues, in W19 we employed a suite of 40 cosmological N-body simulations to determine the optimal number of bias operators and measured the corresponding coefficients for three different halo mass bins. For that, relying on δ defined by the (rescaled) peculiar gravitational potential ϕ via $\nabla^2\phi = \delta$, we first wrote the bias expansion up until third order,

$$\delta_h = b_0 + b_1\delta + b_{\nabla^2\delta}\nabla^2\delta + b_2\delta^2 + b_{s^2}s^2 + b_3\delta^3 + b_{\delta s^2}\delta s^2 + b_{s^3}s^3 + b_{\Gamma_3}\Gamma_3 \,, \tag{3.1}$$

---

[1] This chapter is in preparation for submission to MNRAS.

with $s^2 = s_{ij}s_{ji}$ and $s^3 = s_{ij}s_{jk}s_{ki}$, where

$$s_{ij} = \partial_i\partial_j\phi - \frac{1}{3}\delta^{\mathrm{K}}_{ij}\delta = \left(\partial_i\partial_j\nabla^{-2} - \frac{1}{3}\delta^{\mathrm{K}}_{ij}\right)\delta = \gamma_{ij}\,\delta\,, \tag{3.2}$$

(with ∇^{-2} the inverse of the Laplacian operator and δ^{K}_{ij} the Kronecker symbol), as well as $p^2 = p_{ij}p_{ji}$ with $p_{ij} = \partial_i\partial_j\phi_v - \frac{1}{3}\delta^{\mathrm{K}}_{ij}\theta$ and $\Gamma_3 = s^2 - p^2 - (2/3)(\delta^2 - \theta^2)$, where ϕ_v is the (rescaled) velocity potential such that $\nabla^2\phi_v = \theta$. In order to measure the bias parameters b_i, we translated the relation into Fourier space and then cross-correlated $\delta_{\mathrm{h}}(\mathbf{k})$ with $\delta(\mathbf{k})$ (both which can be described as random fields) which gives the correlator $\langle\delta_{\mathrm{h}}(\mathbf{k})\,\delta(\mathbf{k}')\rangle$, where the brackets $\langle\ldots\rangle$ denote the average over an ensemble of realizations. The correlator can be written using the cross spectrum between matter and tracers, $P_{\delta_{\mathrm{h}}\delta}(k)$, where $\langle\delta_{\mathrm{h}}(\mathbf{k})\,\delta(\mathbf{k}')\rangle = (2\pi)^3\,P_{\delta_{\mathrm{h}}\delta}(k)\,\delta_{\mathrm{D}}(\mathbf{k} + \mathbf{k}')$ and $\delta_{\mathrm{D}}(\mathbf{k})$ is the Dirac delta distribution in three dimensions. Using the Widely Applicable Information Criterion (WAIC), we showed in W19 that only a subset of those operators from equation (3.1) is needed to accurately describe the distribution of haloes in our simulations up until $k \leq 0.2\,h\,\mathrm{Mpc}^{-1}$, therefore the cross spectrum can be written as

$$P_{\delta_{\mathrm{h}}\delta}(k) = b_1 P_{\delta\delta}(k) + b_{\nabla^2\delta}P_{\nabla^2\delta\delta}(k) + b_2 P_{\delta^2\delta}(k) + b_{s^2}P_{s^2\delta}(k)\,. \tag{3.3}$$

The r.h.s. of this relation represents the model and the l.h.s. the data. We measured all power and cross spectra appearing on both sides directly from the simulations and then fitted the r.h.s. against the l.h.s. to get the bias parameters b_1, b_2, b_{s^2} and $b_{\nabla^2\delta}$.

However, the spectra $P_{\delta^2\delta}(k)$ and $P_{s^2\delta}(k)$, that include the non-linear 'composite operators' δ^2 and s^2, present a peculiarity that we examined in great detail in W19. For various reasons (that we laid out in detail in the previous paper) all density fields that enter the bias expansion need to be smoothed with a filter. To implement this smoothing in our simulations, we chose a sharp cutoff in k-space at three scales $\Lambda = \{0.05, 0.1, 0.2\}\,h\,\mathrm{Mpc}^{-1}$, and set the Fourier modes of the density field above these scales to zero. However, imposing this arbitrary cutoff propagates to the aforementioned cross spectra: Their signal tends to a constant at large scales $(k \to 0)$ that increases for larger values of Λ. This presents a problem since on large scales the signal of $P_{\delta_{\mathrm{h}}\delta}(k)$ is expected to be described solely by a constant, cutoff-independent contribution of the linear bias $b_1 P_{\delta\delta}(k)$. We showed that by adapting the framework of cosmological Standard Perturbation Theory (SPT; see W19 for an overview of the method as well as the notation we use) to simulations, it is possible to 'renormalise' the cross spectra and therefore the linear bias parameter such that afterwards the renormalised bias parameter b_1^{R} is cutoff-independent.

In this paper we want to extend our work from W19 in two different ways: First, we want to focus on the renormalisation of the two non-linear bias parameters b_2 (quadratic bias) and b_{s^2} (tidal bias) which, after the procedure in the previous paper, remain still cutoff dependent. In order to achieve this, we need to bring the renormalisation framework to the level of bispectra (Assassi et al., 2014, hereafter A14), and measure the cross bispectrum of the halo density field with the matter density field, $B_{\delta_{\mathrm{h}}\delta\delta}(k, k_1, k_2)$, where $\langle\delta_{\mathrm{h}}(\mathbf{k})\,\delta(\mathbf{k}_1)\,\delta(\mathbf{k}_2)\rangle = (2\pi)^3\,B_{\delta_{\mathrm{h}}\delta\delta}(k, k_1, k_2)\,\delta_{\mathrm{D}}(\mathbf{k} + \mathbf{k}_1 + \mathbf{k}_2)$, and the bias relation is given as

$$B_{\delta_{\mathrm{h}}\delta\delta}(k, k_1, k_2) = b_1 B_{\delta\delta\delta}(k, k_1, k_2) + b_2 B_{\delta^2\delta\delta}(k, k_1, k_2) + b_{s^2}B_{s^2\delta\delta}(k, k_1, k_2) + b_{\nabla^2\delta}B_{\nabla^2\delta\delta\delta}(k, k_1, k_2)\,. \tag{3.4}$$

Second, we want to apply the renormalisation method to the halo power spectrum, $P_{\delta_{\mathrm{h}}\delta_{\mathrm{h}}}(k)$, which is a quantity that is particularly interesting for galaxy redshift surveys. In contrast to

the halo-matter cross spectrum, which only exists in simulations, the halo power spectrum is directly measurable, and therefore it is a crucial task to check the renormalisation procedure also in this case.

The structure of this paper is as follows: In section 3.2 we will introduce briefly the renormalisation framework and then perform an elaborate derivation of the renormalisation expressions at second order, both in SPT and adapted to N-body simulations. We then show how to measure the bispectrum from our suite of simulations in section 3.3, and we present our data, in particular the results of the second-order renormalisation, in section 3.4. In section 3.5 we provide the theoretical and numerical results for the renormalisation of the halo power spectrum. We finally summarize and conclude in section 3.6.

3.2 Bias renormalisation in SPT

In this section we first briefly introduce again the general concept of bias renormalisation. We summarize our results from our previous work, W19, where we performed the renormalisation at first order in a suite of N-body simulations, and succeeded in making b_1 cutoff independent. For more details we refer the reader to this paper.

Building up on that, following A14, we extend the procedure to second order, now aiming at the renormalisation of b_2 and b_{s^2}. We present detailed SPT calculations at the level of bispectra that set up the theoretical framework, and then describe how to implement the expressions into our suite of numerical simulations.

3.2.1 The renormalisation framework

In the bias relation, written as an EFT, appear 'composite operators' $O = \{\delta^2, s^2\}$ that are 'UV-sensitive'. This means they receive power from all scales, in particular also from short-wavelength modes that lie outside the regime for which the EFT is valid, as we see for the Fourier transform of δ^2 as an example,

$$\delta^2(\mathbf{k}) = \int \delta(\mathbf{q}) \, \delta(\mathbf{k} - \mathbf{q}) \, \frac{\mathrm{d}^3 q}{(2\pi)^3} \; . \tag{3.5}$$

This presents a problem, since it makes the resulting expressions sensitive to the cutoff of the integral. Additionally, also the bias parameters become cutoff dependent. A14 developed a framework, based upon cosmological SPT, that allows to consistently renormalise the composite operators and therefore the bias parameters order by order. The essence of this approach is that additional 'counter operators' are introduced that eliminate the UV-sensitive pieces at large scales. The result are renormalised operators $[O]$, defined via

$$\langle [O](\mathbf{q}) \, \delta_1(\mathbf{q}_1) \ldots \delta_1(\mathbf{q}_m) \rangle = \langle O(\mathbf{q}) \, \delta_1(\mathbf{q}_1) \ldots \delta_1(\mathbf{q}_m) \rangle^{(\mathrm{LO})} \; , \tag{3.6}$$

where $\mathbf{q}_i \to 0 \; \forall i$, δ_1 is the linear DM density field (evolved to redshift $z = 0$ by multiplication with the linear growth factor D) and 'LO' means the leading-order term of the r.h.s. Therefore, an operator renormalised to m-th order, $[O]_m$, fulfills equation (3.6) where the cross correlation with δ_1 is written m-fold.

For example, the first-order renormalised $[\delta^2]_1$ is calculated through power spectra. The result

is commonly given as

$$[\delta^2]_1 = \delta^2 - \frac{68}{21}\sigma_1^2(\Lambda)\,\delta\,, \qquad (3.7)$$

where the second term on the r.h.s. is the counter operator, and $\sigma_1^2(\Lambda)$ is the strength of the fluctuations of δ_1 which is given as

$$\sigma_1^2(\Lambda) = \frac{1}{2\pi^2}\int_0^\Lambda q^2\,P_{11}(q)\,\mathrm{d}q\,, \qquad (3.8)$$

with $P_{11}(k)$ the linear power spectrum. The constant prefactor $68/21\sigma_1^2(\Lambda)$ in equation (3.7) is calculated from the expression

$$\lim_{k\to 0}\left[\frac{P_{\delta^2\delta}^{(31)}(k)}{P_{11}(k)}\right] = \lim_{k\to 0}\left[4\int F_2(-\mathbf{q},\mathbf{k})P_{11}(q)\frac{\mathrm{d}^3q}{(2\pi)^3}\right]. \qquad (3.9)$$

where $P_{\delta^2\delta}^{(31)}(k)$ is the (31)-term of the cross spectrum between δ^2 and δ, given as the correlator $2\langle(\delta_1\delta_2)(\mathbf{k})\,\delta_1(\mathbf{k}')\rangle$. In W19 we showed, however, that when comparing to real data, it is crucial to take care of filter functions $W(k)$ in the integral that originate from smoothing the density fields,

$$\lim_{k\to 0}\left[\frac{P_{\delta^2\delta}^{(31)}(k)}{P_{11}(k)}\right] = \lim_{k\to 0}\left[4\,W(k)\int F_2(-\mathbf{q},\mathbf{k})\,P_{11}(q)\,W(q)\,W(|\mathbf{k}-\mathbf{q}|)\frac{\mathrm{d}^3q}{(2\pi)^3}\right], \qquad (3.10)$$

where

$$W(k) = \begin{cases} 1 & \text{if } k < \Lambda\,, \\ 0 & \text{otherwise}\,. \end{cases} \qquad (3.11)$$

This integral gives

$$\lim_{k\to 0}\left[\frac{P_{\delta^2\delta}^{(31)}(k)}{P_{11}(k)\,W(k)}\right] = \frac{68}{21}\sigma_1^2(\Lambda) - \frac{1}{3}\frac{\Lambda^3 P_{11}(\Lambda)}{2\pi^2}\,, \qquad (3.12)$$

which presents a modification to the respective term in equation (3.7). From these considerations follows the 'renormalised cross spectrum' $P_{[\delta^2]_1\delta}(k)$ that enters equation (3.3),

$$P_{[\delta^2]_1\delta}(k) = P_{\delta^2\delta}(k) - \lim_{k'\to 0}\left[\frac{P_{\delta^2\delta}^{(31)}(k')}{P_{11}(k')\,W(k')}\right]P_{11}(k)\,. \qquad (3.13)$$

In perturbative calculations, it is common to use $P_{11}(k)$ on the r.h.s. of equation (3.13), whereas we showed in W19 that the non-linear (NL) power spectrum $P_{\delta\delta}(k)$ should be used to avoid mistakes on mildly non-linear scales, so that

$$P_{[\delta^2]_1\delta}^{(\mathrm{NL})}(k) = P_{\delta^2\delta}(k) - \lim_{k'\to 0}\left[\frac{P_{\delta^2\delta}^{(31)}(k')}{P_{11}(k')\,W(k')}\right]P_{\delta\delta}(k)\,. \qquad (3.14)$$

For the implementation into numerical simulations we measured all spectra consistently from the

data and did not model them with perturbative integrals. Therefore, equation (3.14) becomes

$$
\begin{aligned}
P^{(\mathrm{NL})}_{[\delta^2]_1\delta}(k) &= P_{\delta^2\delta}(k) - \frac{P_{\delta^2\delta_1}(k_{\min})}{P_{11}(k_{\min})} P_{\delta\delta}(k) \\
&\equiv P_{\delta^2\delta}(k) - \alpha_{\delta^2} P_{\delta\delta}(k) \,,
\end{aligned}
\tag{3.15}
$$

where $k_{\min}$ is the minimum k value accessible in the simulations which is given as $k_{\min} = 2\pi/L$ with L the box length. We demonstrated that when computing the renormalised cross spectra as in equation (3.15) (analogously for s^2) the renormalised linear bias parameter b_1^{R} shows consistent values for all Λ.

3.2.2 Renormalisation at second order

Now we want to extend the procedure to second order. The goal is to find a bias expansion that allows to measure all terms directly from the simulations, which can then be fitted against $B_{\delta_{\mathrm{h}}\delta\delta}(k, k_1, k_2)$ to obtain the renormalised b_2 and b_{s^2}. Following equation (3.6), the renormalised operators $[\delta^2]_2$ and $[s^2]_2$ need to fulfill the relation

$$
\langle [O]_2(\mathbf{k})\,\delta_1(\mathbf{k}_1)\,\delta_1(\mathbf{k}_2) \rangle = \langle [O]_1(\mathbf{k})\,\delta_1(\mathbf{k}_1)\,\delta_1(\mathbf{k}_2) \rangle^{(\mathrm{LO})} \,,
\tag{3.16}
$$

with $\mathbf{k}_i \to 0\ \forall i$, where we write $[O]_1$ on the r.h.s. to indicate that we start the procedure from the operators already renormalised at first order. Therefore, the terms that we need to subtract (which can be written as the counter operators) are given by taking the $\mathbf{k}_1$, $\mathbf{k}_2 \to 0$ limit of the next-to-leading-order (NLO) term of the r.h.s. of equation (3.16), $\langle [O]_1(\mathbf{k})\,\delta_1(\mathbf{k}_1)\,\delta_1(\mathbf{k}_2)\rangle^{(\mathrm{NLO})}$, which coincides with the cross bispectrum $B^{(\mathrm{NLO})}_{[O]_1\delta_1\delta_1}(k, k_1, k_2)$. We now want to calculate this bispectrum explicitly, since our first goal is to derive the respective counter operators. This was already done by A14 who provided the final result in a compact way (their equation 2.42). We, however, want to present the calculation in a much more detailed and intuitive way to the reader, and with this also confirm the earlier result. Again we use δ^2 as an example. Furthermore, for now we only write the purely theoretical expressions without taking filter functions into account. This gives

$$
B^{(\mathrm{NLO})}_{[\delta^2]_1\delta_1\delta_1}(k, k_1, k_2) = B^{([22]11)}_{\delta^2\delta_1\delta_1}(k, k_1, k_2) + B^{([13]11)}_{\delta^2\delta_1\delta_1}(k, k_1, k_2) - \frac{68}{21}\sigma_1^2(\Lambda)\, B^{(211)}_{\delta\delta_1\delta_1}(k, k_1, k_2) \,.
\tag{3.17}
$$

where $B^{([22]11)}_{\delta^2\delta_1\delta_1}(k, k_1, k_2)$ relates to the correlator $\langle (\delta_2\delta_2)(\mathbf{k})\,\delta_1(\mathbf{k}_1)\,\delta_1(\mathbf{k}_2)\rangle$, $B^{([13]11)}_{\delta^2\delta_1\delta_1}(k, k_1, k_2)$ can be identified with $\langle (\delta_1\delta_3)(\mathbf{k})\,\delta_1(\mathbf{k}_1)\,\delta_1(\mathbf{k}_2)\rangle$, and $B^{(211)}_{\delta\delta_1\delta_1}(k, k_1, k_2)$ is given by $\langle \delta_2(\mathbf{k})\,\delta_1(\mathbf{k}_1)\,\delta_1(\mathbf{k}_2)\rangle$. From now on we define

$$
B_{22}(k, k_1, k_2) \equiv B^{([22]11)}_{\delta^2\delta_1\delta_1}(k, k_1, k_2) \,,
\tag{3.18}
$$

$$
B_{13}(k, k_1, k_2) \equiv B^{([13]11)}_{\delta^2\delta_1\delta_1}(k, k_1, k_2) \,,
\tag{3.19}
$$

and

$$
R_1(k, k_1, k_2) \equiv B^{(211)}_{\delta\delta_1\delta_1}(k, k_1, k_2) \,,
\tag{3.20}
$$

We explicitly calculate these expressions now and derive the counter terms.

Calculation of $B_{22}(k, k_1, k_2)$

In the framework of SPT, $B_{22}(k, k_1, k_2)$ can be written as

$$B_{22}(k, k_1, k_2) = \int_{a,b,c,d,p,q} \langle F_2(\mathbf{c}, \mathbf{d}) \, \delta_1(\mathbf{c}) \, \delta_1(\mathbf{d}) \, \delta_D(\mathbf{p} - (\mathbf{c} + \mathbf{d})) \, F_2(\mathbf{a}, \mathbf{b}) \, \delta_1(\mathbf{a}) \, \delta_1(\mathbf{b}) \, \delta_D(\mathbf{q} - (\mathbf{a} + \mathbf{b}))$$

$$\delta_D(\mathbf{k} - (\mathbf{p} + \mathbf{q})) \, \delta_1(\mathbf{k}_1) \, \delta_1(\mathbf{k}_2) \rangle \frac{1}{(2\pi)^3} \,, \tag{3.21}$$

where we introduced the notation

$$\int_x \cdots = \int \cdots \frac{\mathrm{d}^3 x}{(2\pi)^3} \,. \tag{3.22}$$

Therefore,

$$B_{22}(k, k_1, k_2) = \frac{1}{(2\pi)^3} \int_{a,c,q} F_2[\mathbf{c}, \mathbf{k} - (\mathbf{q} + \mathbf{c})] \, F_2(\mathbf{a}, \mathbf{q} - \mathbf{a})$$

$$\langle \delta_1(\mathbf{a}) \, \delta_1(\mathbf{c}) \, \delta_1(\mathbf{q} - \mathbf{a}) \, \delta_1[\mathbf{k} - (\mathbf{q} + \mathbf{c})] \, \delta_1(\mathbf{k}_1) \, \delta_1(\mathbf{k}_2) \rangle \,. \tag{3.23}$$

The average is computed by applying Wick's theorem for six fields. We omit the lengthy calculation here and arrive at

$$B_{22}(k, k_1, k_2) = \frac{4}{(2\pi)^3} P_{11}(k_1) \, P_{11}(k_2) \int_a [F_2(\mathbf{a}, \mathbf{k}_1) \, F_2(\mathbf{a}, -\mathbf{k}_2) + F_2(\mathbf{a}, \mathbf{k}_2) \, F_2(\mathbf{a}, -\mathbf{k}_1)] \, P_{11}(a) \,. \tag{3.24}$$

Inserting the expression for F_2 into the kernel $[\dots]$ of equation (3.24) gives

$$[\dots] = \frac{50}{49} + \frac{20}{49} \left(\mu^2 + \nu^2 \right) + \frac{8}{49} \mu^2 \nu^2 - \frac{1}{2} \mu \nu \left(\frac{a}{k_1} + \frac{k_1}{a} \right) \left(\frac{a}{k_2} + \frac{k_2}{a} \right) \,, \tag{3.25}$$

where we introduced $\mu = \mathbf{a} \cdot \mathbf{k}_1 / a k_1$ and $\nu = \mathbf{a} \cdot \mathbf{k}_2 / a k_2$. We also define $\gamma = \mathbf{k}_1 \cdot \mathbf{k}_2 / k_1 k_2$. We perform the integration in spherical coordinates, i.e. over the radial coordinate a and two angular coordinates ϕ and θ. We put the coordinate system in a way that the z-axis points into the direction of $\mathbf{k}_1$ and that $\cos \theta = \mu$. From this follows a relation between μ, ν and γ,

$$\nu = \gamma \sin \theta \cos \phi \sin \theta_{12} + \sin \theta \sin \phi \sin \theta_{12} \sin \phi_{12} + \mu \gamma \,, \tag{3.26}$$

that we need for the integration. θ_{12} and ϕ_{12} form the angles between $\mathbf{k}_1$ and $\mathbf{k}_2$. Before finally performing the integral we need to look at the last term in more detail. It can be written as

$$-\frac{1}{2} \mu \nu \left(\frac{a}{k_1} + \frac{k_1}{a} \right) \left(\frac{a}{k_2} + \frac{k_2}{a} \right) = -\frac{1}{2} \mu \nu \left(\frac{a^2}{k_1 k_2} + \frac{k_1}{k_2} + \frac{k_2}{k_1} + \frac{k_1 k_2}{a^2} \right) \,. \tag{3.27}$$

Following equation (3.16), k_1 and $k_2 \to 0$. Since the last term of equation (3.27) is of second order in k_1 and k_2, we omit it. Also, the first term on the r.h.s. will not give $\sigma_1^2(\Lambda)$, but a higher moment because of the a^2 in the numerator. We therefore also omit it, and keep only the combinations of k_1 and k_2. Inserting now equation (3.26) into equation (3.25) and performing

the integral (where we integrate over μ from -1 to 1 and over a from 0 to the cutoff Λ) we obtain

$$B_{22}(k, k_1, k_2) = \left[\frac{3832}{735} - \frac{2}{3}\gamma \left(\frac{k_1}{k_2} + \frac{k_2}{k_1} \right) + \frac{192}{2205}\gamma^2 \right] \sigma_1^2(\Lambda) \, P_{11}(k_1) \, P_{11}(k_2) \,. \tag{3.28}$$

We point out that terms of odd orders in μ vanish during the integration since we integrate over a symmetric interval.

Calculation of $B_{13}(k, k_1, k_2)$

In the framework of SPT, $B_{13}(k, k_1, k_2)$ is

$$B_{13}(k, k_1, k_2) = 2 \int_{a,b,c,p,q} \langle \delta_1(\mathbf{p}) \, F_3(\mathbf{a}, \mathbf{b}, \mathbf{c}) \, \delta_1(\mathbf{a}) \, \delta_1(\mathbf{b}) \, \delta_1(\mathbf{c})$$

$$\delta_D[\mathbf{q} - (\mathbf{a} + \mathbf{b} + \mathbf{c})] \, \delta_D[\mathbf{k} - (\mathbf{p} + \mathbf{q})] \, \delta_1(\mathbf{k}_1) \, \delta_1(\mathbf{k}_2) \rangle \frac{1}{(2\pi)^3}$$

$$= \frac{2}{(2\pi)^3} \int_{a,c,q} F_3[\mathbf{a}, \mathbf{b}, \mathbf{q} - (\mathbf{a} + \mathbf{b})] \, \langle \delta_1(\mathbf{a}) \, \delta_1(\mathbf{c}) \, \delta_1(\mathbf{q} - \mathbf{a}) \, \delta_1[\mathbf{k} - (\mathbf{q} + \mathbf{c})] \, \delta_1(\mathbf{k}_1) \, \delta_1(\mathbf{k}_2) \rangle$$

$$= \frac{6}{(2\pi)^3} P_{11}(k_1) \, P_{11}(k_2) \int_a \left[F_3(\mathbf{a}, -\mathbf{a}, \mathbf{k}_1) + F_3(\mathbf{a}, -\mathbf{a}, \mathbf{k}_2) \right.$$

$$+ 2 F_3(\mathbf{a}, -\mathbf{k}_1, -\mathbf{k}_2) \Big] \, P_{11}(a) \,. \tag{3.29}$$

From the definition of F_3 (e.g. Carrasco et al., 2014) we find $F_3(\mathbf{a}, -\mathbf{a}, \mathbf{k}_1) = F_3(\mathbf{a}, -\mathbf{a}, \mathbf{k}_2) = 0$ so that only the last term remains of interest. We examine this term in more detail,

$$F_3(\mathbf{a}, -\mathbf{k}_1, -\mathbf{k}_2) = \frac{G_2(\mathbf{a}, -\mathbf{k}_1)}{|\mathbf{a} - \mathbf{k}_1|^2} \left[\frac{-2K^2}{54} \frac{\mathbf{k}_2 \cdot (\mathbf{a} - \mathbf{k}_1)}{k_2^2} + \frac{7}{54} \mathbf{K} \cdot (\mathbf{a} - \mathbf{k}_1) \right]$$

$$+ \frac{G_2(\mathbf{a}, -\mathbf{k}_2)}{|\mathbf{a} - \mathbf{k}_2|^2} \left[\frac{-2K^2}{54} \frac{\mathbf{k}_1 \cdot (\mathbf{a} - \mathbf{k}_2)}{k_1^2} + \frac{7}{54} \mathbf{K} \cdot (\mathbf{a} - \mathbf{k}_2) \right]$$

$$+ \frac{7}{54} \mathbf{K} \cdot \left[\frac{\mathbf{a}}{a} F_2(\mathbf{k}_1, \mathbf{k}_2) - \frac{\mathbf{k}_1}{k_1} F_2(\mathbf{a}, -\mathbf{k}_2) - \frac{\mathbf{k}_2}{k_2} F_2(\mathbf{a}, -\mathbf{k}_1) \right]$$

$$- \frac{G_2(\mathbf{k}_1, \mathbf{k}_2)}{|\mathbf{k}_1 + \mathbf{k}_2|^2} \left[\frac{2K^2}{54} \frac{\mathbf{a} \cdot (\mathbf{k}_1 + \mathbf{k}_2)}{a^2} + \frac{7}{54} \mathbf{K} \cdot (\mathbf{k}_1 + \mathbf{k}_2) \right]$$

$$\equiv t_1 + t_2 + t_3 + t_4 \,, \tag{3.30}$$

with $\mathbf{K} = \mathbf{a} - (\mathbf{k}_1 + \mathbf{k}_2)$. We will evaluate the four different terms t_i, each written in one line, separately, where the first and second line have the same shape, just with exchanged $\mathbf{k}_1$ and $\mathbf{k}_2$. The last line, t_4, we can write as

$$t_4 = \frac{G_2(\mathbf{k}_1, \mathbf{k}_2)}{k^2} \left[\frac{2}{54} \left(ak\beta + 2k^2\beta^2 + \frac{k^3\beta}{a} \right) + \frac{7}{54} \left(ak\beta + k^2 \right) \right] \,, \tag{3.31}$$

where $\beta = \mathbf{a} \cdot \mathbf{k}/ak$. All terms of odd order in β will vanish during the integration, so the expression simplifies,

$$t_4 = \left[\frac{4}{54}\beta^2 + \frac{7}{54} \right] \left[\frac{3}{7} + \frac{1}{2} \left(\frac{k_1}{k_2} + \frac{k_2}{k_1} \right) \gamma + \frac{4}{7}\gamma^2 \right] \,. \tag{3.32}$$

We now turn to t_3, and omit terms of odd order in μ, ν or multiplicative combinations of those. We obtain

$$t_3 = \frac{5}{18} + \frac{1}{27}\left(\mu^2 + \nu^2\right) + \frac{7}{108}\mu\nu\left(\frac{k_1}{k_2} + \frac{k_2}{k_1}\right) + \gamma\left[\frac{17}{108}\left(\frac{k_1}{k_2} + \frac{k_2}{k_1}\right) + \frac{1}{27}\left(\frac{k_1}{k_2}\mu^2 + \frac{k_2}{k_1}\nu^2\right)\right] + \frac{1}{27}\gamma^2 . \quad (3.33)$$

The terms t_1 and t_2 are more complicated. To make progress with the calculation, we need to Taylor-expand the prefactor up until second order in $\mathbf{k}_i$,

$$\frac{1}{|\mathbf{a} - \mathbf{k}_1|^2} = \frac{1}{a^2} - \frac{2\mu k_1}{a^3} + (4\mu^2 - 1)\frac{k_1^2}{a^4} + O\left(k_1^3\right) , \quad (3.34)$$

and

$$\frac{1}{|\mathbf{a} - \mathbf{k}_2|^2} = \frac{1}{a^2} - \frac{2\nu k_2}{a^3} + (4\nu^2 - 1)\frac{k_2^2}{a^4} + O\left(k_2^3\right) . \quad (3.35)$$

This is justified since the procedure is designed to work in the limit $\mathbf{k}_i \to 0$. After expanding, we can simplify the terms further. This is now straightforward, but very lengthy. Many terms appear, but a lot of them can be cancelled due to three different reasons: (i) Again they are of odd order in μ or ν, (ii) they are of order higher than one in $\mathbf{k}_i$ and therefore small compared to the first-order terms, or (iii) they are of order different than zero in a and therefore do not contribute to $\sigma_1^2(\Lambda)$ after integration. Calculating both t_1 and t_2 gives

$$t_1 + t_2 = \frac{1}{9} + \frac{11}{108}\mu\nu\left(\frac{k_1}{k_2} + \frac{k_2}{k_1}\right) + \frac{20}{189}\left(\mu^2 + \nu^2\right) - \frac{4}{63}\mu^2\nu^2$$
$$+ \left[\frac{4}{189}\left(\frac{k_1}{k_2}\mu^2 + \frac{k_2}{k_1}\nu^2\right) + \frac{1}{63}\left(\frac{k_1}{k_2} + \frac{k_2}{k_1}\right) + \frac{4}{27}\mu\nu\right]\gamma . \quad (3.36)$$

We are now in the position to add the t_i and, inserting everything into equation (3.29), perform the integration as for $B_{22}(k, k_1, k_2)$. We end up with

$$B_{13}(k, k_1, k_2) = \left[\frac{688}{105} + \frac{82}{21}\gamma\left(\frac{k_1}{k_2} + \frac{k_2}{k_1}\right) + \frac{314}{945}\gamma^2\right]\sigma_1^2(\Lambda)\,P_{11}(k_1)\,P_{11}(k_2) . \quad (3.37)$$

Calculation of $R_1(k, k_1, k_2)$

We write $R_1(k, k_1, k_2)$ as

$$R_1(k, k_1, k_2) = \int_{a,b} \left\langle \delta_1(\mathbf{a})\,\delta_1(\mathbf{b})\,F_2(\mathbf{a}, \mathbf{b})\,\delta_D[\mathbf{k} - (\mathbf{a} + \mathbf{b})]\,\delta_1(\mathbf{k}_1)\,\delta_1(\mathbf{k}_2)\right\rangle \frac{1}{(2\pi)^3}$$
$$= \int_a F_2(\mathbf{a}, \mathbf{k} - \mathbf{a})\left\langle \delta_1(\mathbf{a})\,\delta_1(\mathbf{k} - \mathbf{a})\,\delta_1(\mathbf{k}_1)\,\delta_1(\mathbf{k}_2)\right\rangle \frac{1}{(2\pi)^3}$$
$$= 2\,F_2(\mathbf{k}_1, \mathbf{k}_2)\,P_{11}(k_1)\,P_{11}(k_2)$$
$$= \left[\frac{10}{7} + \left(\frac{k_1}{k_2} + \frac{k_2}{k_1}\right)\gamma + \frac{4}{7}\gamma^2\right]P_{11}(k_1)\,P_{11}(k_2) . \quad (3.38)$$

Complete expression for $B^{(\text{NLO})}_{[\delta^2]_1 \delta_1 \delta_1}(k, k_1, k_2)$

Adding the results for $B_{22}(k, k_1, k_2)$, $B_{13}(k, k_1, k_2)$ and $R_1(k, k_1, k_2)$, following equation 3.17, we find

$$B^{(\text{NLO})}_{[\delta^2]_1 \delta_1 \delta_1}(k, k_1, k_2) = \left[\frac{5248}{735} + \frac{508}{2205}\gamma^2 \right] \sigma^2(\Lambda)\, P_{11}(k_1)\, P_{11}(k_2). \tag{3.39}$$

Note that the expression consists of a purely γ-dependent prefactor, multiplied with $P_{11}(k_1)\, P_{11}(k_2)$. The UV sensitivity is contained within this prefactor which does not go to zero for $k_1, k_2 \to 0$. Therefore, it must be subtracted at all finite k_1 and k_2 in form of a counter term,

$$\lim_{k'_1, k'_2 \to 0} \left\{ \frac{B^{(\text{NLO})}_{[O]_1 \delta_1 \delta_1}\left[k(\gamma), k'_1, k'_2 \right]}{P_{11}(k'_1)\, P_{11}(k'_2)} \right\} P_{11}(k_1)\, P_{11}(k_2), \tag{3.40}$$

where $\gamma = [k^2 - (k_1^2 + k_2^2)]/(2k_1 k_2)$. This expression is analogous to e.g. our equation (31) in W19. From equation (3.39) follows the renormalisation of δ^2 at second order,

$$[\delta^2]_2 = \delta^2 - \sigma^2(\Lambda)\left[1 + \frac{68}{21}\delta + \frac{2869}{735}\delta^2 + \frac{254}{2205}s^2 \right]. \tag{3.41}$$

We therefore confirm the result by A14. An analogous calculation can be performed for s^2.

3.3 Measuring the bispectrum

In this section, we show how we measure the bispectra from the simulations, and present the data. For the physical and numerical details on our suite of 40 DM-only simulations, we refer the reader to our previous work W19.

For measuring the overdensity fields $\delta_{\text{h}}(\mathbf{x})$ and $\delta(\mathbf{x})$ on a grid, we employ a 'cloud in cell' (CIC) interpolation method. At a redshift of $z = 0$, we start from the positions of the DM particles and the haloes, respectively, in the simulation box of side length $L = 1200\, h^{-1}$ Mpc, and arrive at a regular Cartesian mesh with $N_{\text{g}} = 256$ cells on each grid side. We correct for the mass assignment scheme, and then use the fast-Fourier-transform (FFT) algorithm to compute $\delta_{\text{h}}(\mathbf{k})$ and $\delta(\mathbf{k})$. We apply low-pass smoothing by multiplying the fields in Fourier space with the window function $W(k)$ for three values of $\Lambda = \{0.05, 0.1, 0.2\}\, h\, \text{Mpc}^{-1}$, and then use spectral methods to compute $s_{ij}(\mathbf{k})$ and $\nabla^2 \delta(\mathbf{k})$. After transforming the fields back to real space, we obtain $\delta^2(\mathbf{x})$, $s^2(\mathbf{x})$ and $\nabla^2 \delta(\mathbf{x})$.

From these fields, the bispectrum, in principle, is computed as

$$B_{\delta\delta\delta}(\mathbf{k}, \mathbf{k}_1, \mathbf{k}_2) = \frac{1}{(2\pi)^3 N_\Delta} \sum_{n \in \Delta} \delta(\mathbf{k})\, \delta(\mathbf{k}_1)\, \delta(\mathbf{k}_2), \tag{3.42}$$

where Δ is the set of triangles with side lengths $\{\mathbf{k}, \mathbf{k}_1, \mathbf{k}_2\}$ with $\mathbf{k} + \mathbf{k}_1 + \mathbf{k}_2 = 0$, and N_Δ is their number. However, computing the bispectrum in this way involves nested loops, which numerically results in a very time-consuming task. Therefore, instead we use a bispectrum estimator based on FFT, developed by Scoccimarro (2015) and Watkinson et al. (2017), and implemented in the code of Alkhanishvili (2018), which reduces the number of loops that must
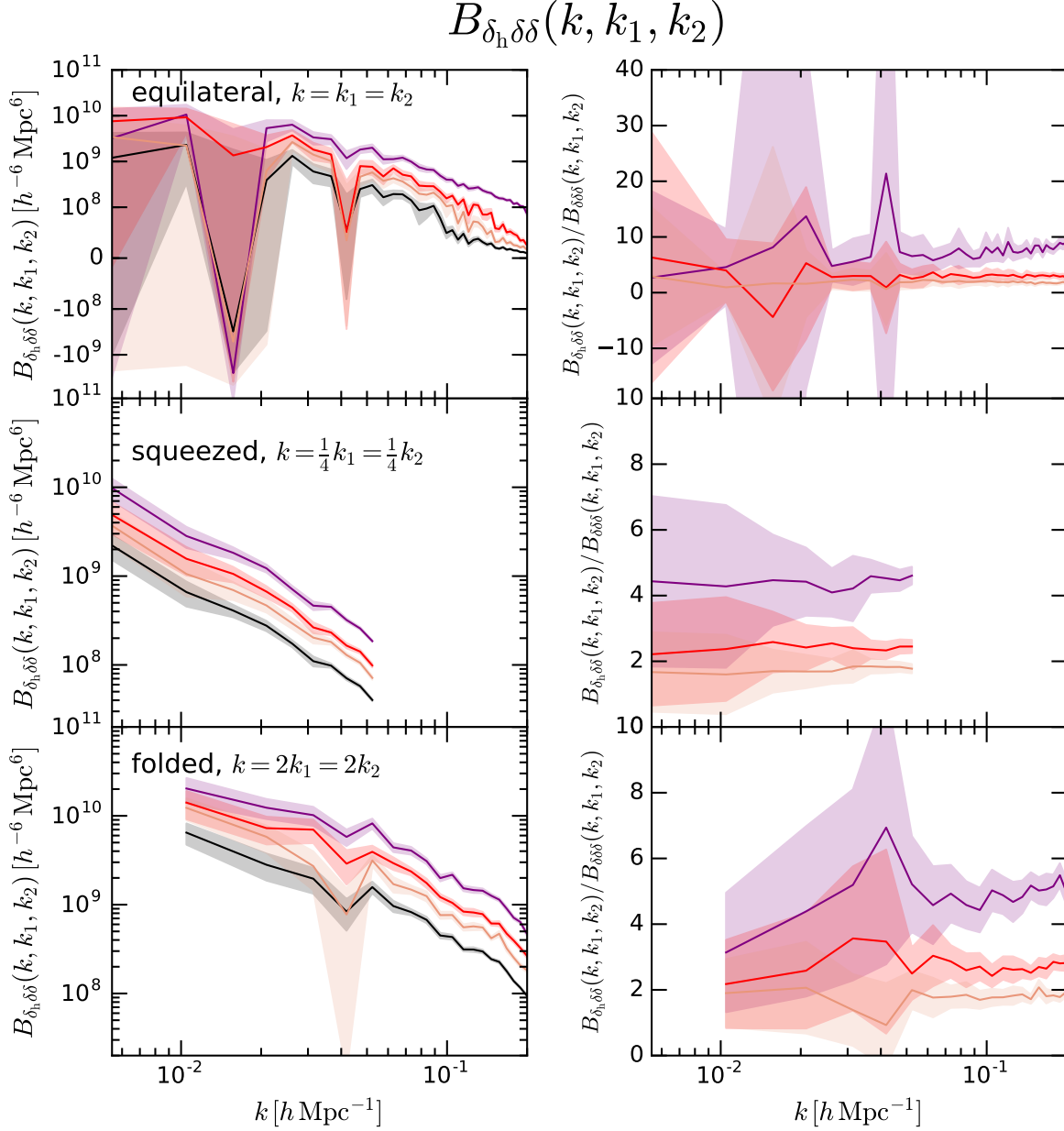
Figure 3.1: The halo-matter cross bispectra $B_{\delta_h\delta\delta}(k, k_1, k_2)$ and the matter bispectrum $B_{\delta\delta\delta}(k, k_1, k_2)$, averaged over the 40 simulations (left column). Shaded regions represent the standard error of the mean. We show the halo-matter cross bispectrum for the three different halo mass bins (light-brown, red, purple, in order of increasing mean mass of the halo mass bin) and the matter bispectrum in black. The different rows represent three different triangle configurations with fixed ratio between k, k_1 and k_2 (equilateral, squeezed and folded triangles, as indicated in the respective panel), where k is the running variable. In the right column we show the ratio $B_{\delta_h\delta\delta}(k, k_1, k_2)/B_{\delta\delta\delta}(k, k_1, k_2)$ for the same triangle configurations. Note the symmetrically logarithmic scaling on the y-axis for the top left panel.
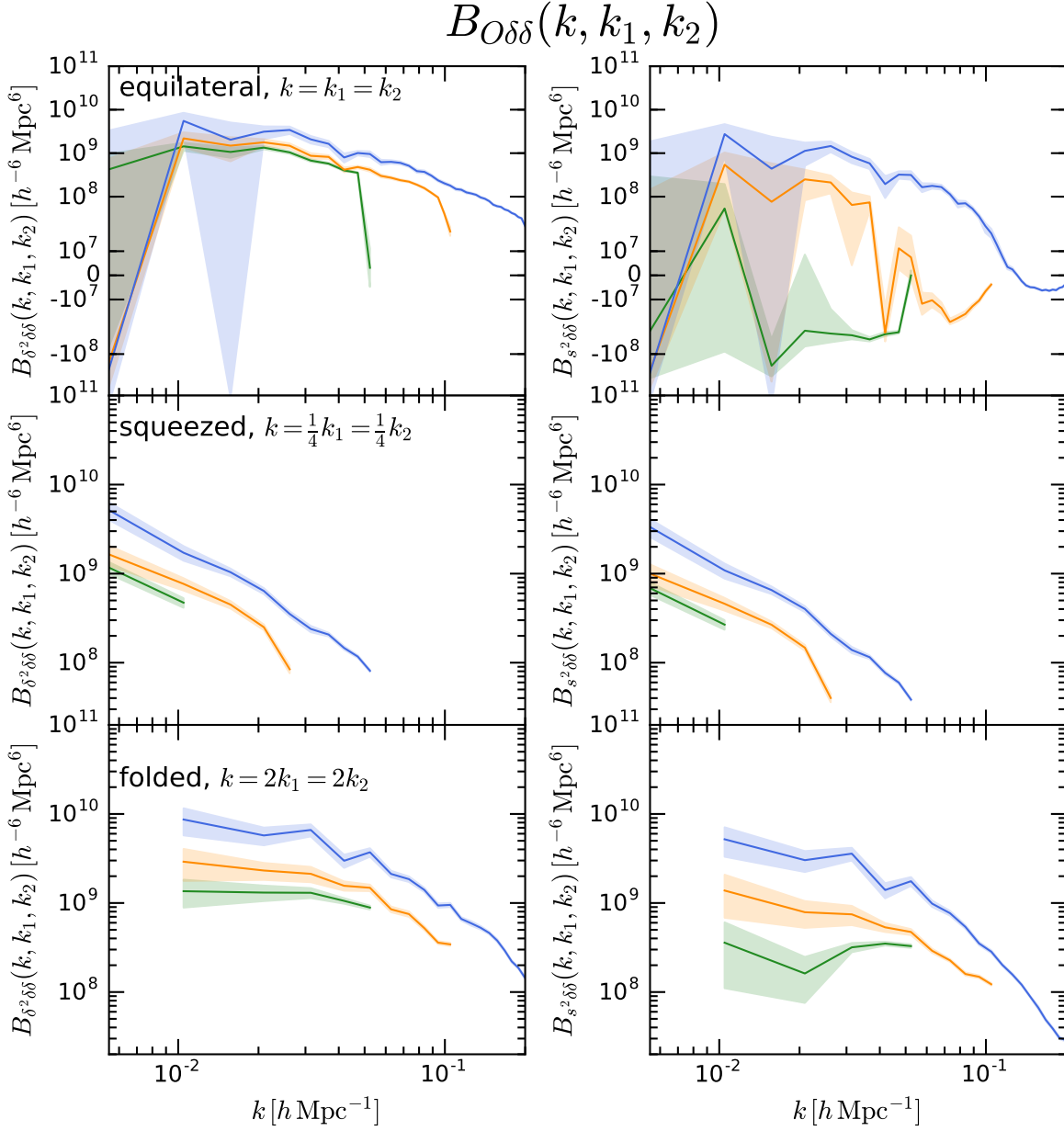
Figure 3.2: The cross bispectra between δ^2 and s^2 and the matter density field, $B_{\delta^2\delta\delta}(k, k_1, k_2)$ and $B_{s^2\delta\delta}(k, k_1, k_2)$ (left and right column, respectively), averaged over the 40 simulations. Shaded regions represent the standard error of the mean. We show the measurements for the same triangle configurations as in Fig. 3.1. The different colours represent the different cutoff scales Λ that were used to smooth the fields (with $\Lambda = 0.05$, 0.1 and $0.2\,h\,\mathrm{Mpc}^{-1}$ coloured in green, orange and blue). Note the symmetrically logarithmic scaling on the y-axis for the first row.

be computed. The estimator is written as

$$B(\mathbf{k}, \mathbf{k}_1, \mathbf{k}_2) \approx \frac{V^2}{N_{\mathrm{pix}}^3} \frac{\sum_{\mathbf{n}}^{N_{\mathrm{pix}}} \delta(\mathbf{n}, \mathbf{k})\, \delta(\mathbf{n}, \mathbf{k}_1)\, \delta(\mathbf{n}, \mathbf{k}_2)}{\sum_{\mathbf{n}}^{N_{\mathrm{pix}}} I(\mathbf{n}, \mathbf{k})\, I(\mathbf{n}, \mathbf{k}_1)\, I(\mathbf{n}, \mathbf{k}_2)} \,, \tag{3.43}$$

where $V = L^3$ and $N_{\mathrm{pix}} = N_{\mathrm{g}}^3$. Furthermore, we define

$$\delta(\mathbf{n}, \mathbf{k}_i) = \sum_{\mathbf{I}_i \pm s/2} \delta_{\mathrm{FFT}}(\mathbf{m}_i)\, e^{2\pi i\, \mathbf{n}\cdot\mathbf{m}_i/N_{\mathrm{g}}} \,, \tag{3.44}$$

$$I(\mathbf{n}, \mathbf{k}_i) = \sum_{\mathbf{I}_i \pm s/2} e^{2\pi i\, \mathbf{n}\cdot\mathbf{m}_i/N_{\mathrm{g}}} \,, \tag{3.45}$$

with $\mathbf{I}_i = |\mathbf{k}_i/k_{\mathrm{f}} - \mathbf{m}_i|$. It is $k_{\mathrm{f}} = 2\pi/L$ the fundamental frequency, so that $\mathbf{k}_i = k_{\mathrm{f}}\, \mathbf{m}_i$, s is the bin width, and

$$\delta_{\mathrm{FFT}}(\mathbf{m}_i) = \sum_{\mathbf{n}} \delta(\mathbf{n})\, e^{2\pi i\, \mathbf{n}\cdot\mathbf{m}_i/N_{\mathrm{g}}} \,, \tag{3.46}$$

where $\mathbf{x} = \mathbf{n}L/N_{\mathrm{g}}$. To build a cross bispectrum from various fields, we just need to replace one or more of the functions on the r.h.s. of equation (3.43) with the respective operator. We bin the bispectra in $\{10, 20, 40\}$ bins of bin width k_{f} for each side of the triangle for $\Lambda = 0.05, 0.1, 0.2\, h\,\mathrm{Mpc}^{-1}$.

In Fig. 3.1 we show the halo-matter cross bispectrum $B_{\delta_{\mathrm{h}}\delta\delta}(k, k_1, k_2)$ and the matter bispectrum $B_{\delta\delta\delta}(k, k_1, k_2)$, averaged over the 40 simulations for three exemplary triangle configurations. In the left column we plot them separately, and in the right column we plot the ratio. Each line represents a certain triangle configuration with fixed ratio between k, k_1 and k_2. We plot the bispectrum value of the respective configuration and choose k as the independent variable. In the first line we focus on the equilateral configuration, where all triangle sides have the same length, $k = k_1 = k_2$. The second line shows a squeezed configuration, where in general $k_1 \simeq k_2 \gg k$, and we choose the explicit configuration $k = 1/4k_1 = 1/4k_2$. Finally, in the third line, we plot the folded configuration where $k = 2k_1 = 2k_2$. The shaded regions indicate the standard error of the mean over the 40 simulations. As a general trend we find that $B_{\delta_{\mathrm{h}}\delta\delta}(k, k_1, k_2)$ behaves similarly as $B_{\delta\delta\delta}(k, k_1, k_2)$. The larger the mean mass of the halo bin (for the exact values see W19), the stronger is the signal of the halo-matter cross bispectrum for all k. Note the fluctuations of the signal between positive and negative values for some k, where also the errors are large. This behaviour is symptomatic of noise.

Fig. 3.2 shows the cross bispectra of δ^2 and s^2 with the matter, $B_{\delta^2\delta\delta}(k, k_1, k_2)$ (left column) and $B_{s^2\delta\delta}(k, k_1, k_2)$ (right column). Plotted are the spectra of the same triangle configurations as in Fig. 3.1 for three values of Λ. Blue colour indicates $\Lambda = 0.2\, h\,\mathrm{Mpc}^{-1}$, orange $\Lambda = 0.1\, h\,\mathrm{Mpc}^{-1}$, and green represents $\Lambda = 0.05\, h\,\mathrm{Mpc}^{-1}$. Unless stated otherwise, from now on, in this paper this colouring scheme will always indicate the presentation of data for these three values of Λ, so we will not mention it explicitly anymore. We find that the larger Λ is, the stronger is the overall signal for all k. In particular, the spectra approach a Λ-dependent constant for $k \to 0$. From this, we clearly find that the bispectra are UV-sensitive.

3.4 Renormalisation in simulations

We want to build a procedure to eliminate the UV-sensitivity on large scales. In the PT calculations, this is given by equation (3.40). In the simulations, to obtain the renormalised bispectra $B_{[\delta^2]_2\delta\delta}(k, k_1, k_2)$ and $B_{[s^2]_2\delta\delta}(k, k_1, k_2)$, we therefore need to compute

$$B_{[O]_2\delta\delta}(k, k_1, k_2) = B_{[O]_1\delta\delta}(k, k_1, k_2) - \left\{ \frac{B^{(\text{NLO})}_{[O]_1\delta_1\delta_1}[k(\gamma), k_{\min}, k_{\min}]}{P_{11}(k_{\min}) P_{11}(k_{\min})} \right\} P_{11}(k_1) P_{11}(k_2)$$

$$\equiv B_{[O]_1\delta\delta}(k, k_1, k_2) - f_O(\gamma) P_{11}(k_1) P_{11}(k_2),\tag{3.47}$$

where, following equations (3.15) and (3.17),

$$B_{[O]_1\delta\delta}(k, k_1, k_2) = B_{O\delta\delta}(k, k_1, k_2) - \alpha_O B_{\delta\delta\delta}(k, k_1, k_2),\tag{3.48}$$

and

$$B_{[O]_1\delta_1\delta_1}(k, k_1, k_2) = B_{O\delta_1\delta_1}(k, k_1, k_2) - \alpha_O B_{\delta\delta_1\delta_1}(k, k_1, k_2).\tag{3.49}$$

Furthermore, to obtain $f_O(\gamma)$, we compute

$$B^{(\text{NLO})}_{[O]_1\delta_1\delta_1}(k, k_1, k_2) = B_{[O]_1\delta_1\delta_1}(k, k_1, k_2) - B^{(\text{LO})}_{[O]_1\delta_1\delta_1}(k, k_1, k_2)$$

$$= B_{[O]_1\delta_1\delta_1}(k, k_1, k_2) - B_{O_1\delta_1\delta_1}(k, k_1, k_2),\tag{3.50}$$

under the assumption that $B_{[O]_1\delta_1\delta_1}(k, k_1, k_2)$ is dominated by first- and second-order terms, and higher-order terms are negligible. Note that when introducing $f_O(\gamma)$ in equation (3.47) we are using an ansatz, i.e. we assume that the SPT result which depends only on γ (equation 3.39) holds also in the simulations. To compute $f_O(\gamma)$, we use the triangle configurations with the smallest values for k_1 and k_2, calculate $\gamma = [k^2 - (k_1^2 + k_2^2)]/(2k_1 k_2)$ and then bin $B^{(\text{NLO})}_{[O]_1\delta_1\delta_1}(k, k_1, k_2)$ in that. We use the configurations $\{k_1, k_2, k\} = \{\{211\}, \{111\}, \{122\}, \{223\}, \{112\}\}$ in units of k_f and in order of increasing $\gamma = [-1, 1]$. Note that we do not only include triangles with $\{k_1, k_2\} = k_{\min} = k_f$, but also those with $\{k_1, k_2\} = 2k_{\min}$ to improve the quality of $f_O(\gamma)$. We obtain $f_O(\gamma)$ separately for each simulation and then, to calculate the complete counter term $f_O(\gamma) P_{11}(k_1) P_{11}(k_2)$ for a fixed triangle configuration, we loop over k, k_1 and k_2, and interpolate $f_O(\gamma)$ to obtain the respective value.

3.4.1 First-order renormalisation

To give an impression of the influence of the first-order renormalisation on the bispectrum level, in Fig. 3.3, we plot $\alpha_{\delta^2} B_{\delta\delta\delta}(k, k_1, k_2)$ (left) and $\alpha_{s^2} B_{\delta\delta\delta}(k, k_1, k_2)$ (right), i.e. the second term on the r.h.s. of equation (3.48), using the same triangle configurations as in Fig. 3.2. We find that the overall amplitude changes with Λ, however the shape in k is the same for all cutoff scales. This is expected from theoretical considerations: For the calculation of $B_{\delta\delta\delta}(k, k_1, k_2)$ no integrals, which introduce small-scale power to the result and are usually cut off at an arbitrary value, are needed. Therefore, this spectrum is not affected by the cutoff. The change in normalization with Λ is fully attributed to α_O. We then show the effect of the first-order renormalisation on the full cross bispectrum in Fig. 3.4 where we plot $B_{[\delta^2]_1\delta\delta}(k, k_1, k_2)$ and $B_{[s^2]_1\delta\delta}(k, k_1, k_2)$. Overall, the value of the spectra slightly decreases, but the change in shape is only minor.
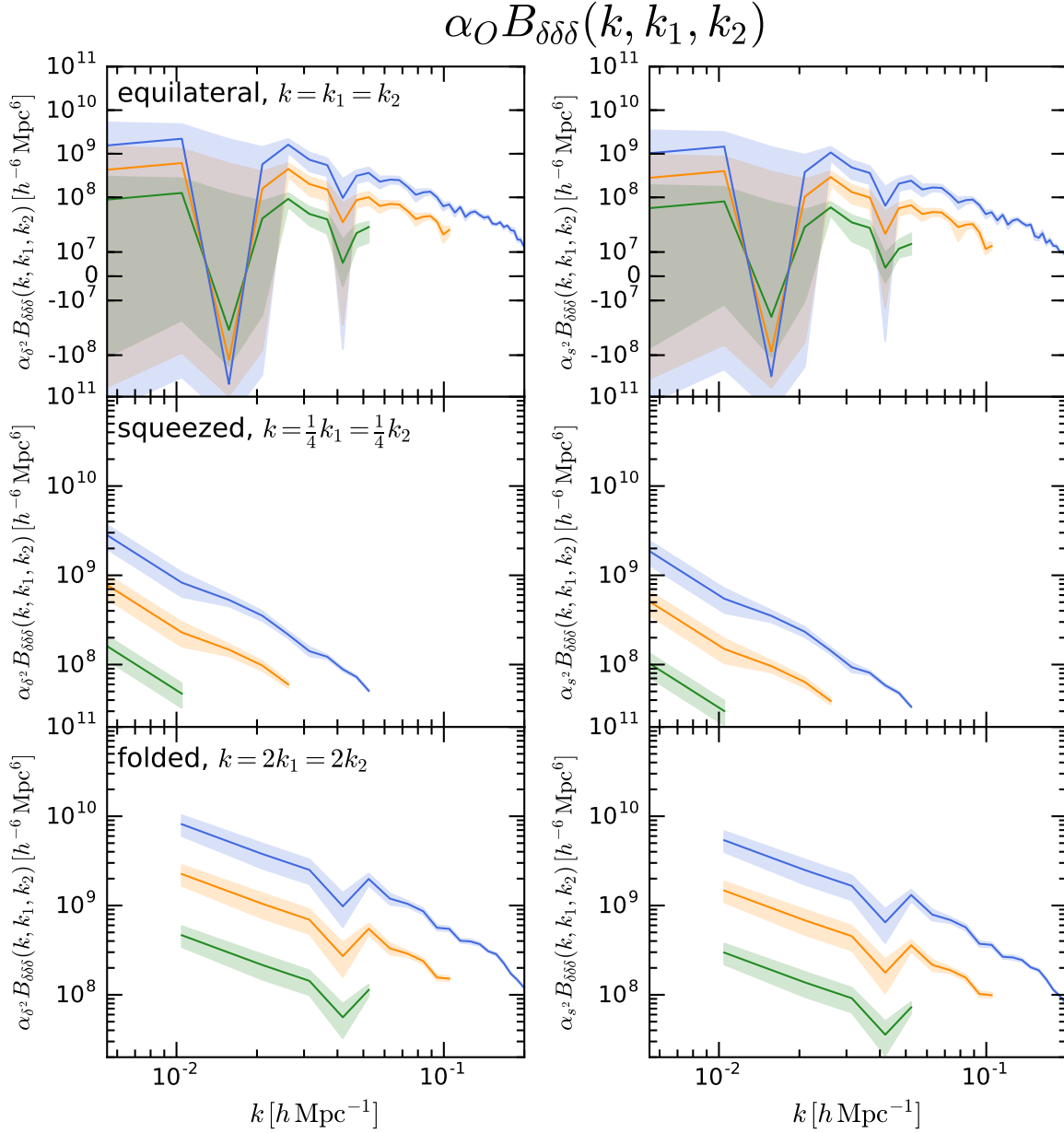
Figure 3.3: The same as Fig. 3.2, but for the first-order renormalisation term $\alpha_{\delta^2} B_{\delta\delta\delta}(k, k_1, k_2)$ and $\alpha_{s^2} B_{\delta\delta\delta}(k, k_1, k_2)$.

In Fig. 3.5 we show the cross bispectrum of $[\delta^2]_1$ and $[s^2]_1$ with the linear density field, $B_{[\delta^2]_1 \delta_1 \delta_1}(k, k_1, k_2)$ and $B_{[s^2]_1 \delta_1 \delta_1}(k, k_1, k_2)$. The signal increases both for decreasing k and increasing Λ. Overall, it presents features very similar to Fig. 3.4.
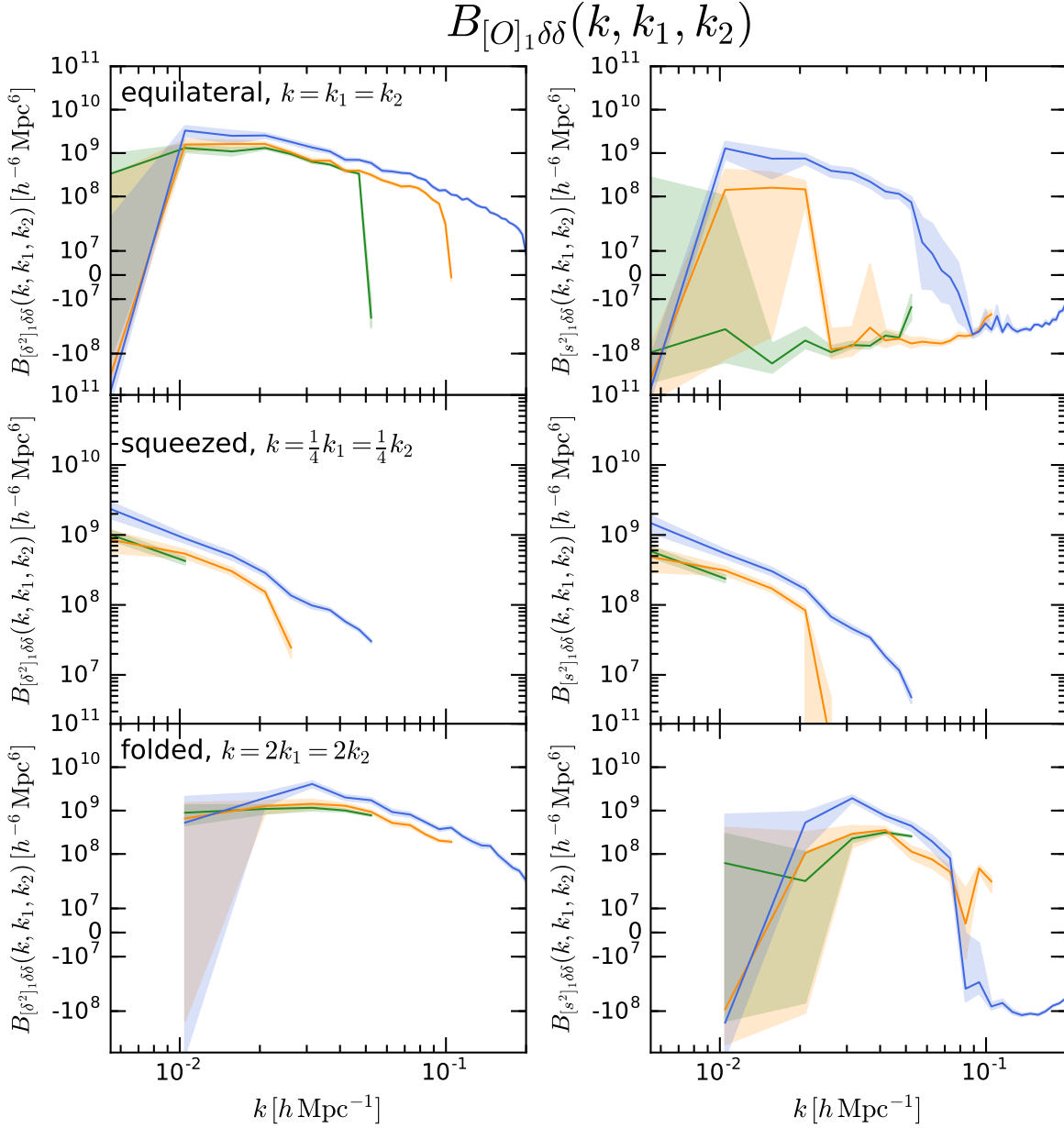
$$B_{[O]_1\delta\delta}(k, k_1, k_2)$$

Figure 3.4: The same as Fig. 3.2, but for the first-order renormalised cross bispectra of δ^2 and s^2 with the matter density field, $B_{[\delta^2]_1\delta\delta}(k, k_1, k_2)$ and $B_{[s^2]_1\delta\delta}(k, k_1, k_2)$. Note the symmetrically logarithmic scaling on the y-axis for the first and third row.

3.4.2 Second-order renormalisation

Using equation (3.50), we split $B_{[O]_1\delta_1\delta_1}(k, k_1, k_2)$ into its two contributions, $B_{[O]_1\delta_1\delta_1}^{(\text{LO})}(k, k_1, k_2)$ and $B_{[O]_1\delta_1\delta_1}^{(\text{NLO})}(k, k_1, k_2)$, and show them in Figs. 3.6 and 3.7. The LO terms in Fig. 3.6, measured from
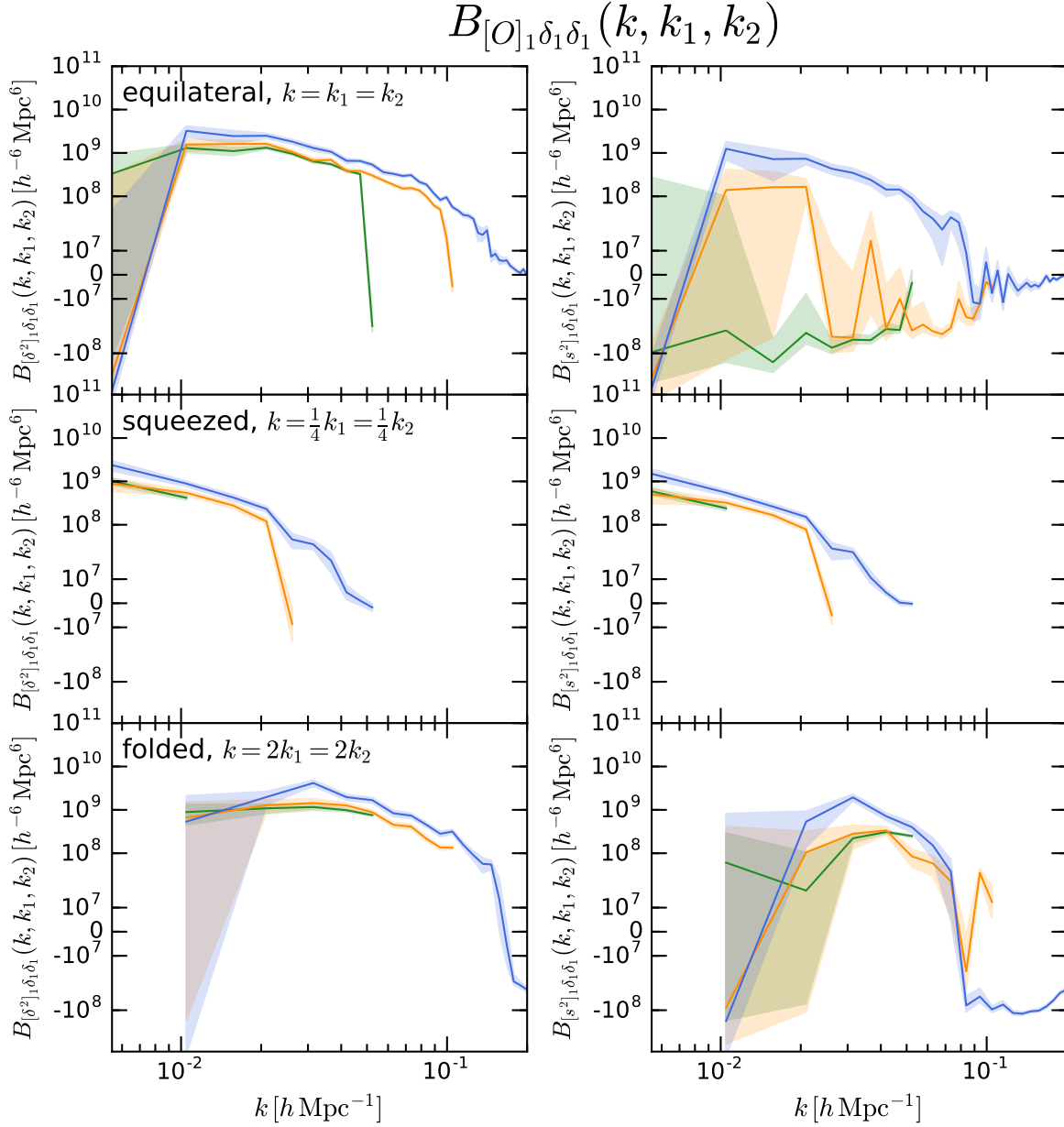
$$B_{[O]_1\delta_1\delta_1}(k, k_1, k_2)$$

Figure 3.5: The same as Fig. 3.2, but for the cross bispectra of $[\delta^2]_1$ and $[s^2]_1$ with the linear matter density field, $B_{[\delta^2]_1\delta_1\delta_1}(k, k_1, k_2)$ and $B_{[s^2]_1\delta_1\delta_1}(k, k_1, k_2)$. Note the symmetrically logarithmic scaling on the y-axis for all panels.

the simulations (solid), look similar for all values of Λ (apart from some noise), in particular the signal for $k_1, k_2 \to 0$ does not change substantially. This is expected from theoretical SPT calculations (dashed) which are computed as $B_{\delta_1^2\delta_1\delta_1}(k, k_1, k_2) = 2P_{11}(k_1)\, P_{11}(k_2)\, W(k_1)\, W(k_2)$ and $B_{s_1^2\delta_1\delta_1}(k, k_1, k_2) = 2P_{11}(k_1)\, P_{11}(k_2)\, S_2(\mathbf{k}_1, \mathbf{k}_2)\, W(k_1)\, W(k_2)$. In Fig. 3.7, $B_{[O]_1\delta_1\delta_1}^{(\text{NLO})}(k, k_1, k_2)$, however,
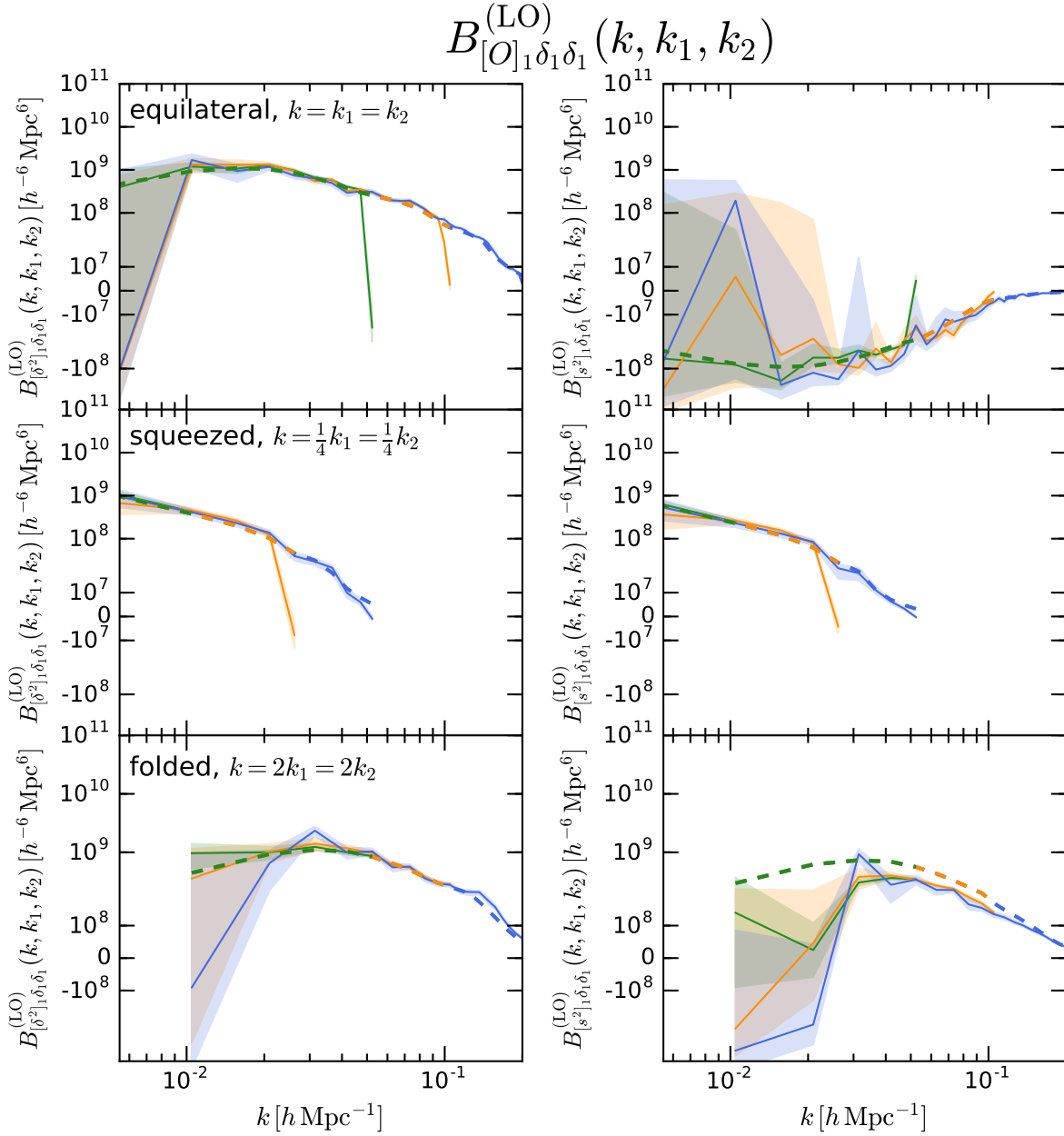
Figure 3.6: The same as Fig. 3.5, but showing only the LO terms, $B_{\delta_1^2 \delta_1}(k, k_1, k_2)$ and $B_{s_1^2 \delta_1}(k, k_1, k_2)$ (solid). We also show the theoretical results computed from SPT (dashed). Note the symmetrically logarithmic scaling on the y-axis for all panels.

is Λ-dependent, as expected both from SPT, and the way it is calculated from equation (3.50). Similar to the other cutoff-dependent quantities, the signal increases for larger values of Λ. A note is in order here: In a well-behaved expansion, a term of order $n+1$ should always contribute less to the overall result than a term of order n. Otherwise, truncating the expansion at some
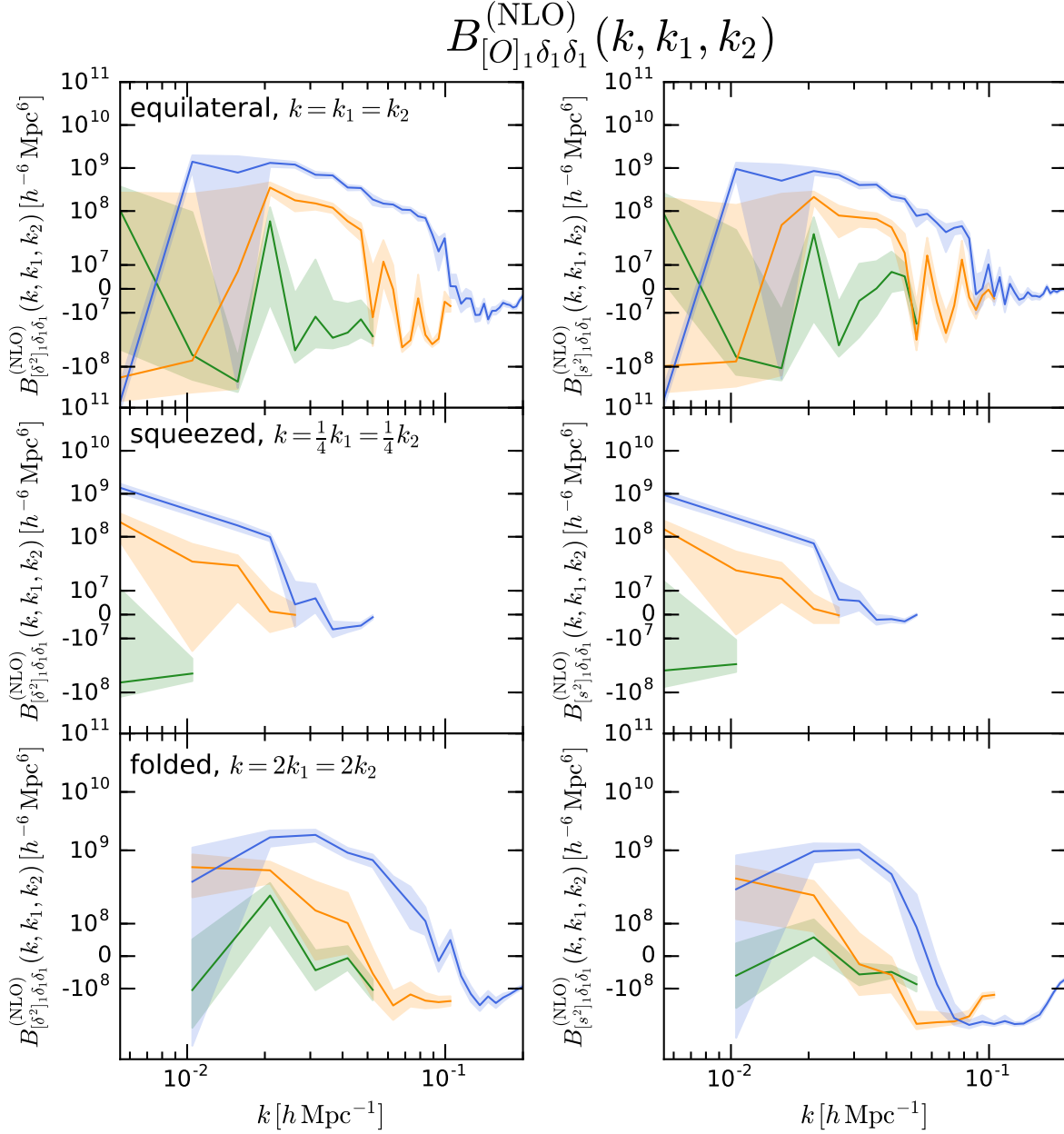
Figure 3.7: The same as Fig. 3.5, but showing only the NLO terms, $B_{[\delta^2]_1\delta_1\delta_1}(k,k_1,k_2) - B_{\delta_1^2\delta_1\delta_1}(k,k_1,k_2)$ and $B_{[s^2]_1\delta_1\delta_1}(k,k_1,k_2) - B_{s_1^2\delta_1\delta_1}(k,k_1,k_2)$. Note the symmetrically logarithmic scaling on the y-axis for all panels.

order will introduce errors and is therefore not allowed. In the case of $B_{[O]_1\delta_1\delta_1}^{(\mathrm{NLO})}(k,k_1,k_2)$, for $\Lambda = 0.2\,h\,\mathrm{Mpc}^{-1}$, however, the NLO contribution is larger than the LO one for all triangle configurations. This shows that a cutoff value of $0.2\,h\,\mathrm{Mpc}^{-1}$ is already too large to build a proper expansion. Nevertheless, we still use these data, because we want to test the renormalisaton procedure also in a case where formally the expansion is not well-behaved.
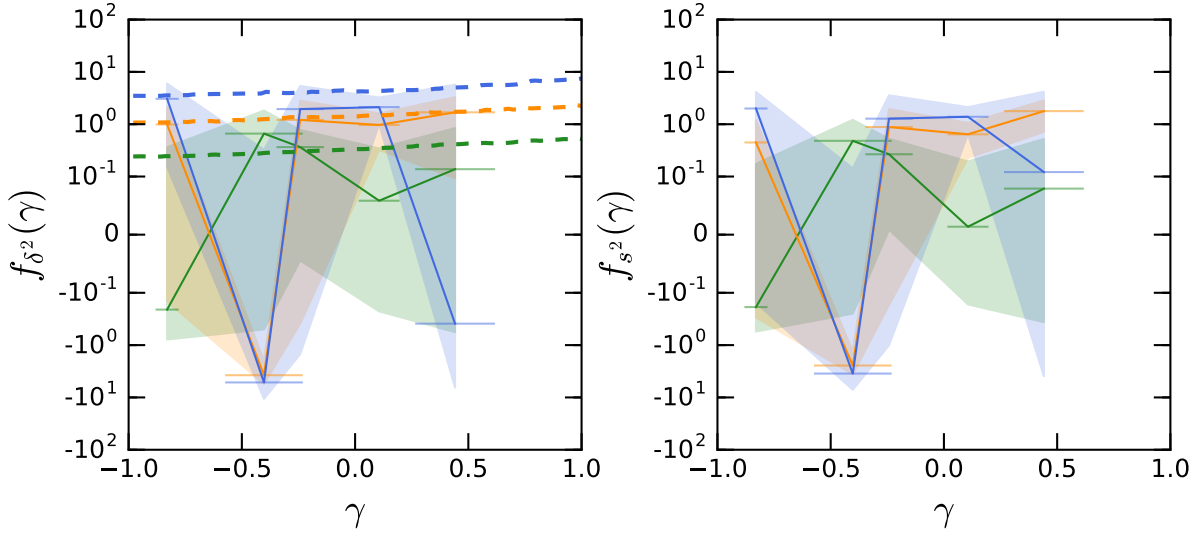
Figure 3.8: The renormalisation prefactors $f_{\delta^2}(\gamma)$ (left, solid) and $f_{s^2}(\gamma)$ (right, solid), computed as in equation (3.47), plotted over $\gamma = \mathbf{k}_1 \cdot \mathbf{k}_2/(k_1 k_2)$, the cosine of the angle between $\mathbf{k}_1$ and $\mathbf{k}_2$. We show the median of the 40 simulations. Shaded regions represent the standard error of the median. Dashed lines represent the theoretical SPT result, obtained from evaluating equations (3.21), (3.29) and (3.38) numerically, including filter functions. The horizontal position of the data points is obtained by calculating γ separately for each triangle configuration and then performing the average in each bin. Horizontal error bars indicate the standard error of the mean.

From $B^{\mathrm{(NLO)}}_{[O]_1 \delta_1 \delta_1}(k, k_1, k_2)$ and $P_{11}(k)$ (for which we used the same binning as for the bispectrum; for more details see W19), we calculate $f_O(\gamma)$, using equation (3.47). We show the results in Fig. 3.8, both for $f_{\delta^2}(\gamma)$ (left) and $f_{s^2}(\gamma)$ (right), using the median of the 40 simulations. We calculate γ separately for each triangle configuration and then plot the mean for each bin. The horizontal error bars indicate the standard error of the mean on γ over the bin. Using the median for $f_O(\gamma)$ is motivated by Fig. 3.9 which shows the probability density function (PDF) of $f_{\delta^2}(\gamma)$ (top three rows) and $f_{s^2}(\gamma)$ (bottom three rows) for each value of γ (five panels in each row, following the order of data points in Fig. 3.8) and Λ (different rows), respectively. It becomes clear that $f_O(\gamma)$ exhibits a great amount of scatter, and is prone to both negative and positive outliers. The median, therefore, is a more stable quantity than the mean, and better represents the true value of $f_O(\gamma)$. Shaded regions indicate the standard error of the median which is computed as 1.2533 times the standard error of the mean. Additionally, in Fig. 3.8, for $f_{\delta^2}(\gamma)$ we also plot the theoretical SPT result that was obtained by evaluating equations (3.21), (3.29) and (3.38) numerically, including filter functions (dashed lines). We find that for $\Lambda = 0.05 \, h \, \mathrm{Mpc}^{-1}$ the measurements agree with the theory. The errors, however, are large, which indicates that for a precise measurement of $f_O(\gamma)$ even more simulations are needed. For $\Lambda = 0.1$ and $0.2 \, h \, \mathrm{Mpc}^{-1}$ the signal is more unstable, but still in acceptable agreement with the theory for some values of γ. It is unclear at that point whether the data points with negative values originate from a too small number of simulations, or whether the break-down of SPT plays a role at these cutoff scales.

Finally, in Fig. 3.10 we show the second-order renormalised cross bispectra $B_{[\delta^2]_2 \delta \delta}(k, k_1, k_2)$ and $B_{[s^2]_2 \delta \delta}(k, k_1, k_2)$, obtained from equation (3.47). We find that the signal for $\Lambda = 0.05 \, h \, \mathrm{Mpc}^{-1}$ does
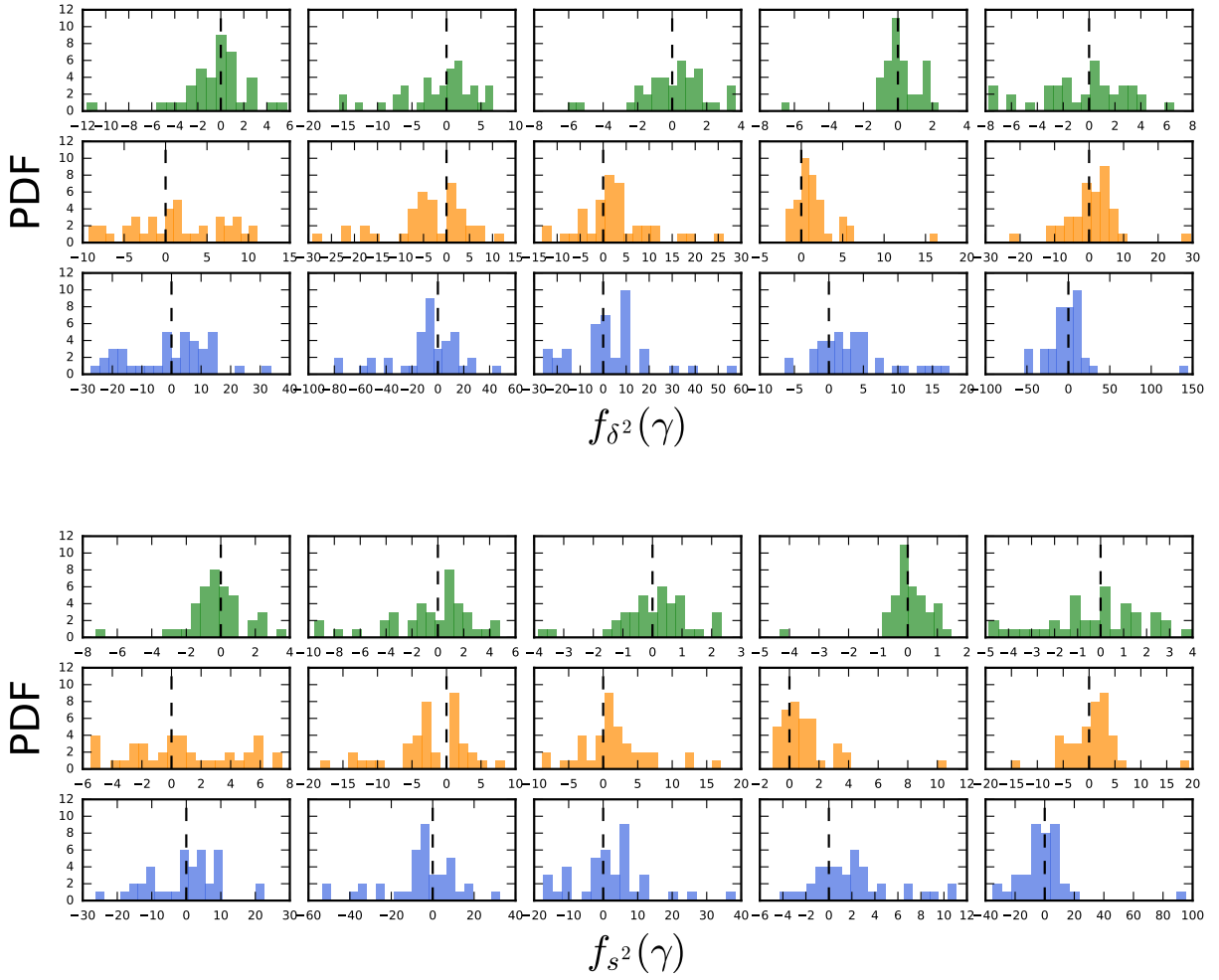
Figure 3.9: The PDF of $f_{\delta^2}(\gamma)$ (top three rows) and $f_{s^2}(\gamma)$ (bottom three rows) of the 40 simulations for the five bins of γ from Fig. 3.8 (from left to right).

not change substantially in comparison to the first-order renormalised bispectrum. The overall amplitude decreases slightly, but the spectrum still presents large, positive values in almost all cases. For $\Lambda = 0.1$ and $0.2\,h\,\mathrm{Mpc}^{-1}$, however, the spectra become completely negative and now show a flatter shape than before. This behaviour is consistent with what we found for Fig. 3.8: Also for $f_{\delta^2}(\gamma)$ and $f_{s^2}(\gamma)$ the two larger cutoffs give a similar measurement, whereas the one for $\Lambda = 0.05\,h\,\mathrm{Mpc}^{-1}$ differs. These results can be explained in the context of Figs. 3.6 and 3.7: We already pointed out that in particular for $\Lambda = 0.2\,h\,\mathrm{Mpc}^{-1}$ the NLO terms show an overall larger signal than the LO terms, which should not happen when writing an expansion. Additionally, also for $\Lambda = 0.1\,h\,\mathrm{Mpc}^{-1}$ the NLO results are similar to the LO ones which can lead to the same problems. This suggests that when measuring the bispectrum at $z = 0$, the analysis must be restricted to cutoff scales $\Lambda < 0.1\,h\,\mathrm{Mpc}^{-1}$. For these scales, $B_{O\delta\delta}(k, k_1, k_2)$ is dominated by the
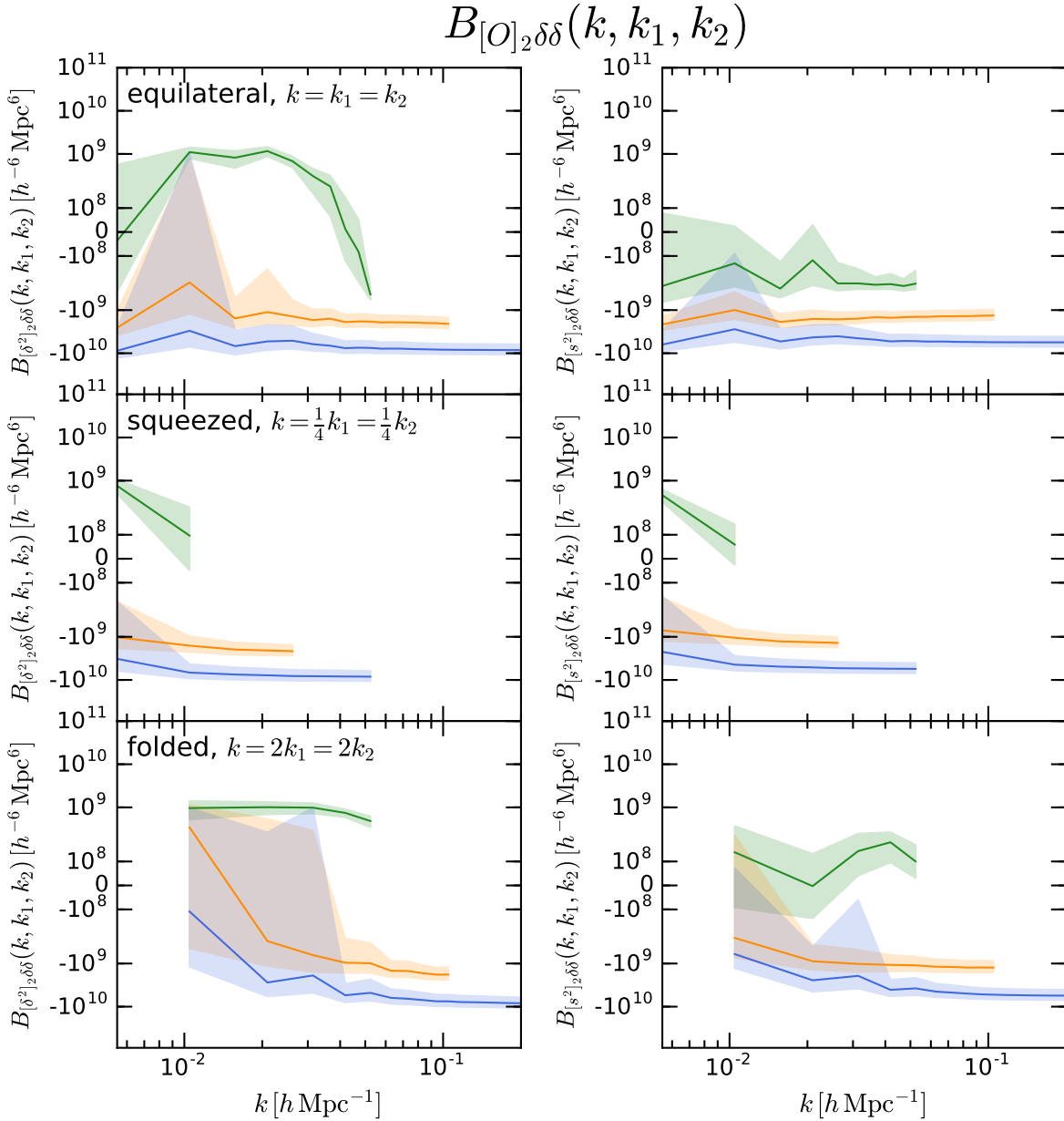
Figure 3.10: The same as Fig. 3.2, but for the second-order renormalised cross bispectra $B_{[\delta^2]_2\delta\delta}(k, k_1, k_2)$ and $B_{[s^2]_2\delta\delta}(k, k_1, k_2)$. Note the symmetrically logarithmic scaling on the y-axis for all panels.

LO term, and the NLO term only adds a subdominant contribution so that the computation of $B_{[O]_2\delta\delta}(k, k_1, k_2)$ gives a meaningful result. It is therefore not possible at this stage to claim success of the renormalisation procedure in simulations. With only the results for one cutoff scale, $\Lambda = 0.05 \, h\,\mathrm{Mpc}^{-1}$, at hand, we are not in the position to make a comparison between cutoff scales, and therefore not possible to say whether the dependency on it could be eliminated.

3.5 Renormalising the halo power spectrum

Another interesting test of the renormalisation framework is to apply it to the halo power spectrum $P_{\delta_h \delta_h}(k)$. In contrast to the halo-matter cross spectrum, which can only be measured in numerical simulations, the halo (or galaxy) power spectrum is a quantity that is actually accessible by galaxy redshift surveys. Therefore, testing how well it can be renormalised within the developed framework is a crucial task. Under the assumption that only those operators appearing in equation (3.3) are needed, we use equation (3.1) and write the theoretical halo power spectrum until fourth order in the perturbations (McDonald and Roy, 2009; Desjacques, Jeong and Schmidt, 2018b),

$$
\begin{aligned}
P_{\delta_h \delta_h}(k) = {}& \left(b_{1,\mathrm{R}}^2 + 2 b_{1,\mathrm{R}} b_{\nabla^2 \delta} k^2 + b_{\nabla^2 \delta}^2 k^4 \right) \left[P_{\delta\delta}^{(\mathrm{LO})}(k) + P_{\delta\delta}^{(\mathrm{NLO})}(k) \right] \\
& + 2 \left(b_{1,\mathrm{R}} b_2 + b_{\nabla^2 \delta} b_2 k^2 \right) P_{[\delta^2]_1 \delta}(k) + 2 \left(b_{1,\mathrm{R}} b_{s^2} + b_{\nabla^2 \delta} b_{s^2} k^2 \right) P_{[s^2]_1 \delta}(k) \\
& + b_2^2 P_{[\delta^2]_1 [\delta^2]_1}(k) + b_{s^2}^2 P_{[s^2]_1 [s^2]_1}(k) + 2 b_2 b_{s^2} P_{[\delta^2]_1 [s^2]_1}(k) - \frac{1}{n_\mathrm{h}} \,,
\end{aligned} \tag{3.51}
$$

where the last term represents shot noise that must be subtracted, modelled by using the inverse of the halo density n_h. Some of the spectra we already examined in detail in W19. The terms where δ^2 and s^2 are cross-correlated with themselves or with each other can be written as

$$
P_{[O]_1 [O']_1}(k) = P_{OO'}^{(22)}(k) - \lim_{k \to 0} P_{OO'}^{(22)}(k) \,, \tag{3.52}
$$

where

$$
P_{\delta^2 \delta^2}^{(22)}(k) = \int P_{11}(q) \, P_{11}(|\mathbf{k} - \mathbf{q}|) \, \frac{\mathrm{d}^3 q}{(2\pi)^3} \,, \tag{3.53}
$$

$$
P_{s^2 s^2}^{(22)}(k) = \int P_{11}(q) \, P_{11}(|\mathbf{k} - \mathbf{q}|) \, S_2(\mathbf{q}, \mathbf{k} - \mathbf{q})^2 \, \frac{\mathrm{d}^3 q}{(2\pi)^3} \,, \tag{3.54}
$$

$$
P_{\delta^2 s^2}^{(22)}(k) = \int P_{11}(q) \, P_{11}(|\mathbf{k} - \mathbf{q}|) \, S_2(\mathbf{q}, \mathbf{k} - \mathbf{q}) \, \frac{\mathrm{d}^3 q}{(2\pi)^3} \,, \tag{3.55}
$$

and

$$
\lim_{k \to 0} P_{\delta^2 \delta^2}^{(22)}(k) = \int P_{11}(q)^2 \, \frac{\mathrm{d}^3 q}{(2\pi)^3} \,, \tag{3.56}
$$

$$
\lim_{k \to 0} P_{s^2 s^2}^{(22)}(k) = \frac{4}{9} \int P_{11}(q)^2 \, \frac{\mathrm{d}^3 q}{(2\pi)^3} \,, \tag{3.57}
$$

$$
\lim_{k \to 0} P_{\delta^2 s^2}^{(22)}(k) = \frac{2}{3} \int P_{11}(q)^2 \, \frac{\mathrm{d}^3 q}{(2\pi)^3} \,. \tag{3.58}
$$

From equations (3.56) – (3.58) it becomes clear that the expressions at $k \to 0$ are not k-dependent (in contrast to the renormalisation term in equation 3.13), which is interpreted as an additional, cutoff-dependent noise contribution to the spectra.

So far, we wrote the integrals without the filter functions. As shown in W19 and explained in section 3.2.1, however, when comparing SPT results to simulation data, the filters are needed.
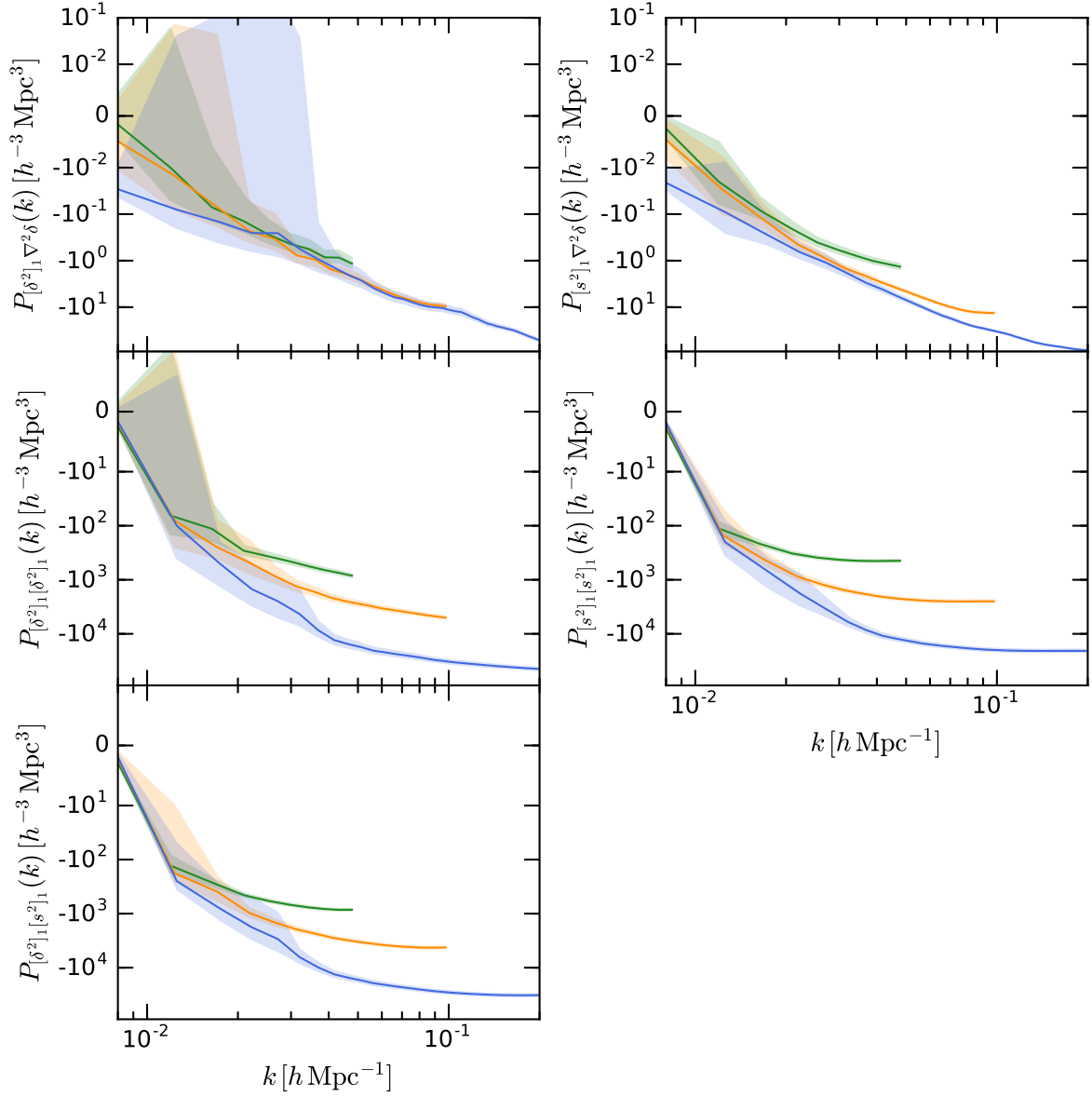
Figure 3.11: The renormalised cross spectra appearing in the the halo power spectrum, $P_{[\delta^2]_1\nabla^2\delta}(k)$ (top left), $P_{[s^2]_1\nabla^2\delta}(k)$ (top right), $P_{[\delta^2]_1[\delta^2]_1}(k)$ (middle left), $P_{[s^2]_1[s^2]_1}(k)$ (middle right), and $P_{[\delta^2]_1[s^2]_1}(k)$ (bottom). The results were obtained by measuring the expressions in equations (3.61) and (3.62) for three values of Λ from the simulations and performing the average. Shaded regions represent the standard error of the mean.

The integral expressions therefore become

$$P_{OO'}^{(22)}(k) = \int P_{11}(q)\, P_{11}(|\mathbf{k} - \mathbf{q}|)\, \Sigma_{OO'}(\mathbf{q}, \mathbf{k} - \mathbf{q})\, W(q)\, W(|\mathbf{k} - \mathbf{q}|)\, \frac{\mathrm{d}^3 q}{(2\pi)^3}\,, \tag{3.59}$$

with

$$\Sigma_{OO'} = \begin{cases} 1 & \text{for } O = O' = \delta^2\,, \\ S_2(\mathbf{q}, \mathbf{k} - \mathbf{q})^2 & \text{for } O = O' = s^2\,, \\ S_2(\mathbf{q}, \mathbf{k} - \mathbf{q}) & \text{for } O = \delta^2,\, O' = s^2\,. \end{cases} \tag{3.60}$$

Since the independence on k in the limit $k \to 0$ is unchanged by introducing the filters, we therefore perform the renormalisation in the simulations as

$$P_{[O]_1[O']_1}(k) = P_{OO'}(k) - P_{OO'}(k_{\min})\,. \tag{3.61}$$

Furthermore, the renormalisation of the spectra involving $O = \{\delta^2,\, s^2\}$ and $\nabla^2\delta$ is computed analogously to equation (3.15),

$$P_{[O]_1\nabla^2\delta}(k) = P_{O\nabla^2\delta}(k) - \alpha_O P_{\nabla^2\delta\delta}(k)\,. \tag{3.62}$$

Inserting equations (3.61) and (3.62) into equation (3.51), we write the complete halo power spectrum $P_{\delta_h \delta_h}(k)$, measured from the simulations, as

$$\begin{aligned} P_{\delta_h \delta_h}(k) = {} & b_{1,\mathrm{R}}^2 P_{\delta\delta}(k) + 2 b_{1,\mathrm{R}} b_{\nabla^2\delta} P_{\nabla^2\delta\delta}(k) + b_{\nabla^2\delta}^2 P_{\nabla^2\delta\nabla^2\delta}(k) \\ & + 2\left[b_{1,\mathrm{R}} b_2 P_{[\delta^2]_1\delta}(k) + b_2 b_{\nabla^2\delta} P_{[\delta^2]_1\nabla^2\delta}(k) \right] + 2\left[b_{1,\mathrm{R}} b_{s^2} P_{[s^2]_1\delta}(k) + b_{s^2} b_{\nabla^2\delta} P_{[s^2]_1\nabla^2\delta}(k) \right] \\ & + b_2^2 P_{[\delta^2]_1[\delta^2]_1}(k) + b_{s^2}^2 P_{[s^2]_1[s^2]_1}(k) + 2 b_2 b_{s^2} P_{[\delta^2]_1[s^2]_1}(k) - \frac{1}{n_h}\,, \end{aligned} \tag{3.63}$$

with $n_h = N_h/V$, where N_h is the number of haloes in the simulation box. We show the renormalised spectra that appear only in the halo power spectrum and were not shown in W19 in Fig. 3.11. We find similar behavior for all spectra: For small k, the signal approaches zero, independently of the value of Λ. This shows that also for these terms the first-order renormalisation procedure was fully successful. The amplitude of all spectra grows towards more negative values with increasing k, whereas the signal obtains larger absolute values for increasing Λ. In total, the renormalised results show very similar characteristics to those presented in W19. While from this it might first seem as if the spectra were giving degenerate contributions to $P_{\delta_h \delta_h}(k)$, this is not true. They do differ slightly in amplitude and shape on the smaller scales, and it is exactly at these small scales where these higher-order contributions are expected to provide the greatest modification to the LO spectrum.

3.6 Summary

In this paper we extended the procedure to renormalise halo bias in simulations, developed in our previous work W19, in two ways. In the former paper, we successfully renormalised the cross spectra $P_{\delta^2\delta}(k)$ and $P_{s^2\delta}(k)$ in the halo-matter cross spectrum $P_{\delta_h\delta}(k)$, and therefore also the linear bias parameter b_1 (first-order renormalisation). Now, we mainly focused on renormalising the relevant spectra in the halo-matter-matter cross bispectrum $B_{\delta_h\delta\delta}(k, k_1, k_2)$ and therefore

the bias parameters b_2 and b_{s^2} (second-order renormalisation). Additionally, we applied the procedure to the halo power spectrum $P_{\delta_h \delta_h}(k)$ and successfully renormalised the relevant spectra. Our main results can be summarized as follows:

1. We performed a detailed SPT calculation for the renormalisation term at bispectrum level $B^{(\text{NLO})}_{[O]_1 \delta_1 \delta_1}(k, k_1, k_2)$ (equations 3.28, 3.37, 3.38 and 3.39) and confirmed the result presented by A14 (their equation 2.42).

2. Using an estimator based on FFT, we measured $B_{\delta_h \delta \delta}(k, k_1, k_2)$ from the simulations for the three halo mass bins that we introduced in W19, and compared it to $B_{\delta \delta \delta}(k, k_1, k_2)$ for three different triangle configurations (Fig. 3.1). While the data show a certain amount of noise, the halo-matter cross bispectrum looks similar to the matter bispectrum for all configurations and scales. The larger the mean halo mass of the bin is, the stronger is the signal of $B_{\delta_h \delta \delta}(k, k_1, k_2)$.

3. For the three different values of the cutoff $\Lambda = \{0.05, 0.1, 0.2\}\, h\,\text{Mpc}^{-1}$ we measured the cross bispectra between $O = \{\delta^2,\ s^2\}$ and the matter (Fig. 3.2), which are clearly cutoff dependent since their overall amplitude increases with increasing Λ. We renormalised these spectra to first order, using the result for the renormalisation term we obtained in W19, $[O]_1 = O - \alpha_O \delta$ (Fig. 3.4).

4. We adapted the SPT result for renormalisation at second order to apply it to real data (equations 3.47 – 3.50), and we measured all the appearing bispectra from the simulations (Figs. 3.5 – 3.7). In particular, we obtained the renormalisation term which must be subtracted from the first-order renormalised cross bispectra to obtain the second-order renormalised ones.

5. We performed the second-order renormalisation in simulations (Fig. 3.10). For $\Lambda = 0.05\, h\,\text{Mpc}^{-1}$ the procedure had a minor influence, in contrast to the measurements for $\Lambda = 0.1$ and $0.2\, h\,\text{Mpc}^{-1}$, where too much was subtracted. This issue arises since for these cutoff scales the NLO terms present a signal close to or larger than the LO term. Clearly, this indicates that the expansion itself ceases to be valid, therefore the whole procedure must be restricted to $\Lambda < 0.1\, h\,\text{Mpc}^{-1}$ at $z = 0$.

6. We compared the LO term, $B_{O_1 \delta_1 \delta_1}(k, k_1, k_2)$, to SPT results, evaluated numerically including filter functions (Fig. 3.6). We find good agreement for all scales and values of Λ. Furthermore, in the case of δ^2 we calculated the prefactor of the renormalisation term, $f_{\delta^2}(\gamma)$, from SPT including filter functions. Particularly for $\Lambda = 0.05\, h\,\text{Mpc}^{-1}$ it compares well to the data. For larger values of Λ we find an increased divergence between theory and data which could provide a hint that SPT looses its applicability at these cutoff scales.

7. We adapted the first-order renormalisation procedure to the bias expansion of the halo power spectrum $P_{\delta_h \delta_h}(k)$ (equation 3.63) and measured a set of renormalised cross spectra (Fig. 3.11). Since the signal approaches zero in the case of $k \to 0$ for all values of Λ the first-order renormalisation was successful.

In summary, the results suggest that the second-order renormalisation procedure has only a major impact in a small interval of cutoff scales between 0.05 and $0.1\, h\,\text{Mpc}^{-1}$. Future work should aim at constraining this interval by repeating the measurements from this work at more

values of Λ. It is also possible to perform the analysis for larger redshifts where the procedure should be valid for greater cutoff scales. It is then of interest to fit the bias expansion at bispectrum level against $B_{\delta_h \delta \delta}(k, k_1, k_2)$ using the fitting method developed in W19. This will allow to obtain values for the set of bias parameters, and it will provide insight whether it is possible to renormalise b_2 and b_{s^2}.

Furthermore, the successful renormalisation of the bias expansion of $P_{\delta_h \delta_h}(k)$ clearly motivates an application of the model to data, both in simulations and also in real galaxy redshift surveys.

Summary & Outlook

Accurate models to describe the bias of dark-matter (DM) tracers (e.g. haloes or galaxies) are a crucial ingredient in the analysis process of galaxy redshift surveys. In this work, we approached the task of phrasing a halo-bias relation (often in the form of an ordered expansion; e.g. McDonald and Roy, 2009; Kehagias et al., 2014; Senatore, 2015) from several perspectives. After providing a theoretical motivation for a set of bias models within the framework of an Effective Field Theory (EFT) in combination with cosmological Standard Perturbation Theory (SPT), we ran a suite of 40 cosmological DM-only simulations in order to obtain a numerical testbed with enormous statistical power. Besides our investigation of the optimal bias model based on the application of model selection techniques, we particularly directed our efforts towards implementing and therefore testing the renormalisation of halo bias (a scheme first introduced by McDonald, 2006) within our simulations. This technique aims at eliminating unphysical artifacts that, within the otherwise powerful mathematical framework, are unavoidably introduced to the bias expansion. It prescribes how to rewrite individual terms of the model order by order with the intent of obtaining a physically meaningful description of bias. In this study, for the first time, we demonstrated how to successfully adapt this method to numerical data and, therefore, how to renormalise the bias expansion in practice.

In chapter 2 we focused on the renormalisation of linear bias. For each of our models the DM density field was expanded in a different number of bias operators O_i (where the full set of operators is $\{\delta, \delta^2, s^2, \nabla^2\delta, \Gamma_3, k^2\}$), each weighted with a bias parameter b_i. In order to obtain the bias parameters from the simulations, after smoothing the density field with a sharp cutoff in Fourier space, we cross-correlated the halo density field and the bias model with δ and measured the resulting power and cross spectra, where we found a clear dependency of the halo-matter cross spectrum $P_{\delta_h\delta}(k)$ on the halo mass. For three different halo mass bins we finally fitted the bias model against the halo-matter cross spectrum, using a novel method that takes into account the covariance matrix of all spectra, and we found that even without any renormalisation the data were in very good agreement with the model. However, the bias parameters did not contain any physical meaning – while the linear bias b_1 should dominate on large scales, it was contaminated by a cutoff-dependent signal from the quadratic (b_{δ^2}) and tidal (b_{s^2}) biases. We addressed this issue by modeling the cross spectra $P_{\delta^2\delta}(k)$ and $P_{s^2\delta}(k)$ within the framework of SPT and isolating the cutoff-dependent (UV-sensitive) terms on large scales. We demonstrated, both analytically and numerically, that when comparing SPT calculations to numerical data filter functions must be multiplied to each density field, which leads to a modification of the prefactor α_O of the UV-sensitive terms (contrary to what was claimed by Desjacques, Jeong and

Schmidt, 2018a). After measuring the cutoff-dependent terms in the simulations, we subtracted them from the cross spectra to obtain the renormalised bias expansion and bias parameters. In this context we found that the linear growth factor, that multiplies the linear density field, requires very precise measurement, and therefore we extracted it directly from the simulations. By fitting the renormalised bias relation to the halo-matter cross spectrum we were able to measure a renormalised linear bias parameter b_1^R that presented the same value for each cutoff scale. We repeated the same procedure for eleven different bias models, and using statistical model selection techniques we found that a four-parameter model, containing δ, δ^2, s^2 and $\nabla^2\delta$, fitted the data best at redshift $z = 0$ on scales $k \leq 0.2\,h\,\mathrm{Mpc}^{-1}$. Using fewer parameters resulted in inaccuracy on small scales, whereas using more parameters lead to overfitting.

In light of the success of adapting the renormalisation method to the halo bias expansion, it is expected to be useful also for galaxies and other tracers of the DM that are directly observable. Even while the cross spectrum between tracers and DM only exists in simulations, it is still of great value to have at hand a working model that can also be applied to other numerical data. In particular, it will be interesting to measure the bias parameters at higher redshifts or for tracer populations binned in a quantity different than mass (e.g. colour or luminosity) to shed more light on the formation processes of the large-scale structure of the Universe. Additionally, efforts should be spent on pushing the model and the renormalisation technique to even smaller scales. While it is in principle straightforward to obtain good fitting results also on smaller scales by introducing higher-order operators (even if it remains to be seen which exactly are needed), it is unclear whether the renormalisation method, based on SPT, will survive this extension. Already at $k = 0.2\,h\,\mathrm{Mpc}^{-1}$ we observe a divergence between the results given by the perturbative integrals and the numerical measurements. Repeating the analysis for other cutoffs is therefore an important task.

In chapter 3 we extended our work with the aim of renormalising the higher-order bias parameters, b_2 and b_{s^2}, that so far still remained cutoff-dependent. Where the renormalisation of linear bias is best achieved on the level of 2-point statistics, for higher-order parameters we must turn to 3-point statistics, i.e. the bispectrum (Assassi et al., 2014). We cross-correlated the halo density field and the bias expansion with $\delta\delta$ to measure the halo-matter-matter cross bispectrum $B_{\delta_h\delta\delta}(k, k_1, k_2)$ from our suite of simulations where we found a similar behaviour in halo mass as in the previous chapter. Consistently, the cross bispectra including $B_{\delta^2\delta\delta}(k, k_1, k_2)$ and $B_{s^2\delta\delta}(k, k_1, k_2)$ presented a cutoff dependency which we aimed to isolate within the framework of SPT. While in principle the approach is the same as for linear bias, on the bispectrum level the UV-sensitivity is given by not only one, but two different perturbative correlators. Because of the higher complexity of the task, in a first step, we explicitly calculated these expressions and successfully compared the final result to the literature. Building up on that, we identified the SPT integrals with the analogous quantities in the simulations and obtained the UV-sensitive term. In contrast to the linear bias, the prefactor $f_O(\gamma)$ of this renormalisation term is not a constant anymore, but instead depends on the triangle configuration $\{k, k_1, k_2\}$ on large scales. We performed the second-order renormalisation by subtracting this term successfully for the smallest cutoff scale, for the larger ones, however, the perturbative approach already broke down. This leads to the conclusion that the halo bias relation and with it the second-order renormalisation at bispectrum level must be restricted to scales $k < 0.1\,h\,\mathrm{Mpc}^{-1}$. For the smallest cutoff scales, visually the influence of the second-order renormalisation was only minor. It is worth pointing out, however, that whereas on the power spectrum level the quadratic and tidal cross spectra are fully dominated by a loop term, on bispectrum level they are given as the combination of a tree and loop term. We therefore expect the renormalisation to only have a

subdominant influence on the signal, in comparison to the absolute value.

A more quantitative analysis of the success of the technique will be possible when the renormalised bias expansion is fitted against the halo-matter cross bispectrum, using the same method as in the previous chapter, since this allows to obtain the bias parameters. It is important to measure the spectra and parameters for an additional set of smaller cutoff scales, complementing those that we had used so far, where the SPT approach is still valid. This will give clear insight whether the UV-sensitivity can be consistently removed also for b_2 and b_{s^2}. Furthermore, fitting the bispectrum will provide complementary bias parameter results to the power spectrum fit and therefore allow to cross-check the different statistics against each other. In particular, it is important to confirm the cutoff independency of b_1^R also on bispectrum level. Furthermore, it will be valuable to obtain an expression for the renormalisation term not only for the bispectrum, but already on the field level. For the linear bias, this is easily achievable, since the UV-sensitive term is given by a single correlator, that can be directly translated into a counter operator that must be subtracted (McDonald and Roy, 2009). For higher-order bias, however, several correlators come into play. While in SPT, neglecting filter functions, it is possible to derive two counter operators on field level also from that (which are exactly δ^2 and s^2, therefore leading to the renormalisation of b_2 and b_{s^2}), it remains an open question whether this is also possible for real data. It will be helpful to investigate this in more detail, since the discovery of these potential counter operators would possibly allow the renormalisation of quadratic and tidal bias even on power spectrum level, making the method even more powerful and attractive.

Finally, in a straightforward fashion, we adapted the first-order renormalisation technique to the halo power spectrum, $P_{\delta_h \delta_h}(k)$. We successfully renormalised the various cross spectra in the bias relation (which appear additionally to those from the halo-matter cross spectrum), which either also modify the linear bias, or add unto the shot noise that naturally comes in the halo power spectrum. Since the power spectrum of haloes – and therefore also other luminous tracers – is directly observable from redshift surveys, it would be an exciting next step to test the renormalised bias model on a variety of tracer populations in simulations, and possibly eventually on real survey data.

Bibliography

Abbott, T. M. C. et al. (2019), *Dark Energy Survey Year 1 Results: Measurement of the Baryon Acoustic Oscillation scale in the distribution of galaxies to redshift 1*, Mon. Not. R. Astron. Soc. **483** 4866 (cit. on p. 9).

Abidi, M. M. and T. Baldauf (2018), *Cubic halo bias in Eulerian and Lagrangian space*, JCAP **7**, 029 029, arXiv: 1802.07622 (cit. on pp. 38, 68).

Akaike, H. (1973), *Maximum likelihood identification of Gaussian autoregressive moving average models*, Biometrika **60** 255 (cit. on p. 61).

Albareti, F. D. et al. (2017), *The 13th Data Release of the Sloan Digital Sky Survey: First Spectroscopic Data from the SDSS-IV Survey Mapping Nearby Galaxies at Apache Point Observatory*, Astrophys. J. Suppl. Ser. **233**, 25 25, arXiv: 1608.02013 (cit. on pp. 12, 13).

Alkhanishvili, D. (2018), *Matter bispectrum with multi-point propagators*, MA thesis: University of Bonn (cit. on p. 81).

Allen, S. W., A. E. Evrard and A. B. Mantz (2011), *Cosmological Parameters from Observations of Galaxy Clusters*, **49** 409, arXiv: 1103.4829 [astro-ph.CO] (cit. on p. 11).

Amendola, L. et al. (2018), *Cosmology and fundamental physics with the Euclid satellite*, Living Reviews in Relativity **21**, 2 2, arXiv: 1606.00180 (cit. on p. 13).

Angulo, R. E. et al. (2015), *The one-loop matter bispectrum in the Effective Field Theory of Large Scale Structures*, JCAP **10**, 039 039, arXiv: 1406.4143 (cit. on pp. 20, 42, 49).

Assassi, V. et al. (2014), *Renormalized halo bias*, JCAP **8**, 056 056, arXiv: 1402.5916 (cit. on pp. 28, 38, 47, 48, 74, 100).

Baldauf, T., V. Desjacques and U. Seljak (2015), *Velocity bias in the distribution of dark matter halos*, Phys. Rev. D. **92**, 123507 123507, arXiv: 1405.5885 (cit. on p. 32).

Baldauf, T., U. Seljak, V. Desjacques et al. (2012), *Evidence for quadratic tidal tensor bias from the halo bispectrum*, Phys. Rev. D. **86**, 083540 083540, arXiv: 1201.4827 [astro-ph.CO] (cit. on pp. 31, 38, 68).

Baldauf, T., U. Seljak, L. Senatore et al. (2011), *Galaxy bias and non-linear structure formation in general relativity*, JCAP **10**, 031 031, arXiv: 1106.5507 (cit. on p. 19).

– (2016), *Linear response to long wavelength fluctuations using curvature simulations*, JCAP **9**, 007 007, arXiv: 1511.01465 (cit. on p. 38).

Bardeen, J. M. et al. (1986), *The Statistics of Peaks of Gaussian Random Fields*, Astrophys. J. **304** 15 (cit. on pp. 11, 18, 24, 30).

Beckwith, S. V. W. et al. (2006), *The Hubble Ultra Deep Field*, **132** 1729, eprint: astro-ph/0607632 (cit. on pp. 1, 2).

Behroozi, P. S., R. H. Wechsler and H.-Y. Wu (2013a), *The ROCKSTAR Phase-space Temporal Halo Finder and the Velocity Offsets of Cluster Cores*, Astrophys. J. **762**, 109 109, arXiv: 1110.4372 [astro-ph.CO] (cit. on p. 35).

– (2013b), *The ROCKSTAR Phase-space Temporal Halo Finder and the Velocity Offsets of Cluster Cores*, Astrophys. J. **762**, 109 109, arXiv: 1110.4372 [astro-ph.CO] (cit. on p. 51).

Bel, J., K. Hoffmann and E. Gaztañaga (2015), *Non-local bias contribution to third-order galaxy correlations*, Mon. Not. R. Astron. Soc. **453** 259, arXiv: `1504.02074` (cit. on p. 38).

Berlind, A. A. and D. H. Weinberg (2002), *The Halo Occupation Distribution: Toward an Empirical Determination of the Relation between Galaxies and Mass*, Astrophys. J. **575** 587, eprint: `astro-ph/0109001` (cit. on p. 18).

Bernardeau, F. (1994), *The effects of smoothing on the statistical properties of large-scale cosmic fields*, Astron. Astrophys. **291** 697, eprint: `astro-ph/9403020` (cit. on p. 41).

Bernardeau, F. et al. (2002), *Large-scale structure of the Universe and cosmological perturbation theory*, **367** 1, eprint: `astro-ph/0112551` (cit. on pp. 4, 16, 40, 41).

Beutler, F. et al. (2017), *The clustering of galaxies in the completed SDSS-III Baryon Oscillation Spectroscopic Survey: baryon acoustic oscillations in the Fourier space*, Mon. Not. R. Astron. Soc. **464** 3409, arXiv: `1607.03149` (cit. on p. 20).

Blake, C. et al. (2010), *The WiggleZ Dark Energy Survey: the selection function and z = 0.6 galaxy power spectrum*, Mon. Not. R. Astron. Soc. **406** 803, arXiv: `1003.5721` (cit. on p. 20).

Blas, D., M. Garny and T. Konstandin (2014), *Cosmological perturbation theory at three-loop order*, JCAP **1**, 010 010, arXiv: `1309.3308` (cit. on p. 41).

Blot, L. et al. (2016), *Non-linear matter power spectrum covariance matrix errors and cosmological parameter uncertainties*, Mon. Not. R. Astron. Soc. **458** 4462, arXiv: `1512.05383` (cit. on p. 26).

Bond, J. R., S. Cole et al. (1991), *Excursion Set Mass Functions for Hierarchical Gaussian Fluctuations*, Astrophys. J. **379** 440 (cit. on p. 31).

Bond, J. R., L. Kofman and D. Pogosyan (1996), *How filaments of galaxies are woven into the cosmic web*, **380** 603, eprint: `astro-ph/9512141` (cit. on p. 2).

Bond, J. R. and S. T. Myers (1996), *The Peak-Patch Picture of Cosmic Catalogs. I. Algorithms*, Astrophys. J. Suppl. Ser. **103** 1 (cit. on p. 17).

Borzyszkowski, M., A. D. Ludlow and C. Porciani (2014), *The formation of cold dark matter haloes - II. Collapse time and tides*, Mon. Not. R. Astron. Soc. **445** 4124, arXiv: `1405.7367` (cit. on p. 17).

Borzyszkowski, M., C. Porciani et al. (2017), *ZOMG - I. How the cosmic web inhibits halo growth and generates assembly bias*, Mon. Not. R. Astron. Soc. **469** 594, arXiv: `1610.04231` (cit. on p. 17).

Bryan, G. L. and M. L. Norman (1998), *Statistical Properties of X-Ray Clusters: Analytic and Numerical Comparisons*, Astrophys. J. **495** 80, eprint: `astro-ph/9710107` (cit. on p. 51).

Campanelli, L. et al. (2011), *Testing the isotropy of the Universe with type Ia supernovae*, Phys. Rev. D. **83**, 103503 103503, arXiv: `1012.5596 [astro-ph.CO]` (cit. on p. 5).

Carlson, J., M. White and N. Padmanabhan (2009), *Critical look at cosmological perturbation theory techniques*, Phys. Rev. D. **80**, 043531 043531, arXiv: `0905.0479 [astro-ph.CO]` (cit. on p. 41).

Carrasco, J. J. M. et al. (2014), *The 2-loop matter power spectrum and the IR-safe integrand*, JCAP **7**, 056 056, arXiv: `1304.4946` (cit. on p. 79).

Catelan, P., F. Lucchin et al. (1998), *The bias field of dark matter haloes*, Mon. Not. R. Astron. Soc. **297** 692, eprint: `astro-ph/9708067` (cit. on p. 37).

Catelan, P., C. Porciani and M. Kamionkowski (2000), *Two ways of biasing galaxy formation*, Mon. Not. R. Astron. Soc. **318** L39, eprint: `astro-ph/0005544` (cit. on pp. 37, 68).

Chan, K. C., R. Scoccimarro and R. K. Sheth (2012), *Gravity and large-scale nonlocal bias*, Phys. Rev. D. **85**, 083509 083509, arXiv: `1201.3614 [astro-ph.CO]` (cit. on pp. 38, 68).

Chan, K. C., R. K. Sheth and R. Scoccimarro (2017), *Effective window function for Lagrangian halos*, Phys. Rev. D. **96**, 103543 103543, arXiv: `1511.01909` (cit. on p. 69).

Chevallier, M. and D. Polarski (2001), *Accelerating Universes with Scaling Dark Matter*, International Journal of Modern Physics D **10** 213, eprint: `gr-qc/0009008` (cit. on p. 11).

Chisari, N. E. and M. Zaldarriaga (2011), *Connection between Newtonian simulations and general relativity*, Phys. Rev. D. **83**, 123505 123505, arXiv: `1101.3555 [astro-ph.CO]` (cit. on p. 32).

Cole, S. and N. Kaiser (1989), *Biased clustering in the cold dark matter cosmogony*, Mon. Not. R. Astron. Soc. **237** 1127 (cit. on p. 31).

Cole, S., W. J. Percival et al. (2005), *The 2dF Galaxy Redshift Survey: power-spectrum analysis of the final data set and cosmological implications*, Mon. Not. R. Astron. Soc. **362** 505, eprint: `astro-ph/0501174` (cit. on p. 20).

Coles, P. (1993), *Galaxy formation with a local bias*, Mon. Not. R. Astron. Soc. **262** 1065 (cit. on p. 38).

Colless, M. et al. (2001), *The 2dF Galaxy Redshift Survey: spectra and redshifts*, Mon. Not. R. Astron. Soc. **328** 1039, eprint: `astro-ph/0106498` (cit. on pp. 2, 3).

Cooray, A. and R. Sheth (2002), *Halo models of large scale structure*, **372** 1, eprint: `astro-ph/0206508` (cit. on p. 18).

Crocce, M. and R. Scoccimarro (2006), *Memory of initial conditions in gravitational clustering*, Phys. Rev. D. **73**, 063520 063520, eprint: `astro-ph/0509419` (cit. on p. 34).

Davis, M. et al. (1985), *The evolution of large-scale structure in a universe dominated by cold dark matter*, Astrophys. J. **292** 371 (cit. on pp. 35, 37).

Dawson, K. S. et al. (2016), *The SDSS-IV Extended Baryon Oscillation Spectroscopic Survey: Overview and Early Data*, **151**, 44 44, arXiv: `1508.04473` (cit. on p. 13).

Dekel, A. and M. J. Rees (1987), *Physical mechanisms for biased galaxy formation*, **326** 455 (cit. on p. 37).

Desjacques, V. (2008), *Baryon acoustic signature in the clustering of density maxima*, Phys. Rev. D. **78**, 103503 103503, arXiv: `0806.0007` (cit. on pp. 32, 38, 69).

– (2013), *Local bias approach to the clustering of discrete density peaks*, Phys. Rev. D. **87**, 043505 043505, arXiv: `1211.4128 [astro-ph.CO]` (cit. on p. 19).

Desjacques, V., M. Crocce et al. (2010), *Modeling scale-dependent bias on the baryonic acoustic scale with the statistics of peaks of Gaussian random fields*, Phys. Rev. D. **82**, 103529 103529, arXiv: `1009.3449 [astro-ph.CO]` (cit. on pp. 21, 38).

Desjacques, V., D. Jeong and F. Schmidt (2018a), *Large-scale galaxy bias*, **733** 1, arXiv: `1611.09787` (cit. on pp. 4, 18, 21, 27, 31, 99).

– (2018b), *Large-scale galaxy bias*, **733** 1, arXiv: `1611.09787` (cit. on pp. 42, 48, 50, 94).

– (2018c), *The galaxy power spectrum and bispectrum in redshift space*, JCAP **12**, 035 035, arXiv: `1806.04015` (cit. on pp. 20, 42).

Efstathiou, G., M. Davis et al. (1985), *Numerical techniques for large cosmological N-body simulations*, Astrophys. J. Suppl. Ser. **57** 241 (cit. on p. 33).

Efstathiou, G., C. S. Frenk et al. (1988), *Gravitational clustering from scale-free initial conditions*, Mon. Not. R. Astron. Soc. **235** 715 (cit. on p. 35).

Efstathiou, G., W. J. Sutherland and S. J. Maddox (1990), *The cosmological constant and cold dark matter*, **348** 705 (cit. on p. 4).

Eggemeier, A., R. Scoccimarro and R. E. Smith (2019), *Bias loop corrections to the galaxy bispectrum*, Phys. Rev. D. **99**, 123514 123514, arXiv: `1812.03208` (cit. on p. 38).

Eisenstein, D. J. et al. (2005), *Detection of the Baryon Acoustic Peak in the Large-Scale Correlation Function of SDSS Luminous Red Galaxies*, Astrophys. J. **633** 560, eprint: `astro-ph/0501171` (cit. on pp. 4, 11).

Elia, A., A. D. Ludlow and C. Porciani (2012), *The spatial and velocity bias of linear density peaks and protohaloes in the Λ cold dark matter cosmology*, Mon. Not. R. Astron. Soc. **421** 3472, arXiv: `1111.4211` (cit. on p. 69).

Fitzgerald, A. P. (1951), *Some Aspects of Primitive Astronomy*, Irish Astronomical Journal **1** 197 (cit. on p. 1).

Frigo, M. and S. G. Johnson (2005), *The Design and Implementation of FFTW3*, IEEE Proc. **93** 216 (cit. on p. 33).

Fry, J. N. and E. Gaztanaga (1993), *Biasing and hierarchical statistics in large-scale structure*, Astrophys. J. **413** 447, eprint: `astro-ph/9302009` (cit. on pp. 18, 20, 37, 38).

Fujita, T. et al. (2016), *Very Massive Tracers and Higher Derivative Biases*, arXiv e-prints, `1609.00717` (cit. on p. 38).

Gaztanaga, E. and C. M. Baugh (1998), *Testing deprojection algorithms on mock angular catalogues - Evidence for a break in the power spectrum*, Mon. Not. R. Astron. Soc. **294** 229, eprint: `astro-ph/9704246` (cit. on p. 38).

Gaztanaga, E. and J. A. Frieman (1994), *Bias and high-order galaxy correlation functions in the APM galaxy survey*, Astrophys. J. Lett **437** L13, eprint: `astro-ph/9407079` (cit. on p. 20).

Gelman, A., J. Hwang and A. Vehtari (2014), *Understanding predictive information criteria for Bayesian models*, English, Statistics and Computing **24** 997 (cit. on p. 62).

Goroff, M. H. et al. (1986), *Coupling of modes of cosmological mass density fluctuations*, Astrophys. J. **311** 6 (cit. on pp. 16, 40).

Granett, B. R. et al. (2012), *The power spectrum from the angular distribution of galaxies in the CFHTLS-Wide fields at redshift 0.7*, Mon. Not. R. Astron. Soc. **421** 251, arXiv: `1112.0008` [`astro-ph.CO`] (cit. on p. 20).

Gunn, J. E. and J. R. Gott III (1972), *On the Infall of Matter Into Clusters of Galaxies and Some Effects on Their Evolution*, Astrophys. J. **176** 1 (cit. on p. 17).

Guth, A. H. (1981), *Inflationary universe: A possible solution to the horizon and flatness problems*, Phys. Rev. D. **23** 347 (cit. on p. 22).

Hahn, O. and T. Abel (2011), *Multi-scale initial conditions for cosmological simulations*, Mon. Not. R. Astron. Soc. **415** 2101, arXiv: `1103.6031` (cit. on p. 51).

Harrison, E. R. (1970), *Fluctuations at the Threshold of Classical Cosmology*, Phys. Rev. D. **1** 2726 (cit. on p. 24).

Hastings, W. K. (1970), *Monte Carlo Sampling Methods using Markov Chains and their Applications*, Biometrika **57** 97 (cit. on p. 28).

Heavens, A. F., S. Matarrese and L. Verde (1998), *The non-linear redshift-space power spectrum of galaxies*, Mon. Not. R. Astron. Soc. **301** 797, eprint: `astro-ph/9808016` (cit. on pp. 38, 44, 46, 54).

Hoffleit, D. and W. H. Warren Jr. (1987), *The Bright Star Catalogue, 5th revised edition.*, Astronomical Data Center Bulletin **1** 285 (cit. on p. 1).

Hoffmann, K., J. Bel and E. Gaztañaga (2015), *Comparing halo bias from abundance and clustering*, Mon. Not. R. Astron. Soc. **450** 1674, arXiv: `1503.00313` (cit. on pp. 38, 67).

– (2017), *Linear and non-linear bias: predictions versus measurements*, Mon. Not. R. Astron. Soc. **465** 2225, arXiv: `1607.01024` (cit. on pp. 38, 67).

Hoffmann, K., E. Gaztañaga et al. (2018), *Testing the consistency of three-point halo clustering in Fourier and configuration space*, Mon. Not. R. Astron. Soc. **476** 814, arXiv: `1708.08941` (cit. on p. 38).

Hubble, E. (1929), *A Relation between Distance and Radial Velocity among Extra-Galactic Nebulae*, Proceedings of the National Academy of Science **15** 168 (cit. on p. 8).

Hubble, E. and M. L. Humason (1931), *The Velocity-Distance Relation among Extra-Galactic Nebulae*, Astrophys. J. **74** 43 (cit. on pp. 6, 7).

Huchra, J. et al. (1983), *A survey of galaxy redshifts: 4. The data.*, Astrophys. J. Suppl. **52** L89, [Astrophys. J. Suppl.52,89(1983)] (cit. on p. 19).

Huterer, D. and D. L. Shafer (2018), *Dark energy two decades after: observables, probes, consistency tests*, Reports on Progress in Physics **81**, 016901 016901, arXiv: `1709.01091` (cit. on p. 11).

Inglis, M. (2018), *Astronomy of the Milky Way* (cit. on p. 1).

Jenkins, A. et al. (1998), *Evolution of Structure in Cold Dark Matter Universes*, Astrophys. J. **499** 20, eprint: `astro-ph/9709010` (cit. on pp. 11, 24, 32).

Jones, D. O. et al. (2018), *Measuring Dark Energy Properties with Photometrically Classified Pan-STARRS Supernovae. II. Cosmological Parameters*, Astrophys. J. **857**, 51 51, arXiv: `1710.00846` (cit. on pp. 9, 10).

Kaiser, N. (1984), *On the spatial correlations of Abell clusters*, Astrophys. J. Lett **284** L9 (cit. on pp. 18, 20, 30, 37).

Karachentsev, I. D. et al. (2004), *A Catalog of Neighboring Galaxies*, **127** 2031 (cit. on p. 21).

Kehagias, A. et al. (2014), *Consequences of symmetries and consistency relations in the large-scale structure of the universe for non-local bias and modified gravity*, Nuclear Physics B **883** 83, arXiv: `1311.0786` (cit. on pp. 38, 42, 99).

Knebe, A. et al. (2011), *Haloes gone MAD: The Halo-Finder Comparison Project*, Mon. Not. R. Astron. Soc. **415** 2293, arXiv: `1104.0949` (cit. on p. 35).

Knollmann, S. R. and A. Knebe (2009), *AHF: Amiga's Halo Finder*, Astrophys. J. Suppl. Ser. **182** 608, arXiv: `0904.3662` (cit. on p. 35).

Kuhlen, M., M. Vogelsberger and R. E. Angulo (2012), *Numerical simulations of the dark universe: State of the art and the next decade*, Physics of the Dark Universe **1** 50, arXiv: `1209.5745 [astro-ph.CO]` (cit. on p. 32).

Lazeyras, T. and F. Schmidt (2018), *Beyond LIMD bias: a measurement of the complete set of third-order halo bias parameters*, JCAP **9**, 008 008, arXiv: `1712.07531` (cit. on p. 38).

– (2019), *A robust measurement of the first higher-derivative bias of dark matter halos*, arXiv e-prints, 1904.11294 (cit. on pp. 38, 69).

Lazeyras, T., C. Wagner et al. (2016), *Precision measurement of the local bias of dark matter halos*, JCAP **2**, 018 018, arXiv: `1511.01096` (cit. on pp. 31, 38, 67).

Lee, S., C. Park and S. G. Biern (2014), *Exact third-order density perturbation and one-loop power spectrum in general dark energy models*, Physics Letters B **736** 403, arXiv: `1407.7325` (cit. on pp. 26, 41).

Lemaître, G. (1927), *Un Univers homogène de masse constante et de rayon croissant rendant compte de la vitesse radiale des nébuleuses extra-galactiques*, Annales de la Société Scientifique de Bruxelles **47** 49 (cit. on p. 7).

Lewis, A. and A. Challinor (2011), *CAMB: Code for Anisotropies in the Microwave Background*, ascl: `1102.026` (cit. on p. 34).

Li, Y., W. Hu and M. Takada (2016), *Separate universe consistency relation and calibration of halo bias*, Phys. Rev. D. **93**, 063507 063507, arXiv: `1511.01454` (cit. on p. 38).

Linder, E. V. (1997), *First Principles of Cosmology* (cit. on p. 4).

Manera, M. and E. Gaztañaga (2011), *The local bias model in the large-scale halo distribution*, Mon. Not. R. Astron. Soc. **415** 383, arXiv: `0912.0446` (cit. on p. 37).

Matsubara, T. (2011), *Nonlinear perturbation theory integrated with nonlocal bias, redshift-space distortions, and primordial non-Gaussianity*, Phys. Rev. D. **83**, 083518 083518, arXiv: `1102.4619 [astro-ph.CO]` (cit. on p. 37).

McConnachie, A. W. (2012), *The Observed Properties of Dwarf Galaxies in and around the Local Group*, **144**, 4 4, arXiv: `1204.1562` (cit. on p. 21).

McDonald, P. (2006), *Clustering of dark matter tracers: Renormalizing the bias parameters*, Phys. Rev. D. **74**, 103512 103512, eprint: `astro-ph/0609413` (cit. on pp. 28, 38, 46, 99).

McDonald, P. and A. Roy (2009), *Clustering of dark matter tracers: generalizing bias for the coming era of precision LSS*, JCAP **8**, 020 020, arXiv: `0902.0991 [astro-ph.CO]` (cit. on pp. 19, 21, 28, 38, 42, 46–49, 94, 99, 101).

Mirbabayi, M., F. Schmidt and M. Zaldarriaga (2015), *Biased tracers and time evolution*, JCAP **7**, 030 030, arXiv: `1412.5169` (cit. on pp. 20, 42).

Mo, H. J., Y. P. Jing and S. D. M. White (1997), *High-order correlations of peaks and haloes: a step towards understanding galaxy biasing*, Mon. Not. R. Astron. Soc. **284** 189, eprint: `astro-ph/9603039` (cit. on p. 37).

Mo, H. J. and S. D. M. White (1996), *An analytic model for the spatial clustering of dark matter haloes*, Mon. Not. R. Astron. Soc. **282** 347, eprint: `astro-ph/9512127` (cit. on p. 37).

Mo, H., F. C. van den Bosch and S. D. M. White (2010), *Galaxy Formation and Evolution* (cit. on p. 18).

Modi, C., E. Castorina and U. Seljak (2017), *Halo bias in Lagrangian space: estimators and theoretical predictions*, Mon. Not. R. Astron. Soc. **472** 3959, arXiv: `1612.01621` (cit. on pp. 38, 68).

More, S., B. Diemer and A. V. Kravtsov (2015), *The Splashback Radius as a Physical Halo Boundary and the Growth of Halo Mass*, Astrophys. J. **810**, 36 36, arXiv: `1504.05591` (cit. on pp. 17, 18).

Navarro, J. F., C. S. Frenk and S. D. M. White (1997), *A Universal Density Profile from Hierarchical Clustering*, Astrophys. J. **490** 493, eprint: `astro-ph/9611107` (cit. on p. 4).

Nishimichi, T. et al. (2009), *Modeling Nonlinear Evolution of Baryon Acoustic Oscillations: Convergence Regime of N-body Simulations and Analytic Models*, Publ. Astron. Soc. Jap. **61** 321, arXiv: `0810.0813` (cit. on p. 41).

Peebles, P. J. E. (1980), *The large-scale structure of the universe* (cit. on pp. 4, 13, 24).

Percival, W. J. (2007), "Cosmological Constraints from Galaxy Clustering", *The Invisible Universe: Dark Matter and Dark Energy*, ed. by L. Papantonopoulos, vol. 720, Lecture Notes in Physics, Berlin Springer Verlag 157, eprint: `astro-ph/0601538` (cit. on p. 13).

Percival, W. J., C. M. Baugh et al. (2001), *The 2dF Galaxy Redshift Survey: the power spectrum and the matter content of the Universe*, Mon. Not. R. Astron. Soc. **327** 1297, eprint: `astro-ph/0105252` (cit. on p. 2).

Percival, W. J., R. C. Nichol et al. (2007), *The Shape of the Sloan Digital Sky Survey Data Release 5 Galaxy Power Spectrum*, Astrophys. J. **657** 645, eprint: `astro-ph/0608636` (cit. on p. 20).

Perlmutter, S. et al. (1999), *Measurements of Ω and Λ from 42 High-Redshift Supernovae*, Astrophys. J. **517** 565, eprint: `astro-ph/9812133` (cit. on p. 11).

Planck Collaboration (2016), *Planck 2015 results. XIII. Cosmological parameters*, Astron. Astrophys. **594**, A13 A13, arXiv: `1502.01589` (cit. on p. 51).

– (2018a), *Planck 2018 results. I. Overview and the cosmological legacy of Planck*, arXiv e-prints, arXiv: `1807.06205` (cit. on p. 22).

– (2018b), *Planck 2018 results. VI. Cosmological parameters*, arXiv e-prints, arXiv: `1807.06209` (cit. on pp. 4, 5, 9, 10, 14, 24, 25).

– (2019), *Planck 2018 results. IX. Constraints on primordial non-Gaussianity*, arXiv e-prints, arXiv: `1905.05697` (cit. on p. 22).

Pollack, J. E., R. E. Smith and C. Porciani (2012), *Modelling large-scale halo bias using the bispectrum*, Mon. Not. R. Astron. Soc. **420** 3469, arXiv: `1109.3458` (cit. on pp. 27, 37).

– (2014), *A new method to measure galaxy bias*, Mon. Not. R. Astron. Soc. **440** 555, arXiv: `1309.0504` (cit. on p. 37).

Porciani, C. et al. (1998), *Excursion set approach to the clustering of dark matter haloes in Lagrangian space*, Mon. Not. R. Astron. Soc. **298** 1097, eprint: `astro-ph/9801290` (cit. on p. 37).

Power, G., G. P. Johari and J. K. Vij (2003), *Relaxation strength of localized motions in D-sorbitol and mimicry of glass-softening thermodynamics*, **119** 435 (cit. on p. 33).

Press, W. H. and P. Schechter (1974), *Formation of Galaxies and Clusters of Galaxies by Self-Similar Gravitational Condensation*, Astrophys. J. **187** 425 (cit. on p. 30).

Primack, J. R. and M. A. K. Gross (2001), "Hot dark matter in cosmology", *Current aspects of neutrino physics*, ed. by D. O. Caldwell 287 (cit. on p. 11).

Rees, M. J. (1985), *Mechanisms for biased galaxy formation*, Mon. Not. R. Astron. Soc. **213** 75P (cit. on p. 37).

Riess, A. G., A. V. Filippenko et al. (1998), *Observational Evidence from Supernovae for an Accelerating Universe and a Cosmological Constant*, **116** 1009, eprint: `astro-ph/9805201` (cit. on pp. 4, 11).

Riess, A. G., L. M. Macri et al. (2016), *A 2.4% Determination of the Local Value of the Hubble Constant*, Astrophys. J. **826**, 56 56, arXiv: `1604.01424` (cit. on pp. 9, 10).

Robertson, H. P. (1935), *Kinematics and World-Structure*, Astrophys. J. **82** 284 (cit. on p. 5).

Roth, N. and C. Porciani (2011), *Testing standard perturbation theory and the Eulerian local biasing scheme against N-body simulations*, Mon. Not. R. Astron. Soc. **415** 829, arXiv: `1101.1520` (cit. on pp. 37, 38).

Saito, S. et al. (2014), *Understanding higher-order nonlocal halo bias at large scales by combining the power spectrum with the bispectrum*, Phys. Rev. D. **90**, 123522 123522, arXiv: `1405.1447` (cit. on pp. 38, 39, 48, 65).

Salazar-Albornoz, S. et al. (2017), *The clustering of galaxies in the completed SDSS-III Baryon Oscillation Spectroscopic Survey: angular clustering tomography and its cosmological implications*, Mon. Not. R. Astron. Soc. **468** 2938, arXiv: `1607.03144` (cit. on p. 20).

Scaramella, R., G. Vettolani and G. Zamorani (1991), *The distribution of clusters of galaxies within 300 Mpc/h and the crossover to an isotropic and homogeneous universe*, Astrophys. J. Lett **376** L1 (cit. on p. 5).

Scherrer, R. J. and D. H. Weinberg (1998), *Constraints on the Effects of Locally Biased Galaxy Formation*, Astrophys. J. **504** 607, eprint: `astro-ph/9712192` (cit. on p. 38).

Schmidt, F., D. Jeong and V. Desjacques (2013), *Peak-background split, renormalization, and galaxy clustering*, Phys. Rev. D. **88**, 023515 023515, arXiv: `1212.0868 [astro-ph.CO]` (cit. on p. 38).

Schmittfull, M. et al. (2018), *Modeling Biased Tracers at the Field Level*, arXiv e-prints, 1811.10640 (cit. on p. 38).

Schneider, A. et al. (2016), *Matter power spectrum and the challenge of percent accuracy*, JCAP **4**, 047 047, arXiv: `1503.05920` (cit. on p. 56).

Scoccimarro, R. (2015), *Fast estimators for redshift-space clustering*, Phys. Rev. D. **92**, 083532 083532, arXiv: `1506.02729` (cit. on p. 81).

Scoccimarro, R. et al. (1998), *Nonlinear Evolution of the Bispectrum of Cosmological Perturbations*, Astrophys. J. **496** 586, eprint: `astro-ph/9704075` (cit. on pp. 17, 27).

Senatore, L. (2015), *Bias in the effective field theory of large scale structures*, JCAP **11**, 007 007, arXiv: `1406.7843` (cit. on pp. 20, 38, 39, 42, 48, 49, 99).

Sheth, R. K., K. C. Chan and R. Scoccimarro (2013), *Nonlocal Lagrangian bias*, Phys. Rev. D. **87**, 083002 083002, arXiv: `1207.7117 [astro-ph.CO]` (cit. on p. 19).

Sheth, R. K., H. J. Mo and G. Tormen (2001), *Ellipsoidal collapse and an improved model for the number and spatial distribution of dark matter haloes*, Mon. Not. R. Astron. Soc. **323** 1, eprint: `astro-ph/9907024` (cit. on p. 31).

Slipher, V. M. (1917), *Nebulae*, Proceedings of the American Philosophical Society **56** 403 (cit. on p. 7).

Smith, R. E. et al. (2003), *Stable clustering, the halo model and non-linear cosmological power spectra*, Mon. Not. R. Astron. Soc. **341** 1311, eprint: `astro-ph/0207664` (cit. on p. 26).

Sofue, Y. and V. Rubin (2001), *Rotation Curves of Spiral Galaxies*, **39** 137, eprint: `astro-ph/0010594` (cit. on pp. 4, 11).

Spiegelhalter, D. J. et al. (2002), *Bayesian measures of model complexity and fit*, J. Roy. Statist. Soc. **B64** 583 (cit. on p. 61).

Springel, V. (2005), *The cosmological simulation code GADGET-2*, Mon. Not. R. Astron. Soc. **364** 1105, eprint: `astro-ph/0505010` (cit. on pp. 4, 33, 51).

Springel, V., C. S. Frenk and S. D. M. White (2006), *The large-scale structure of the Universe*, **440** 1137, eprint: `astro-ph/0604561` (cit. on p. 19).

Springel, V., S. D. M. White, A. Jenkins et al. (2005), *Simulations of the formation, evolution and clustering of galaxies and quasars*, **435** 629, eprint: `astro-ph/0504097` (cit. on p. 19).

Springel, V., S. D. M. White, G. Tormen et al. (2001), *Populating a cluster of galaxies - I. Results at [formmu2]z=0*, Mon. Not. R. Astron. Soc. **328** 726, eprint: `astro-ph/0012055` (cit. on p. 35).

Suzuki, N. et al. (2012), *The Hubble Space Telescope Cluster Supernova Survey. V. Improving the Dark-energy Constraints above z 1 and Building an Early-type-hosted Supernova Sample*, Astrophys. J. **746**, 85 85, arXiv: `1105.3470 [astro-ph.CO]` (cit. on p. 11).

Szalay, A. S. (1988), "Constraints on the Biasing of Density Fluctuations", *Large Scale Structures of the Universe*, ed. by J. Audouze et al., vol. 130, IAU Symposium 163 (cit. on p. 38).

Tinker, J. L. et al. (2010), *The Large-scale Bias of Dark Matter Halos: Numerical Calibration and Model Tests*, Astrophys. J. **724** 878, arXiv: `1001.3162` (cit. on pp. 31, 66, 67).

Tsujikawa, S. (2003), *Introductory review of cosmic inflation*, arXiv High Energy Physics - Phenomenology e-prints, eprint: `hep-ph/0304257` (cit. on p. 22).

Vogelsberger, M. et al. (2014), *Introducing the Illustris Project: simulating the coevolution of dark and visible matter in the Universe*, Mon. Not. R. Astron. Soc. **444** 1518, arXiv: `1405.2921` (cit. on p. 4).

Walker, A. G. (1937), *On Milne's Theory of World-Structure*, Proceedings of the London Mathematical Society, (Series 2) volume 42, p. 90-127 **42** 90 (cit. on p. 5).

Watanabe, S. (2010), *Asymptotic Equivalence of Bayes Cross Validation and Widely Applicable Information Criterion in Singular Learning Theory*, J. Mach. Learn. Res. **11** 3571, ISSN: 1532-4435, URL: `http://dl.acm.org/citation.cfm?id=1756006.1953045` (cit. on p. 61).

Watkinson, C. A. et al. (2017), *A fast estimator for the bispectrum and beyond - a practical method for measuring non-Gaussianity in 21-cm maps*, Mon. Not. R. Astron. Soc. **472** 2436, arXiv: `1705.06284` (cit. on p. 81).

Weinberg, S. (1977), *The first three minutes. A modern view of the origin of the universe* (cit. on p. 3).

Werner, K. F. and C. Porciani (2019), *Renormalisation of linear halo bias in N-body simulations*, arXiv e-prints, arXiv: `1907.03774` `[astro-ph.CO]` (cit. on pp. 37, 73).

White, M. (2014), *The Zel'dovich approximation*, Mon. Not. R. Astron. Soc. **439** 3630, arXiv: `1401.5466` (cit. on p. 34).

White, S. D. M. et al. (1987), *Galaxy distribution in a cold dark matter universe*, **330** 451 (cit. on p. 37).

Yankelevich, V. and C. Porciani (2019), *Cosmological information in the redshift-space bispectrum*, Mon. Not. R. Astron. Soc. **483** 2078, arXiv: `1807.07076` (cit. on p. 27).

Zel'dovich, Y. B. (1970), *Gravitational instability: An approximate theory for large density perturbations.*, Astron. Astrophys. **5** 84 (cit. on p. 34).

Zeldovich, Y. B. (1972), *A hypothesis, unifying the structure and the entropy of the Universe*, Mon. Not. R. Astron. Soc. **160** 1P (cit. on p. 24).

Zhan, H. and J. A. Tyson (2018), *Cosmology with the Large Synoptic Survey Telescope: an overview*, Reports on Progress in Physics **81**, 066901 066901, arXiv: `1707.06948` (cit. on p. 13).

Posterior distributions of the bias parameters

In Figs. A.1 – A.3 we show the marginalised one- and two-dimensional posterior distributions of the bias parameters, measured in chapter 2 with our MCMC routine where we implemented the fitting scheme from section 2.5.1. Shown are the bias parameters obtained by fitting equations (2.69) and (2.71) against $P_{\delta_{\rm h}\delta}(k)$ for the three halo mass bins and three values of Λ. Light and dark shadings indicate the 68.3 and 95.4 per cent credibility regions, respectively. The larger Λ is, the better constrained are the bias parameters due to the increased number of data points considered in the fit.
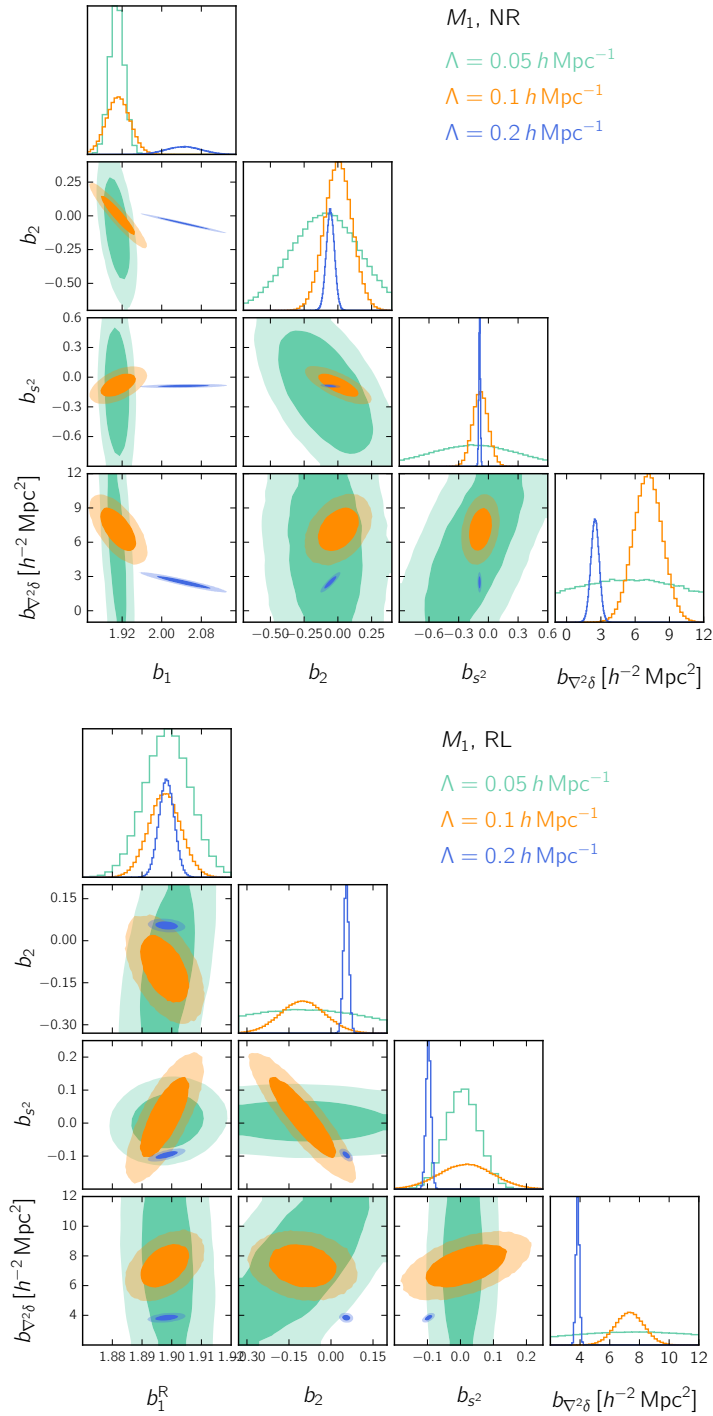
Figure A.1: Posterior distributions of the bias parameters b_1, b_2, b_{s^2} and $b_{\nabla^2\delta}$ obtained by fitting $P_{\delta_{\mathrm{h}}\delta}(k)$ for three values of Λ. Results are shown for the halo mass bin M_1. The top and bottom panels refer to the NR model given in equation (2.69) and the RL one in equation (2.71), respectively. The shaded areas indicate 68.3 and 95.4 per cent credibility intervals.
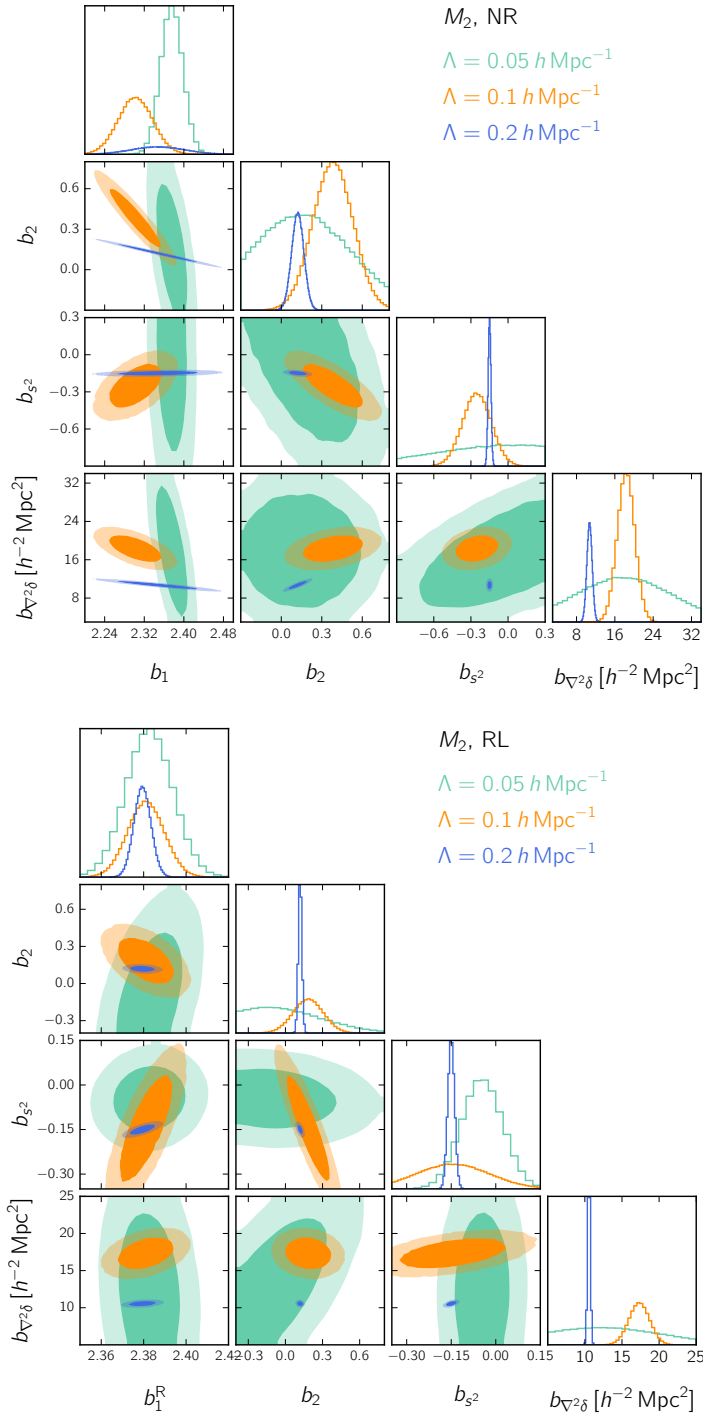
Figure A.2: The same as Fig. A.1, but for halo mass bin M_2.
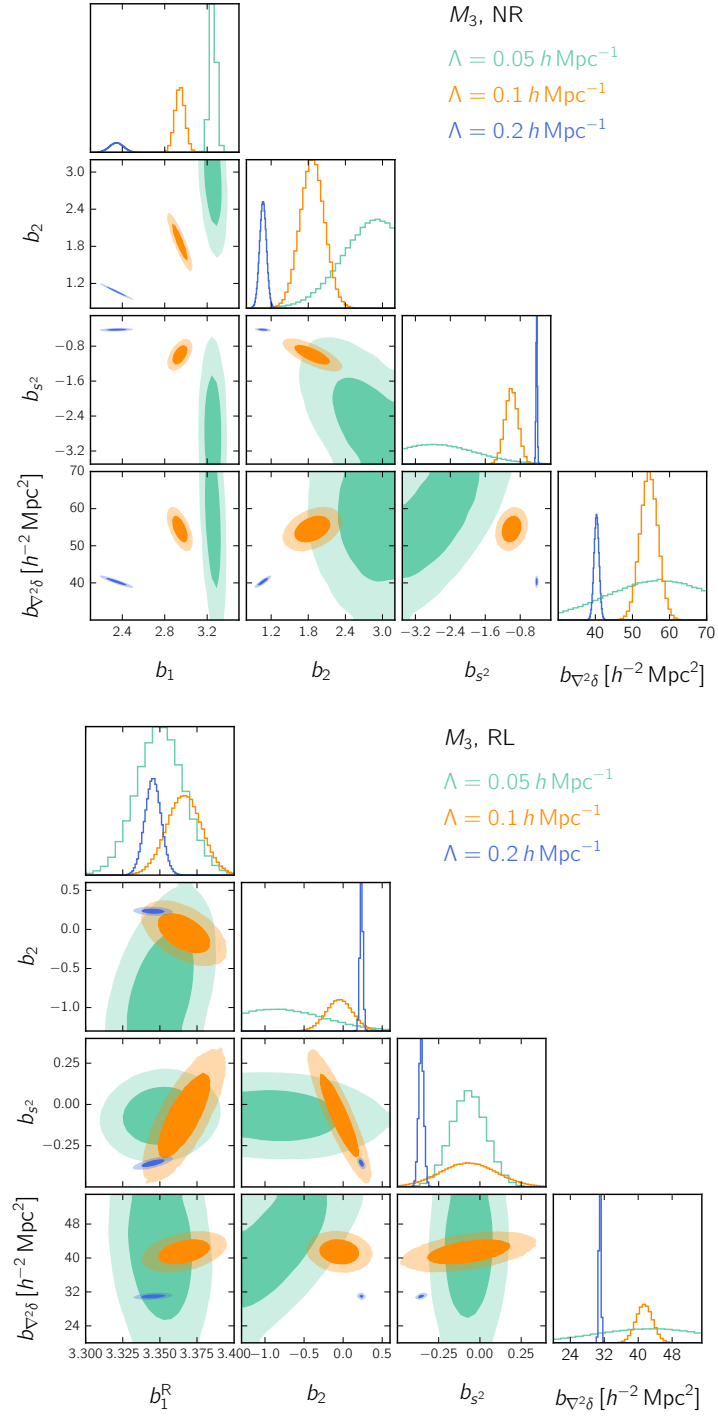
Figure A.3: The same as Fig. A.1, but for halo mass bin M_3.

Three-dimensional impression of one simulation

In Fig. B.1 we show a three-dimensional artistic impression of the actual particle distribution in one of the cosmological simulations. Displayed is a cube of side length $L = 150\,h^{-1}\,\mathrm{Mpc}$ which coincides with one corner of the simulation. The figure was generated using the rendering software BLENDER[1] by placing light-emitting particles in otherwise dark three-dimensional space on top of a diffusely reflecting surface, and solving the render equations for this setup.

---

[1] https://www.blender.org/
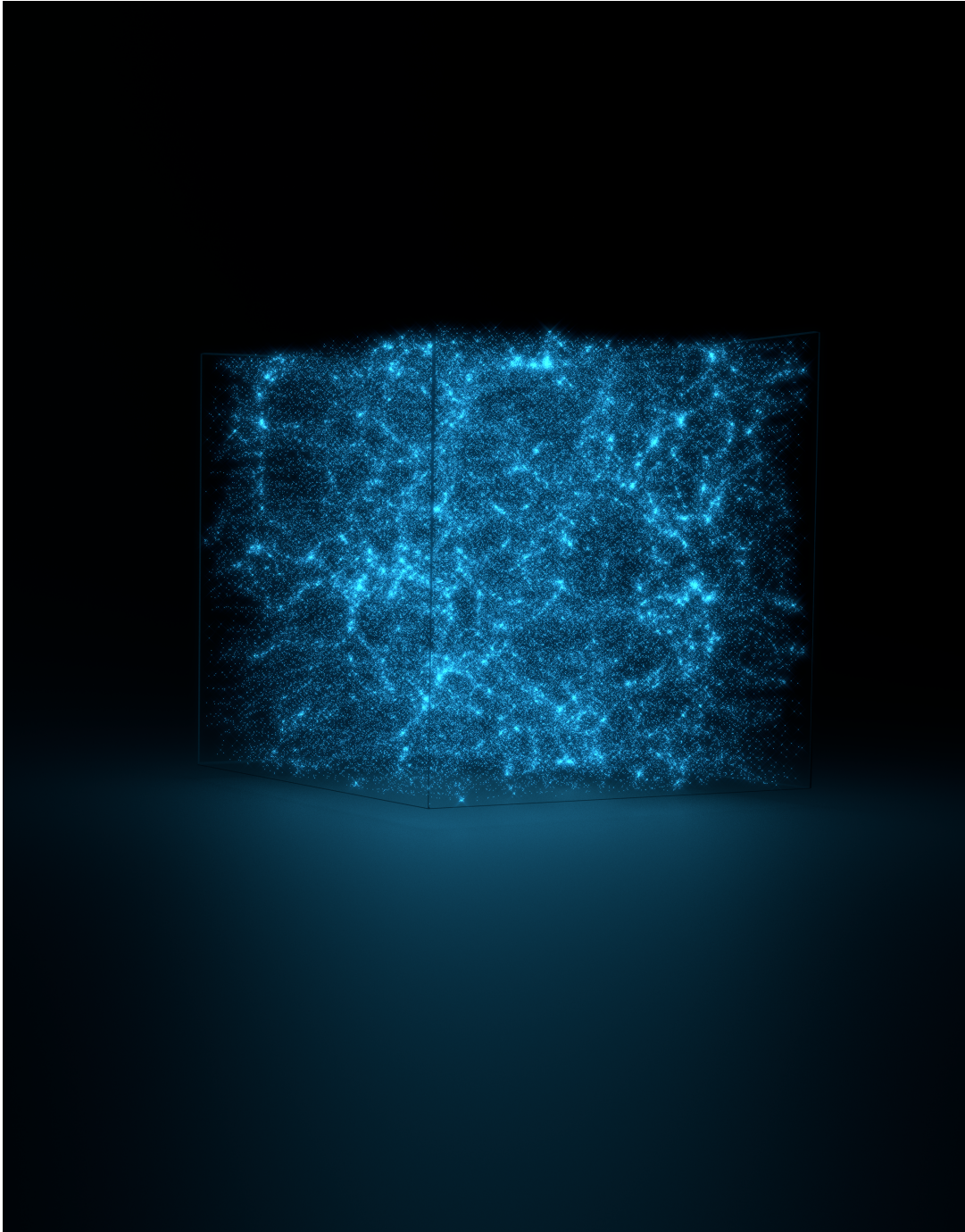
Figure B.1: A three-dimensional impression of the particle distribution in one of the simulations in form of a cube with side length $L = 150\,h^{-1}\,\mathrm{Mpc}$. Image Credit (technical implementation): Alexander Schäbe.

List of Figures

List of Tables

Acknowledgements